Editorial corner – a personal view
(Multi)functional polymers and composites via Diels-Alder reactions

J. Karger-Kocsis[*]

Department of Polymer Engineering, Faculty of Mechanical Engineering, Budapest University of Technology and Economics, and MTA-BME Research Group for Composite Science and Technology, Műegyetem rkp. 3., Budapest H-1111, Hungary

Nowadays, research activities address the development of (multi)functional (also termed to as intelligent, smart, responsive) materials. The attribute 'functional' refers to a combination of properties which are essentially independent of each other. Accordingly, the related materials – apart from the required load bearing capability – exhibit 'functional' properties, such as shape memory, self healing, sensing/actuation, electric conductivity, reprocessability etc.

Chemical approaches, and especially those offered by the click chemistry can well be used to produce multifunctional polymers and related composites. In the Diels-Alder (DA) reaction a cyclic compound is formed in the reaction between a diene (usually furan, cyclopentadiene, anthracene) and a dienophil (usually maleimide, methacrylate, dicyclopentadiene). The discovery of this thermoreversible reaction is credited to O. Diels and K. Alder (1924) who have been awarded by the Nobel prize in 1950. A further beauty of the DA reaction is that it can be performed in aqueous media, solutions and melts, as well. DA adducts can be repeatedly generated after retro DA reactions liberating the initial functional groups. This feature has been used to demonstrate the feasibility of intrinsic self healing (DOI: 10.1126/science.1065879). This pioneering work triggered vivid interest for adapting DA reactions for self healing and recycling (i.e. reprocessing) of highly crosslinked thermosets, especially epoxy resins (DOI: 10.1039/c2py20957h; DOI: 10.1002/pola.27655). The most versatile polymer synthesis, namely that of polyure-thanes, is in the forefront of DA-related research. The furan/maleimide reaction proved to be a straightforward tool to create reprocessable rubbers, the characteristics of which are similar to traditionally crosslinked ones (DOI: 10.1021/acs.macromol.5b01422). DA reaction is a promising route also to create self healing interphase in polymer composites (DOI: 10.1016/j.compscitech.2015.08.015; DOI: 10.1016/j.pmatsci.2015.02.003). Recent efforts focus on the exploitation of hetero DA reactions in the synthesis of functional polymers (DOI: 10.1039/c4py00644e). In the meantime exhaustive reviews appeared on the use of DA reactions to produce multifunctional polymer and related composites. The interested reader will find several contributions also in our Journal when searching for 'Diels-Alder' on the web site of *eXPRESS Polymer Letters*, and they will be even more.

On the other hand, the versatility of DA is still less explored at present because most of the publications follow the furan/maleimide reaction pathway (DOI: 10.1016/j.progpolymsci.2012.04.002). So, why not to explore further the 'offer' of the DA reactions?

Prof. Dr. Dr. h.c. József Karger-Kocsis
Editor-in-Chief

[*]Corresponding author, e-mail: karger@pt.bme.hu

Novel method of polymer/low-melting-point metal alloy/light metal fiber composite fabrication

J. Park, K. S. Shin[*]

Magnesium Technology Innovation Center, Department of Materials Science and Engineering, Seoul National University, 1 Gwanak-ro, Gwanak-gu, Seoul 08826, Republic of Korea

Abstract. A novel method of polymer/low-melting-point metal alloy (LMA)/light metal fiber composite fabrication is proposed to solve problems of polymer/metal composites. The first step is mixing light metal particles with LMA at a temperature above the melting point of the LMA. The second step is cold extrusion of the LMA/light metal particles to fabricate LMA/light metal fibers. Thus, the LMA/light metal fibers with a density of ~4.5 g/cm^3 were obtained. The last step is compounding a polymer with the LMA/light metal fibers at the processing temperature of the polymer above the melting points of the LMA. The effects of the length and the cross-sectional shape of light metal fiber on the morphology of the LMA/light metal fibers in the polymer matrix were studied, as were electrical conductivities and mechanical properties of the composites. As the length and/or the cross-sectional aspect ratio of the fibers was increased, the domains of LMA/light metal fibers formed more networks so that the electrical conductivity increased, and specific surface area of the domains increased so that notched Izod impact strength was improved. Thus, the polymer/LMA/light metal fiber composites were fabricated without degrading processability even at 60 vol% loading and the electrical conductivities over 10^3 S/cm were achieved.

Keywords: polymer composites, low-melting-point metal alloy, light metal fiber, electrical conductivity

1. Introduction

Electrically conductive polymer composites have drawn a lot of attentions of scientists and engineers due to their applications in various areas, such as electronic components, energy storage devices, electromagnetic interference shielding, antistatic materials, and sensors [1–3]. A traditional approach in fabrication of such a composite material is addition of electrically conductive fillers into insulating polymer to incorporate two complementary properties of electrical conductivity and processability. For example, carbon fillers such as graphite, carbon black and carbon fibers are commercially added to the insulating polymers [4–8]. They have advantages of low density and good conductivity; however, the addition of a high amount of carbon fillers for producing conductivity causes increase of viscosity resulting in degradation of processability. Carbon nanotube is one of promising alternatives. Small amounts of addition can enhance conductivity significantly due to its high aspect ratio with nanometer thick diameter [9–10]. However, it still has limitations of high cost and poor dispersibility in the polymer matrix due to van der Waals and Coulomb attractions.

Electrically conductive metal fillers can also be used as conductive filler in polymer composites, such as magnesium, aluminum, nickel, copper, silver, stainless steel and etc. [11–13]. Typically, inclusion of metal fillers increases the overall weight of composites due to their high densities when the same volume of fillers are added. Also large amounts of addition yield poor processability. Exceptionally, magnesium and aluminum are known for light-

---

weight-metal showing relatively low density comparing to other metals. However, magnesium has a low corrosion resistance requiring additional treatment for corrosion protection [14]. In the case of aluminum, a dense oxidation layer formed on the surface increases the electrical resistivity of the composite [15].

An interesting approach was proposed to maintain processability at high filler loading by applying a low-melting-point metal alloy (LMA) by Zhang *et al.* [16]. Since LMA melts at the processing temperature of polymer, it does not increase viscosity of the composite due to the low viscosity of molten LMA. However, as LMA droplets were fused into large domains above melting temperature, electrical networks was not formed, resulting in a low electrical conductivity under 10^{-15} S/cm [17]. To disperse the domains of LMA, solid metal particles were combined with LMA. Small loadings of nickel particulates prevented coalescence of the molten LMA droplets resulting in high conductivity of ~10^2 S/cm [18]. Compounding copper fibers and LMA together with a polymer improved the dispersability of LMA and increased the filler efficiency due to large aspect ratios of LMA domains showing very high conductivity of ~10^4 S/cm [19]. It was suggested that the solid particle acts as a mechanical aid; increasing the viscosity of the LMA droplet and slowing down the coalescence process. However, LMA/solid metal particle also has a high density, therefore the polymer composite still remains heavy.

In order to solve these problems, a polymer/LMA/light metal fiber composite is proposed in this study. LMA was designed to be mixed with the light metal overcoming the difference of the densities of LMA and the light metal. As it encapsulates the light metal in the composite, it can play the role of blocking the increase in electrical resistance due to oxidation of the surface of the light metal. And it melts at the processing temperature of polymer and maintains processability of the composites during compounding with polymer. The light metal fiber reduces the density of the metal filler to minimize the increase in the weight of the composite. It also increases the efficiency as conductive filler by presenting a fiber form. Furthermore, it improves the dispersibility of the LMA domain by maintaining a solid state during compounding. The resulting composites exhibited high electrical conductivity and enhanced mechanical properties.

2. Experimental
2.1. Materials
Polystyrene-acrylonitrile (SAN) was used as polymer matrix and was supplied by Samsung SDI Co., Ltd. (Republic of Korea). The physical properties of SAN are as follows: The acrylonitrile content of SAN is 24.5 wt%, the weight-average molecular weight is 140 000, the melt flow index is 2.7 g/10 min in 200 °C/5.86 kg condition, and the notched Izod impact strength is 21.6 J/m. Aluminum (Al) was selected as the light metal particles with density of 2.7 g/cm^3. Al particles with spherical shape and particle size of 44~100 μm were used. Sn-Zn30 alloy having tin (Sn) 70 wt% with zinc (Zn) 30 wt% was used as LMA, which starts to melt from 230 °C.

2.2. Preparation of composite samples
Composite samples were prepared through the processes shown in Figure 1. Mixture of Sn-Zn30 and Al particles with the ratio of 40/60 vol% was stirred at 50 rpm and 270 °C for 10 minutes. Then, a cylindrical billet with a diameter of 76.2 mm and a height of 200 mm was molded. Afterwards, Sn-Zn30/Al fiber was fabricated using a 600 ton extruder at 170 °C which is lower than the solidus temperature of Sn-Zn30. During the extrusions, the shape of the die was varied so that the metal fiber being generated through the extrusion process was made to have different lengths and cross-sectional shapes: circular diameter 24 mm, extrusion ratio 10; circular diameter 15.2 mm, extrusion ratio 25; and, rectangular width 26 mm, thickness 7 mm, extrusion ratio 25. The extrusion ratio is defined as the starting cross-sectional area divided by the cross-sectional area of the final extrusion. The processing conditions and the densities of the Sn-Zn30/Al fiber are organized in Table 1. It was found that lighter metal fillers (~4.5 g/cm^3) were fabricated than typical metal fillers (7–9 g/cm^3). Figure 2 shows that Al fibers were elongated and thinned according to the increase in the extrusion ratio. In addition, when the shape of the extrusion die was rectangular, the width of the Al fibers increased and the thickness of the Al fibers decreased, in other words the Al fibers became flattened. From these results, it can be implied that the length of the Al fiber increases with increasing the extrusion ratio and the cross-sectional aspect ratio of the Al fiber increases when a rectangular die is used. Subsequently, Sn-Zn30/Al fiber was compounded with SAN for 5 minutes under the conditions of
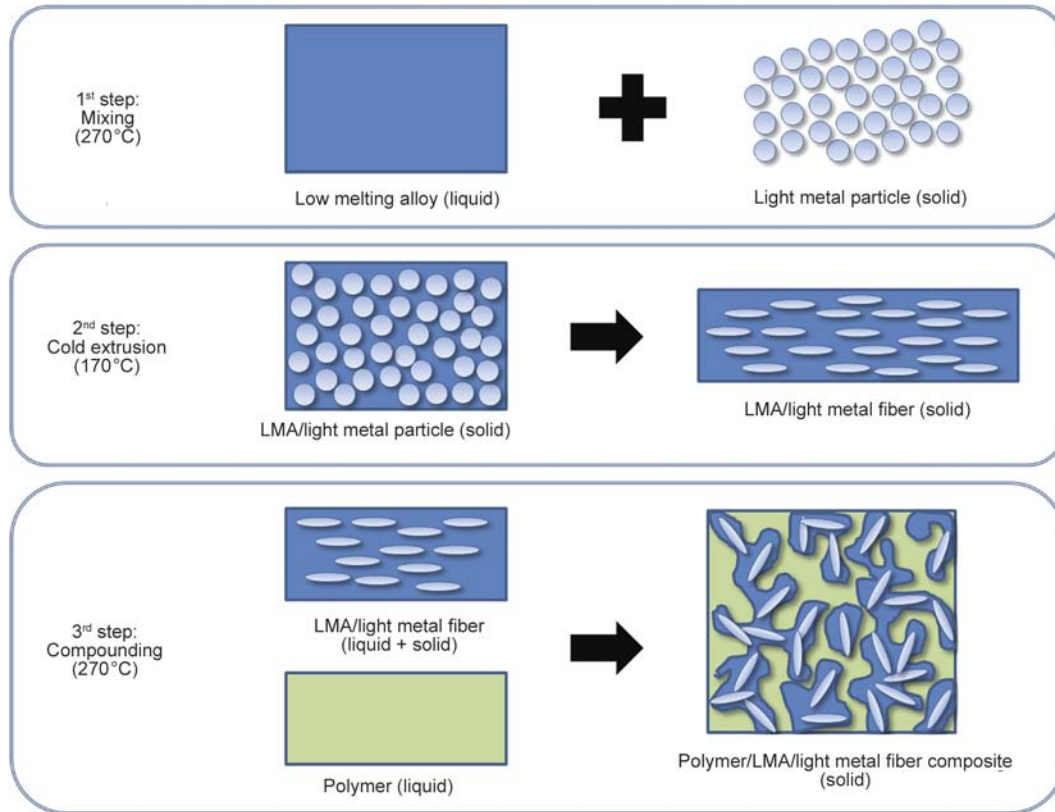
Figure 1. The technological process of preparing polymer/LMA/light metal fiber composite

Table 1. Processing conditions and densities of the metal fillers prepared

Sn-Zn30/Al fiber code	Die shape	Extrusion ratio	Density [g/cm³]
C10	Circle	10	4.48
C25	Circle	25	4.54
R25	Rectangular	25	4.55

270 °C at 50 rpm, using an internal mixer (HAAKE Polylab QC, Thermo Fischer Scientific, USA) with roller rotors. Samples were prepared varying the content of Sn-Zn30/Al fiber of 20, 40, and 60 vol%, respectively. And in order to see the effects of LMA on the processability, for comparative evaluation, Al particles 20, 40, and 60 vol% was compounded with SAN under the same conditions. Through hot pressing, composites and pure SAN (without fillers) were made into a 150 mm×150 mm×3.2 mm plate, and from that, specimens were produced that had a standard dimension for measuring electrical properties and mechanical properties.

2.3. Measurements

The morphology of Sn-Zn30/Al fiber in SAN matrix was observed using field emission scanning electron microscopy (FE-SEM, SU-70, Hitachi, Japan) with energy dispersive spectroscopy (EDS, Hariba, Japan).

The max torque was measured as the maximum value of torque on the rotors of the internal mixer during the compounding of each sample using the HAAKE Polysoft software package. For samples with an electrical conductivity higher than 10^{-7} S/cm, the electrical conductivity was measured by a four-point probe method at room temperature. The dimensions of the sample for electrical conductivity measurements were 60 mm×12.7 mm×3.2 mm. A constant current was applied using a source meter (2400, Keithley, USA) to the outer probes of the four contacts, and the corresponding voltage was measured between inner probes using a nanovolt meter (2182, Keithley, USA) as shown in Figure 3. For samples with an electrical conductivity lower than 10^{-7} S/cm, the measurements were performed by a two-point probe method using only a source meter. Density was measured according to the ASTM D792 test method using a densimeter (Toyoseki, Japan). Notched Izod impact strength was measured according to the ASTM D256 test method (DG-1B, Toyoseki, Japan). The thickness of the testing sample was about 3.2 mm. The three-point bending flexural modulus tests were conducted according to the ASTM D790 test method (UTM 3367, Instron, USA). The cross-head speed was 1.4 mm/min and the distance
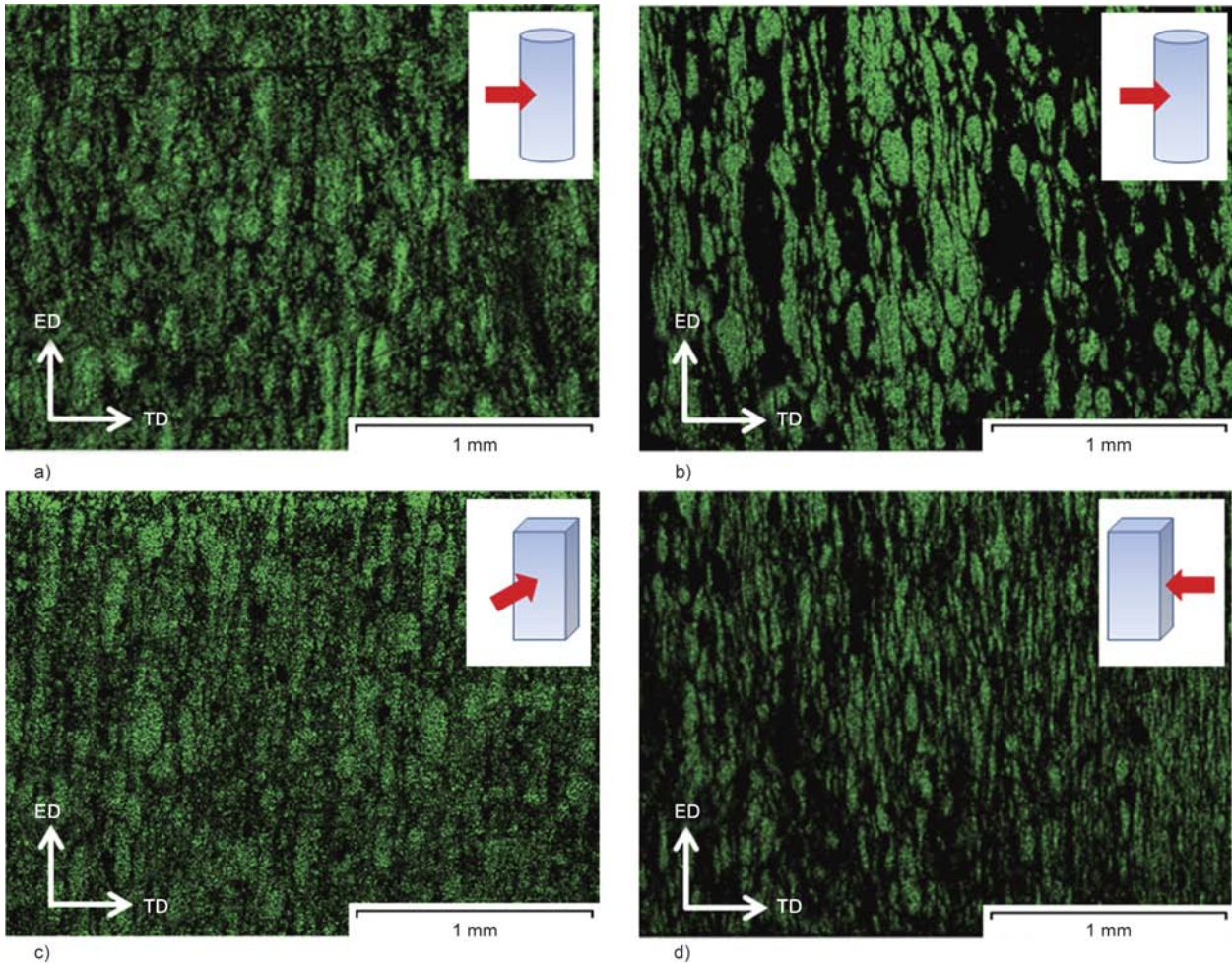
Figure 2. Aluminum (green color) EDS mapping results of extruded Sn-Zn30/Al fiber (red arrow is the direction of observation in inner picture); (a) C10, (b) C25, (c-d) R25
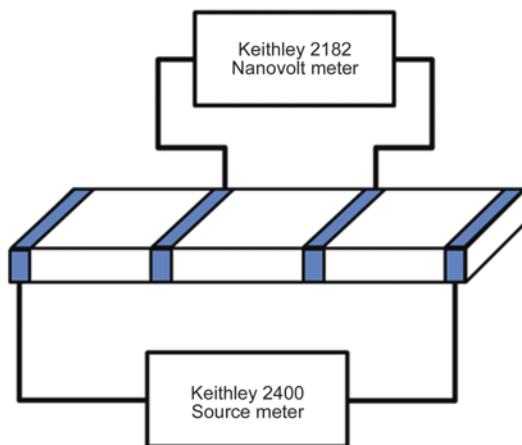

Figure 3. Electrical measurement set-up

between the two bottom points was 50 mm. The typical dimensions of the sample beams were 70 mm×12.7 mm×3.2 mm. The tensile tests were conducted according to the ASTM D638 test method (UTM 3367, Instron USA) at a crosshead speed of 5 mm/min. The specimens for tensile tests were type I with thickness 3.2 mm. The electrical and mechani-

cal properties were measured for 5 specimens of each composite and the average values were used for results and discussion.

3. Results and discussion
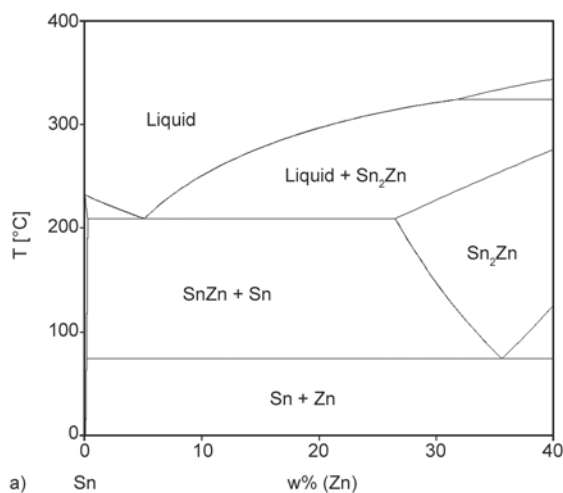### 3.1 Composition of LMA

As can be seen in Figure 1, LMA becomes the matrix of LMA/light metal particles mixture in the first and second processes but act as conductive filler which is dispersed in the polymer matrix during the third process. Sn is a good candidate for LMA since it has a melting temperature of 230 °C similar to the processing temperature of SAN. However, since the density of Sn (7.29 g/cm^3) is much higher than Al, Al particles floated on top of the liquid Sn during the mixing process. The large difference in density made it very difficult to mix Al particles in liquid Sn. With regard to sedimentation, the particle velocity in the liquid under gravity would be Equation (1) [20]:

$$v = \frac{2a^2(\rho_P - \rho)}{9\eta} g \qquad (1)$$

where v is the sedimentation velocity of the particle, a is the radius of the particle, ρ_P is the density of the particle, ρ is that of the liquid, η is the viscosity of the liquid and g is the acceleration of gravity. Assuming that a is 70 μm, ρ_P is 2.7 g/cm³, ρ is 7.29 g/cm³, and η is 1.5 mPa·s [21], the sedimentation velocity of the Al particle is –3 mm/s. As the value of the sedimentation velocity of the Al particle is negative, the Al particle is floating onto liquid Sn. The velocity is too fast for Al particles to be mixed with liquid Sn. When the density of the liquid and particle and the radius of the particle are fixed in Equation (1), the method for slowing the velocity is to increase η. However, for pure metal, it is difficult to control the viscosity since the viscosity will rapidly change during the phase transition from solid to liquid. Thus in order to increase the viscosity, a coexisting region with liquid and solid at the processing temperature of about 270 °C is needed. For a general solid-liquid suspension, the viscosity is a function of the fraction of solid. An equation which has been obtained from the empirical data can be expressed as Equation (2) [22]:

$$\frac{\eta_s}{\eta_0} = 1 + 2.5\Phi + 10.05\Phi^2 + A\exp(B\Phi) \qquad (2)$$

where η_s is the viscosity of the solid-liquid suspension, η_0 is the viscosity of the pure liquid, Φ is the volume fraction of solid in the suspension, and A and B are constants which are found to be 0.00273 and 16.6 respectively. We utilized thermodynamic program Pandat™ to calculate phase fraction plot of Sn-Zn30 alloy as shown Figure 4. Calculation results show that solidus and liquidus temperature are 230 and 320 °C, respectively. And solid volume fraction is 0.7 at 270 °C. Taking these values into Equation (2), the viscosity of suspension is calculated to be 220 Pa·s. Then the velocity of the sedimentation of the Al particle is much decreased to $-2 \cdot 10^{-5}$ mm/s obtained from Equation (1). When mixing the Al particles in pure tin at 270 °C, they were immiscible and the Al particles became oxidized and blackened, and only the tin was solidified. However, when the Al particles were mixed into Sn-Zn30, it mixed well as shown in Figure 5.

3.2. Max torque during compounding of SAN/Sn-Zn30/Al fiber composites

In order to examine processability, the maximum value of torque on the rotors of the internal mixer was measured during the compounding of each sample. Figure 6 shows that the max torque increases as the filler content increased, indicating that the viscosity of the composite increases due to addition of Sn-Zn30/Al fiber. On the contrary, in the previous study of Zhang *et al.* [23], viscosity was decreased while LMA content was increasing in polystyrene/Sn-Pb30 (Sn 70 wt% and lead (Pb) 30 wt%). In case of polystyrene/Sn-Pb30 composites, LMA was entirely liquid at the processing temperature of 190 °C. Meanwhile, in current study, Sn-Zn30 is in coexisting state of solid and liquid and Al fibers is also solid at the processing temperature of 270 °C. Therefore the viscosity of SAN/Sn-Zn30/Al fiber composites increases, when the filler content is increased. Comparing to sample of Al particles used alone, SAN/Sn-Zn30/Al fiber composites show sig-
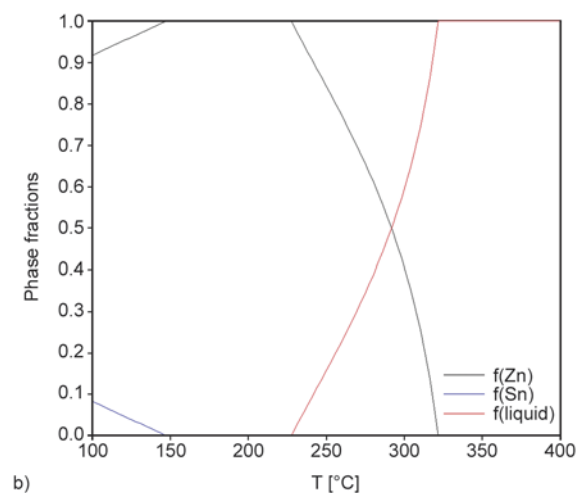

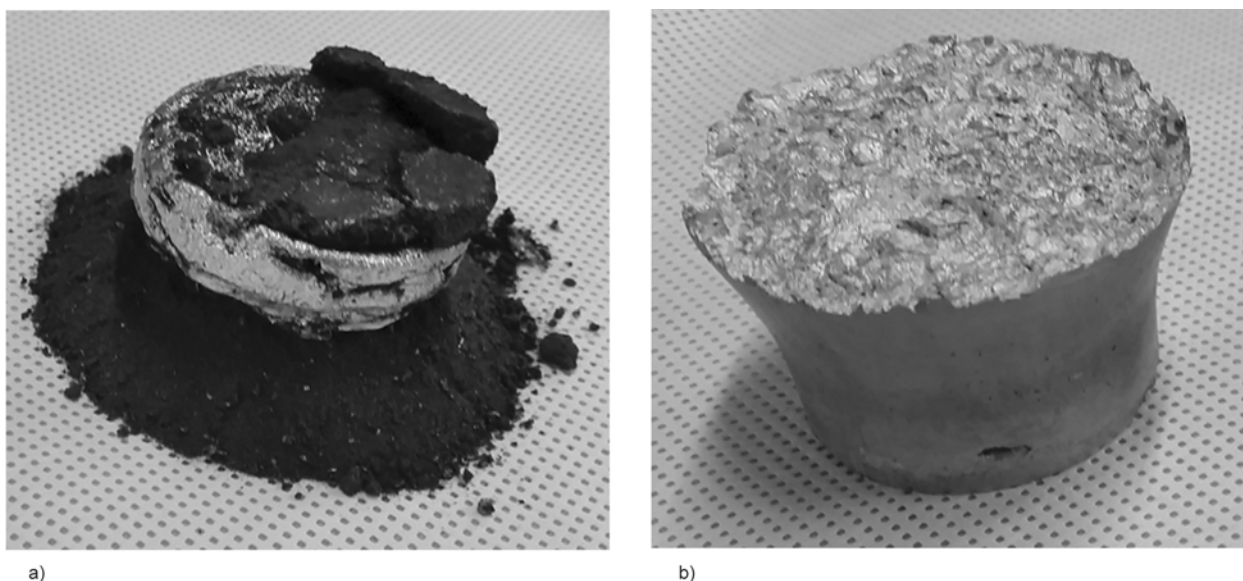**Figure 4.** (a) Phase diagram of Sn-Zn, (b) phase fraction plot of Sn-Zn30 as a function of temperature

Figure 5. Mixture after 10 min mixing under 50 rpm stirring; (a) pure tin and aluminum particles, (b) Sn-Zn30 and aluminum particles
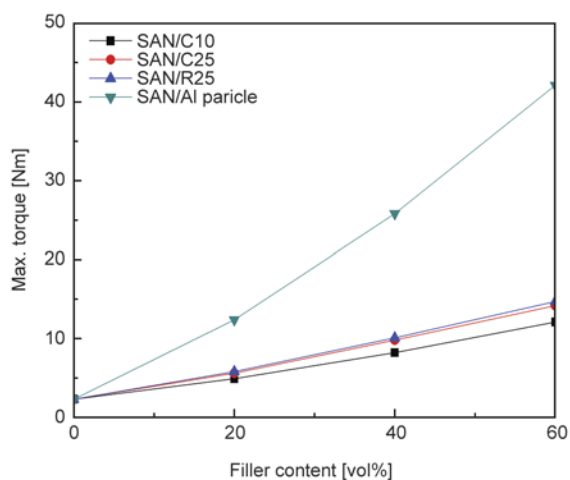

Figure 6. Max torque of the internal mixer during compounding of the SAN/Sn-Zn30/Al fiber composites

nificantly lower torque, indicating that the molten Sn-Zn30 mitigates the shear stress applied to the solid in the filler lowering the viscosity of the filler. In case that the extrusion ratio was high, the max torque was slightly higher. We presumed that, as the length of fiber is increased, the excluded volume of the fiber is also increased, resulting in an increase of the viscosity [24].

3.3. Morphology of Sn-Zn30/Al fiber in the SAN matrix

The morphology of Sn-Zn30/Al fiber in SAN matrix was observed using EDS. The Al fibers were wrapped around by Sn and Zn and well-dispersed as can be seen in Figure 7. During cold extrusion, the oxidation layer of Al surface might become thin and/or

be broken as Al particles were elongated. Therefore, Sn-Zn30/Al fiber through cold extrusion can reduce the oxidation layer of Al surface which can affect the wetting behavior. Since the surface tension of Sn-Zn30 is much greater than that of SAN, a large domain must be formed thermodynamically by aggregation. However, the dispersibility of the filler is improved because the solid Al fibers physically help the dispersion and slow the rate of aggregation with increase of the viscosity of the filler within molten Sn-Zn30 [18]. The domains of the metal filler became elongated with the increase in the extrusion ratio of the Sn-Zn30/Al fiber, indicating that the domain shape of the filler can be controlled by the shape of Al fiber. When polymer/metal composites were prepared using LMA alone, the domains of LMA in the polymer/LMA composite generally formed large spherical droplet due to the surface tension of LMA, therefore the efficiency as conductive filler decreased [17]. In contrast, Sn-Zn30/Al fiber system can improve the efficiency as conductive filler by increasing the length of Al fiber. It is believed that the efficiency as conductive filler relates to the connectivity between the domains of the filler. When the extrusion ratio increased and/or the shape of the extrusion die was rectangular, as with samples C25 and R25, the connectivity improved since the specific surface area increased as the length and/or the cross-sectional aspect ratio of the Al fiber increased. In addition, although the domains of the filler became larger with increasing filler content, the connectivity improved by maintaining the
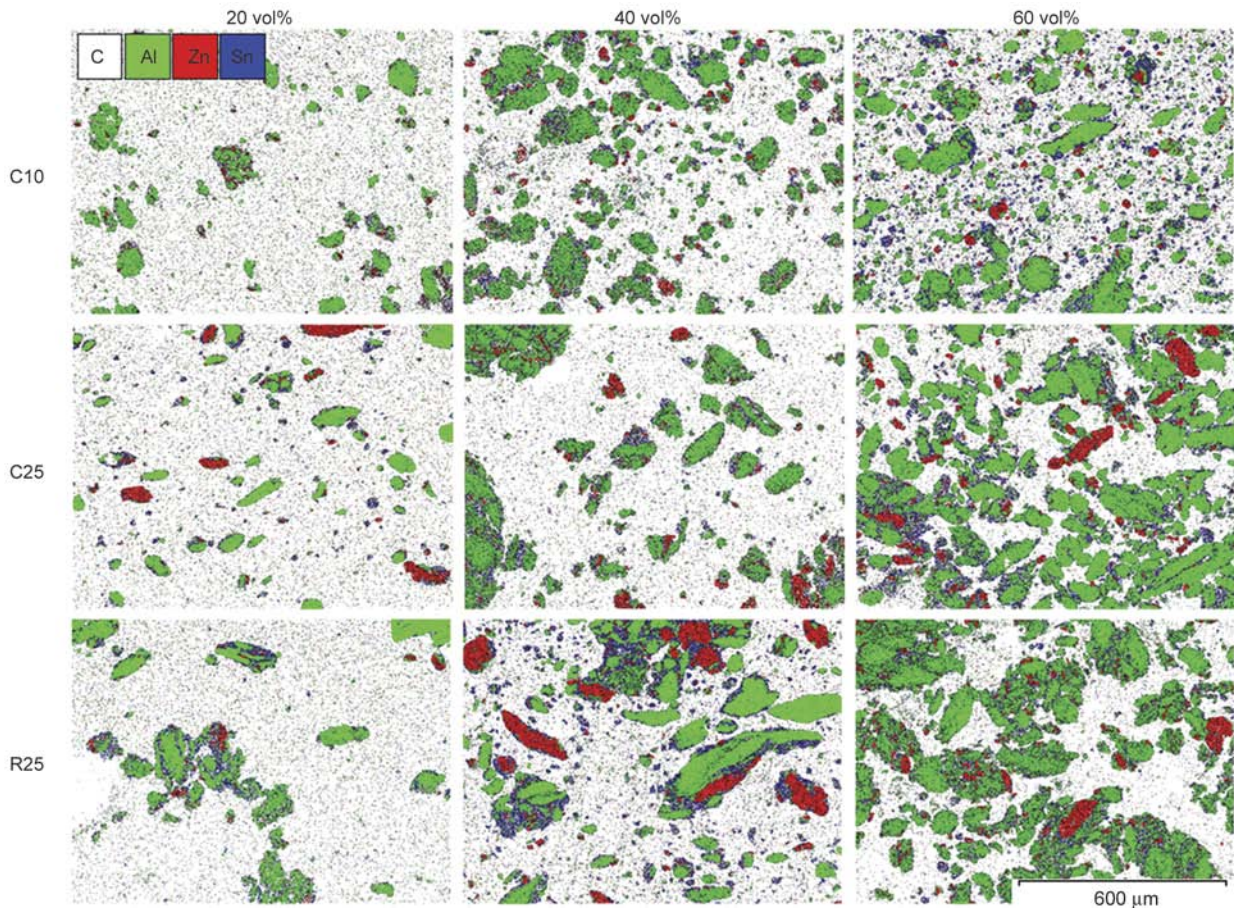
Figure 7. EDS mapping images of SAN/Sn-Zn30/Al fiber composites

elongated domains due to the Al fibers. It can be concluded that the incorporation of Al fiber is critical in the dispersion of the filler and in the improvement of the efficiency as conductive filler.

3.4. Electrical conductivity

Figure 7 shows that the connectivity between the domains of Sn-Zn30/Al fiber increases as the content of Sn-Zn30/Al fiber, the length of Al fiber, and the cross-sectional aspect ratio of Al fiber increases. It is generally believed that the conductivity of the composite derives from the formation of a conducting network by the fillers in the matrix, and the increase of conductivity paths facilitates the improvement of the composite conductivity [25]. Such formation of a conducting network would improve the electrical conductivity of SAN/Sn-Zn30/Al fiber composites. Thus, Figure 8 shows that the electrical conductivities of the composites increased with increasing the filler content. The composites with filler at 20 vol% resulted in low conductivities of ~10^{-12} S/cm since the conducting networks were not formed, as shown in Figure 7. From a filler content of 40 vol% and higher, the conductivities
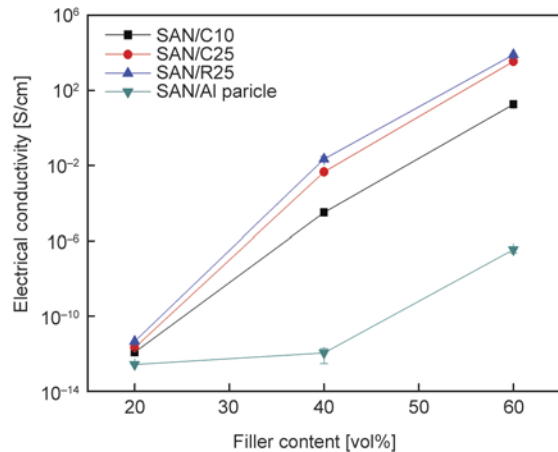

Figure 8. Electrical conductivity of SAN/LMA/Al fiber composites

increased dramatically. In addition, the electrical conductivities of SAN/C25 and R25 were higher than that of SAN/C10 at the same filler content. This indicates that as the domains are more elongated, the electrical conductivity increases due to improving the connectivity between the fillers. As the electrical conductivities of SAN/Sn-Zn30/Al fiber composites were higher than those of SAN/Al particle composites, it is implied that the oxide layer on the

surface of Al fiber could not impede the electrical conductivity due to the encapsulation of Sn-Zn30. For SAN/R25 at 60 vol% loading, the polymer matrix and the domains of fillers formed almost co-continuous structure as shown in Figure 8, resulting in the electrical conductivity of 7900 S/cm. This electrical conductivity is higher than that (~10^2 S/cm) of polymer/LMA/nickel particle at 60 vol% loading [18], indicating that Al fiber is more effective than nickel particle due to the fibrous shape.

3.5. Density and mechanical properties

The results of density and mechanical properties were summarized in Table 2. As the density of Sn-Zn30/Al fiber (~4.5 g/cm³) is relatively lighter than that of other LMA fillers (7–9 g/cm³), the density of SAN/Sn-Zn30/Al fiber composite is lighter than other polymer/LMA filler composites. While the estimated density of polymer/LMA/nickel particle composite with the filler content of 60 vol% is ~5.6 g/cm³ [18], the density of SAN/R25 with the same content is 3.14 g/cm³.

The impact strength decreased slightly with the filler content of 20 vol%, but the impact strength was enhanced with the increase of the filler content as shown in Figure 9. In addition, when the extrusion ratio was increased and the shape of the extrusion die was rectangular, the growth rate was much larger. The fractured surfaces after notched Izod testing were observed through SEM as shown in Figure 10. It can be seen that the fracture occurred at the interface of SAN and the filler. Since the interaction between SAN and the filler is weak, the filler acts as a defect and reduces the notched Izod impact strength. In other words, the interfacial energy between SAN and metal filler would be a dominant factor for the impact strength of the SAN/Sn-Zn30/Al fiber com-
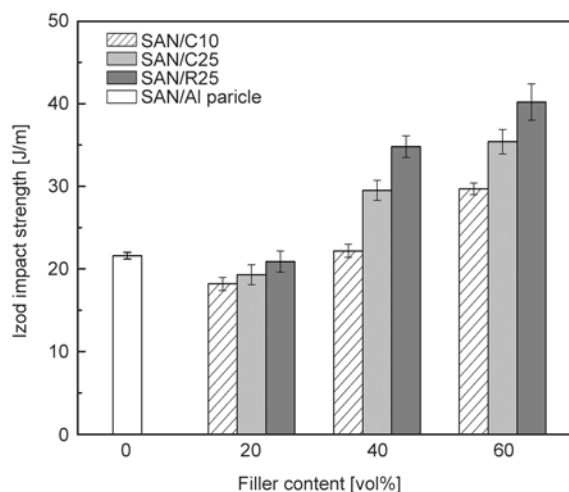

Figure 9. Notched Izod impact strength of the SAN/Sn-Zn30/Al fiber composites

posite [26]. When the length and the cross-sectional aspect ratio of the Al fiber are increased, the specific surface area of the domain of the filler will be increased more than in the case of the spherical filler domain, and this can contribute to the increase in impact strength by increasing the total interfacial energy. In addition, as the filler content increases, not only the surface area of the domains of the filler increases, but the connectivity between the domains of the filler is increased, resulting in the enhancement of the impact strength.

As shown in Figures 9 and 11, the notched Izod impact strength increased from 21.6 J/m for pure SAN to 29.7–40.2 J/m for composites with 60 vol% by approximately 40–90%, the flexural modulus increased from 2.11 GPa for pure SAN to 10.1–10.5 GPa for composites with 60 vol% filler content by approximately 400%. With regard to the filler content, the enhancement of the flexural modulus is larger than that of the notched Izod impact strength. However, in contrast to the notched Izod impact

Table 2. Density and mechanical properties of the SAN/Sn-Zn30/Al fiber composites

|	Filler content [vol%]	Density [g/cm³]	Impact strength [J/m]	Flexural modulus [GPa]	Tensile strength [MPa]	Tensile modulus [GPa]	Elongation at break [%]
pure SAN	0	1.08	21.6	2.11	59.7	2.45	2.93
SAN/C10	20	1.75	18.2	2.88	39.6	3.32	1.22
	40	2.41	22.2	4.60	46.9	5.26	0.89
	60	3.10	29.7	10.50	86.1	10.80	0.81
SAN/C25	20	1.76	19.3	2.89	40.1	3.34	1.21
	40	2.43	29.5	4.82	50.9	5.37	0.96
	60	3.13	35.4	10.10	96.5	10.70	0.91
SAN/R25	20	1.76	20.9	2.84	41.3	3.35	1.25
	40	2.43	34.8	4.75	52.2	5.34	0.98
	60	3.14	40.2	10.40	98.1	10.60	0.95
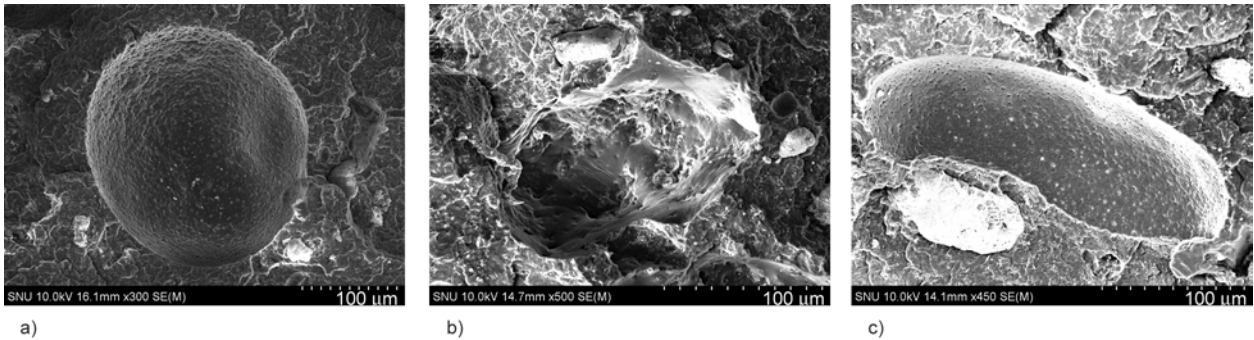
Figure 10. SEM images of the factured surfaces of composites with the metal filler content of 20 vol%; (a) C10, (b) C25, (c) R25
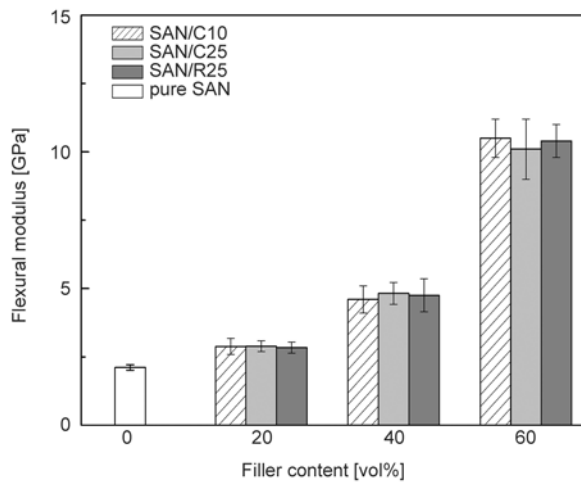

Figure 11. Flexural modulus of the SAN/Sn-Zn30/Al fiber composites

strength, its growth rate was not as high even with the increase in the extrusion ratio, indicating that the flexural modulus follows the rule of mixture being influenced by the contents of the filler rather than the shape of the filler [27].

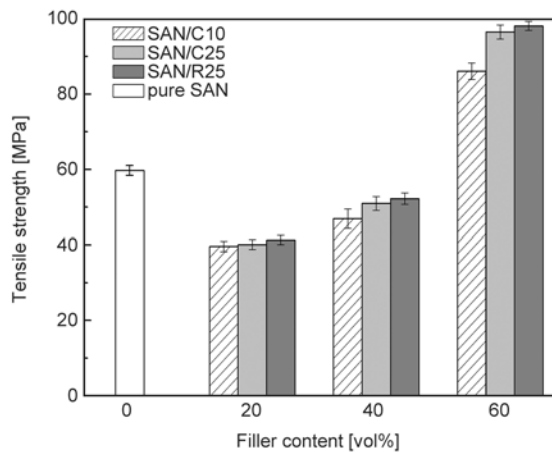The tensile strength decreased with the filler content of 20 vol%, but the impact strength was enhanced

Figure 12. Tensile strength of the SAN/Sn-Zn30/Al fiber composites

with the increase of the filler content as shown in Figure 12 and Table 2. Although the tensile modulus increased as the filler content increased, the elongation decreased considerably due to addition of the filler. As a result the tensile strengths of the composites with the filler contents of 20, 40 vol% were lower than that of pure SAN. However, as the increase in the tensile modulus was larger than the decrease in the elongation at the filler content of 60 vol%, the tensile strengths of the composites with the filler content of 60 vol% were higher than that of pure SAN.

4. Conclusions

We have established a novel method of fabricating metal filler with lightness and excellent electrical conductivity that can be compounded with polymer without degrading the processability. Using Sn-Zn30 having a coexisting region with liquid and solid at a mixing temperature, Sn-Zn30 and Al particles could be mixed. Through the cold extrusion of Sn-Zn30/Al particles, Sn-Zn30/Al fiber was fabricated to increase the efficiency as conductive filler. When Al particles were elongated, the oxidation layer of Al surface could become thin and/or be broken, resulting in an improvement of the wettability of Sn-Zn30 and Al fiber. The results of EDS show that the light metal fibers were wrapped around by Sn-Zn30 after compounding Sn-Zn30/Al fiber with polymer. When Sn-Zn30/Al fiber was compounded with polymer, the molten Sn-Zn30 maintained the processability, and the dispersibility of Sn-Zn30/Al fiber was improved due to the solid Al fiber. As the shape of Al fiber was controlled by varying the extrusion conditions, it was found that electrical conductivity and the notched Izod impact strength are improved when the length and the cross-sectional aspect ratio of Al fiber increases. Furthermore, as Sn-Zn30/Al fiber (~4.5 g/cm^3) is relatively lighter than other LMA

fillers (7–9 g/cm^3), the SAN/Sn-Zn30/Al fiber composite (3.14 g/cm^3 at filler content of 60 vol%) is lighter than other polymer/LMA filler composites (5–6 g/cm^3 at same content). We anticipate that with these characteristics this polymer/LMA/light metal fiber composite can be utilized in a variety of industrial applications.

Acknowledgements

References

[1] Chung D. D. L.: Electromagnetic interference shielding effectiveness of carbon materials. Carbon, **39**, 279–285 (2001).
DOI: 10.1016/S0008-6223(00)00184-6

[2] Zhang Q-H., Chen D-J.: Percolation threshold and morphology of composites of conducting carbon black/polypropylene/EVA. Journal of Materials Science, **39**, 1751–1757 (2004).
DOI: 10.1023/B:JMSC.0000016180.42896.0f

[3] Li C., Thostenson E. T., Chou T-W.: Sensors and actuators based on carbon nanotubes and their composites: A review. Composites Science and Technology, **68**, 1227–1249 (2008).
DOI: 10.1016/j.compscitech.2008.01.006

[4] Balberg I.: A comprehensive picture of the electrical phenomena in carbon black–polymer composites. Carbon, **40**, 139–143 (2002).
DOI: 10.1016/S0008-6223(01)00164-6

[5] Heo S. I., Yun J. C., Oh K. S., Han K. S.: Influence of particle size and shape on electrical and mechanical properties of graphite reinforced conductive polymer composites for the bipolar plate of PEM fuel cells. Advanced Composite Materials, **15**, 115–126 (2006).
DOI: 10.1163/156855106776829356

[6] Chung D. D. L.: Comparison of submicron-diameter carbon filaments and conventional carbon fibers as fillers in composite materials. Carbon, **39**, 1119–1125 (2001).
DOI: 10.1016/S0008-6223(00)00314-6

[7] Dani A., Ogale A. A.: Electrical percolation behavior of short-fiber composites: Experimental characterization and modeling. Composites Science and Technology, **56**, 911–920 (1996).
DOI: 10.1016/0266-3538(96)00054-1

[8] Deng S. H., Zhao J. J., Lin Q. F., Fan C. J., Zhou X. D.: Formation of interfacial network structure via photo-crosslinking in carbon fiber/epoxy composites. Express Polymer Letters, **8**, 505–516 (2014).
DOI: 10.3144/expresspolymlett.2014.54

[9] Bauhofer W., Kovacs J. Z.: A review and analysis of electrical percolation in carbon nanotube polymer composites. Composites Science and Technology, **69**, 1486–1498 (2009).
DOI: 10.1016/j.compscitech.2008.06.018

[10] Auilar J. O., Bautista-Quijano J. R., Avilés F.: Influence of carbon nanotube clustering on the electrical conductivity of polymer composite films. Express Polymer Letters, **4**, 292–299 (2010).
DOI: 10.3144/expresspolymlett.2010.37

[11] Bigg D. M.: Mechanical, thermal, and electrical properties of metal fiber-filled polymer composites. Polymer Engineering and Science, **19**, 1188–1192 (1979).
DOI: 10.1002/pen.760191610

[12] Li Y-J., Xu M., Feng J-Q., Dang Z-M.: Dielectric behavior of a metal-polymer composite with low percolation threshold. Applied Physics Letters, **89**, 072902/1–072902/3 (2006).
DOI: 10.1063/1.2337157

[13] Bloor D., Donnelly K., Hands P. J., Laughlin P., Lussey D.: A metal–polymer composite with unusual properties. Journal of physics D: Applied Physics, **38**, 2851–2860 (2005).
DOI: 10.1088/0022-3727/38/16/018

[14] Kumar A. M., Kwon S. H., Jung H. C., Shin K. S.: Corrosion protection performance of single and dual plasma electrolytic oxidation (PEO) coating for aerospace applications. Materials Chemistry and Physics, **149–150**, 480–486 (2015).
DOI: 10.1016/j.matchemphys.2014.10.049

[15] Song J-H., Nam K-S., Moon J-I., Choi Y-J., Lim D-Y.: Influence of the duty cycle on structural and mechanical properties of oxide layers on Al-1050 by a plasma electrolytic oxidation process. Metals and Materials International, **20**, 451–458 (2014).
DOI: 10.1007/s12540-014-3025-2

[16] Zhang X., Pan Y., Shen L., Yi X.: Novel low melting point alloy-loaded polymer composite. II. Resistivity–temperature behavior. Journal of Applied Polymer Science, **77**, 756–763 (2000).
DOI: 10.1002/(SICI)1097-4628(20000725)77:4<756::AID-APP7>3.0.CO;2-Y

[17] Zhang X., Pan Y., Shen L., Zheng Q., Yi X.: A novel low-melting-point alloy-loaded polymer composite. I. Effect of processing temperature on the electrical properties and morphology. Journal of Applied Polymer Science, **77**, 1044–1050 (2000).
DOI: 10.1002/1097-4628(20000801)77:5<1044::AID-APP11>3.0.CO;2-D

[18] Mrozek R. A., Cole P. J., Mondy L. A., Rao R. R., Bieg L. F., Lenhart J. L.: Highly conductive, melt processable polymer composites based on nickel and low melting eutectic metal. Polymer, **51**, 2954–2958 (2010).
DOI: 10.1016/j.polymer.2010.04.067

[19] Michaeli W., Pfefferkorn T. G.: Electrically conductive thermoplastic/metal hybrid materials for direct manufacturing of electronic components. Polymer Engineering and Science, **49**, 1511–1524 (2009).
DOI: 10.1002/pen.21374

[20] Batchelor G. K.: Sedimentation in a dilute dispersion of spheres. Journal of Fluid Mechanics, **52**, 245–268 (1972).
DOI: 10.1017/S0022112072001399

[21] Battezzati L., Greer A. L.: The viscosity of liquid metals and alloys. Acta Metallurgica, **37**, 1791–1802 (1989).
DOI: 10.1016/0001-6160(89)90064-3

[22] Thomas D. G.: Transport characteristics of suspension: VIII. A note on the viscosity of newtonian suspensions of uniform spherical particles. Journal of Colloid Science, **20**, 267–277 (1965).
DOI: 10.1016/0095-8522(65)90016-4

[23] Zhang X., Pan Y., Cheng J., Yi X.: The influence of low-melting-point alloy on the rheological properties of a polystyrene melt. Journal of Materials Science, **35**, 4573–4581 (2000).
DOI: 10.1023/A:1004845426786

[24] Starý Z., Krückel J., Weck C., Schubert D. W.: Rheology and conductivity of carbon fibre composites with defined fibre lengths. Composites Science and Technology, **85**, 58–64 (2013).
DOI: 10.1016/j.compscitech.2013.06.006

[25] Allaoui A., Bai S., Cheng H. M., Bai J. B.: Mechanical and electrical properties of a MWNT/epoxy composite. Composites Science and Technology, **62**, 1993–1998 (2002).
DOI: 10.1016/S0266-3538(02)00129-X

[26] Wetzel B., Haupert F., Friedrich K., Zhang M. Q., Rong M. Z.: Impact and wear resistance of polymer nanocomposites at low filler content. Polymer Engineering and Science, **42**, 1919–1927 (2002).
DOI: 10.1002/pen.11084

[27] Thomason J. L., Vlug M. A.: Influence of fibre length and concentration on the properties of glass fibre-reinforced polypropylene: 1. Tensile and flexural modulus. Composites Part A: Applied Science and Manufacturing, **27**, 447–484 (1996).
DOI: 10.1016/1359-835X(95)00065-A

Characterization and kinetic study of Diels-Alder reaction: Detailed study on *N*-phenylmaleimide and furan based benzoxazine with potential self-healing application

Ž. Štirn, A. Ručigaj, M. Krajnc[*]

University of Ljubljana, Faculty of Chemistry and Chemical Technology, Večna pot 113, 1000 Ljubljana, Slovenia

Abstract. The Diels-Alder reaction between *N*-phenylmaleimide and benzoxazine bearing furan group was investigated for the purpose of successful appliance of self-healing in benzoxazine polymer networks. The reaction as a function of temperature/time was performed in molten state and in a solution, where also the kinetic study was performed. The Diels-Alder reaction leads to a mixture of two diastereomers: *endo* presented at lower cyclo-reversion temperature and *exo* at higher. Therefore, the conversion rates and *exo*/*endo* ratio were studied in detail for both systems. For instance, in molten state the Diels-Alder reaction was triggered by the temperature of the melting point at 60 °C with *exo*/*endo* ratio preferable to the *endo* adduct. The study of the kinetics in a solution revealed that the Diels-Alder reaction followed typical bimolecular reversible second-order reaction. The activation energies were close to the previous literature data; 48.4 and 51.9 kJ·mol^{-1} for Diels-Alder reaction, and 91.0 and 102.3 kJ·mol^{-1} for retro-Diels-Alder reaction, in acetonitrile and chloroform, respectively. The reaction equilibrium in a solution is much more affected by the retro-Diels-Alder reaction than in a molten state. This study shows detailed investigation of DA reaction and provides beneficial knowledge for further use in self-healing polymer networks.

Keywords: thermal properties, Diels-Alder reaction, kinetics, benzoxazine, maleimide

1. Introduction

The Diels-Alder (DA) reaction, known as (4+2) cycloaddition reaction between diene and dienophile, is one of the most useful reactions in organic [1] and material synthesis [2, 3]. DA reaction belongs to the group of 'click' reactions known as almost completely versatile, efficient and selective synthesis [4]. Furthermore, DA reactions at appropriate temperature range undergo a reverse reaction called retro-DA (rDA) reaction that regenerates starting materials. DA adduct is the mixture of two diastereomers called *endo* and *exo* adducts. Temperature of the rDA reaction leading to the appearance of the *endo* adduct is typically lower than that of the *exo* adduct [5, 6]. Due to the thermal reversibility of DA

reactions, they are frequently applied in the production of remendable and recyclable materials [7–10]. During the development of self-healing material much attention is often given to the understanding the mechanistic perspective of a given reaction as much as possible. Such studies are frequently accompanied by kinetic investigations of the reaction [11–16]. Benzoxazines, because of their unique characteristics, are recently gaining much attention in polymer synthesis and design. Inclusion of DA-reaction in benzoxazine main chain is one way of integrating them with remendability. According to the literature, some work has been done in synthetic aspect of modifying benzoxazines with furan or maleimide chains. So far, the majority of the research was

---

focused on the modified benzoxazines describing effects of maleimide or furan functionality on the mechanical properties of polymeric benzoxazines, while the use of Diels-Alder reaction in self-healing perspective has not yet been recognized [17–22]. Needless to say, numerous studies were performed to date dealing with the DA reaction based on maleimide and furan functionalities [6, 16, 23–28]. Only a few examples in literature exist, where benzoxazines were used in DA reactions to form linear polymeric materials [29, 30]. Authors have shown a synthetic preparation of linear benzoxazine chains, where the linker was DA based reaction, between modified benzoxazine (by furan functionality) and bismaleimides. However, their goals were to describe newly formed properties of cured benzoxazine samples, and no work was done on either describing possible remendability properties or the kinetics of the DA reaction.

On the other hand there might be a reason, why there is not yet a known self-remendable benzoxazine polymer material with DA reaction based remendability. The reason being high curing temperature needed for polymerization of benzoxazines [31, 32], usually quite above the temperature of rDA reaction (~100 °C) of normally used diene and dienophile system (furan and maleimide) [5, 6]. This means that DA connections are broken and starting compounds are formed. When this happens, maleimide double bond is exposed and starts to polymerize, which is not the desirable reaction in order to achieve self-healing based on DA reaction. This being said the curing temperatures of benzoxazines are probably the major drawbacks in the development of functional self-remendable polybenzoxazines based on DA reaction.

The focus of this paper is on the thermal evaluation of the DA reaction between *N*-phenylmaleimide (PMI) and guaiacol furfuryl amine based benzoxazine (GF). Experiments were performed in the molten state and in solution and the differences between both systems were investigated. Progress of the reaction in the absence of solvent was systematically determined by DSC analysis accompanied with ^{1}H NMR and kinetic study of the DA reaction was performed in solution. By temperature controlled FTIR (Fourier transform infrared spectroscopy) analysis kinetic parameters were derived. Higher conversions and easier manipulation of *exo/endo* ratio were achieved in a molten state due to

the more explicit boundary between DA and rDA reaction than in a solution. It is interesting to further investigate the use of benzoxazine based compounds bearing furan and maleimide functional groups in self-healing polymer networks activated by Diels-Alder reaction. The main goal of this publication is to establish the valuable knowledge of thermal behaviour of DA/rDA reaction in order to successfully apply self-healing in benzoxazine polymer networks.

2. Materials and methods
2.1. Materials
Reactant *N*-phenylmaleimide (PMI, 97%) was purchased from Aldrich (Chemie GmbH, Steinheim, Germany). Reactant 3-(furan-2-ylmethyl)-8-methoxy-3,4-dihydro-2*H*-benzo[e][1,3]oxazine (GF) was synthesized according to the literature [33]. Aniline (99.5%), acetic anhydride (98.5%) and hexane were purchased from Merck (Darmstadt, Germany). Guaiacol (98%), furfurylamine (99%), maleic anhydride (97%) and paraformaldehyde were purchased from Aldrich (Chemie GmbH, Steinheim, Germany), and deuterated chloroform (99.8% D) was purchased from Euriso-top (Saint-Aubin, France). All chemicals were used as received.

2.2. Characterization
The proceeding of the DA/rDA reaction was studied by differential scanning calorimetry (DSC), ^{1}H NMR (nuclear magnetic resonance) and IR spectrometry.

Calorimetric studies were carried out on Mettler Toledo DSC1 instrument with intra-cooler using STAR software (Greifensee, Switzerland). In and Zn standards were used for the temperature calibration and for the determination of the instrument time constant. Samples of around 10 mg were weighed in standard 40 μL aluminium pans. DSC measurements were performed in nitrogen atmosphere with 30 mL/min nitrogen flow rate. In order to observe the heating behaviour of each reactive compound and their mixture, DSC experiments were performed by a heating rate 10 K·min⁻¹ in the range of 20 to 350 °C. For samples isothermally heated at 70 °C DSC scans were performed from 20 to 160 °C with the heating rate 5 K·min⁻¹.

^{1}H NMR analyses were performed on a Bruker Avance III 500 MHz NMR spectrometer (Billerica, USA) at the temperature 296 K and frequency 500.13 MHz and on Bruker DPX 300 MHz NMR at

the temperature 296 K and frequency 300.13 MHz (Billerica, USA). Deuterated chloroform (CDCl$_3$) was used as solvent. *Endo* and *exo* standards were obtained from DA reaction between PMI and GF by separating reaction mixture by chromatography on a silica gel column using petroleum ether:ethyl acetate (2:1) as mobile phase. Characteristic peaks monitored in reaction mixture (Figure 1): for starting materials a signal at 6.85 ppm, corresponding to maleimide protons at a carbon double bond (C*H*=C*H*, peak 3), for benzoxazine singlets at 4.02 and 3.95 ppm which correspond to CH$_2$ in benzoxazine ring (NC*H*$_2$C, peak 1) and CH$_2$ attached to a furan ring (NC*H*$_2$CO, peak 2). Products were monitored by multiplet at 5.40 ppm, corresponding to protons in a newly formed six-membered ring in both *endo* and *exo* adducts (CHC*H*O, peak 4). While doublet at 3.54 ppm is characteristic for NC*H*$_2$CO (peak 5) in *endo* adduct, doublets at 3.13 and 2.97 ppm corresponds to succinimide type protons in *exo*-adduct (COC*H*C and COC*H*CH, peak 7 and 6).
Detailed spectra are assigned as follows:
N-phenylmaleimide (PMI): ^{1}H NMR (CDCl$_3$, 300 MHz, δ, ppm): 7.46 (m, 2H, Ph), 7.35 (m, 3H, Ph), 6.83 (s, 2H, C*H*=C*H*).
3-(furan-2-ylmethyl)-8-methoxy-3,4-dihydro-2*H*-benzo[e][1,3]oxazine (GF). ^{1}H NMR (CDCl$_3$, 300 MHz, δ, ppm): 7.41 (dd, J_1 = 0.84 Hz, J_2 = 1.8 Hz, 1H, Ar), 6.80 (m, 2H, Ar), 6.58 (m, 1H, Ar), 6.33 (dd, J_1 = 1.9 Hz, J_2 = 3.2 Hz, 1H, Ar), 6.25

(dd, J_1 = 0.6 Hz, J_2 = 3.2 Hz, 1H, Ar), 4.99 (s, 2H, OC*H*$_2$N), 4.02 (s, 2H, NC*H*$_2$C), 3.95 (s, 2H, NC*H*$_2$CO), 3.89 (s, 3H, OC*H*$_3$).
(3a*R*,4*R*,7*S*,7a*S*)-4-((8-methoxy-2*H*-benzo[e][1,3] oxazin-3(4*H*)-yl)methyl)-2-phenyl-3a,4,7,7a-tetra-hydro-1*H*-4,7-epoxyisoindole-1,3(2*H*)-dione (*endo* adduct). ^{1}H NMR (CDCl$_3$, 500 MHz, δ, ppm): 7.41 (m, 3H, Ar), 7.12 (m, 2H, Ar), 6.84 (m, 1H, Ar), 6.76 (m, 1H, Ar), 6.58 (m, 2H, Ar and C*H*=CH), 6.47 (d, J = 5.8 Hz, 1H, CH=C*H*), 5.40 (dd, J_1 = 1.5 Hz, J_2 = 5.5 Hz, 1H, CHC*H*O), 5.04 (d, J = 9.9 Hz, 1H, OC*H*$_2$N), 5.00 (d, J = 9.9 Hz, 1H, OC*H*$_2$N), 4.19 (d, J = 16.8 Hz, 1H, NC*H*$_2$C), 4.10 (d, J = 16.8 Hz, 1H, NC*H*$_2$C), 3.88 (s, 3H, OC*H*$_3$), 3.78 (dd, J_1 = 5.5 Hz, J_2 = 7.7 Hz, 1H, COC*H*CH), 3.69 (d, J = 15.1 Hz, 1H, NC*H*$_2$CO), 3.64 (d, J = 7.7 Hz, 1H, COC*H*C), 3.54 (d, J = 15.1 Hz, 1H, NC*H*$_2$CO).
(4*R*,7*S*,7a*R*)-4-((8-methoxy-2*H*-benzo[e][1,3]oxazin-3(4*H*)-yl)methyl)-2-phenyl-3a,4,7,7a-tetrahydro-1H-4,7-epoxyisoindole-1,3(2*H*)-dione (*exo*-adduct). ^{1}H NMR (CDCl$_3$, 500 MHz, δ, ppm): 7.40 (m, 3H, Ar), 7.24 (m, 2H, Ar), 6.81 (m, 1H, Ar), 6.73 (m, 1H, Ar), 6.58 (m, 3H, Ar and C*H*=CH), 5.39 (d, J = 1.45 Hz, 1H, CHC*H*O), 4.98 (m, 2H, OC*H*$_2$N), 4.12 (m, 2H, NC*H*$_2$C), 3.86 (s, 3H, OC*H*$_3$), 3.64 (d, J = 15.2 Hz, 1H NC*H*$_2$CO), 3.45 (d, J = 15.2 Hz, 1H, NC*H*$_2$CO), 3.13 (d, J = 6.5 Hz 1H, COC*H*C), 2.97 (d, J = 6.5 Hz, 1H, COC CH).

IR spectra were recorded on Mettler Toledo ReactIR diamond composite probe (Greifensee, Switzerland) allowing *in situ* FTIR spectroscopy. The spectra were recorded in the range of 4000–400 cm^{-1}. Each DA reaction was monitored via IR until equilibrium was achieved allowing kinetic parameter determination. A given reaction mixture was considered to have reached the equilibrium when the conversion remained constant over multiple reaction time points.

2.3. Procedure of Diels-Alder experiments

DA reaction was investigated by non-isothermal and isothermal heating of the PMI/GF mixture in the absence of solvent. Separately, the proceeding of the DA reaction was studied also in solution as a function of temperature in order to perform kinetic studies. Diels-Alder/retro-Diels-Alder investigations were performed by isothermal heating of the PMI/GF mixture at a temperature higher than the melting point. Reactants were grounded in a mortar and mixed in stoichiometric amounts. The process of the reaction as a function of time was monitored by ^{1}H NMR
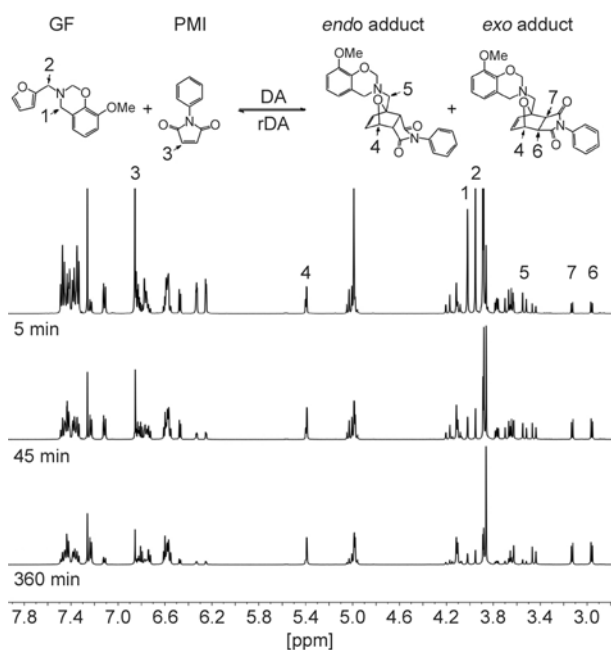

Figure 1. ^{1}H NMR assigned spectra of the reaction mixture between PMI and GF at different reaction times

analysis after the sample was rapidly cooled down by liquid nitrogen to the ambient temperature. Different temperatures were applied with the intention to study the conversion and *exo*/*endo* ratio.

Reactions in solution were performed in chloroform and acetonitrile at different temperatures. Stoichiometric amounts of reactants were added reaching the initial reactants' concentration 0.5 mol·L^{-1}. Reactions were monitored by *in situ* FTIR spectroscopy. The reaction mixture was mixed with magnetic stirrer in a glass vial. Glass vial was closed with a polyethylene cap, which had a perfectly cut hole for ReactIR probe to tightly fit. Parafilm was used to additionally prevent solvent evaporation.

3. Results and discussion
3.1. Diels-Alder reaction in molten state
The product of the Diels-Alder reaction (DA adduct) is the mixture of two diastereomers called *endo* and *exo* adducts (Figure 2). While the *endo* compound is kinetically favoured, the *exo* is thermodynamically favoured and thus more stable [5, 6]. The aim of the detailed study of the thermal behaviour of the PMI/GF mixture is its possible further application as a self-healing polymer network.

Thermal behaviour of the reaction between PMI and GF started with DSC experiments in order to determine the approximate starting temperature of DA and retro-DA reaction. Due to the fact that both reactants melted at the same temperature, the mixture melted at lower temperature as a consequence of the freezing point depression (Figure 3). Namely, the presence of impurity in the pure compound causes a decrease in the melting point and a broadening of the melting point range. The Diels-Alder reaction started after the beginning of the melting of PMI/GF mixture (Figure 3) due to the higher mobility of functional groups. It can be concluded that DA reaction was actually triggered by melting of the prepared mixture. The melting peak value of the 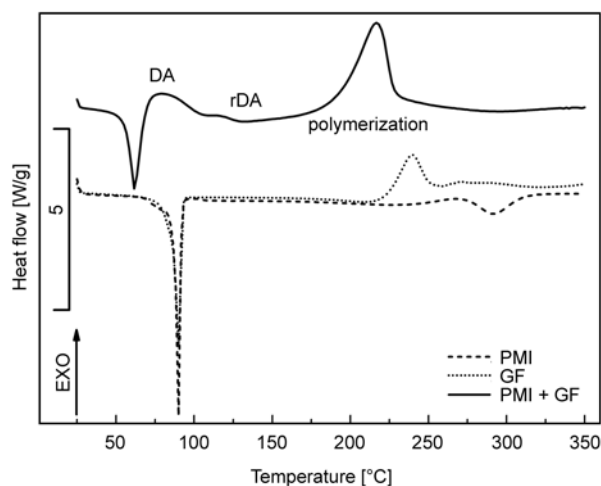PMI/GF system was in fact lower than the sum of each individual compound, which is the result of the beginning of the DA reaction and its exothermic contribution. The exothermic peak of a DA reaction reached the maxima at 80 °C and lasted up to approximately 100 °C when the evident endothermic peak of rDA appeared. The exothermic event from 170–240 °C could be explained by polymerization reaction of benzoxazine and maleimide [34]. Unfortunately, there was no clear boundary between the end of the rDA reaction and start of polymerization. The exothermic peak of GF that extended over 200 °C represents a polymerization reaction of benzoxazine [33]. On the other hand, we presumed that DSC curve of PMI showed an endothermic peak at around 275 °C, due to the combination of polymerization reaction of maleimide and its evaporation at higher temperatures.

It is worth mentioning that DSC analysis is not an appropriate tool for kinetic studies of DA reaction, because accurate differentiation between the individual processes is not clear. For that reason non-isothermal heating was associated with ^{1}H NMR analysis allowing detailed insight into the reaction process as a function of temperature (Figure 4). After reaching the examined temperature by a heating rate of 10 K·min^{-1}, the sample was rapidly cooled down by

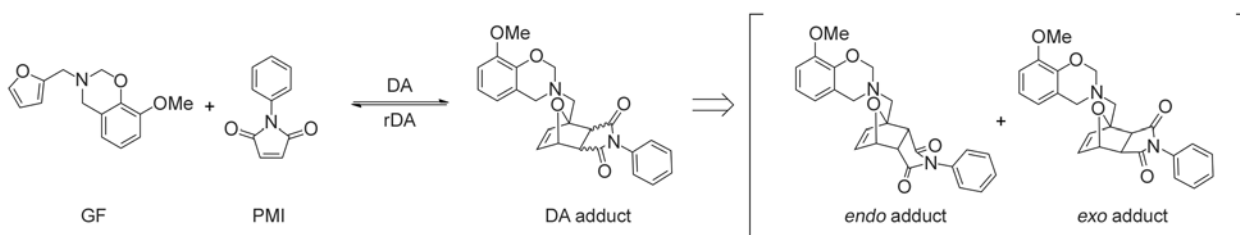**Figure 3.** DSC analyses of PMI, GF and PMI/GF mixture

Figure 2. Diels-Alder reaction between benzoxazine bearing furan group (GF) and *N*-phenylmaleimide (PMI) forms DA-adduct
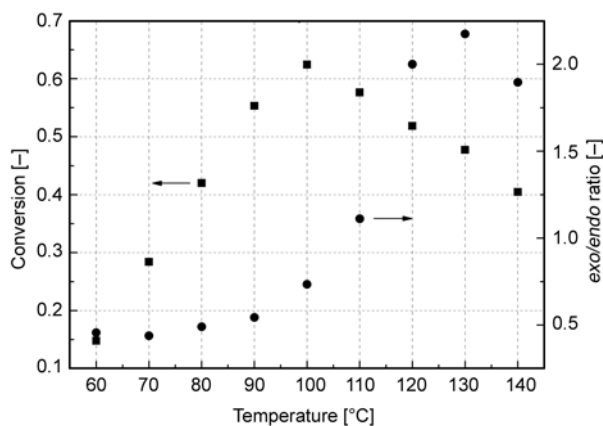
Figure 4. Conversion and *exo*/*endo* ratio for non-isothermal heating of a PMI/GF mixture in a range from 60 to 140 °C

liquid nitrogen. The range from 60 to 140 °C was studied analysing the conversion and *endo*/*exo* adducts behaviour. The conversion linearly increased up to 100 °C, when a linear drop in conversion value was observed as a consequence of rDA reaction. The mentioned followed also from the heat flow of a DSC analysis, where a shift from exothermic to insignificant endothermic peak was observed.

In contrast to the measured value, more evident endothermic behaviour was expected due to the progress of endothermic rDA reaction and drop in conversion from 0.62 to 0.40. Interestingly, although the conversion started to decrease, the increase of *exo*/*endo* ratio was observed up to 130 °C due to the thermodynamically favoured *exo* adduct. Additionally, when the sample was kept at 140 °C for another 10 minutes, no further drop in the conversion was observed. This may indicate that formed adduct was transformed into reactants by rDA reaction instantaneously. By achieving merely 15% of conversion at 60 °C it was proven that DA reaction started during the melting of the sample.

Further investigation was designed towards the isothermal heating of PMI/GF mixture above the temperature of the melting point. The intention was to observe the evolution of conversion and *exo*/*endo* ratio as a function of time. Although the self-healing effects are out of scope of this research, renewing the *exo*/*endo* ratio in self-healing studies could be interesting. The precise results of *endo* and *exo* compounds were likewise obtained by ^{1}H NMR analysis. Since only DA reaction during isothermal heating was studied thoroughly, only the results applying temperatures up to 100 °C were obtained.

The temperature of 100 °C was used as a limited temperature between DA and rDA reaction.

Considering the results of DSC analysis the first experiment was performed at 60 °C. The sample fully melted after approximately 15 minutes, when the sample was first analysed, and reached the final conversion at 75%. Clearly, the reaction at higher temperature was faster; however the same final conversion was achieved at 70 and 80 °C and reached the final value after 50 minutes. Differently, at 90 and 100 °C conversion after 180 minutes started to decrease due to the effect of the beginning of rDA reaction. Although the conversion at 70 and 80 °C was similar, there was an important difference between the ratio of *exo*/*endo* adduct. Due to the fact that *exo* adduct is thermodynamically favoured [5, 6], the ratio is increasing with temperature and time. At 60 °C *endo* adduct was the predominant product and there was no significant increase in ratio by time indicating that temperature was not yet in favour of *exo* emergence. Obviously, at prolonged heating times, temperatures of about 90 °C indicated the end of DA and start of rDA reaction. This trend was evident also from the *exo*/*endo* ratio. While up to 60 minutes the increase of the ratio was linear and higher than at lower temperatures, afterwards the ratio started to decrease gradually. The effect of the heating temperature on *exo*/*endo* ratio is even more evident at 100 °C, when the ratio started to decrease after 30 minutes. Among that, the decrease in conversion was observed after 60 minutes. The trend shown in Figure 5 therefore suggests that the extension of the heating time does not lead to further progression of the reaction; it does, however, affect the *exo* and *endo* ratio. The maximum amount of *exo* adduct could consequently be achieved in the range of 70–80 °C at extended heating times. Conversely, if the goal is to maximize of *endo* adduct, the temperature should be as low as possible and the heating should be stopped right after the equilibrium conversion is achieved.

It has been previously reported [5] that rDA reaction of *endo* adduct has significantly lower activation barrier compared to *exo* adduct. Calorimetric analyses should noticeably demonstrate the progress of the *endo* and *exo* adduct in rDA reaction. For that reason DA adduct obtained in isothermal heating at 70 °C was further analysed by DSC analysis (Figure 6). When sample was isothermally heated for 1
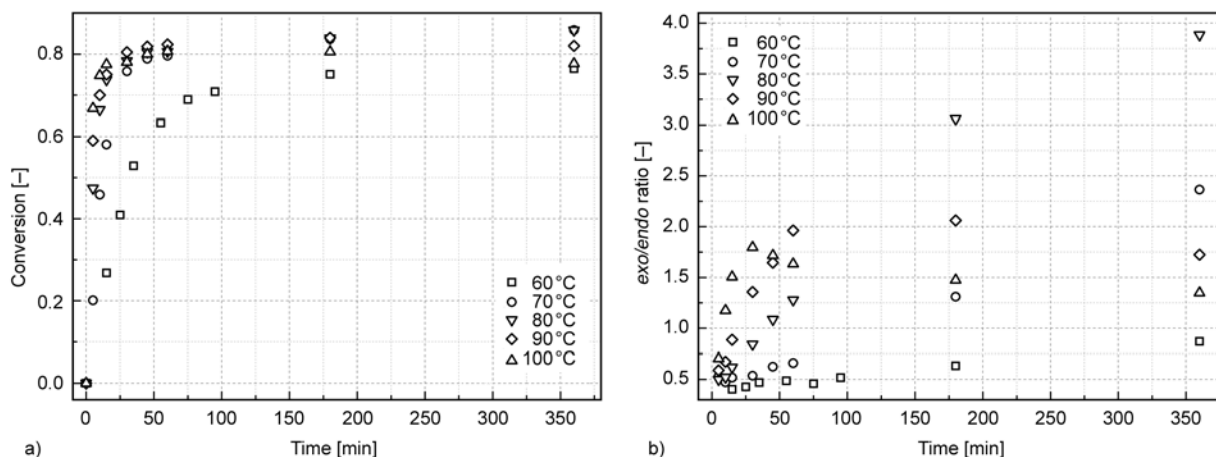
Figure 5. Progress of conversion (a) and *exo*/*endo* (b) for isothermal experiments at different temperatures in a molten state

and 3 hours (initial *exo*/*endo* ratio was 0.66 and 1.31, respectively) an exothermic peak occurred inside the broad endothermic peak. On the other hand, at higher *exo*/*endo* ratios (2.36 for 6 hours and 3.83 for 12 hours) the previously observed exothermic peak disappeared.

The appearance of the exothermic peak at 1 and 3 hours could be explained by a three-step process. First the endothermic peak appeared as a result of transformation of *endo* DA adduct into PMI and GF driven by rDA reaction. Following that, the new *exo*/*endo* adducts mixture was quickly formed leading to the exothermic peak on DSC thermogram. In conclusion, endothermic peak that started at approximately 105 °C belonged to the *exo*'s rDA reaction (Figure 6). By increasing the sample's heating time, the previously observed exothermic peak of *exo* adduct disappeared due to the increasing *exo*/*endo* ratio (Figure 5b). It can be deduced that the amount of *endo* adduct in the *exo*/*endo* mixture at 6 and

12 hours is apparently too low to have any exothermic effect noticeable by DSC method. DSC scans at 6 and 12 hours are consequently showing only broad endothermic peak corresponding mainly to the retro-DA reaction of *exo* adduct (Figure 6).

The general idea of further use of DA reaction is in self-healing applications of polymer networks. As it has already been mentioned, the rDA reaction of *endo* adduct is faster than the rDA reaction of its stereoisomer, *exo* adduct. Hence, in the synthesis of material depending only on DA linkages, two principles could be used. The first could be based on the synthesis of material at low DA reaction temperature (60–70 °C for our system) favouring the majority of *endo* DA connections. The damaged material can be healed also at lower temperature; at a temperature high enough to convert *endo* form into *exo*, however not high enough to reach the rDA reaction of *exo* adduct. Under the outlined condition the material could be conditionally healed by a pulse heating in the *endo* rDA reaction range without deformation of the material shape. In this case, the *exo* adduct would actually play a role of a structural basis of the material.

It is worth mentioning that such principle of a self-healing is limited. Once all the *endo* adduct is transformed into *exo* form, only the step of *exo* rDA reaction remains. The second principle depends on self-healing of the material at elevated temperatures by triggering the rDA reaction of the *exo* adduct meaning the recycling of material to the initial reactants. Consequently, if the material is based only on Diels-Alder bonds, breakdown of the *exo* adduct leads to the material shape loss. Nevertheless, the main issue of benzoxazine polymerization below the temperature of the rDA reaction remains, however, future
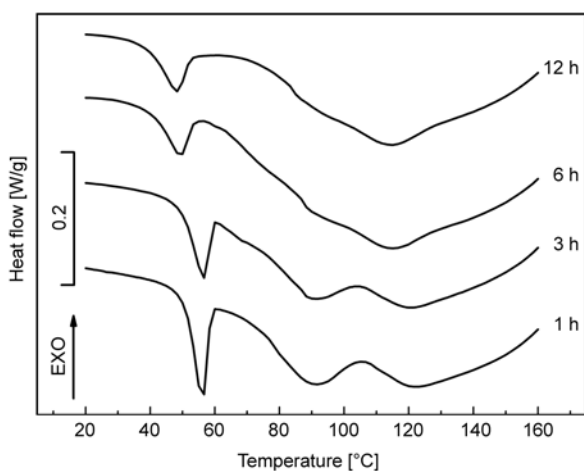

Figure 6. Evolution of DSC thermograms versus time of pre-cured samples of PMI/GF at 70 °C

study based on preliminary DA/rDA study would be interesting.

3.2. Kinetic study of the Diels-Alder reaction in acetonitrile and chloroform

The kinetics of the model DA reaction in a solvent was monitored by IR spectroscopy. Chloroform and acetonitrile were used as solvents due to the optimal visibility of reactants' peaks shifting as a function of time. To study the DA model reaction kinetics, DA reactions between PMI and GF were carried out at different temperatures (30, 40 and 50 °C for chloroform, and 40, 50, 60 and 70 °C for acetonitrile) until the equilibrium was reached. DA reaction in a solution started at a lower temperature than in the molten state due to the solvent-diene-dienophile interaction, when in molten state the mobility of the functional group was achieved via sample melting. Figure 7 shows the evolution of IR spectra versus time of the reaction between PMI and GF in acetonitrile and chloroform presenting the characteristic peaks and their increase or depletion.

According to the results of the preliminary experiments we focused on the signal with the wavenumber 832 cm^{-1}, since the peak was isolated and unaffected by solvent or other reactant. The observed peak showed the decrease in intensity and belonged to the characteristic C–H vibration of double bond in PMI. Due to the overlapping of the reactant with either solvent and/or the opposite reactant, other peaks were inappropriate for quantitative measurements and further conversion calculations. To clarify, since the stoichiometric amount of reactants was presented in the mixture, furan and maleimide

functionalities are consumed at the same rate. Consequently, it is enough to observe either maleimide or furan functional group. The formation of the DA-adduct may be slightly detected at 1778 cm^{-1}, however the occurrence was barely visible. Another specific absorption of DA adducts was detected at 1181 cm^{-1}, even though it was observable only in acetonitrile. The signal at 1151 cm^{-1} in acetonitrile (shifted to 1148 cm^{-1} in chloroform) belonged to the C–N–C vibration. Peak at 1600 cm^{-1} belonged to the C=C vibration in PMI and GF, whereas 1515 cm^{-1} represented C–H vibration in aromatic ring. Unfortunately, distinguishing between the *endo* and *exo* form is not possible by IR analysis, which is why the formation of summarized DA adduct form was merely predicted.

Due to the fact that the ReactIR allows *in situ* measurements its usage is ideal for DA reaction kinetic studies. However, in DA kinetic studies IR spectroscopy is often mentioned as inaccurate and used preferably only for qualitative measurements. For that reason, the accuracy of the maleimide group consumption and conversion calculations were verified performing two concurrent reactions at 40 °C: one performed in chloroform and analysed by ReactIR, and other performed in deuterated chloroform followed by ^{1}H NMR characterization. The comparison of the results showed that the calculations of conversion from the IR absorbance of the characteristic peak showed similar results as the conversion from ^{1}H NMR peak integrals (Figure 8). Reasonably, due to the simplicity of the reaction implementation at different temperatures, all reactions were analysed by the ReactIR instrument further on. It
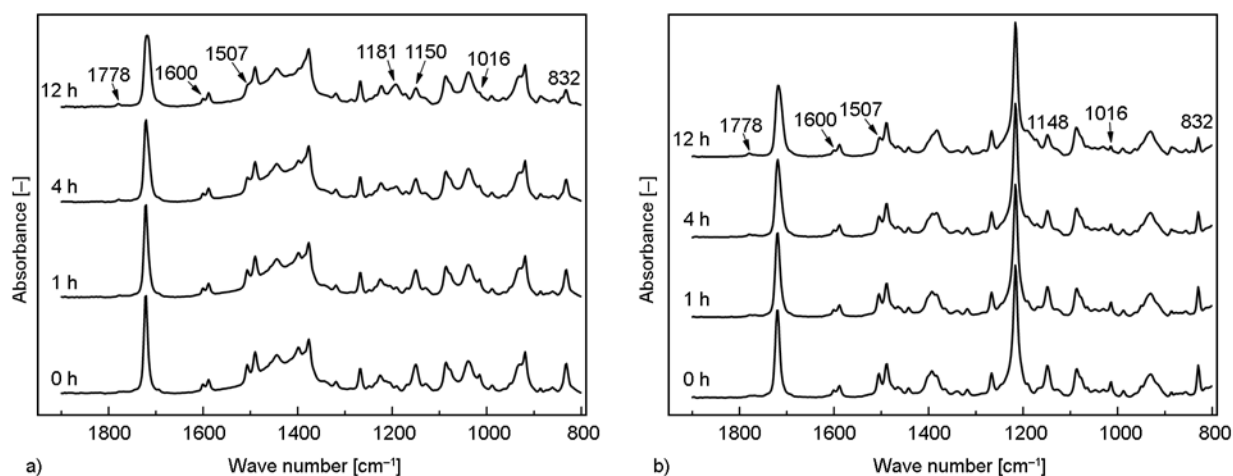

Figure 7. Evolution of the ReactIR spectra of the DA reaction between PMI and GF in acetonitrile (a) and chloroform (b) at 40 °C
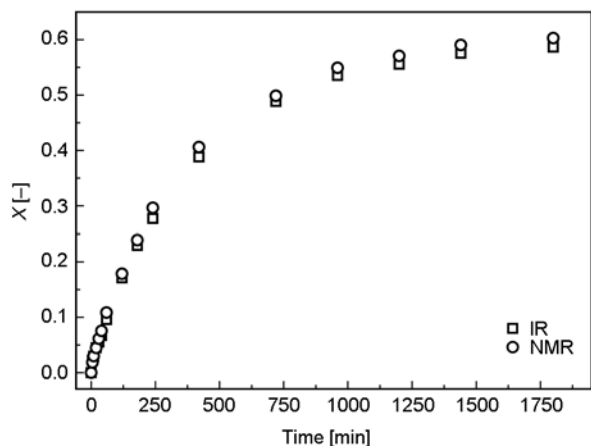
Figure 8. Experimental results of reaction performed in chloroform analysed separately by IR and ^{1}H NMR method

has to be noted that calibration curves of peak intensities at different concentrations of reactants showed good linear relationship in both chloroform and acetonitrile, which is why only the absorbance values were used in conversion calculations.

The concentration of PMI being proportional to the absorbance at 832 cm^{-1}, conversion X is expressed by Equation (1):

$$X(t) = 1 - \frac{A_{PMI}(t)}{A_{PMI}(0)} \tag{1}$$

To determine the kinetic parameters, the overall reaction rate of maleimide (M) in the reversible DA reaction with furan (F) is written by Equation (2):

$$\frac{d[M]}{dt} = -k_{DA}[M][F] + k_{rDA}[A] \tag{2}$$

where [M] is the concentration of maleimide as PMI functional group, [F] is the concentration of

furan as GF function group, and [A] is the concentration of adduct. For the purposes of kinetic studies DA adduct was the sum of its *endo* and *exo* form. Kinetic parameters k_{DA} and k_{rDA} presents the reaction rate constants of the forward and reverse DA reaction. For stoichiometric mixtures of PMI and GF, Equation (2) can be re-written in a form of conversion X (Equation (3)):

$$\frac{dX}{dt} = k_{DA}[M]_0(1-X)^2 - k_{rDA}X \tag{3}$$

Once the equilibrium conversion is known, the equilibrium constant can be calculated as (Equation (4)):

$$K_C = \frac{k_{DA}}{k_{rDA}} = \frac{[A]}{[M][F]} = \frac{X}{[M]_0(1-X_e)^2} \tag{4}$$

where $[M]_0$ is the initial PMI concentration. Further on, when applying equilibrium conversion and equilibrium constant in Equatuon (3), linearized form of Equatoin (3) can be derived and used in verification of bimolecular-type second-order reversible reaction (Equatoin (5)).

$$\ln\left(\frac{X_e(1-X_eX)}{X_e-X}\right) = k_{DA}[M]_0\left(\frac{1}{X_e}-X_e\right)t \tag{5}$$

The results of experiments in acetonitrile and chloroform are straightforward. Since the derivation of experimental data and kinetic parameters followed the same procedure, graphical presentation is demonstrated only for experiments in acetonitrile (Figure 9). Figure 9 shows that the higher the temperature the faster the conversion increases, which is in accordance with the kinetic laws.
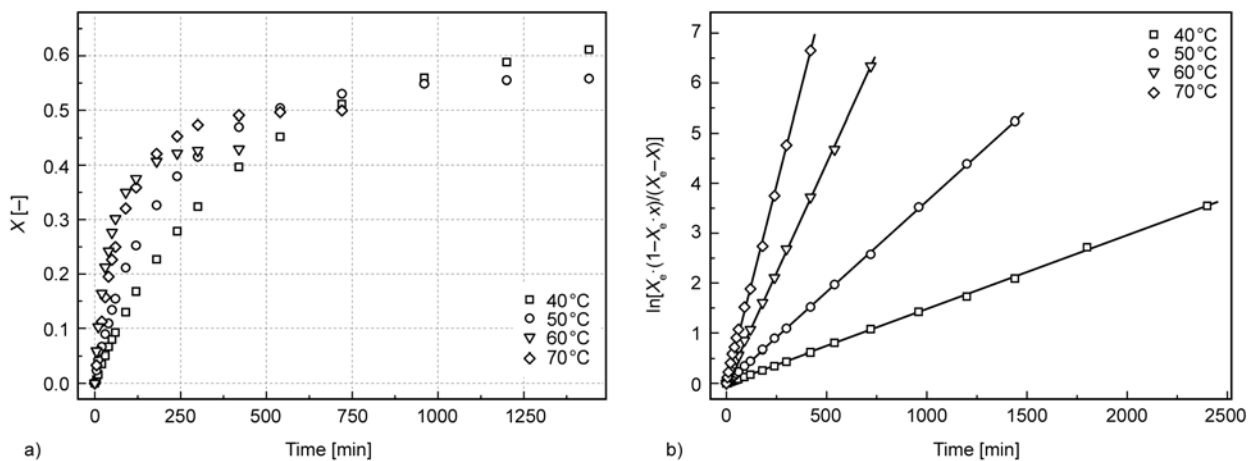

Figure 9. Evolution of the conversion versus time at different temperatures (a) and bimolecular second-order reversible reaction kinetic model (b)

Table 1. Equilibrium conversion (X_e) and kinetic rate constants (k_{DA}, k_{rDA}) describing the kinetics of DA reaction as indicated in Figure 9

T [°C]	Acetonitrile			Chloroform		
	X_e	$k_{DA} \cdot 10^3$ [L·mol^{-1}·min^{-1}]	$k_{rDA} \cdot 10^3$ [min^{-1}]	X_e	$k_{DA} \cdot 10^3$ [L·mol^{-1}·min^{-1}]	$k_{rDA} \cdot 10^3$ [min^{-1}]
30				0.70	1.902	0.122
40	0.66	3.461	0.303	0.60	3.525	0.470
50	0.56	5.939	1.027	0.52	6.819	1.511
60	0.50	11.917	2.979			
70	0.43	16.704	6.311			

Our studied system fitted typical bimolecular second-order reversible reaction (Figure 9b). Applying the Equation (5), a satisfactory fit was achieved from which kinetic parameters k_{DA} and k_{rDA} were calculated (Table 1). The goodness of fit was verified by R^2 value, which was over 0.999 for all experiments. The DA reaction was in balance between the blocked and the unblocked form. The ratio depended upon the temperature and reached the plateau during the rDA reaction (Figure 9). By increasing the reaction temperature the equilibrium conversion started to decrease as a consequence of rDA effect. In order to determine the DA/rDA equilibrium as a function of temperature the reaction system was allowed to reach the equilibrium. It took more than two days to reach the equilibrium at 30 and 40 °C. The kinetic parameters in chloroform were slightly higher than in acetonitrile, which affected also the equilibrium conversion that was consequently higher in acetonitrile than in chloroform.

The reaction between PMI and GF was carried out at different temperatures. For that reason it is possible to apply the Arrhenius law (Equation (6)) with the aim to determine activation energy and pre-exponential factor:

$$\ln k = -\frac{E_a}{RT} + \ln A \qquad (6)$$

The activation energy for DA in acetonitril was 48.4 and 51.9 kJ·mol^{-1} in chloroform. For the reversible part the activation energy values were 91.0 and 102.3 kJ·mol^{-1}, respectively. The determined activation energies were reasonable and expected according to the already reported values for maleimide/furan systems [24, 27]. Nevertheless, the observed differences originated from the nature of DA building blocks and network density.

While in molten state the DA reaction started when reactants started to melt as a prerequisite for func-

tional groups mobility, the DA reaction in solution was possible even at ambient temperature, however, at a very slow reaction rate. According to the literature, the solvation energy contributes to the total free energy of the reactants and the transition states. For that reason, when in molten state the conversion at 70 °C reached 75% constituted mainly of *endo* adduct, in acetonitrile the equilibrium conversion of merely 45% was achieved. The reaction equilibrium in solution was obviously much more affected by the rDA reaction, which started to affect at lower temperatures rather than in molten state. Therefore, there is no clear boundary between the end of the DA reaction and the beginning of the rDA reaction in solution, which makes its use difficult in preparing the DA adduct at high conversion with desirable *exo/endo* ratio. For that reason synthesis of the product depends on thermo-reversibility of DA reaction which is much more suitable in the molten state, where the limit between DA/rDA reactions is unambiguous.

4. Conclusions

In summary, this study showed a detailed investigation of the DA reaction and provided useful knowledge for further use in self-healing polymer networks. Experiments were performed in the molten state and in solution and the differences between both forms were discussed. By non-isothermal DSC heating of the PMI and GF mixture accompanied by ^{1}H NMR, approximate temperatures of the DA and rDA reaction were determined. We especially focused on *exo/endo* ratio and its dependence on temperature, and on the Diels-Alder kinetics. The activation energy and pre-exponential factor of the forward and reverse DA reaction in a solution were determined by FTIR spectroscopy. The obtained activation energies in acetonitrile and chloroform agreed to be similar with those reported in the literature.

Moreover, the reaction equilibrium in solution is significantly affected by rDA reaction in comparison to the molten state. Considering the reaction in the molten state compared to reaction in solution, there was a clear temperature difference between the length of the DA reaction and rDA reaction which followed afterwards. For that reason, preparation of the material based on the absence of solvent is a better option as the reaction is easily manageable from a conversion and *exo*/*endo* ratio perspective. The presented paper showed the already known common points of the Diels-Alder reaction extended to the detailed thermal behaviour of the reaction in a molten state and solution. Due to this study it is possible to adapt the obtained knowledge in further self-healing studies.

Acknowledgements

References

[1] Woodward R. B., Sondheimer F., Taub D., Heusler K., McLamore W. M.: The total synthesis of steroids. Journal of the American Chemical Society, **74**, 4223-4251 (1952).
DOI: 10.1021/ja01137a001

[2] Tasdelen M. A.: Diels–Alder 'click' reactions: Recent applications in polymer and material science. Polymer Chemistry, **2**, 2133–2145 (2011).
DOI: 10.1039/C1PY00041A

[3] Liu Y-L., Chuo T-W.: Self-healing polymers based on thermally reversible Diels–Alder chemistry. Polymer Chemistry, **4**, 2194–2205 (2013).
DOI: 10.1039/c2py20957h

[4] Kolb H. C., Finn M. G., Sharpless K. B.: Click chemistry: Diverse chemical function from a few good reactions. Angewandte Chemie International Edition, **40**, 2004–2021 (2001).
DOI: 10.1002/1521-3773(20010601)40:11<2004::AID-ANIE2004>3.0.CO;2-5

[5] Canadell J., Fischer H., De With G., van Benthem R.: Stereoisomeric effects in thermo-remendable polymer networks based on Diels-Alder crosslink reactions. Journal of Polymer Science Part A: Polymer Chemistry, **48**, 3456–3467 (2010).
DOI: 10.1002/pola.24134

[6] Froidevaux V., Borne M., Laborbe E., Auvergne R., Gandini A., Boutevin B.: Study of the Diels-Alder and retro-Diels-Alder reaction between furan derivatives and maleimide for the creation of new materials. RSC Advances, **5**, 37742–37754 (2015).
DOI: 10.1039/c5ra01185j

[7] Li J., Zhang G., Deng L., Zhao S., Gao Y., Jiang K., Sun R., Wong C.: *In situ* polymerization of mechanically reinforced, thermally healable graphene oxide/polyurethane composites based on Diels-Alder chemistry. Journal of Materials Chemistry A, **2**, 20642–20649 (2014).
DOI: 10.1039/C4TA04941A

[8] Yu S., Zhang R., Wu Q., Chen T., Sun P.: Bio-inspired high-performance and recyclable cross-linked polymers. Advanced Materials, **25**, 4912–4917 (2013).
DOI: 10.1002/adma.201301513

[9] Pramanik N. B., Nando G. B., Singha N. K.: Self-healing polymeric gel *via* RAFT polymerization and Diels-Alder click chemistry. Polymer, **69**, 349–356 (2015).
DOI: 10.1016/j.polymer.2015.01.023

[10] Kötteritzsch J., Hager M. D., Schubert U. S.: Tuning the self-healing behavior of one-component intrinsic polymers. Polymer, **69**, 321–329 (2015).
DOI: 10.1016/j.polymer.2015.03.027

[11] Weizman H., Nielsen C., Weizman O. S., Nemat-Nasser S.: Synthesis of a self-healing polymer based on reversible Diels-Alder reaction: An advanced undergraduate laboratory at the interface of organic chemistry and materials science. Journal of Chemical Education, **88**, 1137–1140 (2011).
DOI: 10.1021/ed101109f

[12] Du P., Wu M., Liu X., Zheng Z., Wang X., Joncheray T., Zhang Y.: Diels-Alder-based crosslinked self-healing polyurethane/urea from polymeric methylene diphenyl diisocyanate. Journal of Applied Polymer Science, **131**, 40234/1–40234/7 (2014).
DOI: 10.1002/app.40234

[13] Li J., Zhang G., Deng L., Jiang K., Zhao S., Gao Y., Sun R., Wong C.: Thermally reversible and self-healing novolac epoxy resins based on Diels-Alder chemistry. Journal of Applied Polymer Science, **132**, 42167/1–42167/7 (2015).
DOI: 10.1002/app.42167

[14] Tian Q., Yuan Y. C., Rong M. Z., Zhang M. Q.: A thermally remendable epoxy resin. Journal of Materials Chemistry, **19**, 1289–1296 (2009).
DOI: 10.1039/b811938d

[15] Mineo P., Barbera V., Romeo G., Ghezzo F., Scamporrino E., Spitaleri F., Chiacchio U.: Thermally reversible highly cross-linked polymeric materials based on furan/maleimide Diels-Alder adducts. Journal of Applied Polymer Science, **132**, 42314/1–42314/9 (2015).
DOI: 10.1002/app.42314

[16] Bose R. K., Kötteritzsch J., Garcia S. J., Hager M. D., Schubert U. S., van der Zwag S.: A rheological and spectroscopic study on the kinetics of self-healing in a single-component Diels-Alder copolymer and its underlying chemical reaction. Journal of Polymer Science Part A: Polymer Chemistry, **52**, 1669–1675 (2014).
DOI: 10.1002/pola.27164

[17] Agag T., Takeichi T.: Preparation, characterization, and polymerization of maleimidobenzoxazine monomers as a novel class of thermosetting resins. Journal of Polymer Science Part A: Polymer Chemistry, **44**, 1424–1435 (2006).
DOI: 10.1002/pola.21245

[18] Ambrožič R., Šebenik U., Krajnc M.: Synthesis, curing kinetics, thermal and mechanical behavior of novel cardanol-based benzoxazines. Polymer, **76**, 203–212 (2015).
DOI: 10.1016/j.polymer.2015.08.065

[19] Gaina C., Ursache O., Gaina V., Musteata V-E.: High performance thermosets based on multifunctional intermediates containing allyl, maleimide and benzoxazine groups. Journal of Polymer Research, **20**, 263/1–263/11 (2013).
DOI: 10.1007/s10965-013-0263-9

[20] Jin L., Agag T., Ishida H.: Bis(benzoxazine-maleimide)s as a novel class of high performance resin: Synthesis and properties. European Polymer Journal, **46**, 354–363 (2010).
DOI: 10.1016/j.eurpolymj.2009.09.013

[21] Liu Y-L., Chang C-Y., Hsu C-Y., Tseng M-C., Chou C-I.: Preparation, characterization, and properties of fluorene-containing benzoxazine and its corresponding cross-linked polymer. Journal of Polymer Science Part A: Polymer Chemistry, **48**, 4020–4026 (2010).
DOI: 10.1002/pola.24187

[22] Zhong H., Lu Y., Chen J., Xu W., Liu X.: Preparation, characterization, and polymerization of novel maleimidobenzoxazine containing carboxylic moiety and its cocuring behaviors with epoxy resin. Journal of Applied Polymer Science, **118**, 705–710 (2010).
DOI: 10.1002/app.32503

[23] Liu X., Du P., Liu L., Zheng Z., Wang X., Joncheray T., Zhang Y.: Kinetic study of Diels-Alder reaction involving in maleimide–furan compounds and linear polyurethane. Polymer Bulletin, **70**, 2319–2335 (2013).
DOI: 10.1007/s00289-013-0954-8

[24] Adzima B. J., Aguirre H. A., Kloxin C. J., Scott T. F., Bowman C. N.: Rheological and chemical analysis of reverse gelation in a covalently cross-linked Diels-Alder polymer network. Macromolecules, **41**, 9112–9117 (2008).
DOI: 10.1021/ma801863d

[25] Goiti E., Heatley F., Huglin M. B., Rego J. M.: Kinetic aspects of the Diels-Alder reaction between poly (styrene-*co*-furfuryl methacrylate) and bismaleimide. European Polymer Journal, **40**, 1451–1460 (2004).
DOI: 10.1016/j.eurpolymj.2004.01.036

[26] Koehler K. C., Durackova A., Kloxin C. J., Bowman C. N.: Kinetic and thermodynamic measurements for the facile property prediction of Diels-Alder-conjugated material behavior. AIChE Journal, **58**, 3545–3552 (2012).
DOI: 10.1002/aic.13733

[27] Scheltjens G., Diaz M. M., Brancart J., Van Assche G., Van Mele B.: A self-healing polymer network based on reversible covalent bonding. Reactive and Functional Polymers, **73**, 413–420 (2013).
DOI: 10.1016/j.reactfunctpolym.2012.06.017

[28] Yuan Y. C., Yin T., Rong M. Z., Zhang M. Q.: Self healing in polymers and polymer composites. Concepts, realization and outlook: A review. Express Polymer Letters, **2**, 238–250 (2008).
DOI: 10.3144/expresspolymlett.2008.29

[29] Chen N-H., Li H-Y., Lai J-Y., Liu Y-L.: Synthesis and characterization of benzoxazine-containing, crosslinkable, and sulfonated polymer through Diels-Alder reaction for direct methanol fuel cells. Polymer, **54**, 2096–2104 (2013).
DOI: 10.1016/j.polymer.2013.02.037

[30] Chou C-I., Liu Y-L.: High performance thermosets from a curable Diels-Alder polymer possessing benzoxazine groups in the main chain. Journal of Polymer Science Part A: Polymer Chemistry, **46**, 6509–6517 (2008).
DOI: 10.1002/pola.22960

[31] Chow W. S., Grishchuk S., Burkhart T., Karger-Kocsis J.: Gelling and curing behaviors of benzoxazine/epoxy formulations containing 4,4′-thiodiphenol accelerator. Thermochimica Acta, **543**, 172–177 (2012).
DOI: 10.1016/j.tca.2012.05.015

[32] Ručigaj A., Alič B., Krajnc M., Šebenik U.: Curing of bisphenol A-aniline based benzoxazine using phenolic, amino and mercapto accelerators. Express Polymer Letters, **9**, 647–657 (2015).
DOI: 10.3144/expresspolymlett.2015.60

[33] Wang C., Sun J., Liu X., Sudo A., Endo T.: Synthesis and copolymerization of fully bio-based benzoxazines from guaiacol, furfurylamine and stearylamine. Green Chemistry, **14**, 2799–2806 (2012).
DOI: 10.1039/c2gc35796h

[34] Liu Y-L., Yu J-M.: Cocuring behaviors of benzoxazine and maleimide derivatives and the thermal properties of the cured products. Journal of Polymer Science Part A: Polymer Chemistry, **44**, 1890–1899 (2006).
DOI: 10.1002/pola.21290

Polyether from a biobased Janus molecule as surfactant for carbon nanotubes

V. Barbera[1], S. Musto[1], A. Citterio[1], L. Conzatti[2], M. Galimberti[1]*

[1]Politecnico di Milano, Department of Chemistry, Materials and Chemical Engineering 'G. Natta', Via Mancinelli 7, 20131 Milano, Italy
[2]National Council of Research, Institute for the Study of Macromolecules, Via De Marini 6, 16149 Genova, Italy.

Abstract. A new polyether (PE) was prepared from a biobased Janus molecule, 2-(2,5-dimethyl-1*H*-pyrrol-1-yl)-1,3-propanediol (serinol pyrrole, **SP**). **SP** was synthesized with very high yield (about 96%) and high atom efficiency (about 80%) by reacting a biosourced molecule, such as serinol, with 2,5-hexanedione in the absence of solvent or catalyst. The reaction of **SP** with 1,6-dibromohexane led to PE oligomers, that were used as surfactants for multiwalled carbon nanotubes (MWCNT), in ecofriendly polar solvents such as acetone and ethyl acetate. The synergic interaction of aromatic rings and oxyalkylene sequences with the carbon allotrope led to dramatic improvement of surfactant efficiency: only 24% of **SP** based PE was extracted with ethyl acetate from the adduct with MWCNT, versus 98% of a typical pluronic surfactant. Suspensions of MWCNT-PE adducts in ethyl acetate were stable for months. High resolution transmission electron microscopy revealed a film of oligomers tightly adhered to MWCNT surface.

Keywords: nanomaterials, serinol, polyether, carbon nanotubes, surfactant

1. Introduction

Carbon Nanotubes (CNT) possess exceptional mechanical properties and the ability of conducting electrons without dissipating energy as heat. Research activity is performed on both single-walled [1, 2] and multi-walled [3, 4] CNT; one of main objectives is the preparation of even and stable CNT dispersions, both in liquid media and in polymer matrices, in view of many industrial applications. It is widely acknowledged [5–9] that the preparation of stable dispersions of CNT in liquid media has to overcome important obstacles: due to their large molar mass, not only CNT are insoluble in all known solvents but also they are greatly entangled. CNT are thus modified and partially coated with a dispersant phase that favors their compatibility with the liquid. Surfactants are the preferred molecules to prepare such a phase. Main goal of the research is to prepare stable CNT dispersions through simple processes that could preserve CNT integrity.

CNT are thus functionalized, through covalent chemical modification [5–8] or non covalent supramolecular interactions [8]. The latter ones are based on a variety of non bonded interactions such as π-π stacking, cation-π and charge transfer.

Polynuclear aromatic molecules are among the preferred compounds for non-covalent functionalization [8]. Recently, polymers with aromatic repeating units have been employed. Water dispersible nanofibrillar-polyaniline was wrapped on multiwalled carbon nanotubes (MWCNT) by an *in situ* polymerization [10]. Stable dispersions of MWCNT were obtained in organic solvents: in dimethylacetamide by modifying MWCNT with a poly(benzoxazole) (PBO) precursor [4] and obtaining by heating CNT/PBO adduct film, in THF and toluene by using poly(2,7-

carbazole)s [5]. Single-walled carbon nanotubes (SWCNT) were dispersed in the same solvents thanks to poly(phenylacetylene)s with long alkyl tails on the side-chains [6].

Polyalkylene oxides are also acknowledged as efficient surfactants and research on these molecules is steadily performed [11–23]. Poly(ethylene oxide) and pluronic surfactants, i.e. triblock copolymers based on ethylene oxide and propylene oxide, are the preferred solubilizing polymers, particularly in view of biomedical applications. Since the first studies, it was reported that such surfactants, added at low percents, have a positive effect on the tube debundling [19]. Fluorescent labels on nanotubes were brought thanks to fluorescein-polyethylene glycol [11]. Polyoxyethylene sorbitan monooleate-suspended SWCNT were reported to favor the preparation of nanotubes suspensions for in vitro toxicological studies [12].

Objective of this work was to design a surfactant for CNT with much improved efficiency, thanks to the synergy between aromatic rings and oxyalkylene sequences. Such surfactant should be able to develop very efficient supramolecular interaction with CNT and to promote their dispersion in both hydrophobic and hydrophilic environments. To achieve such a goal, a poly(ether) based on the molecule shown in Figure 1 (2-(2,5-dimethyl-1*H*-pyrrol-1-yl)-1,3-propanediol, serinol pyrrole, **SP**) was prepared.

SP is a derivative of 2-amino-1,3-propanediol, known as serinol. It is directly obtainable from renewable sources [24] and can also be prepared from glycerol, a cheap, easily available raw material, non toxic and biodegradable. Glycerol comes from the biodiesel industry and a total amount of 1.2 million ton was available in 2010 [25–29]. Serinol is an interesting molecule for developing innovative synthetic strategies, thanks to the chemoselectivity of amino and hydroxyl groups. In recent papers, polymers from serinol have been reported: cyclic carbonates derivatives were converted into polymers through organocatalytic ring opening polymerization [30] and a compound obtained from the reaction of serinol with
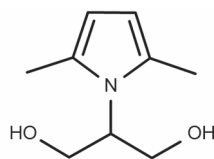
succinimidyl ester of trimethyl-locked benzoquinone was used to prepare water soluble biodegradable polyester [31].

In this work, serinol chemoselectivity was exploited [32–34], preparing **SP** through the Paal-Knorr reaction [34, 35] of serinol (**S**) with 2,5-hexanedione (**HD**), performing the reaction in the absence of solvents and catalysts. **SP** has been defined as a Janus molecule [36], that means a molecule with two faces and, hence, a dual reactivity. The Roman god Janus, represented (for example in coins) as having two faces in one body, inspired the definition 'Janus' first to describe micro- and nanoparticles with at least two physically or chemically differing surfaces [37, 38] and then, more in general, molecules having two faces, a hydrophobic and a hydrophilic one, such as colloids [39] dendritic multiester [40], supermolecular liquid crystals [41], a binding protein for vitamin E [42], block copolymers with (meth)acrylic acid segments [43].

The Paal-Knorr reaction changes the sp^3 hybridization of the nitrogen atom of the amino group and leads to the formation of sp^2 atoms in the aromatic pyrrole ring. Pyrrole can give rise to π-π stacking with aromatic compounds such as CNT and the hydroxyl groups allow the preparation of polymers such as polyethers by step-growth polymerization. First example of polymer obtained by step-growth polymerization, polyurethane, has been recently reported [33]. In this manuscript, polyethers from the reaction of **SP** with 1,6-dibromohexane are reported. They were characterized by means of infrared spectroscopy, ^{1}H and ^{13}C nuclear magnetic resonance (NMR), thermogravimetric analysis (TGA). MWCNT-PE adducts were prepared; their structure was studied by means of high transmission electron microscopy (HRTEM). MWCNT-PE suspensions were prepared in eco-friendly solvents, such as acetone and ethyl acetate, assessing their stability after several month storage, through UV-Vis spectroscopy.

2. Experimental section
2.1. Materials
Purified multi-walled nanotubes (NC7000 series) were purchased from NANOCYL™ Inc (www.nanocyl.com) and used as-supplied. Pluronic RPE 310 was poly(propylene glycol)-block-poly(ethylene glycol)-block-poly(propylene glycol) (PPG-PEG-PPG, M_n = 3000) from BASF.

Figure 1. 2-(2,5-dimethyl-1*H*-pyrrol-1-yl)-1,3-propanediol (**SP**)

Reagents and solvents commercially available were purchased and used without further purification: 2,5-hexanedione (Merck – Schuchardt), 2-amino-1,3-propanediol (kindly provided by Bracco), 1,6-dibromohexane (Sigma-Aldrich), potassium hydroxide (Carlo Erba Reagents), *iso*propyl alcohol (Sigma-Aldrich), acetone (Sigma-Aldrich), ethyl acetate (Sigma-Aldrich), DMSO-*d6* (Sigma-Aldrich).

2.2. Synthesis of 2-(2,5-dimethyl-1*H*-pyrrol-1-yl)-1,3-propanediol (SP)

A mixture of 2,5-hexanedione (41.42 g; 0.36 mol) and serinol (30.02 g; 0.36 mol) was poured into a 100 mL round bottomed flask equipped with magnetic stirrer. The mixture was then stirred, at room temperature, for 6 h. Without any purification the mixture reaction was warmed up to 180 °C for 8 h. The pyrrole derivative was isolated by distillation under reduced pressure at 130 °C and 0.1 mbar. Yellow oil was obtained with 96% yield. ^{1}H NMR (400 MHz, DMSO-*d6*, δ in ppm): 2.16 (s, 6H, –CH_3 at C-2,5 of pyrrole moiety); 3.63 (m, 2H, CH_2OH); 3.76 (m, 2H, CH_2OH); 4.10 (quintet, 1H, at C-3 of diol); 4.73 (t, 2H, CH$_2$OH); 5.55 (s, 2H, C-3,4 of pyrrole moiety).

2.3. Polymerization reactions

Run 1 of Table 1
In a 50 mL round bottom flask equipped with a magnetic stirrer were added **SP** (0.200 g, 1.18 mmol) and potassium hydroxide (0.200 g, 2.36 mmol). The resulting mixture was sonicated for 30 minutes in a 2 L sonication bath. After this period, a solution of 1,6-dibromohexane (0.218 mL) in 3 mL of isopropyl alcohol was added and stirred at 90 °C for 30 minutes. A sample was taken for determination of the conversion by ^{1}H NMR spectroscopy. After cooling at room temperature, water (10 mL) was first added and isopropyl alcohol was removed. To the mixture was then added ethyl acetate and extracted (3×25 mL). The organic phase was dried on Na$_2$SO$_4$ and the solvent was removed. The polymer was isolated by dissolution in CH$_2$Cl$_2$ (2 mL), precipitation from excess diethyl ether (50 mL), filtration, and drying *in vacuo*.

Run 2 of Table 1
In a 25 mL round bottom flask equipped with a magnetic stirrer were added in sequence **SP** (0.100 g, 0.59 mmol) and potassium hydroxide (0.100 g, 1.18 mmol). After stirring for 30 minutes, 1,6-dibromohexane (0.109 mL) was added to the mixture and sonicated for 30 minutes in a 2 L sonication bath. After this period, the mixture was irradiated at 130 °C for 30 minutes by microwave. A sample was taken for determination of the conversion by ^{1}H NMR spectroscopy. After cooling at room temperature, water (10 mL) was first added and was extracted using ethyl acetate (3×10 mL). The organic phase was dried on Na$_2$SO$_4$ and the solvent was removed. The polymer was isolated by dissolution in CH$_2$Cl$_2$ (2 mL), precipitation from excess hexane (50 mL), filtration, and drying in vacuo.

Run 3 of Table 1
In a 25 mL round bottom flask equipped with a magnetic stirrer were added in sequence **SP** (0.100 g, 0.59 mmol) and potassium hydroxide (0.100 g, 1.18 mmol). After stirring for 30 minutes, 1,6-dibromohexane (0.109 mL) was added to the mixture. The resulting mixture was sonicated for 30 minutes in a 2 L sonication bath and after was stirred at 130 °C for 60 minutes. A sample was taken for determination of the conversion by ^{1}H NMR spectroscopy. After cooling at room temperature, water (10 mL) was first added and was extracted using ethyl acetate (3×10 mL). The organic phase was dried on Na$_2$SO$_4$ and the solvent removed. The polymer was isolated by dissolution in CH$_2$Cl$_2$ (2 mL), precipitation from excess hexane (50 mL), filtration, and drying *in vacuo*.

2.4. Preparation of MWCNT adducts

With SP based PE
Dispersion of CNT in acetone was prepared (1 mg/mL) sonicating for 30 minutes in a 2 L sonication bath. A PE solution in acetone was added (1 mg/mL) to the previously obtained instable suspension. The mixture was sonicated for other 30 minutes. The powder of MWCNT/SP adduct was isolated by evaporating the solvent.

With Pluronic 3110
The same procedure was followed except that 5 mg of Pluronic 3110 were used.
The resulting suspension was then centrifuged at 5000 rpm for 5 minutes to test its stability.

2.5. Extraction with ethyl acetate of MWCNT adducts

100 mg of MWCNT adduct in the powder form, either with SP based PE or with Pluronic 3110, was placed in a round bottomed flask (50 mL) equipped with a magnetic stirrer and ethyl acetate (25 mL) was added. The ensuing suspension, after being stirred overnight at room temperature, was centrifuged at 9000 rpm for 30 minutes and dried under vacuum. The so obtained black powder was analyzed by TGA.

2.6. Characterization

Nuclear magnetic resonance analysis
One-dimensional ^{1}H- and ^{13}C NMR spectra were measured at 400 and 100 MHz, respectively, using a Bruker AV 400 equipped with a 5 mm multinuclear probe with reverse detection (Bruker, Rheinstetten, Germany). The solvent was deuterated Chloroform and the temperature was 27 °C. The experimental time for ^{13}C NMR spectra was typically 12 h (corresponding to more than 10 000 scans). Data were processed using TOPSPIN 1.1 or MestReNova. Centrifugations were performed using an ALC – Centrifugette 4206.

Thermal gravimetric analysis
TGA analysis under N_2 were performed with a Mettler TGA SDTA/851 instrument according to the standard method ISO 9924-1. Samples (10 mg) were heated from 30 to 300 °C at 10 °C/min, kept at 300 °C for 10 min, and then heated up to 550 °C at 20 °C/min. After being maintained at 550 °C for 15 min, they were further heated up to 650 °C with an heating rate of 30 °C/min and kept at 650 °C for 20 min under flowing air (60 mL/min).

FT-IR spectroscopy attenuated total reflectance (ATR)
IR spectra were recorded between 450 and 4000 cm^{−1} by using a Perkin Elmer FT-IR spectrum one equipped with Universal ATR Sampling Accessory with diamond crystal.

High resolution transmission electron microscopy
HRTEM analysis of the MWCNT adduct with the PE sample containing the pyrrole ring was performed with a Zeiss Libra® 200 FE microscope (Carl Zeiss AG, Oberkochen, Germany) operating at 200 kV and equipped with an in-column OMEGA filter for energy selective imaging and diffraction. Few drops of acetone diluted suspension of the sample were deposited on a holey carbon film supported on a standard Cu grid and air-dried for several hours before analysis.

Wide-angle X-ray diffraction
WAXD patterns were obtained in reflection, with an automatic Bruker D8 Advance diffractometer, with nickel filtered Cu-Kα radiation. They were recorded in 10 and 80° as the 2Θ range, being 2Θ the peak diffraction angle. Distance between crystallographic planes was calculated from the Bragg law. The D_{hkl} correlation length, in the direction perpendicular to the *hkl* crystal graphitic planes, was determined applying the Scherrer equation (Equation (1)):

$$D_{hkl} = \frac{K\lambda}{\beta_{hkl}\cos\Theta_{hkl}} \qquad (1)$$

where K is the Scherrer constant, λ is the wavelength of the irradiating beam (1.5419 Å, Cu-Kα), β_{hkl} is the width at half height, and Θ_{hkl} is the diffraction angle. The instrumental broadening, b, was determined by obtaining a WAXD pattern of a standard silicon powder 325 mesh (99%), under the same experimental conditions. The width at half height, $\beta_{hkl} = (B_{hkl} - b)$ was corrected, for each observed reflection with $\beta_{hkl} < 1°$, by subtracting the instrumental broadening of the closest silicon reflection from the experimental width at half height, B_{hkl}.

UV-Vis spectroscopy
UV-Vis absorption measurements were made using a Hawlett Packard 8452A Diode Array Spectrophotometer.

3. Results and discussion
Synthesis of 2-(2,5-dimethyl-1H-pyrrol-1-yl)-1,3-propanediol (SP)
The synthesis of **SP**, summarized in Figure 2, is described in detail in the experimental part and has been discussed elsewhere [32, 33].
In brief, serinol (**S**) was first reacted with 2,5-hexanedione (**HD**), adopting the Paal-Knorr reaction, obtaining the tricyclic compound 4a,6a-dimethyl-hexahydro-1,4-dioxa-6*b*-azacyclopenta[*cd*]pentalene (**HHP**), that was then converted into **SP**. The reaction is characterized by high atom economy (82%) and water is the only co-product of the first step. In all the **SP** syntheses carried out for the present work,
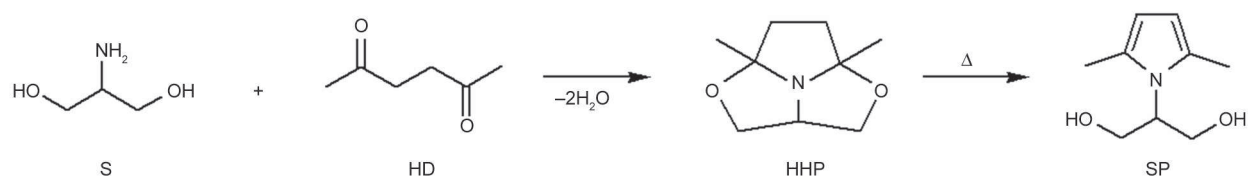
Figure 2. Synthesis of **SP** from serinol (**S**) and 2,5-hexanedione (**HD**)

high yield, about 96%, was easily reproduced. Atom efficiency of about 78% was thus obtained.

Poly(ether)s from SP and 1,6-dibromohexane (DBH)
Polyether synthesis was carried out by using equimolar amounts of **SP** and **DBH**, as it is shown in Figure 3. KOH was used as the base to promote the polymerization: alcolates formed from the OH groups of **SP** performed the nucleophilic attack on the C–Br bond of **DBH**, as in a classical Williamson reaction [44, 45]. Polymerizations here discussed were carried out at different temperatures (90 and 130 °C) and for different times (30 and 60 minutes), either in the absence or in the presence of a solvent such as *iso*-propanol.

Table 1 shows polymerization conditions and data of number average molar mass ($\bar{M}_n$) obtained from NMR analysis.

Low molar masses were obtained in the performed tests. Test carried out in *i-Pr*OH at 90 °C for 30 minutes as the solvent gave $\bar{M}_n$ of about 1800 g·mol^{-1}. Lower molar mass was obtained performing the
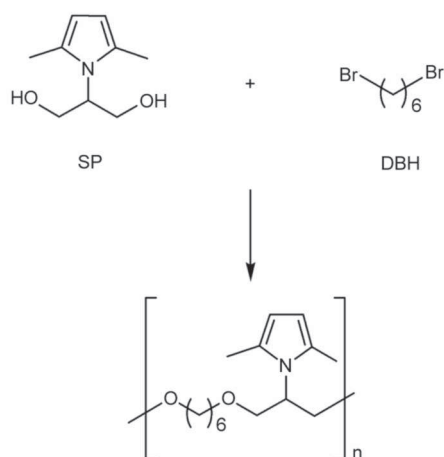
reaction for the same time but in the absence of solvent and at higher temperature (130 °C). Larger value of $\bar{M}_n$, about 2.600 g·mol^{-1}, was achieved at 130 °C, in the absence of a solvent and for a longer polymerization time. Research was not performed in order to enhance the molar mass of poly(ethers), as they were conceived as surfactants for CNT and the low molar mass was seen as beneficial. Research for enhancing the molar mass should carefully control the chemical purity of the comonomers and hence the stoichiometry of the reaction. Moreover, the large steric hindrance of **SP** as the diol, as well as the π-π interactions established by the pyrrole ring, should be investigated.

The nature of functional groups present in the oligomers obtained from runs 1–3 of Table 1 was investi-
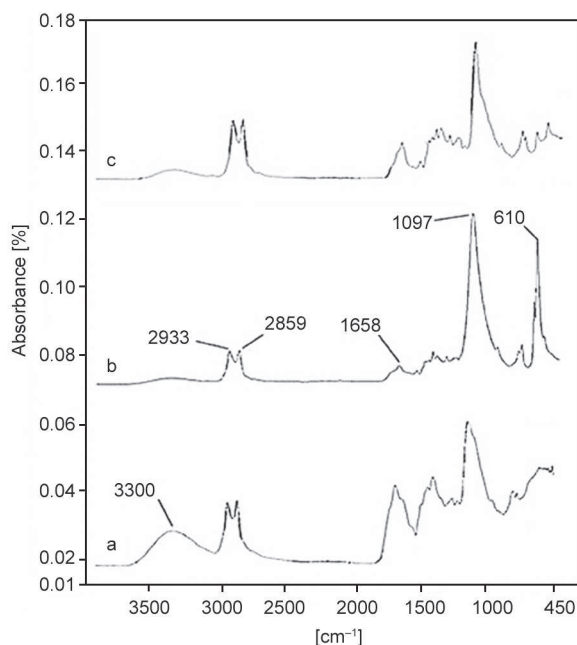
Figure 3. Synthesis of PE from **SP** and **DBH**

Figure 4. FT-ATR spectra [cm^{-1}] of sample from run 1 (a), run 2 (b) and run 3 (c) of Table 1.

Table 1. PE from **SP** and **DBH**: polymerization conditions and molar masses.

Run	DBH [mmol]	SP [mmol]	KOH [mmol]	Solvent	T [°C]	t [min]	$\bar{M}_n$[a] [g·mol^{-1}]
1	1.18	1.18	2.36	iPr-OH[b]	90	30	1.75
2	0.59	0.59	1.18	–	130	30	1.08
3	0.59	0.59	1.18	–	130	60	2.60

[a]number average molar mass from ^{1}H NMR analysis, [b]*iso*propyl alcohol.

gated through FT-ATR spectroscopy. Figure 4 shows the FT-ATR spectra of the reaction products from run 1 (Figure 4 curve a), run 2 (Figure 4 curve b) and run 3 (Figure 4 curve c) of Table 1.

In all the spectra shown in Figure 4, the –C–O–C– ether group is revealed by the characteristic strong band at 1097 cm^{-1}. Peaks due to the pyrrole ring are at 1656, 1461 and 1418 cm^{-1}. Stretching of CH_2 group is revealed by peaks at 2933 and 2859 cm^{-1}.

FT-ATR traces of PE obtained from run 1 and run 2 of Table 1 shown bands of the bromine end group at 610 cm^{-1} (Figure 4 curve a) and of hydroxyl end group (Figure 4 curve b) at 3300 cm^{-1} respectively. The relative intensities of the bands due to the methylene sequence and to the ether linkage, at 2933 cm^{-1} and at 1097 cm^{-1} respectively, can be estimated in the three spectra: values are 1:2, 1:3 and 1:7 for PE from run 3, 1 and 2. Such values appear to be in line with the increasing molar mass.

Oligomers microstructure was studied by means of ^{1}H and ^{13}C NMR analysis. Figure 5 shows the ^{1}H NMR spectra of the reaction products of run 1 (Figure 5 curve a) and run 3 (Figure 5 curve b) of Table 1.

In both ^{1}H NMR spectra of Figure 5, chemical shifts are consistent with the proposed polymer structure. Hydrogen in 3 and 4 position of the pyrrole in the repeating units, should give one signal. In this case, the two singlets at 5.73 and at 5.71 ppm are probably due to the hydrogen atoms of the pyrrole in the repeating units and in the chain ends. The signal at 4.41 ppm can be attributed to the –NC*H* hydrogen near the heterocyclic nitrogen. Peaks at 3.79 and at 3.71 ppm are due to the resonances from diastereotopic hydrogens of ether linkage (C*H*$_2$–O–C).

Peaks at 3.99 and 3.90 ppm in Figure 5 curve a indicate the presence of C*H*$_2$OH terminals, whereas are absent in the spectrum in Figure 5 curve b of the PE, from run 3, with higher molar mass. Both spectra also show at 2.17 ppm the characteristic signals of the methyl group bound in C-2 of the pyrrolic ring.

Thermal stability of **SP** based oligomers was assessed by means of thermal gravimetric analysis. **SP** achieves its boiling point at about 230°C. TGA curve shows decomposition profile made by three main steps. The decomposition of pyrrole moiety, oxygen-containing and alkenylic groups occurs in temperature range
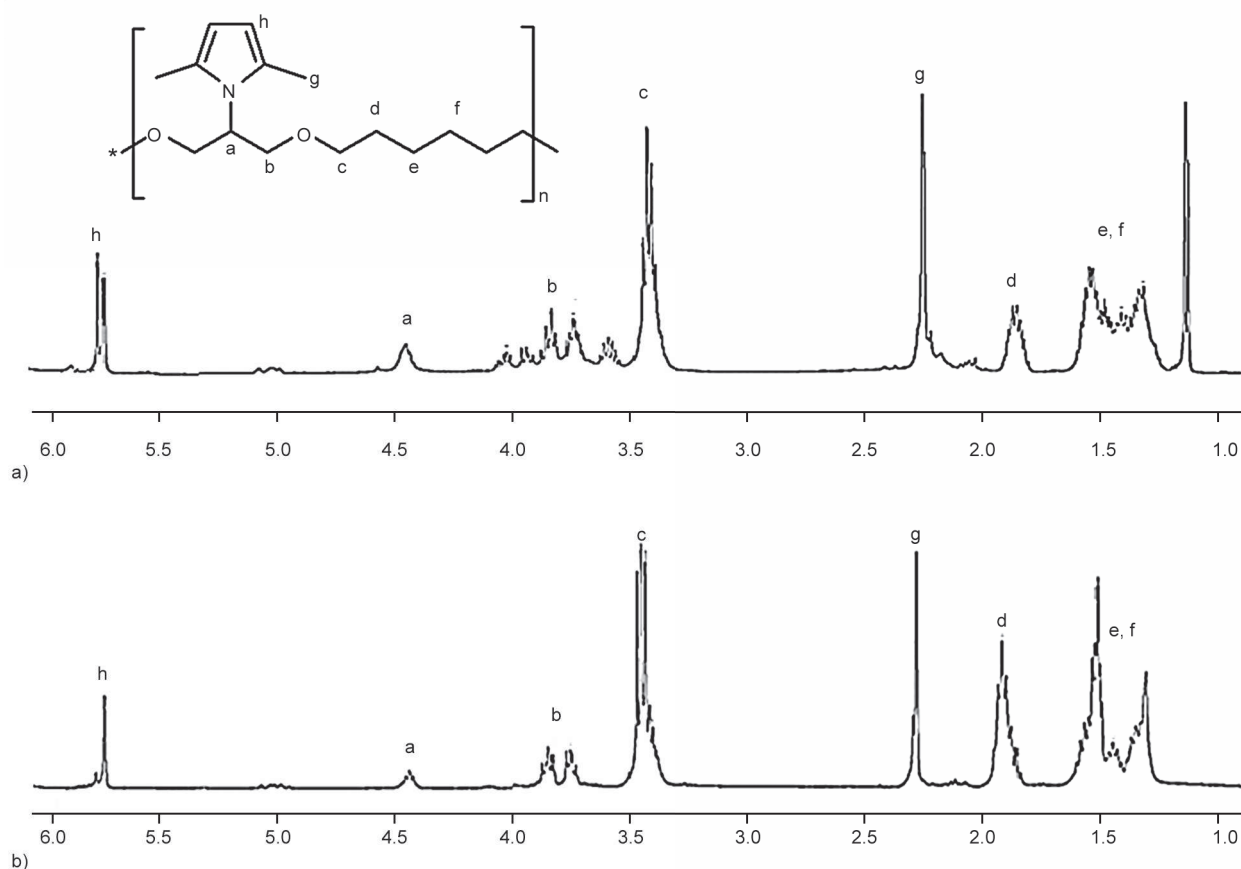

Figure 5. 400 MHz ^{1}H NMR spectra in CDCl$_3$ of sample from run 1 (a) and from run 3 (b) of Table 1

from 150 to 700 °C and the combustion with oxygen (see experimental part) at $T > 700$ °C. Mass loss due to water removal, that could be expected at $T < 150$ °C in consideration of the hydroxyl end groups, is not be detected.

MWCNT-PE adducts

MWCNT-PE adducts were prepared as described in the experimental part. Briefly, a suspension of CNT in acetone (1 mg/mL) was sonicated with a 2 L bath sonicator for 30 minutes, obtaining an unstable suspension. A solution in 5 mL of acetone, of 10 mg of PE sample from run 3 of Table 1, was then added to 5 mL of CNT suspension (10 mg), immediately after its sonication. Further sonication was carried out for 30 minutes. The chemical composition and the structure of CNT coated with PE oligomer (sample from run 3 of Table 1) were then investigated by means of TGA, XRD analysis and HRTEM. Sample for the analysis was isolated by carefully taking the upper part of the supernatant suspension obtained after centrifugation, evaporating then the solvent.

In Figure 6 are reported the thermographs of **SP**, polyether from run 3 of Table 1 and the MWCNT-PE adduct based on such polymer after extraction with ethyl acetate. As reported in Table 2, PE thermal degradation profile shows three main losses due to
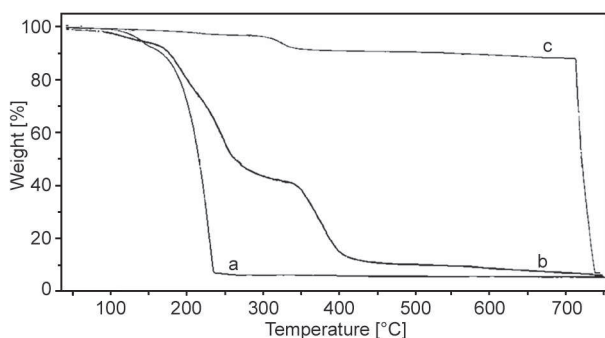
the degradation of the ether-pyrrole moieties and methylene sequences (see Figure 6 curve b). In the MWCNT-PE adduct trace degradation of the adsorbed polymer occurs at a temperature much higher than the one observed in the PE curve. From TGA, the content of PE after extraction with ethyl acetate was calculated to be about 10%.

Figure 7 shows the XRD patterns, in the 10–80° as 2Θ range, of pristine MWCNT (Figure 7 curve a) and of the MWCNT-PE adduct (Figure 7 curve b). XRD pattern of a graphitic crystalline carbon allotrope with many stacked graphene layers, shows, as the most intense peaks, some (00l) and (hkl) reflections, that remain visible also when the number of stacked layers is reduced to few tenths [46]: 002 and 004, at 26.2 and 54.3° as 2Θ value, with a d_{002} interlayer distance of 0.34 nm, 100 and 110 reflections at 42.8 and 77.5° as 2Θ value. The pattern in Figure 7 of MWCNT that has a low number of wrapped layers shows only the two most intense reflections: 002 at 25.3° and 100 at 42.8°. The dimension of crystallites in direction orthogonal to CNT layers can be estimated, by calculating the correlation length D_{00l}, through the Scherrer equation (Equation (1)). A value of about 2.7 nm was obtained for pristine tubes. Taking into account the distance between two successive layers in CNT graphitic crystal, 8 was estimated as the number of CNT layers. In the pattern of MWCMT-PE adduct the 002 and the 110 reflections are clearly visible. The number of wrapped layers was estimated to be about 8.

Morphological analysis of MWCNT and MWCNT-PE adducts was performed through HRTEM analysis at different magnifications. The micrograph in Fig-
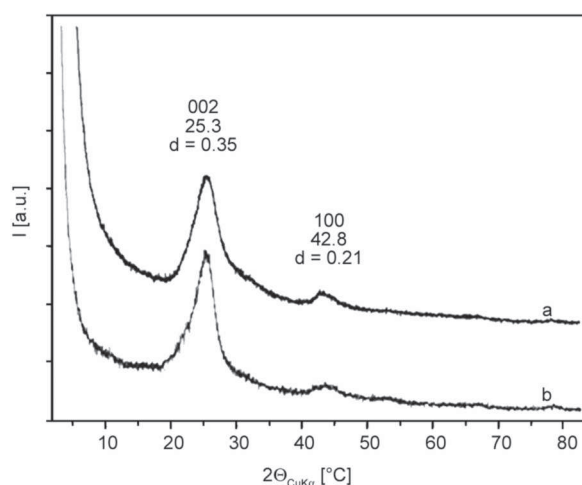

Figure 6. TGA curves taken under N_2 of: **SP** (a), PE (b), MWCNT-PE adduct after extraction with ethyl acetate (c), with PE sample from run 3 of Table 1

Table 2. Mass loss for **SP** and **SP** based oligomers from Table 1 obtained by TGA analysis

Sample	Mass loss [%]		
	T < 250 °C	250 °C < *T* < 500 °C	*T* > 500 °C
SP	100	0	0
PE-1[a]	40	37	23
PE-2[a]	48	31	21
PE-3[a]	52	28	20

[a]polyethers from the runs of Table 1

Figure 7. XRD diffraction spectra of: pristine MWCNT (a) and MWCNT-PE adducts (b)
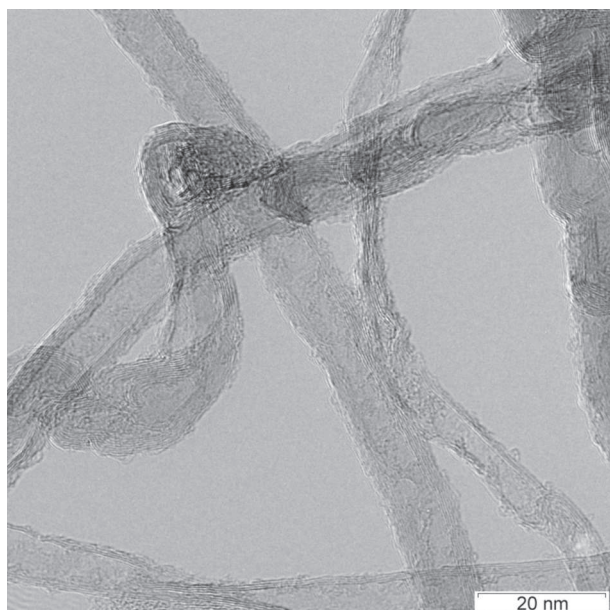
Figure 8. HRTEM micrograph of the MWCNT-PE adduct

Figure 10. UV-Vis traces for ethyl acetate suspensions of: MWCNT (a), MWCNT-PE adduct (b), MWCNT-PE adduct after five months storage (c) (PE from run 3 of Table 1)

ure 8 shows that the multiwalled CNT skeleton remained intact after the treatment with PE oligomers. The average number of CNT layers was calculated equal to 10, a value close to the one estimated from the XRD pattern. The coherence between the results obtained from XRD and HRTEM indicates that the MWCNT-PE adduct shown in Figure 8 (CNT with 10 walls) is representative of the whole sample. CNT external surface resulted decorated with PE chains, which form a not continuous condensed polymer layer (from about 3 to about 9 nm thick) that appears tightly adhered to the CNT external surface.

The suspension of MWCNT-PE adduct was observed to be stable for at least 5 months. Figure 9 shows the pictures of the ethyl acetate suspensions of pristine MWCNT (Figure 9a) and MWCNT-PE after five months (Figure 9c).
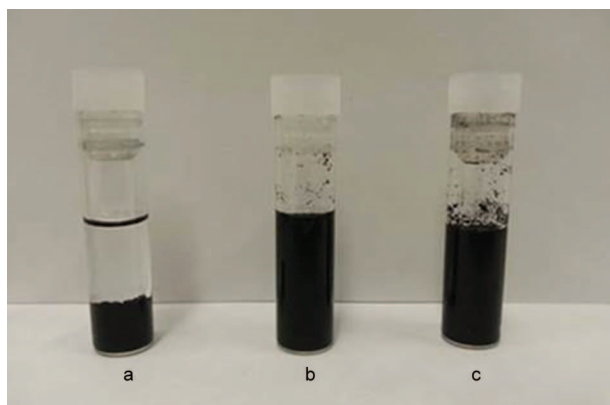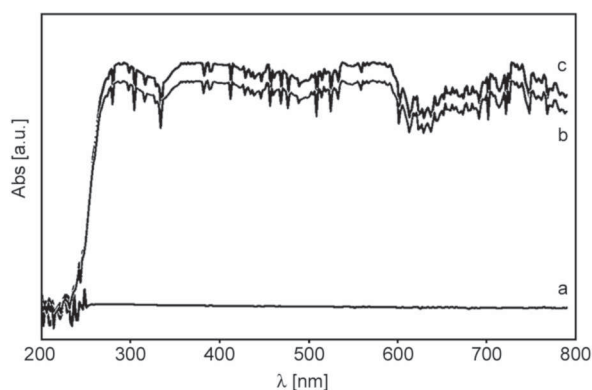

Figure 9. Ethyl acetate suspensions of MWCNT (a), MWCNT-PE (b) and MWCNT-PE adducts after 5 months storage (c) (PE from run 3 of Table 1)

UV–Vis absorption analysis was carried out on the suspensions shown in Figure 9, as described in the experimental part, by carefully taking the upper part of the supernatant suspensions. UV–Vis absorption spectra of such suspensions are reported in Figure 10. It is evident that the same absorbance was detected for the two suspensions, confirming that CNT treated with PE oligomer did not settle down, over five months storage.

As mentioned in the introduction, stable CNT dispersion in liquid media should be obtained through simple preparation processes, preserving CNT integrity. The approach here reported appears to achieve these goals. Thanks to **SP** based PE, a mild sonication is able to promote the formation of the stable suspension, without altering the CNT structure.

Stability of the interaction between **SP** based PE and MWCNT was investigated by solvent extraction. As mentioned in the Introduction, synergy was pursued between aromatic pyrrole rings and poly (oxyalkylene) sequences. Extraction tests with ethyl acetate were thus performed on MWCNT adducts with either **SP** based PE or with the PPG-PEG-PPG block copolymer. The former adduct was from run 3 of Table 1, the latter one was prepared as reported in the experimental part, with the Pluronic surfactant in place of **SP** based PE. TGA analysis of the ensuing products showed that absorbed **SP** based PE in the adduct was 13% before and 10% after (Figure 11a). Instead, the pluronic surfactant was 5% before and 0.1% after extraction (Figure 11b). Mass loss is thus about 24 and 98% for the adduct with **SP** based PE and PPG-PEG-PPG respectively. These results are in line with the analysis of TEM micrographs (Figure 8) that reveal the intimate interaction of MWCNT with
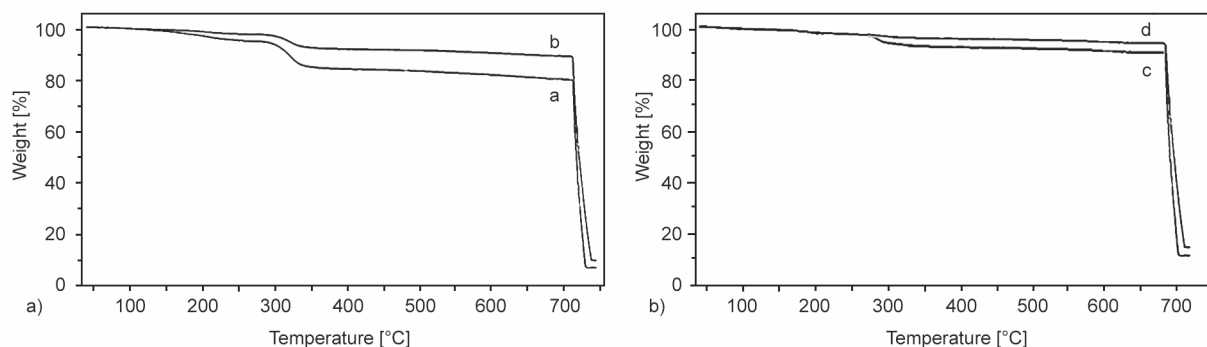
Figure 11. a) TGA curves taken under N$_2$ of MWCNT-PE before (curve a) and after extraction process using ethyl acetate for 12 hours (curve b); (b). MWCNT-Pluronic before (curve c) and after extraction process using ethyl acetate as solvent for 12 hours (curve d)

the **SP** based PE and confirm the superior performance of surfactants containing poly(oxylakylene) sequences and an aromatic ring, inserted in the polymer chain by **SP**.

4. Conclusions

Innovative, green, efficient synthetic strategy was designed and developed for the preparation of polyethers able to establish stable supramolecular interactions with carbon nanotubes. Serinol derivative containing a pyrrole ring, 2-(2,5-dimethyl-1*H*-pyrrol-1-yl)-1,3-propanediol (**SP**), was obtained from the reaction of serinol with 2,5-hexanedione and the subsequent aromatization of the tryciclic compound 4a,6a-dimethyl-hexahydro-1,4-dioxa-6b-azacyclopenta [*cd*]pentalene. High yield solvent free reactions were performed by simply allowing the interaction of the starting reagents. PE oligomers were synthesized through the reaction of **SP** with **DBI** and their adduct with CNT was prepared by sonication in an environmentally friendly solvent such as acetone. Stability of the suspension was verified over months, even after centrifugation. HRTEM analysis revealed that CNT were prevailingly disentangled from the starting bundles, had intact skeleton and were decorated by PE oligomers, tightly adhered to the MWCNT external surface. Stability of the interaction of **SP** based PE with MWCNT was investigated by solvent extraction. With ethyl acetate at room temperature a very minor amount (24%) of the **SP** based PE was extracted, whereas 98% of a PP-PE-PP block copolymer was removed in the same conditions.

This work demonstrates the synergy between the pyrrole rings and the oxyalkylene sequences for es-

tablishing stable interaction with CNT, that can not be achieved by surfactants based only on poly(ethers). These results allow the preparation of even and stable CNT dispersions in a large variety of environments, from environmentally friendly (aqueous) liquids to polymeric matrices. **SP** is thus a versatile monomer for the preparation of polymeric surfactant for carbon allotropes.

Acknowledgements

References
[1] Iijima S., Ichihashi T.: Single-shell carbon nanotubes of 1 nm diameter. Nature, **363**, 603–605 (1993). DOI: 10.1038/363603a0

[2] Bethune D. S., Kiang C. H., de Vries M. S., Gorman G., Savoy R., Vazquez J., Beyers R.: Cobalt-catalysed growth of carbon nanotubes with single-atomic-layer walls. Nature, **363**, 605–607 (1993). DOI: 10.1038/363605a0

[3] Iijima S.: Helical microtubules of graphitic carbon. Nature, **354**, 56–58 (1991). DOI: 10.1038/354056a0

[4] Monthioux M., Kuznetsov V. L.: Who should be given the credit for the discovery of carbon nanotubes? Carbon, **44**, 1621–1623 (2006). DOI: 10.1016/j.carbon.2006.03.019

[5] Dyke C. A., Tour J. M.: Covalent functionalization of single-walled carbon nanotubes for materials applications. The Journal of Physical Chemistry A, **108**, 11151–11159 (2004). DOI: 10.1021/jp046274g

[6] Tasis D., Tagmatarchis N., Bianco A., Prato M.: Chemistry of carbon nanotubes. Chemical Reviews, **106**, 1105–1136 (2006). DOI: 10.1021/cr050569o

[7] Singh P., Campidelli S., Giordani S., Bonifazi D., Bianco A., Prato M.: Organic functionalisation and characterisation of single-walled carbon nanotubes. Chemical Society Reviews, **38**, 2214–2230 (2009). DOI: 10.1039/B518111A

[8] Karousis N., Tagmatarchis N., Tasis D.: Current progress on the chemical modification of carbon nanotubes. Chemical Reviews, **110**, 5366–5397 (2010). DOI: 10.1021/cr100018g

[9] Bergin S. D., Nicolosi V., Streich P. V., Giordani S., Sun Z., Windle A. H., Ryan P., Niraj N. P. P., Wang Z-T. T., Carpenter L., Blau W. J., Boland J. J., Hamilton J. P., Coleman J. N.: Towards solutions of single-walled carbon nanotubes in common solvents. Advanced Materials, **20**, 1876–1881 (2008). DOI: 10.1002/adma.200702451

[10] Jiménez P., Maser W. K., Castell P., Martínez M. T., Benito A. M.: Nanofibrilar polyaniline: Direct route to carbon nanotube water dispersions of high concentration. Macromolecular Rapid Communications, **30**, 418–422 (2009). DOI: 10.1002/marc.200800707

[11] Nakayama-Ratchford N., Bangsaruntip S., Sun X., Welsher K., Dai H.: Noncovalent functionalization of carbon nanotubes by fluorescein–polyethylene glycol: Supramolecular conjugates with pH-dependent absorbance and fluorescence. Journal of the American Chemical Society, **129**, 2448–2449 (2007). DOI: 10.1021/ja068684j

[12] Belyanskaya L., Manser P., Spohn P., Bruinink A., Wick P.: The reliability and limits of the MTT reduction assay for carbon nanotubes–cell interaction. Carbon, **45**, 2643–2648 (2007). DOI: 10.1016/j.carbon.2007.08.010

[13] Otsuka H., Nagasaki Y., Kataoka K.: Self-assembly of poly(ethylene glycol)-based block copolymers for biomedical applications. Current Opinion in Colloid and Interface Science, **6**, 3–10 (2001). DOI: 10.1016/S1359-0294(00)00082-0

[14] Sardella E., Gristina R., Milella A., D'Agostino R., Favia P.: Functionalization of biomedical polymers by means of plasma processes: Plasma treated polymers with limited hydrophobic recovery and PE-CVD of –COOH functional coatings. Journal of Photopolymer Science and Technology, **15**, 341–350 (2002). DOI: 10.2494/photopolymer.15.341

[15] Holm B. A., Bergey E. J., De T., Rodman D. J., Kapoor R., Levy L., Friend C. S., Prasad P. N.: Nanotechnology in biomedical applications. Molecular Crystals and Liquid Crystals **374**, 589–598 (2002). DOI: 10.1080/713738279

[16] Schnabelrauch M., Vogt S., Larcher Y., Wilke I.: Biodegradable polymer networks based on oligolactide macromers: Synthesis, properties and biomedical applications. Biomolecular Engineering, **19**, 295–298 (2002). DOI: 10.1016/S1389-0344(02)00034-5

[17] Leobandung W., Ichikawa H., Fukumori Y., Peppas N. A.: Monodisperse nanoparticles of poly(ethylene glycol) macromers and N-isopropyl acrylamide for biomedical applications. Journal of Applied Polymer Science, **87**, 1678–1684 (2003). DOI: 10.1002/app.11612

[18] Thomas R. N., Guo C.: Surface–functionalized, probe–containing, polymeric nanospheres for biomedical imaging. Spectroscopy, **16**, 387–398 (2002). DOI: 10.1155/2002/818323

[19] Vaisman L., Wagner H. D., Marom G.: The role of surfactants in dispersion of carbon nanotubes. Advances in Colloid and Interface Science, **128–130**, 37–46 (2006). DOI: 10.1016/j.cis.2006.11.007

[20] Rastogi R., Kaushal R., Tripathi S. K., Sharma A. L., Kaur I., Bharadwaj L. M.: Comparative study of carbon nanotube dispersion using surfactants. Journal of Colloid and Interface Science, **328**, 421–428 (2008). DOI: 10.1016/j.jcis.2008.09.015

[21] Pang J., Xu G., Tan Y., He F.: Water-dispersible carbon nanotubes from a mixture of an ethoxy-modified trisiloxane and pluronic block copolymer F127. Colloid and Polymer Science, **288**, 1665–1675 (2010). DOI: 10.1007/s00396-010-2306-7

[22] Blanch A. J., Lenehan C. E., Quinton J. S.: Optimizing surfactant concentrations for dispersion of single-walled carbon nanotubes in aqueous solution. Journal of Physical Chemistry B, **114**, 9805–9811 (2010). DOI: 10.1021/jp104113d

[23] Fernandes R. M. F., Abreu B., Claro B., Buzaglo M., Regev O., Furó I., Marques E. F.: Dispersing carbon nanotubes with ionic surfactants under controlled conditions: Comparisons and insight. Langmuir, **31**, 10955–10965 (2015). DOI: 10.1021/acs.langmuir.5b02050

[24] Andreeßen B., Steinbüchel A.: Serinol: Small molecule − big impact. AMB Express, **1**, 1–6 (2011). DOI: 10.1186/2191-0855-1-12

[25] Pagliaro M., Ciriminna R., Kimura H., Rossi M., Della Pina C.: From glycerol to value-added products. Angewandte Chemie International Edition, **46**, 4434–4440 (2007). DOI: 10.1002/anie.200604694

[26] Zhou C-H., Beltramini J. N., Fan Y-X., Lu G. Q.: Chemoselective catalytic conversion of glycerol as a biorenewable source to valuable commodity chemicals. Chemical Society Reviews, **37**, 527–549 (2008). DOI: 10.1039/B707343G

[27] Rahmat N., Abdullah A. Z., Mohamed A. R.: Recent progress on innovative and potential technologies for glycerol transformation into fuel additives: A critical review. Renewable and Sustainable Energy Reviews, **14**, 987–1000 (2010). DOI: 10.1016/j.rser.2009.11.010

[28] Quispe C. A., Coronado C. J., Carvalho Jr J. A.: Glycerol: Production, consumption, prices, characterization and new trends in combustion. Renewable and Sustainable Energy Reviews, **27**, 475–493 (2013).
DOI: 10.1016/j.rser.2013.06.017

[29] Yang F., Hanna M. A., Sun R.: Value-added uses for crude glycerol – A byproduct of biodiesel production. Biotechnology for Biofuels, **5**, 13/1–13/10 (2012).
DOI: 10.1186/1754-6834-5-13

[30] Venkataraman S., Veronica N., Voo Z. X., Hedrick J. L., Yang Y. Y.: 2-Amino-1,3-propane diols: A versatile platform for the synthesis of aliphatic cyclic carbonate monomers. Polymer Chemistry, **4**, 2945–2948 (2013).
DOI: 10.1039/C3PY00318C

[31] Cho H., Bae J., Garripelli V. K., Anderson J. M., Jun H-W., Jo S.: Redox-sensitive polymeric nanoparticles for drug delivery. Chemical Communications, **48**, 6043–6045 (2012).
DOI: 10.1039/C2CC31463K

[32] Barbera V., Citterio A., Galimberti M. S., Leonardi G., Sebastiano R., Shisodia S. U., Valerio A. M.: Process for the synthesis of 2-(2,5-dimethyl-1h-pyrrol-1-yl)-1,3-propanediol and its substituted derivatives. Word Patent WO/2015/189411 (2015).

[33] Galimberti M., Barbera V., Citterio A., Sebastiano R., Truscello A., Valerio A. M., Conzatti L., Mendichi R.: Supramolecular interactions of carbon nanotubes with biosourced polyurethanes from 2-(2,5-dimethyl-1H-pyrrol-1-yl)-1,3-propanediol. Polymer, **63**, 62–70 (2015).
DOI: 10.1016/j.polymer.2015.02.042

[34] Knorr L.: Einwirkung des diacetbernsteinsäureesters auf ammoniak und primäre aminbasen (in German). Berichte der deutschen chemischen Gesellschaft, **18**, 299–311 (1885).
DOI: 10.1002/cber.18850180154

[35] Paal C.: Synthese von Thiophen- und Pyrrolderivaten (in German). Berichte der deutschen chemischen Gesellschaft, **18**, 2251–2254 (1885).
DOI: 10.1002/cber.18850180175

[36] Galimberti M., Barbera V., Guerra S., Conzatti L., Castiglioni C., Brambilla L., Serafini A.: Biobased Janus molecule for the facile preparation of water solutions of few layer graphene sheets. RSC Advances, **5**, 81142–81152 (2015).
DOI: 10.1039/C5RA11387C

[37] Casagrande C., Fabre P., Raphaël E., Veyssié M.: 'Janus beads': Realization and behaviour at water/oil interfaces. Europhysics Letters, **9**, 251–255 (1989).
DOI: 10.1209/0295-5075/9/3/011

[38] de Gennes P-G.: Soft matter (nobel lecture). Angewandte Chemie International Edition, **31**, 842–845 (1992).
DOI: 10.1002/anie.199208421

[39] Li F., Josephson D. P., Stein A.: Colloidal assembly: The road from particles to colloidal molecules and crystals. Angewandte Chemie International Edition, **50**, 360–388 (2011).
DOI: 10.1002/anie.201001451

[40] Ropponen J., Nummelin S., Rissanen K.: Bisfunctionalized Janus molecules. Organic Letters, **6**, 2495–2497 (2004).
DOI: 10.1021/ol049555f

[41] Saez I. M., Goodby J. W.: 'Janus' supermolecular liquid crystals–giant molecules with hemispherical architectures. Chemistry A European Journal, **9**, 4869–4877 (2003).
DOI: 10.1002/chem.200305100

[42] Ricciarelli R., Zingg J-M., Azzi A.: Vitamin E: protective role of a Janus molecule. The FASEB Journal, **15**, 2314–2325 (2001).
DOI: 10.1096/fj.01-0258rev

[43] Mori H., Müller A. H.: New polymeric architectures with (meth)acrylic acid segments. Progress in Polymer Science, **28**, 1403–1439 (2003).
DOI: 10.1016/S0079-6700(03)00076-5

[44] Morrison R. T., Boyd R. N.: Organic chemistry, sixth edition. Prentice Hall, New York (1987).

[45] Gitsov I., Wooley K. L., Hawker C. J., Ivanova P. T., Frechet J. M.: Synthesis and properties of novel linear-dendritic block copolymers. reactivity of dendritic macromolecules toward linear polymers. Macromolecules, **26**, 5621–5627 (1993).
DOI: 10.1021/ma00073a014

[46] Mauro M., Cipolletti V., Galimberti M., Longo P., Guerra G.: Chemically reduced graphite oxide with improved shape anisotropy. The Journal of Physical Chemistry C, **116**, 24809–24813 (2012).
DOI: 10.1021/jp307112k

Recycling of poly(ethylene terephthalate) – A review focusing on chemical methods

B. Geyer[1], G. Lorenz[1,2], A. Kandelbauer[1,2]*

[1]Reutlingen Research Institute (RRI), Reutlingen University, Alteburgstrasse 150, 72762 Reutlingen, Germany
[2]School of Applied Chemistry, Reutlingen University, Alteburgstrasse 150, 72762 Reutlingen, Germany

Abstract. Recycling of poly(ethylene terephthalate) (PET) is of crucial importance, since worldwide amounts of PET-waste increase rapidly due to its widespread applications. Hence, several methods have been developed, like energetic, material, thermo-mechanical and chemical recycling of PET. Most frequently, PET-waste is incinerated for energy recovery, used as additive in concrete composites or glycolysed to yield mixtures of monomers and undefined oligomers. While energetic and thermo-mechanical recycling entail downcycling of the material, chemical recycling requires considerable amounts of chemicals and demanding processing steps entailing toxic and ecological issues. This review provides a thorough survey of PET-recycling including energetic, material, thermo-mechanical and chemical methods. It focuses on chemical methods describing important reaction parameters and yields of obtained reaction products. While most methods yield monomers, only a few yield undefined low molecular weight oligomers for impaired applications (dispersants or plasticizers). Further, the present work presents an alternative chemical recycling method of PET in comparison to existing chemical methods.

Keywords: *recycling, poly(ethylene terephthalate), degradation, monomers, oligomers*

1. Introduction

From the late 1990s to the year 2011, the worldwide amount of poly(ethylene terephthalate) (PET) increased rapidly from approximately 14 to 60 million tons [1, 2]. Correspondingly, equivalent amounts of PET-waste are generated. Since life cycle assessment studies showed that re-utilization of PET has a positive effect on energy balance and the reduction of CO_2 emissions, for ecological reasons, the need of an appropriate PET-recycling is greater than ever [3–7]. Thus, several PET-recycling methods have been developed, which were partially reviewed in the literature [8–15].

One of these methods is the incineration of the PET-waste using the released heat of combustion (direct energy recovery), which amounts to about 46 MJ·kg^{-1} [13, 14]. Another method, the pyrolysis of the PET-waste is applied to produce a substitute of coal (carbonization) or aromatic and aliphatic compounds as an alternative for fossil fuels (indirect energy recovery). These applications are classified as energetic recycling, since they both use the released thermal energy either directly from incineration of the PET-waste or indirectly from combustion of pyrolysis products [16–31].

For material recycling, the PET-waste is used as an additive in crushed form. In this application, it acts as a partial substitute of natural raw materials such as sand and other natural aggregates and helps reducing the consumption of such resources. It is mixed into composite materials (e.g. asphalt, mortar or concrete) or other polymers to improve their mechanical properties [32–65].

Thermo-mechanical recycling represents another method of re-utilization of PET-waste. Generally, the PET-waste is re-melted without additives. Since this procedure leads to a downcycling of the material due to discoloration or thermal degradation, it is also re-melted with specific additives (complementary colors, inorganic materials or epoxy-chain extenders) to prevent the downcycling [66–94].

In this review, downcycling is used in various meanings. In a strict sense, downcycling means the deterioration of the material properties of PET by damaging or shortening the polymer chains of the polyester. However, processes leading to the utilization of PET in low value applications such as a filler material where the material potential of PET is not fully used can also be considered as some kind of 'downcycling' in a wider sense. Ultimately, thermal degradation processes like incineration, pyrolysis or carbonization which lead to monomers and hence a total loss of efforts for synthesis for virgin PET can also be considered as 'downcycling'. Hence, most energetic and material recycling methods ultimately lead to a downcycling of PET.

In contrast, chemical recycling methods offer the possibility of re-introduction of PET into the material cycle without loss of quality by de-polymerizing PET-waste into monomers. These monomers are used for re-polymerization. Most frequently applied methods use water (hydrolysis), glycols (glycolysis), amines (aminolysis) and alcohols (alcoholysis) for de-polymerization of PET-waste under various reaction conditions. However, these methods require high temperature and high pressure conditions as well as considerable amounts of solvents and degrading agents for de-polymerization [95]. Further, chemical recycling methods generally entail separation and purification steps for product recovery. Thus, this kind of chemical recycling imposes toxic and environmentally hazardous issues.

In the present review a comprehensive survey of PET-recycling methods is given, reviewing both conventional and exceptional methods (carbonization of PET, use of castor oil or ionic liquids for PET de-polymerization). This review focuses on chemical recycling methods with respect to the yields of the obtained reaction products and their usability for value added applications.

2. Classification of recycling poly(ethylene terephthalate)

2.1. Energetic recycling

2.1.1. Pyrolysis

Pyrolysis of PET-waste was first described in 1982 by Day *et al.* [96]. It is an alternative to PET disposal in landfills. In general, PET waste is pyrolysed without further purification of the plastic waste. Pyrolysis is carried out at temperatures between 200 and 900 °C for 0.5 hours to 1 hour [16–19, 21, 24–31, 97–101]. The majority of pyrolyses were conducted to produce aliphatic and aromatic hydrocarbons as an alternative for fossil fuels or as a source for chemicals [17, 19, 21, 24–31]. Other research on pyrolysis was done to either model degradation kinetics or to use PET-wastes in the production of coke for steel making process [98, 100–103]. Finally, Urbanova *et al.* [104] studied the influence of IR laser irradiation for PET pyrolysis. As in conventional pyrolysis, they obtained aliphatic and aromatic hydrocarbons.

2.1.2. Carbonization

Carbonization is a second method of pyrolysing PET-waste. It is carried out at temperatures between 350–1550 °C for 0.5 to 18.5 hours [105–111]. The major application of carbonization is the production of active carbon as adsorbent materials for either waste water or as CO_2-scavenger [105, 108, 110, 111]. Carbonized PET-waste is also used as slag foaming agent and as a substitute of coal in steel making process [106, 107].

2.2. Sorting

Since PET-waste is often supplied in mixtures with other polymers, PET has to be separated from these polymers prior to re-processing. Therefore, several methods have been developed and are described in the literature. These methods comprise froth flotation, wet shaking table, swelling or thermo-mechanical procedures [112–123].

2.2.1. Application of PET as additive

A further use of recycled PET-waste after sorting is its use as additive in stone mastic asphalt, cementitious materials, mortars or concrete composites. The PET-waste is mixed in crushed shape in the corresponding materials to improve mechanical properties of these composites. Moreover, this method is in-

tended to reduce the weight of such composites, when being used as material for the construction of large buildings [32–64]. A second possibility of using PET-waste as an additive is described by de Mello *et al.* [65], who applied PET particles as reinforcing component in polyurethane foams to improve the mechanical strength of the material. Finally, Zou *et al.* [124] studied the use of recycled PET as additive for paper coatings. Although proposing an eco-friendly alternative to energetic recycling methods and land-filling disposal, this method remains a downcycling application for PET-waste in the wider sense since the potential of the material PET is not used to its full extent in this low value application.

2.3. Thermo-mechanical recycling
2.3.1. Re-melting without additives
The simplest way of thermo-mechanical recycling is re-melting the sorted PET-waste. This method is applied in bottle-to-bottle technologies, where sorted PET-bottles are re-melted in crushed shape and re-processed to bottles as beverage packaging. Several studies have been conducted on thermal re-processing PET. During this process, the polymer is exposed to high temperatures, shear forces and pressures. Thus, thermal degradation of PET occurs. As a consequence, reduced thermal and mechanical properties of the re-processed material were the main findings of these investigations (downcycling) [66–78]. Hence, a repeated thermal re-processing of PET-waste finally leads to a downcycling of the material.

2.3.2. Re-melting with additives
To make re-utilization of recycled PET feasible, the application of additives to PET-waste has emerged. Since the collection of PET-waste entails generally a mixture of differently colored PET-materials, such thermally re-processed material leads to undesired coloration of recycled PET. Therefore, the addition of complementary colors to PET-waste has been applied to mask discoloration [79]. Although being an approved procedure, this method probably limits the use of the recycled PET. Likewise, additives were developed to improve viscosity and impact strength of recycled PET, but the recyclate was excluded from food packaging in Europe [80].
Besides such additives, the addition of other polymers (e. g. polyethylene, polypropylene) or inorganic materials (clay minerals) has been applied for thermo-mechanical PET recycling to improve mechanical

properties of the recyclate [81–94]. In addition to blending PET with a second polymer, the use of compatibilizers such as ethylene vinyl acetate, ethylene-butyl acrylate-glycidyl methacrylate copolymer, poly (styrene-ethylene/butylene-styrene) and epoxy-chain extenders has been applied to further improve mechanical properties [82–86]. Although the use of additives to PET can improve properties of thermo-mechanically recycled PET, it ultimately leads to a downcycling of the material, since this material becomes increasingly difficult to be recycled again due to the heterogeneous and inherent composition of PET with the other components.

2.4. Chemical recycling
2.4.1. Ionic liquids
The application of ionic liquids for de-polymerization was first described in the year 2000 by Adams *et al.* [125]. This method was developed to avoid the drawbacks of former methods like methanolysis (high pressure and temperature), glycolysis (heterogeneous reaction products) or acidic and alkaline hydrolysis (pollution problems) to provide an eco-friendly degrading agent for polymers and to enable degradation under moderate reaction conditions. However, no application of the obtained reaction products was described. The general reaction scheme is depicted in Figure 1a [126].
Wang *et al.* [126] depolymerized PET with an excess of the ionic liquid at 120– 200 °C for 6–10 hours. After the reaction was finished, the residual PET was removed, the degradation product precipitated by the addition of water and steam extracted for purification. They used different ionic liquids such as 1-butyl-3-methylimidazolium tetrachloroaluminate ([bmim]$^+$AlCl$_4$$^-$), 1-butyl-3-methylimidazolium chloride ([bmim]$^+$Cl$^-$), 1-butyl-3-methylimidazolium bromide ([bmim]$^+$Br$^-$), 1-ethyl-3-methylimidazolium bromide ([emim]$^+$Br$^-$), 1-butyl-3-methylimidazolium tetrafluoroborate ([bmim]$^+$BF$_4$$^-$), 1-butyl-3-methylimidazolium hexafluorophoasphate ([bmim]$^+$PF$_6$$^-$), 1-butyl-3-methylimidazolium trifluoroacetate ([bmim]$^+$CF$_3$COO$^-$), 1-butyl-3-methylimidazolium acetate ([bmim]$^+$CH$_3$COO$^-$) (Figure 1b). Since the ionic liquid [bmim]$^+$Cl$^-$ was most stable and PET was less soluble in the other liquids, only the reaction with [bmim]$^+$Cl$^-$ was studied. Further, they studied the use of zinc acetate, tetrabutyl titanate and solid superacid as catalysts on the solubility of PET in the ionic liquid, but found that solubility was decreased
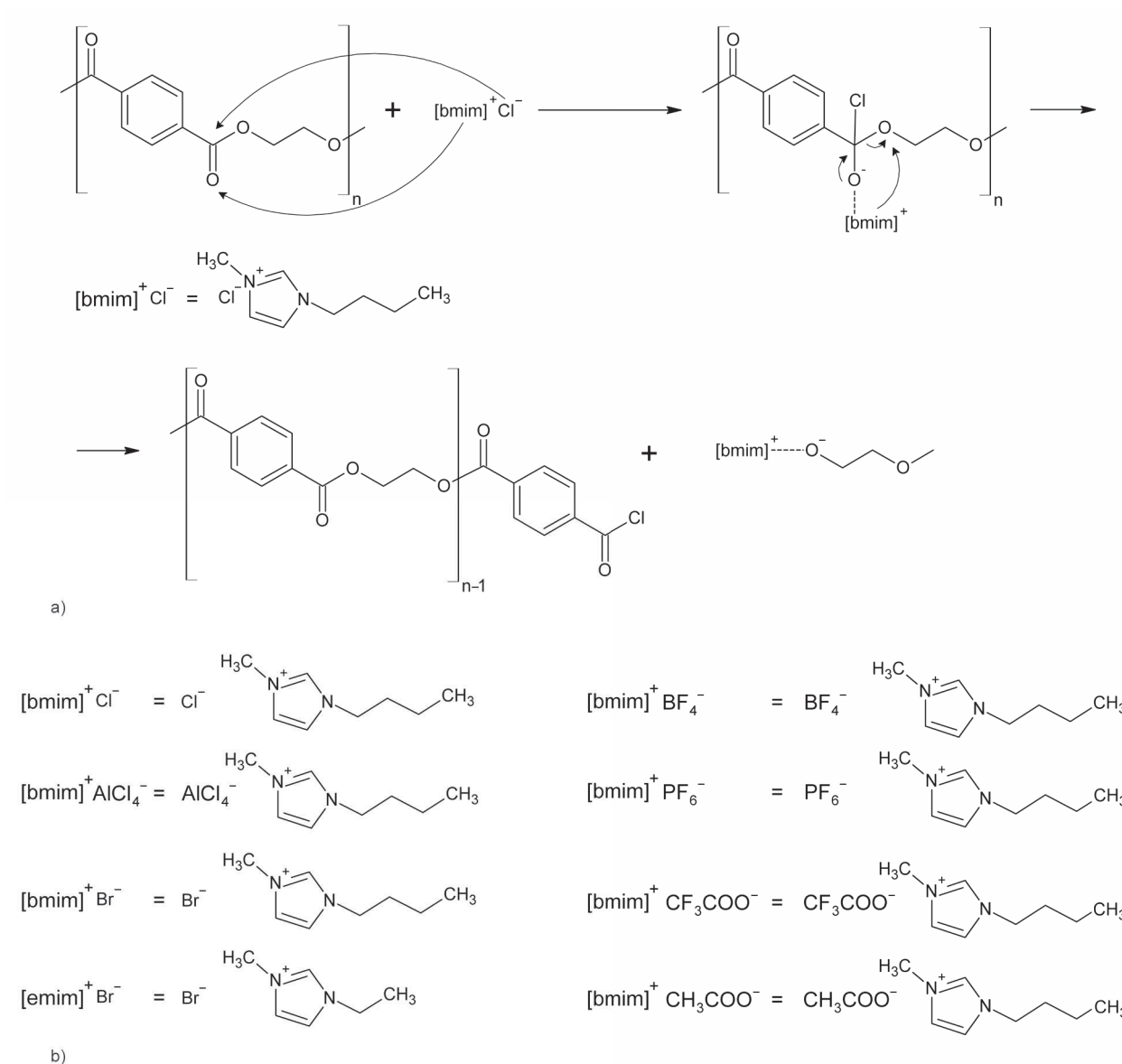
Figure 1. Reaction of the ionic liquid 1-butyl-3-methylimidazolium chloride ([bmim]$^+$Cl$^-$) with PET (a), Applied ionic liquids (b) [126]

independent of the applied catalyst. As expected, they found an increased degradation rate with increasing reaction temperature. The molecular weight (characterized by GPC) of the undefined oligomers was in the range of 777 to 790 g·mol^{-1}. The yield of these products was not determined. The main objectives of their research were the study of the reaction kinetics and the recyclability of the ionic liquids for the de-polymerization reaction of PET in terms of an eco-friendly degrading agent as mentioned above.

2.4.2. Castor oil

The application of castor oil for de-polymerization was first described in the year 1999 by Kržan [127]. This method was developed to provide a renewable

substitute of petrochemical agents (for example, glycols) for PET de-polymerization. After de-polymerization, the reaction products were aimed for the preparation of polyurethane systems. The general reaction scheme is depicted in Figure 2 [128].

Beneš *et al*. [128] depolymerized PET with castor oil at 230–240 °C for 0–2 hours assisted microwaves. After the reaction was finished, solid residues were removed by vacuum filtration. Further, they applied zinc acetate, sodium carbonate and sodium hydrogen carbonate as catalysts. They found that the optimum reaction temperature range is between 230 and 240 °C, whereas below 230 °C almost no reaction was observed. In contrast, reaction temperatures above 240 °C lead to undesired side reactions of the castor
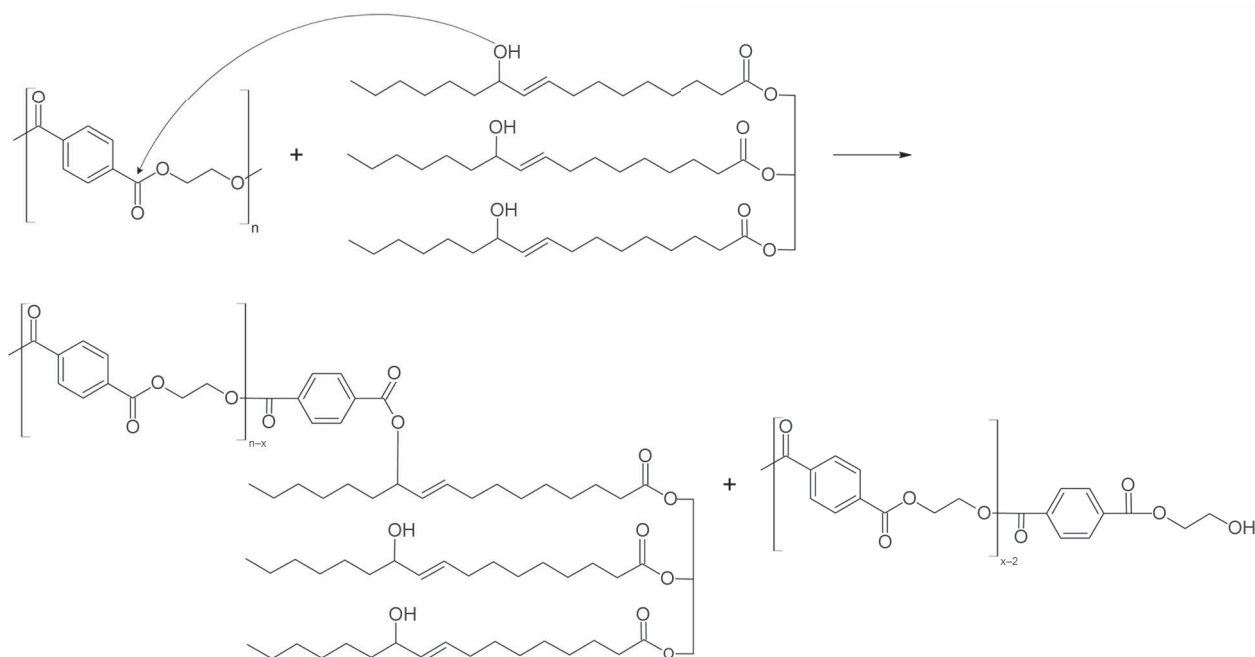
Figure 2. Reaction of castor oil with PET [128]

oil (dehydration, hydrolysis and transesterification). Moreover, zinc acetate seemed to be an efficient catalyst compared to sodium carbonate or sodium hydrogen carbonate. However, it was difficult to determine characteristic molecular weights (characterized by GPC) due to the excessive amount of applied castor oil, but it was stated, that no higher molecular weight PET-oligomers were obtained. Even with precise control of the reaction temperature a heterogeneous mixture of reaction products were obtained.

2.4.3. De-polymerization of PET using enzymes

The degradation of polymers using enzymes was first described in the year 1977 by Tokiwa and Suzuki [129]. As the use of ionic liquids and castor oil, this bio-chemical method was developed to provide an eco-friendly procedure of polymer recycling in contrast to conventional chemical recycling methods like methanolysis (high pressure and temperature), glycolysis (heterogeneous reaction products) or acidic and alkaline hydrolysis (pollution problems). The aimed application of reaction products after de-polymerization is the surface functionalization of polyester materials. Generally, PET was incubated in the enzymatic solution at temperatures between 30 to 60 °C for a period of time ranging from 3 to 14 days. Residual PET and solution were separated for product characterization [130–133].

As shown in Table 1, different enzymes such as *saccharomonospora viridis* cutinase polyesterase, *ther-*

mobifidia fusca hydrolase, cutinase and lipase were applied for PET degradation. Mueller discussed the general applicability of *thermobifidia fusca* hydrolase for PET de-polymerization without mentioning a main degradation product or its yield [131].

Donelli *et al*. [132] only studied the surface morphology of PET treated with cutinase and did not make a qualitative or quantitative statement of possible reaction products. In contrast, Zhang *et al*. [133] studied the application of lipase as degrading agent for diethylene glycol terephthalate (DGTP) and PET at 30 °C and 14 days. They found that lipase is capable of fully converting DGTP to terephthalic acid (TPA), whereas the degradation of PET to TPA was negligible.

Finally, Kawai *et al*. [130] used *saccharomonospora viridis* cutinase polyesterase for degradation of PET at reaction conditions of 63 °C and 3 days. With this enzyme it was possible to obtain 10–27% of TPA form PET degradation.

In these references, the authors conclude, that de-polymerization of PET using enzymes is generally possible as an eco-friendly alternative to conventional chemical recycling methods, since the latter require high pressure and temperature equipment and considerable amounts of toxic as well as hazardous chemicals. However, efficiency is rather low with respect to complete de-polymerization of PET and hence quantitative recovery of homogeneous reaction products for re-use is not possible.

Table 1. Reaction conditions and yields of enzymatic degradation of PET

Reaction product	Yield [%]	Enzyme	Reaction temperature [°C]	Reaction time [days]	Reference
Monomer, TPA[a]	10 to 27	Saccharomonospora viridis cutinase polyesterase	63	3	[130]
Monomer, TPA[a]	negligible	Lipase	30	14	[133]
Not given	not given	Thermobifidia fusca hydrolase	55	not given	[131]
Not given	not given	Cutinase	40	0.1	[132]

[a]TPA: Terephthalic acid

2.4.4. Alcoholysis

Alcoholysis for de-polymerization of PET was first described in the year 1991 by Wang *et al*. [134]. This method was developed to avoid the drawbacks of the methods like glycolysis (heterogeneous reaction products) or acidic and alkaline hydrolysis (pollution problems) to provide a renewable and eco-friendly degrading agent for polymers [135]. The general reaction scheme is depicted in Figure 3a.

Generally, PET is de-polymerized with an excess of an alcohol to yield corresponding esters of terephthalic acid and ethylene glycol [136].

Fávaro *et al*. [135] completely de-polymerized PET with excess supercritical ethanol at 255 °C and 116 bar for 30 to 120 minutes. They obtained diethylene terephthalate with 80% yield (Table 2) as monomer for PET synthesis. However, the obtained ethylene glycol was only suitable for an impaired application as cooling liquid due to its reduced purity.

Mendes *et al*. [34] used pentaerythrytol (PENTE) for alcoholysis of PET at 250 °C for 10 minutes. They melt-mixed PET with different concentrations of PENTE and found with increasing amount of PENTE the trend of formation from branched, undefined low molecular weight oligomers to the monomer bis(tri-hydroxy neopentyl) terephthalate (BTHNPT). This monomer could be used as additive for asphalt or as adhesives.

Nikje and Nazari studied alcoholysis of PET using 1-butanol, 1-pentanol and 1-hexanol. They refluxed PET with excess alcohol under microwave irradiation to accelerate complete de-polymerization of PET and obtained terephthalic acid with high purity in yields between 84 and 96% [137]. The use of microwave irradiation provided short reaction times and no further oxidation of the side product ethylene glycol. In this case, the aimed application of reaction products after de-polymerization was the synthesis of virgin PET.

Likewise, Liu *et al*. [136] used excess 1-butanol for alcoholysis of PET and studied the influence of different catalysts and their re-useability on PET conversion, but did not mention any aimed application of obtained reaction products after de-polymerization. Reaction was carried out at 205 °C for 480 minutes to give the monomer dibutyl terephthalate (DBTP). Highest yield of 95% was obtained using (3-sulfonic acid)-propyltriethylammonium chlorozincinate as catalyst.

In contrast to the previous alcoholytic methods, Dutt and Soni applied excess 2-ethyl-1-hexanol for PET-alcoholysis to produce plasticizers for nitrile rubber
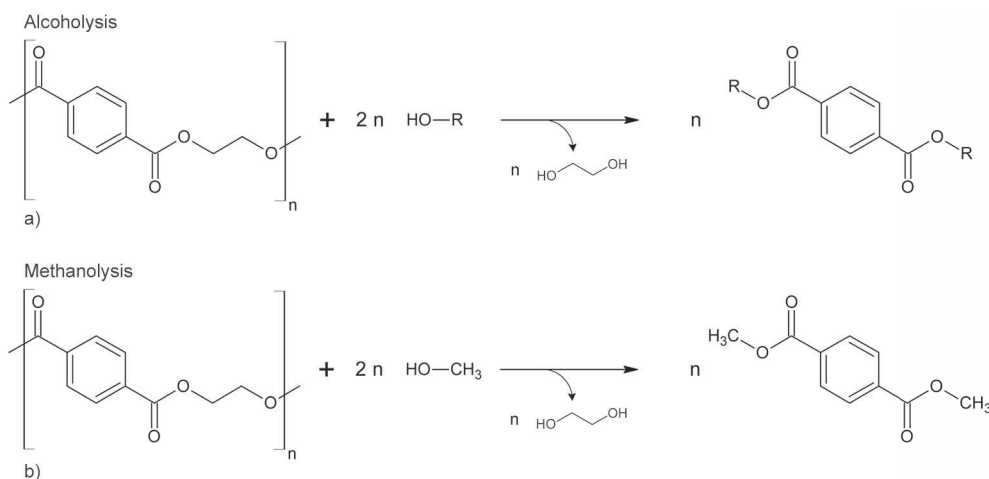

Figure 3. Chemical recycling methods of PET ((a) Alcoholysis, (b) Methanolysis)

Table 2. Reaction conditions and yields of alcoholysis, methanolysis and hydrolysis of PET

Reaction product	Yield [%]	Reagent	Reaction temperature [°C]	Reaction time [min]	Pressure [bar]	Catalyst	Reference
Monomer, DETP[a]	80	Ethanol	255	30–120	116	none	[135]
Monomer, TPA[b]	84	1-Hexanol	100	not given	1[f]	Potassium hydroxide	[137]
Monomer, DBTP[c]	95	1-Butanol	205	480	1[f]	Acidic ionic liquids	[136]
Monomer, TPA[b]	96	1-Butanol	100	not given	1[f]	Potassium hydroxide	[137]
Monomer, TPA[b]	96	1-Pentanol	100	not given	1[f]	Potassium hydroxide	[137]
Monomer, BTHNPT[d]	not given	Pentaerythrytol	250	10	1[f]	Zinc acetate	[34]
Oligomers, [250–1430 g·mol^{-1}]	not given	Titanium alkoxide	270–280	1 to 20	1[f]	none	[139]
Oligomers, [450–900 g·mol^{-1}]	not given	2-Ethyl-1-Hexanol	170–190	600–720	1[f]	none	[138]
Monomer, DMTP[e]	60	Methanol	270	0–90	1–150	none	[142]
Monomer, DMTP[e]	80	Methanol	300	0–90	9.8	none	[141]
Monomer, DMTP[e]	80	Methanol	300–350	2–120	200	none	[144]
Monomer, DMTP[e]	80	Methanol	300	2–120	200	none	[145]
Monomer, DMTP[e]	88	Methanol	200	120	not given	Aluminium triisopropoxide	[146]
Monomer, DMTP[e]	98	Methanol	300	0–90	147	none	[141]
Monomer, DMTP[e]	98	Methanol	330	0–90	1–150	none	[142]
Monomer, DMTP[e]	60–95	Methanol	250–270	0–60	85–140	Zinc acetate	[148]
Monomer, DMTP[e]	not given	Methanol	160–200	0–60	16	Zinc acetate	[147]
Monomer, TPA[b]	85	H_2O, Sodium Hydroxide	99	150	1[f]	none	[166]
Monomer, TPA[b]	90	H_2O	115–145	0–420	1[f]	[(CH$_3$)$_3$N(C$_{16}$H$_{33}$)]$_3$[PW$_{12}$O$_{40}$]	[150]
Monomer, TPA[b]	90	H_2O	250–420	0–60	480	none	[154]
Monomer, TPA[b]	91	H_2O	220–300	6 to 60	32	Zinc acetate	[152]
Monomer, TPA[b]	96	H_2O	200	30–240	16	none	[153]
Monomer, TPA[b]	96	H_2O, Sodium Hydroxide	Molten state[g]	6	1[f]	none	[168]
Monomer, TPA[b]	98	H_2O, Sodium Hydroxide	120–150	60–420	1[f]	none	[163]
Monomer, TPA[b]	98	H_2O, Sodium Hydroxide	70–95	300–360	1[f]	Trioctyl ammonium bromide	[165]
Monomer, TPA[b]	99	H_2O	205	6–240	16	none	[155]
Monomer, TPA[b]	99	H_2O	190	10	1[f]	Hydrotalcite	[156]
Monomer, TPA[b]	99	H_2O, Sodium Hydroxide	90–98	0–60	1[f]	Tetrabutyl ammonium bromide	[164]
Monomer, TPA[b]	99	H_2O, Sodium Hydroxide	90	600–4200	1[f]	Tetrabutyl ammonium iodide	[167]
Monomer, TPA[b]	100	H_2O, Sodium Hydroxide	180	30	1[f]	Trioctylmethyl ammonium bromide	[157]
Monomer, TPA[b]	100	H_2O, Sulfuric Acid	150	60–360	1[f]	none	[161]
Monomer, TPA[b]	not given	H_2O	100–250	120	Autogen	none	[158]
Monomer, TPA[b]	not given	H_2O, Nitric Acid	Reflux	not given	1[f]	none	[160]
Not given	not given	H_2O	140–180	not given	10	none	[151]
Not given	not given	H_2O, Sulfuric Acid	30	6–120	1[f]	none	[159]
Not given	not given	H_2O, Sodium Hydroxide	Ambient temperature	15	1[f]	none	[162]
Not given	not given	H_2O, Sodium Hydroxide	120	not given	1[f]	none	[169]
Not given	not given	H_2O, Sodium Hydroxide	250[h]	not given	1[f]	none	[170]
Oligomers, [540 g·mol^{-1}]	97	H_2O	170	180	1[f]	Zinc acetate	[149]
Oligomers, [2047 g·mol^{-1}]	99	H_2O	170	180	1[f]	Potassium hydroxide	[149]

[a]DETP: Diethyl terephthalate. [b]TPA: Terephthalic acid. [c]DBTP: Dibutyl terephthalate. [d]BTHNPT: Bis(tri-hydroxy neopentyl) terephthalate. [e]DMTP: Dimethyl terephthalate. [f]No pressure was given in the experimental section, thus, atmospheric pressure was assumed. [g]Reaction was carried out in a microwave reactor and reaction mixture was heated until the mixture was completely molten. [h]Temperature during a differential scanning calorimetry measurement.

and nitrile rubber polyvinyl chloride (PVC) blends. The reaction was carried out at 170–190 °C for 10–12 hours. Complete alcoholysis of PET was reached after 12 hours [138]. However, the composition of the obtained reaction mixture with respect to monomers or oligomers is not clarified. Although a molecular structure of low molecular weight oligomers (450–900 g·mol^{-1}) is postulated, it is not clear whether and how many monomers were obtained, since reaction was complete after 12 hours.

Chabert *et al*. [139] used titanium tetra-n-butoxide and titanium tetra-n-propoxide for PET de-polymerization. Concentration of titanium tetra-n-butoxide and titanium tetra-n-propoxide were 22 and 50% in the PET-mixture, which was extruded at 270–280 °C. They found that chain scission of PET proceeded faster using titanium tetra-n-propoxide compared to titanium tetra-n-butoxide. They further studied the number of active alkoxide-groups in corresponding titanium tetra-n-alkoxides and found that mainly two alkoxide-groups of the titanium tetra-n-alkoxide were involved in the chain scission reaction of PET. Mixtures of undefined low molecular weight oligomers in the range between 250 and 1430 g·mol^{-1} were obtained. However, they did not mention any aimed application of reaction products after de-polymerization. This procedure is advantageous in contrast to prior described solvent based procedures, which required additional separation and purification steps. However, functionality of PET-oligomers was limited due to alkyl end-groups.

Among the alcoholysis methods, reaction with methanol has gained special importance because of the low price and the availability of methanol. Methanolysis for de-polymerization of PET was first described in the year 1962 by Heisenberg *et al*. [140]. The application of the reaction products after de-polymerization was to provide the monomers for synthesis of virgin PET. The general reaction scheme is depicted in Figure 3b.

Generally, PET is de-polymerized with an excess of methanol at 160–350 °C (Table 2) to yield the monomer dimethyl terephthalate (DMTP). To increase the yield of DMTP and to shorten reaction times high pressures (9–200 bar, Table 2) are applied [141–148]. Genta and coworkers [141, 142] studied the effect of supercritical methanol compared to vapor methanol for PET de-polymerization. They found that de-polymerization proceeds faster in supercritical methanol than in vapor methanol. The reaction product consist-ed of a mixture of bis(hydroxy-ethylene) terephthalate (BHET), methyl-2-hydroxy ethylene terephthalate (MHET) and dimethyl terephthalate (DMTP). The yield of the main product DMTP was around 80%. Furthermore, the energy consumption of the supercritical methanolysis (2.35·10^6 kJ·kmol^{-1}) was lower than of the vapor methanolysis (2.84·10^6 kJ·kmol^{-1}). Goto reviewed the general applicability of supercritical fluids for de-polymerization, including methanol. Although supercritical methanol was suitable for PET de-polymerization and yielded DMTP as the main reaction product (yield 80%), the reaction mixture also consisted of BHET and MHET and hence entailed further purification steps [143].

Goto and coworkers [144, 145] studied the reaction kinetics during supercritical methanolysis of PET. Reaction was carried out at 300–350 °C at 200 bar (Table 2). Beside terephthalic acid monomethyl ester (TAMME), MHET and BHET, they obtained DMTP as main product in yields of 80%.

Likewise, Yang *et al*. [148] studied the effect of reaction temperature and time during supercritical methanolysis of PET (Table 2). Excess methanol was used for PET de-polymerization. They found that the extent of the reaction increased with increasing temperature and time. The reaction product consisted of DMTP, MHET, BHET and their dimers, which entailed further purification steps of the monomer DMTP. The yield of DMTP ranged from 60–95%.

Kurokawa *et al*. [146] studied the effect of aluminium tri-isopropoxide (ATIP) as catalyst and the solvent mixture of methanol and toluene on methanolysis of PET. Reaction was carried out at 200 °C without high pressure conditions (Table 2). With the application of the catalyst ATIP, the yield of the main product DMTP was raised to 67%. Finally, the application of ATIP combined with the solvent mixture methanol and toluene, the yield of DMTP was maximized to 88%.

Beside the use of supercritical methanol or additional application of a catalyst for methanolysis, Siddiqui *et al*. [147] studied the influence of microwave assisted methanolysis of PET in the temperature range from 160 to 200 °C with the addition of zinc acetate as catalyst. They found that the amount of de-polymerized PET increased with increasing temperature and increasing microwave power from 50 to 200 W. The characterized main product was DMTP, which was not quantified by the authors.

2.4.5. Hydrolysis

Hydrolysis of PET can be classified into neutral, acidic and alkaline hydrolysis (Table 2). The general reaction scheme of neutral and acidic hydrolysis is depicted in Figure 4. Generally, the main application of obtained reaction products after de-polymerization was to provide monomers for the synthesis of virgin PET. Neutral hydrolysis of PET is generally conducted with excess water at high temperature ranges between 115–420 °C and high pressure ranges from 10 to 480 bar. Correspondingly, reaction times are up to 7 hours [149–158].

Güçlü *et al*. [149] found that the solvent xylene provided greater de-polymerization of PET, whereas the catalysts zinc acetate or potassium hydroxide had negligible effect. They obtained low molecular weight oligomers (540+ 2047 g·mol^{-1}, Table 2) with yields of 97+99%.

Other studies investigated the effects of different reaction parameters on neutral hydrolysis of PET, such as catalysts (zinc acetate, potassium hydroxide, phase transfer catalyst, hydrotalcite) [151, 153, 156], steam or plasma treatment [154, 155] and microwave irradiation [157]. Although having different foci in these papers, the monomer TPA was obtained as reaction product in yields of 90–100% (Table 2).

In contrast to neutral hydrolysis, acidic hydrolysis of PET is generally conducted with excess acid (sulfuric or nitric acid) at ambient temperature and atmospheric pressure. Reaction times are in between 6 and 360 minutes [159, 160]. Yoshioka *et al*. [161] conducted acidic hydrolysis at 150 °C. de Carvalho *et al*. [159] completely de-polymerized PET to yield TPA. Kumar and Rajeswara Rao studied kinetics of acidic hydrolysis and Kumar and Rao [160] and Yoshioka *et al*. [161] examined the re-usability of dilute sulfuric acid for the de-polymerization of PET. In both stud-

ies, TPA was obtained. Although neutral and acidic hydrolysis of PET gave high yields of the monomer TPA, purification of the reaction product is solvent consuming, and hence imposes environmental issues. For the alkaline hydrolysis of PET-waste metal hydroxides are used. This method yields the corresponding metal salts of terephthalic acid. By a subsequent acidification of the formed salt, pure terephthalic acid is obtained. Alkaline hydrolysis of PET-waste is generally conducted with excess metal hydroxide (sodium or potassium hydroxide) at temperature ranges between 70–150 °C. Reaction times are between 6 minutes and 70 hours (Table 2). The general reaction scheme of alkaline hydrolysis is depicted in Figure 4 [162–171].

Caparanga *et al*. [162] used alkaline washing as pretreatment of PET-waste before actual recycling. Karayannidis *et al*. [163] completely de-polymerized PET to obtain pure TPA in yields of 98%.

Kosmidis *et al*. [165], Mishra *et al*. [166], Karayannidis *et al*. [170] studied degradation kinetics of alkaline hydrolyis of PET. Kosmidis *et al*. [165] used a catalyst (trioctyl ammonium bromide) and obtained a TPA yield of 98%, whereas Mishra *et al*. [166] did not use a catalyst and obtained a TPA yield of 85%. Karayannidis *et al*. [170] did not determine any yield of any reaction product in alkaline PET hydrolysis.

Additionally to conventional alkaline hydrolysis, Khalaf and Hasan [164], Paliwal and Mungray [167], Shafique *et al*. [168] additionally used microwave or ultrasound irradiation for de-polymerization of PET. Although Khalaf and Hasan as well as Paliwal and Mungray used a catalyst (tetra butyl ammonium bromide, tetra butyl ammonium iodide), their TPA yield of 99% was not significantly greater than the yield of Shafique *et al*. [168] with 96%.
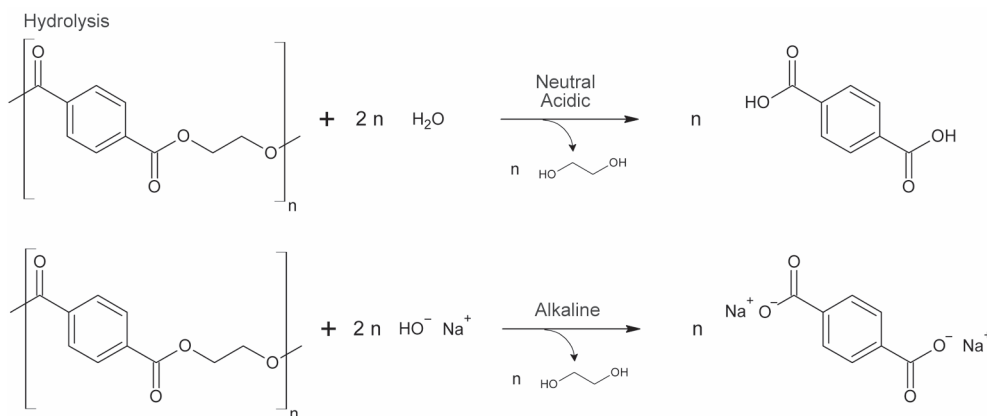

Figure 4. Chemical recycling methods of PET (Neutral, acidic and alkaline Hydrolysis)

Finally, Rosmaninho *et al.* [169] used alkaline hydrolysis for surface modification of PET not to yield PET monomers but to synthesize a cation exchange material as adsorbent for cationic contaminants. They compared this procedure with an acid surface modified PET. They found that acid modification generates more efficiently carboxyl-groups as potential cation exchange positions.

In most cases of the above described procedures, reaction products needed to be separated and purified after complete reaction.

2.4.6. Glycolysis

The general reaction scheme of PET glycolysis is depicted in Figure 5. Glycolysis of PET leads to the formation of PET-monomers and low molecular weight PET-oligomers (Table 3). Thus, a main application of the reaction products after de-polymerization was to provide monomers for the synthesis of virgin PET. The main process parameters of glycolysis are reaction temperature (110–270 °C) and reaction time (up to 15 hours) [99, 172–199]. In contrast to methanolysis, there is only little use of high pressure for glycolysis of PET [10, 180, 200].

Generally, the degrading agent was used in excess for de-polymerization of PET. Predominantly, ethylene glycol was used as degrading agent to give mainly the PET-monomer bis(hydroxy-ethylene) terephthalate (BHET) in yields between 46 to 100% [10, 11, 99, 184, 185, 187–189, 191–193, 195, 198, 200, 201–214]. Saint-Loup and co-workers also used ethylene glycol in reactive extrusion to produce low molecular weight oligomers (1450+1800 g·mol⁻¹) without quantification of their yields for synthesis of PET-polycarbonate polyesters. However, these oligomers had to be separated and purified for further processing, since the crude reaction product consisted of a heterogeneous mixture of BHET-analoga [215–218].

The second most common degrading agent for glycolysis was diethylene glycol. Here, both BHET and low molecular weight oligomers (dimers to hexam-

ers of BHET) were obtained, but no quantification of the yield was made [64, 173, 174, 177–179, 190, 181, 219, 220].

Further, but less applied chemicals for PET-glycolysis were propylene glycol, diethanol amine and triethanol amine. Using propylene glycol, BHET-analogues were obtained, but not quantified, since these intermediates were directly used for synthesis of unsaturated polyester resins [186, 190, 221]. Application of diethanol amine and triethanol amine yielded low molecular weight oligomers (900+1130 g·mol⁻¹, not quantified) for the use as dispersants or synthesis of epoxy resin. Again, additional separation and purification of the reaction products were necessary [176, 196, 197].

The least applied diols were BHET, neopentyl glycol (NPG), tetraethylene glycol (TEEG), poly(ethylene glycol) (400 g·mol⁻¹), poly(tetramethylene oxide) (650 g·mol⁻¹) and terpoly[poly(oxyethylene)-poly-(oxypropylene)-poly(oxyethylene)] (1100 g·mol⁻¹). In case of NPG, the corresponding monomer bis(neopentyl ethylene) terephthalate was obtained in a yield of 70%. With the other diols low molecular weight oligomers were obtained, since de-polymerization agents were already of low molecular weight. These reaction products were used for the synthesis of copolymers containing polyester species. Additionally, a consecutive separation and purification of the obtained products was necessary [175, 182, 194].

Another parameter for PET-glycolysis is the application of a catalyst. A various number has been used for PET-glycolysis and is listed in Table 3. The most important catalysts were zinc acetate and manganese acetate [64, 173–175, 182–186, 192, 193, 200, 202–204, 206, 208, 210, 211, 213, 219]. Further catalysts, but less used metal acetate catalysts, than the aforementioned ones, are cobalt and lead acetate [192, 205, 211]. Baliga and Wong studied the influence of the cation zinc, manganese, cobalt and lead on the catalytic effect of corresponding metal acetates on PET-glycolysis. They found that de-polymerization increased in the order $Pb^{2+} < Co^{2+} < Mn^{2+} < Zn^{2+}$.
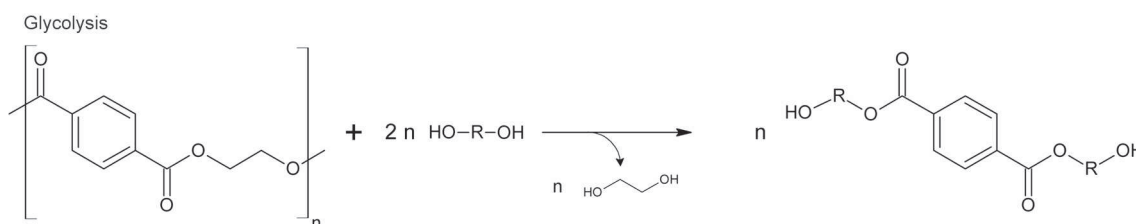

Figure 5. Chemical recycling methods of PET (Glycolysis)

Table 3. Reaction conditions and yields of PET glycolysis

Reaction product	Yield [%]	Reagent	Reaction temperature [°C]	Reaction time [hours]	Pressure [bar]	Catalyst	Reference
Monomers	0.3	EG[a]	300	0.4–0.8	11	none	[10]
Monomers	2.5	EG[a]	350	0.4–0.8	25	none	[10]
Monomers	25	EG[a]	80–200	15	1[q]	$ZnSO_4$	[192]
Monomers	46	EG[a]	150–190	1 to 4	1[q]	$Cu(OAc)_2$-[Bmim][OAc][r]	[194]
Monomers	54	EG[a]	150–190	1 to 4	1[q]	$Zn(OAc)_2$-[Bmim][OAc][s]	[194]
Monomers	57	EG[a]	196	9	1[q]	$FeCl_2$	[190]
Monomers	60	EG[a]	196	8	1[q]	Na_2SO_4	[186]
Monomers	60	EG[a]	196	8	1[q]	Na_2SO_4	[187]
Monomers	60	EG[a]	196	8	1[q]	Zeolithe	[186]
Monomers	61	EG[a]	196	1	1[q]	Na_2CO_3	[203]
Monomers	61	EG[a]	196	9	1[q]	LiCl	[190]
Monomers	61	EG[a]	196	9	1[q]	$MgCl_2$	[190]
Monomers	63	EG[a]	230–300	0.7–1.3	1[q]	Co_3O_4	[11]
Monomers	64	EG[a]	50–175	0.5–2	1[q]	[bmim]Br[t]	[213]
Monomers	65	EG[a]	80–200	15	1[q]	Zinc stearate	[192]
Monomers	67	EG[a]	230–300	0.7–1.3	1[q]	ZnO	[11]
Monomers	68	EG[a]	190	8	1[q]	none	[188]
Monomers	70	EG[a]	196	1 to 8	1[q]	Zinc acetate	[205]
Monomers	70	EG[a]	196	1 to 8	1[q]	Na_2CO_3	[205]
Monomers	70	NPG[b]	200–220	6	1[q]	Zinc acetate	[181]
Monomers	72	EG[a]	196	9	1[q]	Didymium chloride	[190]
Monomers	73	EG[a]	196	9	1[q]	$ZnCl_2$	[190]
Monomers	74	EG[a]	196	1	1[q]	Zinc acetate	[171]
Monomers	74	EG[a]	196	1	1[q]	Na_2CO_3	[171]
Monomers	74	EG[a]	196	1	1[q]	$NaHCO_3$	[171]
Monomers	74	EG[a]	196	1	1[q]	BaOH	[171]
Monomers	74	EG[a]	230–300	0.7–1.3	1[q]	Mn_3O_4	[11]
Monomers	75	EG[a]	198	10	1[q]	Zinc acetate	[191]
Monomers	75	EG[a]	198	10	1[q]	Lead acetate	[191]
Monomers	75	EG[a]	198	10	1[q]	Manganese acetate	[191]
Monomers	75	EG[a]	198	10	1[q]	Cobalt acetate	[191]
Monomers	75	EG[a]	180	8	1[q]	Zinc acetate	[183]
Monomers	75	EG[a]	180	8	1[q]	Lead acetate	[183]
Monomers	75	EG[a]	180	8	1[q]	Manganese acetate	[183]
Monomers	75	EG[a]	180	8	1[q]	Cobalt acetate	[183]
Monomers	76	EG[a]	196	1	1[q]	Zinc acetate	[203]
Monomers	78	EG[a]	190	3.5 hours	1[q]	TBD[u]	[197]
Monomers	78	EG[a]	190	not given	1[q]	Cyclic amidine	[200]
Monomers	78	EG[a]	80–200	15	1[q]	Zinc acetate	[192]
Monomers	79	EG[a]	196	1.50	1[q]	Zn/Al-hydrotalcite	[208]
Monomers	80	EG[a]	165–196	0–10	1[q]	Na_2CO_3	[211]
Monomers	80	EG[a]	165–196	0–10	1[q]	$NaHCO_3$	[211]
Monomers	80	EG[a]	165–196	0–10	1[q]	Na_2SO_4	[211]
Monomers	80	EG[a]	165–196	0–10	1[q]	K_2SO_4	[211]
Monomers	80	EG[a]	195–220	2.5–3.5	1[q]	Zinc acetate	[212]
Monomers	80	EG[a]	196	not given	1[q]	Zinc acetate	[202]
Monomers	80	EG[a]	196	not given	1[q]	Na_2CO_3	[202]
Monomers	81	EG[a]	230–300	0.7–1.3	1[q]	$ZnCo_2O_4$	[11]
Monomers	89	EG[a]	230–300	0.7–1.3	1[q]	$CoMn_2O_4$	[11]
Monomers	90	EG[a]	300	0.6–1.3	11	γ-Fe_2O_3	[199]
Monomers	92	EG[a]	197	3 to 4	1[q]	Zinc acetate	[206]
Monomers	92	EG[a]	230–300	0.7–1.3	1[q]	$ZnMn_2O_4$	[11]
Monomers	94	EG[a]	450	0.4–0.8	153	none	[10]
Monomers	98	EG[a]	198	0.5–2.5	1[q]	Zinc acetate	[210]
Monomers	98	EG[a]	198	0.5–2.5	1[q]	Lead acetate	[210]
Monomers	98	EG[a]	198	0.5–2.5	1[q]	Manganese acetate	[210]

Table 3. Reaction conditions and yields of PET glycolysis (1. continue)

Reaction product	Yield [%]	Reagent	Reaction temperature [°C]	Reaction time [hours]	Pressure [bar]	Catalyst	Reference
Monomers	98	EG[a]	198	0.5–2.5	1[q]	Cobalt acetate	[210]
Monomers	100	EG[a]	reflux	0.5	1[q]	Zinc acetate	[209]
Monomers	not given	DEG[c]	200–220	4	1[q]	Manganese acetate	[176]
Monomers	not given	DEG[c]	180	0.1	1[q]	Manganese acetate	[219]
Monomers	not given	DEG[c]	240	2	1[q]	Zinc acetate	[173]
Monomers	not given	EG[a]	reflux	1	1[q]	Zinc acetate	[172]
Monomers	not given	DEG[c]	240	0.02	1[q]	Zinc acetate	[218]
Monomers	not given	EG[a]	200	not given	1[q]	none	[77]
Monomers	not given	EG[a]	110	not given	1[q]	Cobalt acetate	[204]
Monomers	not given	EG[a]	110–190	0–2	1[q]	Manganese acetate	[99]
Monomers	not given	EG[a]	220	7 to 8	1[q]	Zinc acetate	[201]
Monomers	not given	EG[a]	198	3	1[q]	Zinc acetate	[207]
Monomers	not given	EG[a]	198	3	1[q]	Manganese acetate	[207]
Monomers	not given	EG[a]	196	not given	1[q]	NaHCO$_3$	[202]
Monomers	not given	EG[a]	196	not given	1[q]	Na$_2$SO$_4$	[202]
Monomers	not given	EG[a]	196	not given	1[q]	K$_2$SO$_4$	[202]
Monomers	not given	EG[a]	196	1 to 8	1[q]	NaHCO$_3$	[205]
Monomers	not given	EG[a]	196	1 to 8	1[q]	Na$_2$SO$_4$	[205]
Monomers	not given	EG[a]	196	1 to 8	1[q]	K$_2$SO$_4$	[205]
Monomers	not given	EG[a]	190	8	1[q]	Zinc acetate	[184]
Monomers	not given	DEG[c]	190	8	1[q]	Zinc acetate	[184]
Monomers	not given	PG[d]	190	8	1[q]	Zinc acetate	[184]
Monomers	not given	PG[d]	235	5	2 to 5	none	[179]
Monomers	not given	PG[d]	190+210	6+1	1[q]	Tetrabutoxy titanium	[220]
Monomers	not given	PG[d]	190	8	1[q]	Zinc acetate	[185]
Not given	not given	DEG[c]	210	not given	1[q]	Zinc acetate	[64]
Not given	not given	PG[d]	210	not given	1[q]	Zinc acetate	[64]
Not given	not given	DPG[e]	210	not given	1[q]	Zinc acetate	[64]
Not given	not given	BG[f]	210	not given	1[q]	Zinc acetate	[64]
Not given	not given	DEG[c]	200–220	6	1[q]	Manganese acetate	[180]
Not given	not given	PG[d]	200–220	6	1[q]	Manganese acetate	[180]
Not given	not given	TEG[g]	200–220	6	1[q]	Manganese acetate	[180]
Not given	not given	EG[a]	190	8	1[q]	Zinc acetate	[182]
Oligomers [2840 g·mol^{-1}]	17	PTMO[h]	200–270	8	1[q]	Titanium tetra isopropoxide	[193]
Oligomers [1380 g·mol^{-1}]	18	PEG[i]	200–270	8	1[q]	Titanium tetra isopropoxide	[193]
Oligomers [1120 g·mol^{-1}]	20	TEEG[j]	200–270	8	1[q]	Titanium tetra isopropoxide	[193]
Oligomers [2300 g·mol^{-1}]	23	Pluronic L31[k]	200–270	8	1[q]	Titanium tetra isopropoxide	[193]
Oligomers [1131 g·mol^{-1}]	not given	TEA[l]	190–200	3	1[q]	Manganese acetate	[175]
Oligomers [1360 g·mol^{-1}]	not given	BHET[m]	250	2	1[q]	Zinc acetate	[174]
Oligomers [1450 g·mol^{-1}]	not given	EG[a]	270	not given	1[q]	none	[214]
Oligomers [1450 g·mol^{-1}]	not given	EG[a]	270	not given	1[q]	none	[215]
Oligomers [1450 g·mol^{-1}]	not given	EG[a]	270	not given	1[q]	none	[217]
Oligomers [1648 g·mol^{-1}]	not given	PEG[i]	190–200	8	1[q]	none	[189]
Oligomers [1800 g·mol^{-1}]	not given	EG[a]	270	not given	1[q]	none	[216]
Oligomers [210–595 g·mol^{-1}]	not given	EG[a]	170+190	1 to 6	1[q]	Zinc acetate	[199]

Table 3. Reaction conditions and yields of PET glycolysis (2. continue)

Reaction product	Yield [%]	Reagent	Reaction temperature [°C]	Reaction time [hours]	Pressure [bar]	Catalyst	Reference
Oligomers [300–500 g·mol^{-1}]	not given	DEG[c]	200–220	4	1[q]	Manganese acetate	[177]
Oligomers [450–510 g·mol^{-1}]	not given	DEG[c]	210	4	1[q]	Manganese acetate	[178]
Oligomers [497 g·mol^{-1}]	not given	BD[n]	not given	not given	1[q]	none	[221]
Oligomers [534 g·mol^{-1}]	not given	DEG[c]	190–200	8	1[q]	none	[189]
Oligomers [881 g·mol^{-1}]	not given	TEG[g]	not given	not given	1[q]	none	[221]
Oligomers [900 g·mol^{-1}]	not given	DEA[o]	170–210	3 to 4	1[q]	Manganese acetate	[195]
Oligomers [900 g·mol^{-1}]	not given	TEA[l]	170–210	3 to 4	1[q]	Manganese acetate	[195]
Oligomers [900 g·mol^{-1}]	not given	DEA[o]	180–210	3 to 4	high pressure	Manganese acetate	[196]
Oligomers [900 g·mol^{-1}]	not given	TEA[l]	180–210	3 to 4	high pressure	Manganese acetate	[196]
Oligomers [900 g·mol^{-1}]	not given	DEG[c]	180–210	3 to 4	high pressure	Manganese acetate	[196]
Oligomers [900 g·mol^{-1}]	not given	TMP[p]	180–210	3 to 4	high pressure	Manganese acetate	[196]
Oligomers [957g·mol^{-1}]	not given	DEA[o]	190–200	3	1[q]	Manganese acetate	[175]

[a]EG: Ethylene glycol. [b]NPG: Neopentyl glycol. [c]DEG: Diethylene glycol. [d]PG: Propylene glycol. [e]DPG: Dipropylene glycol. [f]BG: Butylene glycol. [g]TEG: Triethylene glycol. [h]PTMO: Poly(tetramethylene oxide). [i]PEG: Polyethylene glycol. [j]TEEG: Tetraethylene glycol. [k]Pluronic L31: Terpoly[poly(oxyethylene)-poly-(oxypropylene)-poly(oxyethylene)]. [l]TEA: Triethanol amine. [m]BHET: Bis(hydroxy ethylene) terephthalate. [n]BD: Butanediol. [o]DEA: Diethanol amine. [p]TMP: Trimethylol propane. [q]No pressure was given in the experimental section, thus, atmospheric pressure was assumed. [r]Cu(OAc)$_2$-[Bmim][OAc]: 1-butyl-3-methylimidazolium acetate-promoted copper acetate. [s]Zn(OAc)$_2$-[Bmim][OAc]: 1-Butyl-3-methylimidazolium acetate-promoted zinc acetate. [t][bmim]Br: 1-butyl-3-methylimidazolium bromide. [u]TBD: 1,5,7-triazabicyclo[4.4.0]dec-5-ene.

These results were confirmed by Ghaemy and Moassaddegh as well as Goje and Mishra [184, 192, 211]. Pingale *et al*. [191] also studied the influence of different cations, namely zinc, lithium, didymium, magnesium and iron, on the catalytic effect of respective chlorides in the glycolysis of PET. They found zinc chloride to be the most effective catalyst yielding 73% BHET, followed by didymium chloride, magnesium chloride, lithium chloride and ferric chloride. In contrast, Carné Sánchez and Collinson [193] studied the catalytic effect of zinc catalysts on PET-glycolysis with different anions, namely acetate, stearate and sulfate. They found zinc acetate to be the most effective catalyst (Table 3, 78% BHET), followed by zinc stearate (Table 3, 65% BHET) and finally zinc sulfate (Table 3, 25% BHET). Analogously, Pingale and Shukla [172], Duque-Ingunza and coworkers [203, 204, 206, 212] studied PET-glycolysis using different sodium catalysts with different anions (carbonate, bicarbonate and sulfate). The effectiveness of the sodium catalysts on glycolysis yielding BHET decreased in the following order: sodium bicarbonate > sodium carbonate > sodium sulfate.

Finally, there are only few reports about the use of very special catalyst for glycolysis. Al-Sabagh *et al*. [195] and Alnaqbi *et al*. [214] applied ionic liquids (1-butyl-3-methylimidazolium bromide or 1-butyl-3-methylimidazolium acetate as co-catalyst) for complete glycolysis of PET. Further, Fukushima and coworkers [198, 201] used cyclic amidine catalysts (e.g. 1,5,7-triazabicyclo[4.4.0]dec-5-ene, TBD) to de-polymerize PET].

Other authors used very specific catalyst like tetrabutoxy titanium, titanium tetraisopropoxide, zeolite, Zn/Al-hydrotalcite, ZnO, metal oxide spinels (Co$_3$O$_4$ and Mn$_3$O$_4$), mixed metal oxide spinels (ZnMn$_2$O$_4$, CoMn$_2$O$_4$, ZnCo$_2$O$_4$) and γ-Fe$_2$O$_3$ as alternatives to common catalysts [11, 187, 200, 210, 221].

In addition, glycolysis leads to the formation of undesired cyclic oligomers [128]. The monomers and low molecular weight oligomers obtained from glycolysis of PET were generally used for impaired ap-

plications, such as modifiers for PVC or other polymer composites [183, 190, 208, 222]. Further, these glycolyized products were applied for synthesis of co-polymers of undefined composition [174, 179, 181, 182, 194, 219].

2.4.7. Aminolysis/ammonolysis

Aminolysis and ammonolyis were developed, since the reactivity of the amine-group is higher than the hydroxyl-group in glycols or alcohols used in glycolysis or alcoholysis of PET [223, 224]. Further, drawbacks of other conventional chemical recycling methods (hydrolysis, methanolysis) like high temperature and high pressure conditions were aimed of being avoided by aminolysis and ammonolysis. After de-polymerization, in general, the reaction products were applied as curing agents for epoxy resins, as components for polyurethane synthesis or as plasticizers [225–228].

The general reaction scheme of aminolysis and ammonolysis is depicted in Figure 6. Here, corresponding diamides of terephthalic acid are obtained. Aminolysis and ammonolyis are generally conducted at temperatures between 25 and 190 °C. Generally no high pressure is applied and reaction time may vary from few hours to several days (Table 4). The chemicals such as alkyl amines or liquid ammonia are used in excess for PET de-polymerization (Table 4). Aminolysis and ammonolysis mainly yielded the corresponding monomeric amides of terephthalic acid [223, 226–234].

The de-polymerization agent, which was mainly applied, was ethanol amine (EA, Table 4). EA was used to synthesize the bi-functional monomer bis(2-hydroxyl-ethylene) terephthalamide (BHETPA) in yields between 62 to 91% for further polymer syntheses (Table 4) [223, 224, 230, 232]. Further, but less used chemicals for aminolysis or ammonolysis of PET are methyl amine (MA), liquor ammonia (NH_3) and ethylene diamine (EDA). As in case of EA, these chemicals lead to the formation of corresponding bi-functional monomers of terephthalic acid, which could be applied as curing agents for epoxy resins [227, 228, 233]. Hoang and Dang used excess EDA to depolymerize PET to low molecular weight oligomers (250–820 g·mol^{-1}, Table 4). Removal of solid residues by filtration and additional purification gave these oligomers in yields of 30%. These were assumed to be used for synthesis of polyamides or polyimides [235]. Only little use of hydrazine hydrate, triethylene tetramine, tetraethylene pentamine, allylamine, di- or triethanol amine for aminolysis of PET was made. With these chemicals corresponding diamides of terephthalic acid were obtained, which were consecutively applied as additives in concrete mixture or used for further synthesis of antibacterial chemicals [230, 233, 234].

As for glycolysis, different catalysts were also applied for aminolysis, ammonolysis. Mainly metal acetates were used (zinc acetate, sodium acetate, potassium acetate, Table 4) [226, 227, 231, 232]. Shukla and Harad studied the effect of sodium-, potassium acetate and acetic acid on efficiency of PET-aminolysis. They found sodium acetate as the most efficient catalyst, followed by potassium acetate and acetic acid [232]. More *et al*. [224] compared zinc acetate and sodium acetate for PET-aminolysis and found (as in case of glycolysis) zinc acetate to be more efficient for aminolysis reaction. Mittal *et al*. [228] compared aminolysis and ammonolysis using cetyl am-
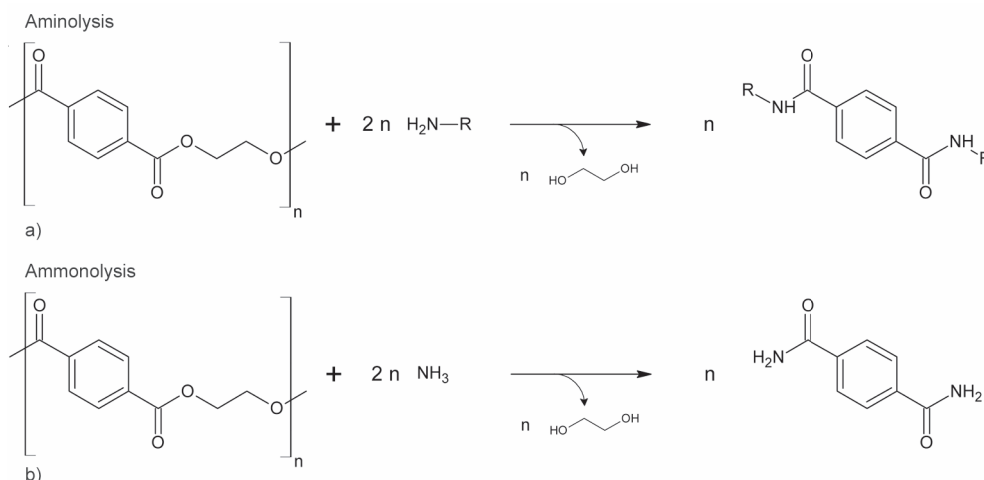
Figure 6. Chemical recycling methods of PET ((a) Aminolysis, (b) Ammonolysis)

Table 4. Reaction conditions and yields of PET aminolysis, ammonolysis

Reaction product	Yield [%]	Reagent	Reaction temperature [°C]	Reaction time [min]	Pressure [bar]	Catalyst	Reference
Monomers	38	NH₃	40	180–2700	1[h]	Cetyl ammonium bromide	[227]
Monomers	62	EA[a]	190	2 to 12	1	Dibutyltinoxide	[222]
Monomers	75	EA[a]	160	2 to 12	1[h]	Sodium acetate	[223]
Monomers	76	EA[a]	172	18	1[h]	Acetic acid	[231]
Monomers	81	EA[a]	160	2 to 12	1[h]	Zinc acetate	[223]
Monomers	85	EA[a]	172	18	1[h]	Sodium acetate	[228]
Monomers	86	Hydrazin hydrate	114	20	1[h]	none	[230]
Monomers	87	EA[a]	172	18	1[h]	Potassium sulphate	[231]
Monomers	91	EA[a]	172	18	1[h]	Sodium acetate	[231]
Monomers	94	MA[b]	40	180–2700	1[h]	Cetyl ammonium bromide	[227]
Monomers	not given	Allylamine	180	not given	15–20	none	[233]
Monomers	not given	EA[a]	180	not given	15–20	none	[233]
Monomers	not given	DEA[c]	180	not given	15–20	none	[233]
Monomers	not given	TEA[d]	180	not given	15–20	none	[233]
Monomers	not given	EDA[e]	Ambient temperature	0–300	1[h]	none	[225]
Monomers	not given	MA[b]	40	180–2700	1[h]	Cetyl ammonium bromide	[232]
Monomers	not given	NH₃	40	180–2700	1[h]	Cetyl ammonium bromide	[232]
Monomers	not given	NH₃	Ambient temperature	180–2700	1[h]	Zinc acetate	[226]
Monomers	quantitative	TETA[f]	130–140	18	1[h]	none	[229]
Monomers	quantitative	TEEPA[g]	130–140	18	1[h]	none	[229]
Oligomers [250–820 g·mol⁻¹]	30	EDA[e]	100	42	1[h]	none	[234]

[a]EA: Ethanol amine. [b]MA: Methyl amine. [c]DEA: Diethanol amine. [d]TEA: Triethanol amine. [e]EDA: Ethylene diamine.
[f]TETA: Triethylene tetramine. [g]TEEPA: Tetraethylene pentamine. [h]No specific pressure was given in the experimental section, thus, atmospheric pressure was assumed.

monium bromide as catalyst. Generally, both reaction types yielded less monomeric reaction product without catalyst. Using the catalyst, they found a higher yield for aminolysis (94%, Table 4) than for ammonolysis (38%, Table 4). Compared to the aforementioned catalysts, di-butyl tinoxide used by Tawfik and Eskander [223] was less efficient for aminolysis of PET (Table 4).

All described chemical recycling methods require either high pressure apparatus (hydrolysis, methanolysis) or toxic chemicals (alkyl amines, glycols, methanol, sulfuric acid, nitric acid) to yield mainly monomers of PET. In case of glycolysis precise process control is of crucial importance either to prevent re-polymerization or other side-reactions [8, 9, 148, 153, 226].

2.4.8. Controlled de-polymerization using blocking chain scission

This method was developed by Geyer *et al.* [95] as an alternative chemical recycling method which prevents uncontrolled de-polymerization. Furthermore, it overcomes some of the drawbacks of the methods described in earlier sections: The need of high temperature and high pressure conditions, the use of toxic and environmentally problematic chemicals (either the de-polymerization agents or the catalysts) and considerable amounts of solvents. The general reaction scheme of blocking chain scission is depicted in Figure 7.

PET was melt-mixed with stoichiometric amounts of adipic acid to yield tailored oligomers of defined molecular weight. With this approach defined oligo-
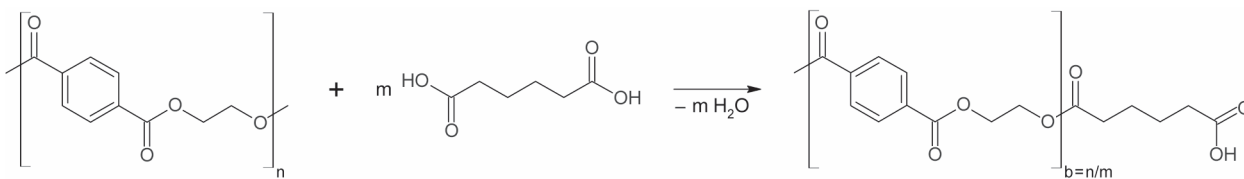
Figure 7. Blocking chain scission of PET using adipic acid [95]

mers of molecular weights in the range of 960–23 500 g·mol^{-1} were readily prepared, which was not possible with former chemical recycling methods [95]. However, this method requires sorted PET-material, which has to be free of contaminants or other polymer species.

Geyer *et al*. [236] used these defined building blocks to synthesize novel block-co-polyesters with tailored surface properties. By the combination of defined PET- and PEN-oligomers PET-PEN-block-co-polyesters with tailored block segment composition were prepared. In dependence of the block segment composition it was possible to control the dispersive surface energy and specific desorption energy of these block-co-polyesters. By tailoring these surface properties, these PET-PEN-block-co-polyesters could be applied as compatibilizing agent to prepare transparent blends of PET and PEN. Since PET and PEN are originally immiscible, leading to opaque products, in contrast, such blends of PET and PEN made transparent could now be used for high-value added applications. For example, as encapsulating material for organic photovoltaics, which require maximum transparency for optimum efficiency of the solar cell. Furthermore, such blends exhibit an improved storage modulus and higher glass transition temperatures compared to pure PET, which makes them especially interesting as materials for hot re-fillable or pasteurizable food packaging [236, 237].

3. Conclusions

A thorough review of conventional and exceptional PET-recycling with a special emphasis on on chemical methods has been given. Energetic recycling methods like incineration or pyrolysis lead to a downcycling of PET (due to thermal degradation), using its reaction products either directly (use of the released heat of combustion) or indirectly (use of obtained chemicals as alternative for fossil fuels) for energy recovery. Although carbonization produces coal, active carbon or adsorbents for chemicals as more eco-friendly applications, again, due to thermal degradation, this method remains a downcycling of PET. On the other hand, thermo-mechanical recycling of PET leads to a downcycling of the material either, since thermal conditions caused thermal degradation of PET and reduced physical and mechanical properties of the recycled PET. In contrast, chemical recycling methods, which provided complete de-polymeriza-

tion of PET yielding monomers, enabled value-added re-usability of reaction products like the synthesis of virgin PET. However, these methods require high temperature and high pressure apparatus. Further, large amounts of chemicals are consumed for de-polymerization and consecutive separation as well as purification steps. Thus, such chemical recycling methods impose toxic and ecological issues. The alternative of producing PET-oligomers with chemical recycling methods is not well solved either. Although glycolysis is generally conducted without high pressure conditions, again, considerable quantities of chemicals are required for partial de-polymerization, separation and purification steps of the reaction products. Hence, as in case of complete de-polymerization of PET, partial de-polymerization imposes toxic and ecological issues either. Further, these less well-defined low molecular weight oligomers are within a heterogeneous mixture of by-products such as monomers, di- or trimers. Moreover, these heterogeneous reaction products are generally used for impaired applications such as dispersants or plasticizers. An alternative chemical recycling of PET was given by the controlled de-polymerization of PET using blocking chain scission with defined amounts of the de-polymerization agent. This method produced PET-oligomers of well-defined molecular weights in a greater range than existing chemical methods (like glycolysis). These building-blocks enabled the synthesis of tailored block-co-polyesters as potential compatibilizers to produce transparent PET-PEN-blends, which are suitable as an encapsulation material for photovoltaic cells or for hot re-fillable and pasteurizable food packaging.

References
[1] Paszun D., Spychaj T.: Chemical recycling of poly (ethylene terephthalate). Industrial and Engineering Chemistry Research, **36**, 1373–1383 (1997).
DOI: 10.1021/ie960563c
[2] Lepoittevin B., Roger P.: Poly(ethylene terephthalate). in 'Handbook of engineering and speciality thermoplastics: Polyethers and polyesters' (eds.: Thomas S., Visakh P. M.) Wiley, Hoboken, 97–126 (2011).
DOI: 10.1002/9781118104729.ch4
[3] Chilton T., Burnley S., Nesaratnam S.: A life cycle assessment of the closed-loop recycling and thermal recovery of post-consumer PET. Resources, Conservation and Recycling, **54**, 1241–1249 (2010).
DOI: 10.1016/j.resconrec.2010.04.002

[4] Farmer N.: The future: Global trends and analysis for the international packaging market in relation to the speed of impact of packaging innovation and likely material changes. in 'Trends in packaging of food, beverages and other fast-moving consumer goods (FMCG)' (ed.: Farmer N.), Elsevier, Oxford, 288–312 (2013).

[5] Intini F., Kühtz S.: Recycling in buildings: an LCA case study of a thermal insulation panel made of polyester fiber, recycled from post-consumer PET bottles. International Journal of Life Cycle Assessment, **16**, 306–315 (2011).
DOI: 10.1007/s11367-011-0267-9

[6] Amienyo D., Gujba H., Stichnothe H., Azapagic A.: Life cycle environmental impacts of carbonated soft drinks. International Journal of Life Cycle Assessment, **18**, 77–92 (2013).
DOI: 10.1007/s11367-012-0459-y

[7] Almeida C. M. V. B., Rodrigues A. J. M., Bonilla S. H., Giannetti B. F. J.: Emergy as a tool for ecodesign: Evaluating materials selection for beverage packages in Brazil. Journal of Cleaner Production, **18**, 32–43 (2010).
DOI: 10.1016/j.jclepro.2009.03.019

[8] Awaja F., Pavel D.: Recycling of PET. European Polymer Journal, **41**, 1453–1477 (2005).
DOI: 10.1016/j.eurpolymj.2005.02.005

[9] Dutt K., Soni R. K.: A review on synthesis of value added products from polyethylene terephthalate (PET) waste. Polymer Science Series B, **55**, 430–452 (2013).
DOI: 10.1134/S1560090413070075

[10] Imran M., Kim B-K., Han M., Cho B. G., Kim D. H.: Sub- and supercritical glycolysis of polyethylene terephthalate (PET) into the monomer bis(2-hydroxyethyl) terephthalate (BHET). Polymer Degradation and Stability, **95**, 1685–1693 (2010)
DOI: 10.1016/j.polymdegradstab.2010.05.026

[11] Imran M., Kim D. H., Al-Masry W. A., Mahmood A., Hassan A., Haider S., Ramay S. M.: Manganese-, cobalt-, and zinc-based mixed-oxide spinels as novel catalysts for the chemical recycling of poly(ethylene terephthalate) *via* glycolysis. Polymer Degradation and Stability, **98**, 904–915 (2013).
DOI: 10.1016/j.polymdegradstab.2013.01.007

[12] Lorenzetti C., Manaresi P., Berti C., Barbiroli G.: Chemical recovery of useful chemicals from polyester (PET) waste for resource conservation: A survey of state of the art. Journal of Polymers and the Environment, **14**, 89–101 (2006).
DOI: 10.1007/s10924-005-8711-1

[13] Nikles D. E., Farahat M. S.: New motivation for the depolymerization products derived from poly(ethylene terephthalate) (PET) waste: A review. Macromolecular Materials and Engineering, **290**, 13–30 (2005).
DOI: 10.1002/mame.200400186

[14] Sinha V., Patel M. R., Patel J. V.: PET waste management by chemical recycling: A review. Journal of Polymers and the Environment, **18**, 8–25 (2010).
DOI: 10.1007/s10924-008-0106-7

[15] Achilias D. S.: Polymer degradation under microwave irradiation. in 'Advances in polymer science' (eds.: Abe A., Albertsson A-C., Coates G. W., Genzer J., Kobayashi S., Lee K-S., Leibler L., Long T. E., Möller M., Okay O., Percec V., Tang B. Z., Terentjev E. M., Theato P., Vicent M. J., Voit B., Wiesner U., Zhang X.) Springer, Berlin, 1–38 (2014).
DOI: 10.1007/12_2014_292

[16] de Marco I., Caballero B., Torres A., Laresgoiti M. F., Chomón M. J., Cabrero M. A.: Recycling polymeric wastes by means of pyrolysis. Journal of Chemical Technology and Biotechnology, **77**, 817–824 (2002).
DOI: 10.1002/jctb.636

[17] Jung C. G., Fontana A.: Production of gaseous and liquid fuels by pyrolysis and gasification of plastics: technological approach. in 'Feedstock recycling and pyrolysis of waste plastics: Converting waste plastics into diesel and other fuels' (eds.: Scheirs J., Kaminsky W.) Wiley, Chichester 266–267 (2006).

[18] López A., de Marco I., Caballero B. M., Laresgoiti M. F., Adrados A.: Dechlorination of fuels in pyrolysis of PVC containing plastic wastes. Fuel Processing Technology, **92**, 253–260 (2011).
DOI: 10.1016/j.fuproc.2010.05.008

[19] Lopez-Urionabarrenechea A., de Marco I., Caballero B. M., Laresgoiti M. F., Adrados A.: Catalytic stepwise pyrolysis of packaging plastic waste. Journal of Analytical and Applied Pyrolysis, **96**, 54–62 (2012).
DOI: 10.1016/j.jaap.2012.03.004

[20] Yoshioka T., Handa T., Grause G., Lei Z., Inomata H., Mizoguchi T.: Effects of metal oxides on the pyrolysis of poly(ethylene terephthalate). Journal of Analytical and Applied Pyrolysis, **73**, 139–144 (2005).
DOI: 10.1016/j.jaap.2005.01.004

[21] Straka P., Buchtele J., Kovářová J.: *Co*-pyrolysis of waste polymers with coal. Macromolecular Symposia, **135**, 19–23 (1998).
DOI: 10.1002/masy.19981350105

[22] Adrados A., de Marco I., Caballero B. M., López A., Laresgoiti M. F., Torres A.: Pyrolysis of plastic packaging waste: A comparison of plastic residuals from material recovery facilities with simulated plastic waste. Waste Management, **32**, 826–832 (2012).
DOI: 10.1016/j.wasman.2011.06.016

[23] Andel L., Kusy J., Vales J., Safarova M.: Pyrolysis process of waste polyethyleneterephtalate. Chemical Product and Process Modeling, **4**, 1–6 (2009)
DOI: 10.2202/1934-2659.1321

[24] Kulesza K., German K.: Chlorinated pyrolysis products of *co*-pyrolysis of poly(vinyl chloride) and poly(ethylene terephthalate). Journal of Analytical and Applied Pyrolysis, **67**, 123–134 (2003).
DOI: 10.1016/S0165-2370(02)00057-8

[25] Kumagai S., Grause G., Kameda T., Yoshioka T.: Simultaneous recovery of benzene-rich oil and metals by steam pyrolysis of metal-poly(ethylene terephthalate) composite waste. Environmental Science and Technology, **48**, 3430–3437 (2014).
DOI: 10.1021/es405047j

[26] Kumagai S., Grause G., Kameda T., Yoshioka T.: Recovery of benzene-rich oil from the degradation of metal- and metal oxide-containing poly(ethylene terephthalate) composites. Journal of Material Cycles and Waste Management, **16**, 282–290 (2014).
DOI: 10.1007/s10163-013-0194-x

[27] Miller S. J., Shah N., Huffman G. P.: Conversion of waste plastic to lubricating base oil. Energy and Fuels, **19**, 1580–1586 (2005).
DOI: 10.1021/ef049696y

[28] Mlynková B., Hájeková E., Bajus M.: Copyrolysis of oils/waxes of individual and mixed polyalkenes cracking products with petroleum fraction. Fuel Processing Technology, **89**, 1047–1055 (2008).
DOI: 10.1016/j.fuproc.2008.04.007

[29] Siddiqui M. N., Redhwi H. H.: Pyrolysis of mixed plastics for the recovery of useful products. Fuel Processing Technology, **90**, 545–552 (2009).
DOI: 10.1016/j.fuproc.2009.01.003

[30] Yoshioka T., Grause G., Eger C., Kaminsky W., Okuwaki A.: Pyrolysis of poly(ethylene terephthalate) in a fluidised bed plant. Polymer Degradation and Stability, **86**, 499–504 (2004).
DOI: 10.1016/j.polymdegradstab.2004.06.001

[31] Hujuri U., Ghoshal A. K., Gumma S.: Temperature-dependent pyrolytic product evolution profile for polyethylene terephthalate. Journal of Applied Polymer Science, **130**, 3993–4000 (2013).
DOI: 10.1002/APP.39681

[32] Ahmadinia E., Zargar M., Karim M. R., Abdelaziz M., Ahmadinia E.: Performance evaluation of utilization of waste polyethylene terephthalate (PET) in stone mastic asphalt. Construction and Building Materials, **36**, 984–989 (2012).
DOI: 10.1016/j.conbuildmat.2012.06.015

[33] Hassani A., Ganjidoust H., Maghanaki A. A.: Use of plastic waste (poly-ethylene terephthalate) in asphalt concrete mixture as aggregate replacement. Waste Management and Research, **23**, 322–327 (2005).
DOI: 10.1177/0734242X05056739

[34] Mendes L. C., Dias M. L., Rodrigues T. C.: Chemical recycling of PET waste with multifunctional pentaerythrytol in the melt state. Journal of Polymers and the Environment, **19**, 254–262 (2011).
DOI: 10.1007/s10924-010-0276-y

[35] Akçaözoğlu S., Ulu C.: Recycling of waste PET granules as aggregate in alkali-activated blast furnace slag/metakaolin blends. Construction and Building Materials, **58**, 31–37 (2014).
DOI: 10.1016/j.conbuildmat.2014.02.011

[36] Albano C., Camacho N., Hernández M., Matheus A., Gutiérrez A.: Influence of high temperatures on PET-concrete properties. Macromolecular Symposia, **286**, 195–202 (2009).
DOI: 10.1002/masy.200951224

[37] Albano C., Camacho N., Hernández M., Matheus A., Gutiérrez A.: Influence of content and particle size of waste pet bottles on concrete behavior at different *w/c* ratios. Waste Management, **29**, 2707–2716 (2009).
DOI: 10.1016/j.wasman.2009.05.007

[38] Choi W-C., Yun H-D., Kang J-W., Kim S-W.: Development of recycled strain-hardening cement-based composite (SHCC) for sustainable infrastructures. Composites Part B: Engineering, **43**, 627–635 (2012).
DOI: 10.1016/j.compositesb.2011.11.060

[39] Choi Y. W., Moon D. J., Kim Y. J., Lachemi M.: Characteristics of mortar and concrete containing fine aggregate manufactured from recycled waste polyethylene terephthalate bottles. Construction and Building Materials, **23**, 2829–2835 (2009).
DOI: 10.1016/j.conbuildmat.2009.02.036

[40] da Silva A. M., de Brito J., Veiga R.: Incorporation of fine plastic aggregates in rendering mortars. Construction and Building Materials, **71**, 226–236 (2014).
DOI: 10.1016/j.conbuildmat.2014.08.026

[41] Foti D., Paparella F.: Impact behavior of structural elements in concrete reinforced with PET grids. Mechanics Research Communications, **57**, 57–66 (2014).
DOI: 10.1016/j.mechrescom.2014.02.007

[42] Fraternali F., Spadea S., Berardi V. P.: Effects of recycled PET fibres on the mechanical properties and seawater curing of Portland cement-based concretes. Construction and Building Materials, **61**, 293–302 (2014).
DOI: 10.1016/j.conbuildmat.2014.03.019

[43] Frigione M.: Recycling of PET bottles as fine aggregate in concrete. Waste Management, **30**, 1101–1106 (2010).
DOI: 10.1016/j.wasman.2010.01.030

[44] Ge Z., Sun R., Zhang K., Gao Z., Li P.: Physical and mechanical properties of mortar using waste polyethylene terephthalate bottles. Construction and Building Materials, **44**, 81–86 (2013).
DOI: 10.1016/j.conbuildmat.2013.02.073

[45] Hannawi K., Kamali-Bernard S., Prince W.: Physical and mechanical properties of mortars containing PET and PC waste aggregates. Waste Management, **30**, 2312–2320 (2010).
DOI: 10.1016/j.wasman.2010.03.028

[46] Hannawi K., Prince W., Kamali-Bernard S.: Effect of thermoplastic aggregates incorporation on physical, mechanical and transfer behaviour of cementitious materials. Waste and Biomass Valorization, **1**, 251–259 (2010).
DOI: 10.1007/s12649-010-9021-y

[47] Jang S-J., Rokugo K., Park W-S., Yun H-D.: Influence of rapid freeze-thaw cycling on the mechanical properties of sustainable strain-hardening cement composite (2SHCC). Materials, **7**, 1422–1440 (2014).
DOI: 10.3390/ma7021422

[48] Jo B-W., Park S-K., Park J-C.: Mechanical properties of polymer concrete made with recycled PET and recycled concrete aggregates. Construction and Building Materials, **22**, 2281–2291 (2008).
DOI: 10.1016/j.conbuildmat.2007.10.009

[49] Kim J-H. J., Park C-G., Lee S-W., Lee S-W., Won J-P.: Effects of the geometry of recycled PET fiber reinforcement on shrinkage cracking of cement-based composites. Composites Part B: Engineering, **39**, 442–450 (2008).
DOI: 10.1016/j.compositesb.2007.05.001

[50] Kim S. B., Yi N. H., Kim H. Y., Kim J-H. J., Song Y-C.: Material and structural performance evaluation of recycled PET fiber reinforced concrete. Cement and Concrete Composites, **32**, 232–240 (2010).
DOI: 10.1016/j.cemconcomp.2009.11.002

[51] Mahdi F., Abbas H., Khan A. A.: Flexural, shear and bond strength of polymer concrete utilizing recycled resin obtained from post consumer PET bottles. Construction and Building Materials, **44**, 798–811 (2013).
DOI: 10.1016/j.conbuildmat.2013.03.081

[52] Marzouk O. Y., Dheilly R. M., Queneudec M.: Valorization of post-consumer waste plastic in cementitious concrete composites. Waste Management, **27**, 310–318 (2007).
DOI: 10.1016/j.wasman.2006.03.012

[53] Vidales J. M. M., Hernández L. N., López J. I. T., Flores E. E. M., Hernández L. S.: Polymer mortars prepared using a polymeric resin and particles obtained from waste pet bottle. Construction and Building Materials, **65**, 376–383 (2014).
DOI: 10.1016/j.conbuildmat.2014.04.114

[54] Rebeiz K. S.: Strength and durability properties of polyester concrete using pet and fly ash wastes. Advanced Performance Materials, **3**, 205–214 (1995).
DOI: 10.1007/BF00136746

[55] Rebeiz K. S., Fowler D. W., Paul D. R.: Polymer concrete and polymer mortar using resins based on recycled poly(ethylene terephthalate). Journal of Applied Polymer Science, **44**, 1649–1655 (1992).
DOI: 10.1002/app.1992.070440919

[56] Reis J. M. L., Carneiro E. P.: Evaluation of PET waste aggregates in polymer mortars. Construction and Building Materials, **27**, 107–111 (2012).
DOI: 10.1016/j.conbuildmat.2011.08.020

[57] Reis J. M. L., Chianelli-Junior R., Cardoso J. L., Marinho F. J. V.: Effect of recycled PET in the fracture mechanics of polymer mortar. Construction and Building Materials, **25**, 2799–2804 (2011).
DOI: 10.1016/j.conbuildmat.2010.12.056

[58] Reis J. M. L., Jurumenha M. A. G.: Investigation on the effects of polymer impregnated aggregate on polymer mortars properties. Materials and Structures, **46**, 1383–1388 (2013).
DOI: 10.1617/s11527-012-9980-5

[59] Safi B., Saidi M., Aboutaleb D., Maallem M.: The use of plastic waste as fine aggregate in the self-compacting mortars: Effect on physical and mechanical properties. Construction and Building Materials, **43**, 436–442 (2013).
DOI: 10.1016/j.conbuildmat.2013.02.049

[60] Saikia N., de Brito J.: Mechanical properties and abrasion behaviour of concrete containing shredded PET bottle waste as a partial substitution of natural aggregate. Construction and Building Materials, **52**, 236–244 (2014).
DOI: 10.1016/j.conbuildmat.2013.11.049

[61] Sikalidis C. A., Zabaniotou A. A., Famellos S. P.: Utilisation of municipal solid wastes for mortar production. Resources, Conservation and Recycling, **36**, 155–167 (2002).
DOI: 10.1016/S0921-3449(02)00018-6

[62] Silva R. V., de Brito J., Saikia N.: Influence of curing conditions on the durability-related performance of concrete made with selected plastic waste aggregates. Cement and Concrete Composites, **35**, 23–31 (2013).
DOI: 10.1016/j.cemconcomp.2012.08.017

[63] Won J-P., Jang C.-I., Lee S-W., Lee S-J., Kim H-Y.: Long-term performance of recycled PET fibre-reinforced cement composites. Construction and Building Materials, **24,** 660–665 (2010).
DOI: 10.1016/j.conbuildmat.2009.11.003

[64] Dębska B., Lichołai L.: A study of the effect of corrosive solutions on selected physical properties of modified epoxy mortars. Construction and Building Materials, **65**, 604–611 (2014).
DOI: 10.1016/j.conbuildmat.2014.05.038

[65] de Mello D., Pezzin S. H., Amico S. C.: The effect of post-consumer PET particles on the performance of flexible polyurethane foams. Polymer Testing, **28**, 702–708 (2009).
DOI: 10.1016/j.polymertesting.2009.05.014

[66] Altun S., Ulcay Y.: Improvement of waste recycling in PET fiber production. Journal of Polymers and the Environment, **12**, 231–237 (2004).
DOI: 10.1007/s10924-004-8150-4

[67] Assadi R., Colin X., Verdu J.: Irreversible structural changes during PET recycling by extrusion. Polymer, **45**, 4403–4412 (2004).
DOI: 10.1016/j.polymer.2004.04.029

[68] Frounchi M.: Studies on degradation of PET in mechanical recycling. Macromolecular Symposia, **144**, 465–469 (1999).
DOI: 10.1002/masy.19991440142

[69] Badia J. D., Strömberg E., Karlsson S., Ribes-Greus A.: The role of crystalline, mobile amorphous and rigid amorphous fractions in the performance of recycled poly (ethylene terephthalate) (PET). Polymer Degradation and Stability, **97**, 98–107 (2012).
DOI: 10.1016/j.polymdegradstab.2011.10.008

[70] Badía J. D., Strömberg E., Ribes-Greus A., Karlsson S.: A statistical design of experiments for optimizing the MALDI-TOF-MS sample preparation of polymers. An application in the assessment of the thermo-mechanical degradation mechanisms of poly (ethylene terephthalate). Analytica Chimica Acta, **692**, 85–95 (2011).
DOI: 10.1016/j.aca.2011.02.063

[71] Badía J. D., Vilaplana F., Karlsson S., Ribes-Greus A.: Thermal analysis as a quality tool for assessing the influence of thermo-mechanical degradation on recycled poly(ethylene terephthalate). Polymer Testing, **28**, 169–175 (2009).
DOI: 10.1016/j.polymertesting.2008.11.010

[72] del Mar Castro López M., Pernas A. I. A., López M. J. A., Latorre A. L., Vilariño J. M. L., Rodríguez M. V. G.: Assessing changes on poly(ethylene terephthalate) properties after recycling: Mechanical recycling in laboratory versus postconsumer recycled material. Materials Chemistry and Physics, **147**, 884–894 (2014).
DOI: 10.1016/j.matchemphys.2014.06.034

[73] Dias M. L., Nascimento C. R.: Thermal properties of post-consumer pet processed in presence of phosphites. Journal of Thermal Analysis and Calorimetry, **69**, 551–559 (2002).
DOI: 10.1023/A:1019963923884

[74] Paci M., La Mantia F. P.: Competition between degradation and chain extension during processing of reclaimed poly(ethylene terephthalate). Polymer Degradation and Stability, **61**, 417–420 (1998).
DOI: 10.1016/S0141-3910(97)00227-9

[75] Paci M., La Mantia F. P.: Influence of small amounts of polyvinylchloride on the recycling of polyethyleneterephthalate. Polymer Degradation and Stability, **63**, 11–14 (1999).
DOI: 10.1016/S0141-3910(98)00053-6

[76] Cruz S. A., Zanin M.: PET recycling: Evaluation of the solid state polymerization process. Journal of Applied Polymer Science, **99**, 2117–2123 (2006).
DOI: 10.1002/app.22526

[77] Koo H. J., Chang G. S., Kim S. H., Hahm W. G., Park S. Y.: Effects of recycling processes on physical, mechanical and degradation properties of PET yarns. Fibers and Polymers, **14**, 2083–2087 (2013).
DOI: 10.1007/s12221-013-2083-2

[78] Holtman K. M., Kodama A., Klamczynski A. P., Flynn A., Bozzi D. V., Torres L., Franqui-Villanueva D., Mao J., Glenn G. M., Orts W. J.: Thermal properties of poly (ethylene terephthalate) recovered from municipal solid waste by steam autoclaving. Journal of Applied Polymer Science, **126**, 1698–1708 (2012).
DOI: 10.1002/app.36752

[79] Holland Colours: Holland's additives mask recycled appearance in PET. Additives for Polymers, **2**, 1–2 (2004).
DOI: 10.1016/S0306-3747(04)00049-1

[80] Kaneka: Modifiers spur growth in PET recycling. Plastics, Additives and Compounding, **7**, 32–33 (2005).
DOI: 10.1016/S1464-391X(05)70430-X

[81] Hamzehlou S., Katbab A. A.: Bottle-to-bottle recycling of pet *via* nanostructure formation by melt intercalation in twin screw compounder: Improved thermal, barrier, and microbiological properties. Journal of Applied Polymer Science, **106**, 1375–1382 (2007).
DOI: 10.1002/app.26730

[82] Cheng H., Tian M., Zhang L.: Toughening of recycled poly(ethylene terephthalate)/glass fiber blends with ethylene–butyl acrylate–glycidyl methacrylate copolymer and maleic anhydride grafted polyethylene–octene rubber. Journal of Applied Polymer Science, **109**, 2795–2801 (2008).
DOI: 10.1002/app.27564

[83] Abdel Tawab K., Ibrahim S. M., Magida M. M.: The effect of gamma irradiation on mechanical, and thermal properties of recycling polyethylene terephthalate and low density polyethylene (r-PET/LDPE) blend compatibilized by ethylene vinyl acetate (EVA). Journal of Radioanalytical and Nuclear Chemistry, **295**, 1313–1319 (2013).
DOI: 10.1007/s10967-012-2163-6

[84] Raffa P., Coltelli M-B., Castelvetro V.: Expanding the application field of post-consumer poly(ethylene terephthalate) through structural modification by reactive blending. Journal of Applied Polymer Science, **131**, 40881/1–40881/11 (2014).
DOI: 10.1002/app.40881

[85] Zhang Y., Zhang H., Yu Y., Guo W., Wu C.: Recycled poly(ethylene terephthalate)/linear low-density polyethylene blends through physical processing. Journal of Applied Polymer Science, **114**, 1187–1194 (2009).
DOI: 10.1002/app.30030

[86] Aminuddin S. F., Wei L. Y., Hamada H., Adnan N.: Recycled poly(ethylene terephthalate)/recycled polypropylene blend: Effect of hygrothermal treatment. in 'IEEE Symposium on Humanities, Science and Engineering Research, SHUSER 2012, Kuala Lumpur, Malaysia' 239–244 (2012).
DOI: 10.1109/SHUSER.2012.6268857

[87] Ávila A. F., Duarte M. V.: A mechanical analysis on recycled PET/HDPE composites. Polymer Degradation and Stability, **80**, 373–382 (2003).
DOI: 10.1016/S0141-3910(03)00025-9

[88] Ávila A. F., Rodrigues P. C. M., Santos D. B., Faria A. C. A.: A dual analysis for recycled particulate composites: Linking micro- and macro-mechanics. Materials Characterization, **50**, 281–291 (2003).
DOI: 10.1016/S1044-5803(03)00124-4

[89] Ávila A. F., Jabbur F. G.: Sheet forming studies using low-cost composites. Journal of Thermoplastic Composite Materials, **18**, 5–22 (2005).
DOI: 10.1177/0892705705041158

[90] Evstatiev M., Fakirov S., Krasteva B., Friedrich K., Covas J. A., Cunha A. M.: Recycling of poly(ethylene terephthalate) as polymer-polymer composites. Polymer Engineering and Science, **42**, 826–835 (2002).
DOI: 10.1002/pen.10994

[91] Kayaisang S., Amornsakchai T., Saikrasun S.: Potential utilization of recycled PET in comparison with liquid crystalline polymer as an additive for HDPE based composite fibers: Comparative investigation on mechanical performance of cross-ply laminates. Journal of Polymer Engineering, **33**, 793–802 (2013).
DOI: 10.1515/polyeng-2013-0155

[92] Kayaisang S., Saikrasun S., Amornsakchai T.: Potential use of recycled PET in comparison with liquid crystalline polyester as a dual functional additive for enhancing heat stability and reinforcement for high density polyethylene composite fibers. Journal of Polymers and the Environment, **21**, 191–206 (2013).
DOI: 10.1007/s10924-012-0446-1

[93] Navarro R., Ferrándiz S., López J., Seguí V. J.: The influence of polyethylene in the mechanical recycling of polyethylene terephthalate. Journal of Materials Processing Technology, **195**, 110–116 (2008).
DOI: 10.1016/j.jmatprotec.2007.04.126

[94] Oromiehie A., Mamizadeh A.: Recycling PET beverage bottles and improving properties. Polymer International, **53**, 728–732 (2004).
DOI: 10.1002/pi.1389

[95] Geyer B., Röhner S., Lorenz G., Kandelbauer A.: Designing oligomeric ethylene terephtalate building blocks by chemical recycling of polyethylene terephtalate. Journal of Applied Polymer Science, **131**, 39786/1–39786/12 (2014).
DOI: 10.1002/app.39786

[96] Day M., Parfenov V., Wiles D. M.: Combustion and pyrolysis of poly(ethylene terephthalate). III. The effect of tris(2,3-dibromopropyl) phosphate on the products of pyrolysis. Journal of Applied Polymer Science, **27**, 575–589 (1982).
DOI: 10.1002/app.1982.070270221

[97] Arena U., Mastellone M. L.: Defluidization phenomena during the pyrolysis of two plastic wastes. Chemical Engineering Science, **55**, 2849–2860 (2000).
DOI: 10.1016/S0009-2509(99)00533-3

[98] Barriocanal C., Díez M. A., Alvarez R.: PET recycling for the modification of precursors in carbon materials manufacture. Journal of Analytical and Applied Pyrolysis, **73**, 45–51 (2005).
DOI: 10.1016/j.jaap.2004.10.002

[99] Chen C-H.: Study of glycolysis of poly(ethylene terephthalate) recycled from postconsumer soft-drink bottles. III. Further investigation. Journal of Applied Polymer Science, **87**, 2004–2010 (2003).
DOI: 10.1002/app.11694

[100] Díez M. A., Alvarez R.: Advances in the recycling of plastic wastes for metallurgical coke production. Journal of Material Cycles and Waste Management, **15**, 247–255 (2013).
DOI: 10.1007/s10163-012-0103-8

[101] Díez M. A., Barriocanal C., Álvarez R.: Plastic wastes as modifiers of the thermoplasticity of coal. Energy and Fuels, **19**, 2304–2316 (2005).
DOI: 10.1021/ef0501041

[102] Brems A., Baeyens J., Beerlandt J., Dewil R.: Thermogravimetric pyrolysis of waste polyethylene-terephthalate and polystyrene: A critical assessment of kinetics modelling. Resources, Conservation and Recycling, **55**, 772–781 (2011).
DOI: 10.1016/j.resconrec.2011.03.003

[103] Brems A., Baeyens J., Vandecasteele C., Dewil R.: Polymeric cracking of waste polyethylene terephthalate to chemicals and energy. Journal of the Air and Waste Management Association, **61**, 721–731 (2011).
DOI: 10.3155/1047-3289.61.7.721

[104] Urbanová M., Šubrt J., Galíková A., Pola J.: IR laser ablative degradation of poly(ethylene terephthalate): Formation of insoluble films with differently bonded C=O groups. Polymer Degradation and Stability, **91**, 2318–2323 (2006).
DOI: 10.1016/j.polymdegradstab.2006.04.016

[105] Arenillas A., Rubiera F., Parra J. B., Ania C. O., Pis J. J.: Surface modification of low cost carbons for their application in the environmental protection. Applied Surface Science, **252**, 619–624 (2005).
DOI: 10.1016/j.apsusc.2005.02.076

[106] Kongkarat S., Khanna R., Koshy P., O'Kane P., Sahajwalla V.: Recycling waste polymers in EAF steelmaking: Influence of polymer composition on carbon/slag interactions. ISIJ International, **52**, 385–393 (2012).
DOI: 10.2355/isijinternational.52.385

[107] Nomura S., Kato K., Nakagawa T., Komaki I.: The effect of plastic addition on coal caking properties during carbonization. Fuel, **82**, 1775–1782 (2003).
DOI: 10.1016/S0016-2361(03)00120-0

[108] Parra J. B., Ania C. O., Arenillas A., Rubiera F., Pis J. J.: High value carbon materials from PET recycling. Applied Surface Science, **238**, 304–308 (2004).
DOI: 10.1016/j.apsusc.2004.05.229

[109] Sahajwalla V., Zaharia M., Kongkarat S., Khanna R., Rahman M., Saha-Chaudhury N., O'Kane P., Dicker J., Skidmore C., Knights D.: Recycling end-of-life polymers in an electric arc furnace steelmaking process: Fundamentals of polymer reactions with slag and metal. Energy and Fuels, **26**, 58–66 (2012).
DOI: 10.1021/ef201175t

[110] Wei L., Yan N., Chen Q.: Converting poly(ethylene terephthalate) waste into carbon microspheres in a supercritical CO_2 system. Environmental Science and Technology, **45**, 534–539 (2011).
DOI: 10.1021/es102431e

[111] Zhang F-S., Itoh H.: Adsorbents made from waste ashes and post-consumer PET and their potential utilization in wastewater treatment. Journal of Hazardous Materials, **101**, 323–337 (2003).
DOI: 10.1016/S0304-3894(03)00208-5

[112] Scheirs J.: Recycling of PET. in 'Polymer recycling' (ed.: Scheirs J.) Wiley, Chichester 121–145 (1998).

[113] Burat F., Güney A., Olgaç Kangal M.: Selective separation of virgin and post-consumer polymers (PET and PVC) by flotation method. Waste Management, **29**, 1807–1813 (2009).
DOI: 10.1016/j.wasman.2008.12.018

[114] Carvalho M. T., Agante E., Durão F.: Recovery of PET from packaging plastics mixtures by wet shaking table. Waste Management, **27**, 1747–1754 (2007).
DOI: 10.1016/j.wasman.2006.08.015

[115] Carvalho T., Durão F., Ferreira C.: Separation of packaging plastics by froth flotation in a continuous pilot plant. Waste Management, **30**, 2209–2215 (2010).
DOI: 10.1016/j.wasman.2010.05.023

[116] Dobrovszky K., Ronkay F.: Alternative polymer separation technology by centrifugal force in a melted state. Waste Management, **34**, 2104–2112 (2014).
DOI: 10.1016/j.wasman.2014.05.006

[117] Dodbiba G., Haruki N., Shibayama A., Miyazaki T., Fujita T.: Combination of sink–float separation and flotation technique for purification of shredded PET-bottle from PE or PP flakes. International Journal of Mineral Processing, **65**, 11–29 (2002).
DOI: 10.1016/S0301-7516(01)00056-4

[118] Dodbiba G., Sadaki J., Okaya K., Shibayama A., Fujita T.: The use of air tabling and triboelectric separation for separating a mixture of three plastics. Minerals Engineering, **18**, 1350–1360 (2005).
DOI: 10.1016/j.mineng.2005.02.015

[119] Hori K., Tsunekawa M., Ueda M., Hiroyoshi N., Ito M., Okada H.: Development of a new gravity separator for plastics – A hybrid-jig –. Materials Transactions, **50**, 2844–2847 (2009).
DOI: 10.2320/matertrans.M-M2009825

[120] Marques G. A., Tenório J. A. S.: Use of froth flotation to separate PVC/PET mixtures. Waste Management, **20**, 265–269 (2000).
DOI: 10.1016/S0956-053X(99)00333-5

[121] Shen H., Forssberg E., Pugh R. J.: Selective flotation separation of plastics by chemical conditioning with methyl cellulose. Resources, Conservation and Recycling, **35**, 229–241 (2002).
DOI: 10.1016/S0921-3449(02)00003-4

[122] Shen H., Pugh R. J., Forssberg E.: Floatability, selectivity and flotation separation of plastics by using a surfactant. Colloids and Surfaces A: Physicochemical and Engineering Aspects, **196**, 63–70 (2002).
DOI: 10.1016/S0927-7757(01)00706-3

[123] Tsunekawa M., Naoi B., Ogawa S., Hori K., Hiroyoshi N., Ito M., Hirajima T.: Jig separation of plastics from scrapped copy machines. International Journal of Mineral Processing, **76**, 67–74 (2005).
DOI: 10.1016/j.minpro.2004.12.001

[124] Zou Y., Hsieh J. S., Mehnert E., Kokoszka J.: The study of PET recyclable polymers as paper coatings. Progress in Organic Coatings, **60**, 127–131 (2007).
DOI: 10.1016/j.porgcoat.2007.07.012

[125] Adams C. J., Earle M. J., Seddon K. R.: Catalytic cracking reactions of polyethylene to light alkanes in ionic liquids. Green Chemistry, **2**, 21–24 (2000).
DOI: 10.1039/A908167D

[126] Wang H., Li Z., Liu Y., Zhang X., Zhang S.: Degradation of poly(ethylene terephthalate) using ionic liquids. Green Chemistry, **11**, 1568–1575 (2009).
DOI: 10.1039/b906831g

[127] Kržan A.: Poly(ethylene terephthalate) glycolysis under microwave irradiation. Polymers for Advanced Technologies, **10**, 603–606 (1999).
DOI: 10.1002/(SICI)1099-1581(199910)10:10<603::AID-PAT914>3.0.CO;2-V

[128] Beneš H., Slabá J., Walterová Z., Rais D.: Recycling of waste poly(ethylene terephthalate) with castor oil using microwave heating. Polymer Degradation and Stability, **98**, 2232–2243 (2013).
DOI: 10.1016/j.polymdegradstab.2013.08.019

[129] Tokiwa Y., Suzuki T.: Hydrolysis of polyesters by lipases. Nature, **270**, 76–78 (1977).
DOI: 10.1038/270076a0

[130] Kawai F., Oda M., Tamashiro T., Waku T., Tanaka N., Yamamoto M., Mizushima H., Miyakawa T., Tanokura M.: A novel Ca^{2+}-activated, thermostabilized polyesterase capable of hydrolyzing polyethylene terephthalate from saccharomonospora viridis AHK190. Applied Microbiology and Biotechnology, **98**, 10053–10064 (2014).
DOI: 10.1007/s00253-014-5860-y

[131] Mueller R-J.: Biological degradation of synthetic polyesters – Enzymes as potential catalysts for polyester recycling. Process Biochemistry, **41**, 2124–2128 (2006).
DOI: 10.1016/j.procbio.2006.05.018

[132] Donelli I., Freddi G., Nierstrasz V. A., Taddei P.: Surface structure and properties of poly-(ethylene terephthalate) hydrolyzed by alkali and cutinase. Polymer Degradation and Stability, **95**, 1542–1550 (2010).
DOI: 10.1016/j.polymdegradstab.2010.06.011

[133] Zhang J., Wang X., Gong J., Gu Z.: A study on the biodegradability of polyethylene terephthalate fiber and diethylene glycol terephthalate. Journal of Applied Polymer Science, **93**, 1089–1096 (2004).
DOI: 10.1002/app.20556

[134] Wang J., Xue L., Wang W., Jiao S.: Synthesis of diisooctyl terephthalate (DOTP) plasticizer (in Chinese). Huaxue Shijie, **32**, 208–210 (1991).

[135] Fávaro S. L., Freitas A. R., Ganzerli T. A., Pereira A. G. B., Cardozo A. L., Baron O., Muniz E. C., Girotto E. M., Radovanovic E.: PET and aluminum recycling from multilayer food packaging using supercritical ethanol. Journal of Supercritical Fluids, **75**, 138–143 (2013).
DOI: 10.1016/j.supflu.2012.12.015

[136] Liu S., Wang Z., Li L., Yu S., Xie C., Liu F.: Butanol alcoholysis reaction of polyethylene terephthalate using acidic ionic liquid as catalyst. Journal of Applied Polymer Science, **130**, 1840–1844 (2013).
DOI: 10.1002/APP.39246

[137] Nikje M. M. A., Nazari F.: Microwave-assisted depolymerization of poly(ethylene terephthalate) [PET] at atmospheric pressure. Advances in Polymer Technology, **25**, 242–246 (2006).
DOI: 10.1002/adv.20080

[138] Dutt K., Soni R. K.: Synthesis and characterization of polymeric plasticizer from PET waste and its applications in nitrile rubber and nitrile–PVC blend. Iranian Polymer Journal, **22**, 481–491 (2013).
DOI: 10.1007/s13726-013-0148-0

[139] Chabert M., Bounor-Legaré V., Mignard N., Cassagnau P., Chamignon C., Boisson F.: Formation of new alkyl functionalized poly(ethylene terephthalate) oligomers through exchange reactions with titanium alkoxides in melt conditions. Polymer Degradation and Stability, **102**, 122–131 (2014).
DOI: 10.1016/j.polymdegradstab.2014.01.030

[140] Siggel E., Heisenberg E., Lotz R.: Regeneration of terephthalic acid dimethyl ester from polyethylene terephthalate. U.S. Patent 3037050, USA (1962).

[141] Genta M., Iwaya T., Sasaki M., Goto M.: Supercritical methanol for polyethylene terephthalate depolymerization: Observation using simulator. Waste Management, **27**, 1167–1177 (2007).
DOI: 10.1016/j.wasman.2006.06.005

[142] Genta M., Iwaya T., Sasaki M., Goto M., Hirose T.: Depolymerization mechanism of poly(ethylene terephthalate) in supercritical methanol. Industrial and Engineering Chemistry Research, **44**, 3894–3900 (2005).
DOI: 10.1021/ie0488187

[143] Goto M.: Chemical recycling of plastics using sub- and supercritical fluids. The Journal of Supercritical Fluids, **47**, 500–507 (2009).
DOI: 10.1016/j.supflu.2008.10.011

[144] Goto M., Koyamoto H., Kodama A., Hirose T., Nagaoka S.: Depolymerization of polyethylene terephthalate in supercritical methanol. Journal of Physics: Condensed Matter, **14**, 11427–11430 (2002).
DOI: 10.1088/0953-8984/14/44/494

[145] Goto M., Koyamoto H., Kodama A., Hirose T., Nagaoka S., McCoy B. J.: Degradation kinetics of polyethylene terephthalate in supercritical methanol. AIChE Journal, **48**, 136–144 (2002).
DOI: 10.1002/aic.690480114

[146] Kurokawa H., Ohshima M-A., Sugiyama K., Miura H.: Methanolysis of polyethylene terephthalate (PET) in the presence of aluminium tiisopropoxide catalyst to form dimethyl terephthalate and ethylene glycol. Polymer Degradation and Stability, **79**, 529–533 (2003).
DOI: 10.1016/S0141-3910(02)00370-1

[147] Siddiqui M. N., Redhwi H. H., Achilias D. S.: Recycling of poly(ethylene terephthalate) waste through methanolic pyrolysis in a microwave reactor. Journal of Analytical and Applied Pyrolysis, **98**, 214–220 (2012).
DOI: 10.1016/j.jaap.2012.09.007

[148] Yang Y., Lu Y., Xiang H., Xu Y., Li Y.: Study on methanolytic depolymerization of PET with supercritical methanol for chemical recycling. Polymer Degradation and Stability, **75**, 185–191 (2002).
DOI: 10.1016/S0141-3910(01)00217-8

[149] Güçlü G., Yalçinyuva T., Özgümüş S., Orbay M.: Hydrolysis of waste polyethylene terephthalate and characterization of products by differential scanning calorimetry. Thermochimica Acta, **404**, 193–205 (2003).
DOI: 10.1016/S0040-6031(03)00160-6

[150] Zhang L.: Kinetics of hydrolysis of poly(ethylene terephthalate) wastes catalyzed by dual functional phase transfer catalyst: A mechanism of chain-end scission. European Polymer Journal, **60**, 1–5 (2014).
DOI: 10.1016/j.eurpolymj.2014.08.007

[151] Kazarian S. G., Martirosyan G. G.: ATR-IR spectroscopy of superheated water and in situ study of the hydrothermal decomposition of poly(ethylene terephthalate). Physical Chemistry Chemical Physics, **4**, 3759–3763 (2002).
DOI: 10.1039/b202119f

[152] Liu Y., Wang M., Pan Z.: Catalytic depolymerization of polyethylene terephthalate in hot compressed water. The Journal of Supercritical Fluids, **62**, 226–231 (2012).
DOI: 10.1016/j.supflu.2011.11.001

[153] Noritake A., Hori M., Shigematsu M., Tanahashi M.: Recycling of polyethylene terephthalate using high-pressure steam treatment. Polymer Journal, **40**, 498–502 (2008).
DOI: 10.1295/polymj.PJ2007237

[154] Sato O., Arai K., Shirai M.: Hydrolysis of poly(ethylene terephthalate) and poly(ethylene 2,6-naphthalene dicarboxylate) using water at high temperature: Effect of proton on low ethylene glycol yield. Catalysis Today, **111**, 297–301 (2006).
DOI: 10.1016/j.cattod.2005.10.040

[155] Mancini S. D., Nogueira A. R., Rangel E. C., da Cruz N. C.: Solid-state hydrolysis of postconsumer polyethylene terephthalate after plasma treatment. Journal of Applied Polymer Science, **127**, 1989–1996 (2013).
DOI: 10.1002/app.37591

[156] Sharma V., Parashar P., Srivastava P., Kumar S., Agarwal D. D., Richharia N.: Recycling of waste PET-bottles using dimethyl sulfoxide and hydrotalcite catalyst. Journal of Applied Polymer Science, **129**, 1513–1519 (2013).
DOI: 10.1002/app.38829

[157] Siddiqui M. N., Achilias D. S., Redhwi H. H., Bikiaris D. N., Katsogiannis K. G., Karayannidis G. P.: Hydrolytic depolymerization of PET in a microwave reactor. Macromolecular Materials and Engineering, **295**, 575–584 (2010).
DOI: 10.1002/mame.201000050

[158] Zope V. S., Mishra S.: Kinetics of neutral hydrolytic depolymerization of PET (polyethylene terephthalate) waste at higher temperature and autogenious pressures. Journal of Applied Polymer Science, **110**, 2179–2183 (2008).
DOI: 10.1002/app.28190

[159] de Carvalho G. M., Muniz E. C., Rubira A. F.: Hydrolysis of post-consume poly(ethylene terephthalate) with sulfuric acid and product characterization by WAXD, ^{13}C NMR and DSC. Polymer Degradation and Stability, **91**, 1326–1332 (2006).
DOI: 10.1016/j.polymdegradstab.2005.08.005

[160] Kumar A., Rao T. R.: Kinetics of hydrolysis of polyethylene terephthalate pellets in nitric acid. Journal of Applied Polymer Science, **87**, 1781–1785 (2003).
DOI: 10.1002/app.11579

[161] Yoshioka T., Sato T., Okuwaki A.: Hydrolysis of waste PET by sulfuric acid at 150 °C for a chemical recycling. Journal of Applied Polymer Science, **52**, 1353–1355 (1994).
DOI: 10.1002/app.1994.070520919

[162] Caparanga A. R., Basilia B. A., Dagbay K. B., Salvacion J. W. L.: Factors affecting degradation of polyethylene terephthalate (PET) during pre-flotation conditioning. Waste Management, **29**, 2425–2428 (2009).
DOI: 10.1016/j.wasman.2009.03.025

[163] Karayannidis G. P., Chatziavgoustis A. P., Achilias D. S.: Poly(ethylene terephthalate) recycling and recovery of pure terephthalic acid by alkaline hydrolysis. Advances in Polymer Technology, **21**, 250–259 (2002).
DOI: 10.1002/adv.10029

[164] Khalaf H. I., Hasan O. A.: Effect of quaternary ammonium salt as a phase transfer catalyst for the microwave depolymerization of polyethylene terephthalate waste bottles. Chemical Engineering Journal, **192**, 45–48 (2012).
DOI: 10.1016/j.cej.2012.03.081

[165] Kosmidis V. A., Achilias D. S., Karayannidis G. P.: Poly(ethylene terephthalate) recycling and recovery of pure terephthalic acid. Kinetics of a phase transfer catalyzed alkaline hydrolysis. Macromolecular Materials and Engineering, **286**, 640–647 (2001).
DOI: 10.1002/1439-2054(20011001)286:10<640::AID-MAME640>3.0.CO;2-1

[166] Mishra S., Zope V. S., Goje A. S.: Kinetic and thermodynamic studies of depolymerisation of poly(ethylene terephthalate) by saponification reaction. Polymer International, **51**, 1310–1315 (2002).
DOI: 10.1002/pi.873

[167] Paliwal N. R., Mungray A. K.: Ultrasound assisted alkaline hydrolysis of poly(ethylene terephthalate) in presence of phase transfer catalyst. Polymer Degradation and Stability, **98**, 2094–2101 (2013).
DOI: 10.1016/j.polymdegradstab.2013.06.030

[168] Shafique U., Zaman W. U., Anwar J., Munawar M. A., Salman M., Dar A., Rehman R., Ashraf U., Ahmad S.: A rapid, economical, and eco-friendly method to recycle terephthalic acid from waste poly (ethylene terphthalate) bottles. International Journal of Polymeric Materials and Polymeric Biomaterials, **60**, 1147–1151 (2011).
DOI: 10.1080/00914037.2011.557802

[169] Rosmaninho M. G., Jardim E., Moura F. C. C., Ferreira G. L., Thom V., Yoshida M. I., Araujo M. H., Lago R. M.: Surface hydrolysis of postconsumer polyethylene terephthalate to produce adsorbents for cationic contaminants. Journal of Applied Polymer Science, **102**, 5284–5291 (2006).
DOI: 10.1002/app.24790

[170] Karayannidis G. P., Achilias D. S.: Chemical recycling of poly(ethylene terephthalate). Macromolecular Materials and Engineering, **292**, 128–146 (2007),
DOI: 10.1002/mame.200600341

[171] Kao C-Y., Cheng W-H., Wan B-Z.: Investigation of alkaline hydrolysis of polyethylene terephthalate by differential scanning calorimetry and thermogravimetric analysis. Journal of Applied Polymer Science, **70**, 1939–1945 (1998).
DOI: 10.1002/(SICI)1097-4628(19981205)70:10<1939::AID-APP8>3.0.CO;2-G

[172] Pingale N. D., Shukla S. R.: Microwave assisted eco-friendly recycling of poly (ethylene terephthalate) bottle waste. European Polymer Journal, **44**, 4151–4156 (2008).
DOI: 10.1016/j.eurpolymj.2008.09.019

[173] Roy P. K, Mathur R., Kumar D., Rajagopal C.: Tertiary recycling of poly(ethylene terephthalate) wastes for production of polyurethane–polyisocyanurate foams. Journal of Environmental Chemical Engineering, **1**, 1062–1069 (2013).
DOI: 10.1016/j.jece.2013.08.019

[174] Colomines G., van der Lee A., Robin J-J., Boutevin B.: X-ray diffraction of the crystallinity of glycolysates derived from PET. European Polymer Journal, **44**, 2874–2885 (2008).
DOI: 10.1016/j.eurpolymj.2008.07.008

[175] El Mejjatti A., Harit T., Riahi A., Khiari R., Bouabdallah I., Malek F.: Chemical recycling of poly(ethylene terephthalate). Application to the synthesis of multiblock copolyesters. Express Polymer Letters, **8**, 544–553 (2014).
DOI: 10.3144/expresspolymlett.2014.58

[176] El-Sherbiny S. I., Morsy F. A., Atta A. M.: Synthesis of new cationic surfactants based on recycled poly(ethylene terephthalate) for deinking of solvent-based ink from low-density polyethylene surface. Journal of Applied Polymer Science, **118**, 1160–1172 (2010).
DOI: 10.1002/app.32488

[177] Farahat M. S.: Mechanical characteristics of modified unsaturated polyester resins derived from poly(ethylene terephthalate) waste. Polymer International, **51**, 183–189 (2002).
DOI: 10.1002/pi.818

[178] Farahat M. S., Nikles D. E.: On the UV Curability and mechanical properties of novel binder systems derived from poly(ethylene terephthalate) (PET) waste for solventless magnetic tape manufacturing, 2. Methacrylated oligoesters. Macromolecular Materials and Engineering, **287**, 353–362 (2002).
DOI: 10.1002/1439-2054(20020501)287:5<353::AID-MAME353>3.0.CO;2-H

[179] Karayannidis G. P., Achilias D. S., Sideridou I. D., Bikiaris D. N.: Alkyd resins derived from glycolized waste poly(ethylene terephthalate). European Polymer Journal, **41**, 201–210 (2005).
DOI: 10.1016/j.eurpolymj.2004.10.001

[180] Barboza E. S., Lopez D. R., Amico S. C., Ferreira C. A.: Determination of a recyclability index for the PET glycolysis. Resources, Conservation and Recycling, **53**, 122–128 (2009).
DOI: 10.1016/j.resconrec.2008.10.002

[181] Abdelaal M. Y., Sobahi T. R., Makki M. S. I.: Chemical transformation of pet waste through glycolysis. Construction and Building Materials, **25**, 3267–3271 (2011).
DOI: 10.1016/j.conbuildmat.2011.03.013

[182] Kathalewar M., Dhopatkar N., Pacharane B., Sabnis A., Raut P., Bhave V.: Chemical recycling of PET using neopentyl glycol: Reaction kinetics and preparation of polyurethane coatings. Progress in Organic Coatings, **76**, 147–156 (2013).
DOI: 10.1016/j.porgcoat.2012.08.023

[183] Abdullah N. M., Ahmad I.: Potential of using polyester reinforced coconut fiber composites derived from recycling polyethylene terephthalate (PET) waste. Fibers and Polymers, **14**, 584–590 (2013).
DOI: 10.1007/s12221-013-0584-7

[184] Baliga S., Wong W. T.: Depolymerization of poly(ethylene terephthalate) recycled from post-consumer softdrink bottles. Journal of Polymer Science Part A: Polymer Chemistry, **27**, 2071–2082 (1989).
DOI: 10.1002/pola.1989.080270625

[185] Pimpan V., Sirisook R., Chuayjuljit S.: Synthesis of unsaturated polyester resin from postconsumer PET bottles: Effect of type of glycol on characteristics of unsaturated polyester resin. Journal of Applied Polymer Science, **88**, 788–792 (2003).
DOI: 10.1002/app.11567

[186] Puangsansuk K., Opaprakasit M., Udomkichdecha W., Potiyaraj P.: Effects of saturated acids on physical properties of UPE resins prepared from recycled PET products. Journal of Polymers and the Environment, **17**, 65–70 (2009).
DOI: 10.1007/s10924-009-0122-2

[187] Shukla S. R., Harad A. M., Jawale L. S.: Recycling of waste PET into useful textile auxiliaries. Waste Management, **28**, 51–56 (2008).
DOI: 10.1016/j.wasman.2006.11.002

[188] Shukla S. R., Harad A. M., Jawale L. S.: Chemical recycling of PET waste into hydrophobic textile dyestuffs. Polymer Degradation and Stability, **94**, 604–609 (2009).
DOI: 10.1016/j.polymdegradstab.2009.01.007

[189] Shukla S. R., Kulkarni K. S.: Depolymerization of poly(ethylene terephthalate) waste. Journal of Applied Polymer Science, **85**, 1765–1770 (2002).
DOI: 10.1002/app.10714

[190] Essawy H. A., Tawfik M. E., Elsayed N. H.: Effect of addition of glycolysis products of poly(ethyleneterephthalate) wastes to urea-formaldehyde resin on its adhesion performance to wood substrates and formaldehyde emission. Journal of Applied Polymer Science, **123**, 2377–2383 (2012).
DOI: 10.1002/app.34750

[191] Pingale N. D., Palekar V. S., Shukla S. R.: Glycolysis of postconsumer polyethylene terephthalate waste. Journal of Applied Polymer Science, **115**, 249–254 (2010).
DOI: 10.1002/app.31092

[192] Ghaemy M., Mossaddegh K.: Depolymerisation of poly(ethylene terephthalate) fibre wastes using ethylene glycol. Polymer Degradation and Stability, **90**, 570–576 (2005).
DOI: 10.1016/j.polymdegradstab.2005.03.011

[193] Carné Sánchez A., Collinson S. R.: The selective recycling of mixed plastic waste of polylactic acid and polyethylene terephthalate by control of process conditions. European Polymer Journal, **47**, 1970–1976 (2011).
DOI: 10.1016/j.eurpolymj.2011.07.013

[194] Maeda Y., Mori H., Maeda T., Itoh O., Yamaguchi K., Kubota S., Nakayama A., Kawasaki N., Yamamoto N., Aiba S.: Characterization of novel biodegradable copolyesters prepared from glycolyzed products of poly(ethylene terephthalate). Journal of Applied Polymer Science, **84**, 1838–1847 (2002).
DOI: 10.1002/app.10462

[195] Al-Sabagh A. M., Yehia F. Z., Eissa A. M. F., Moustafa M. E., Eshaq G., Rabie A. M., ElMetwally A. E.: Cu- and Zn-acetate-containing ionic liquids as catalysts for the glycolysis of poly(ethylene terephthalate). Polymer Degradation and Stability, **110**, 364–377 (2014).
DOI: 10.1016/j.polymdegradstab.2014.10.005

[196] Atta A. M., Abdel-Rauf M. E., Maysour N. E., Abdul-Rahiem A. M., Abdel-Azim A. A. A.: Surfactants from recycled poly (ethylene terephthalate) waste as water based oil spill dispersants. Journal of Polymer Research, **13**, 39–52 (2006).
DOI: 10.1007/s10965-005-9003-0

[197] Atta A. M., El-Kafrawy A. F., Aly M. H., Abdel-Azim A. A. A.: New epoxy resins based on recycled poly (ethylene terephthalate) as organic coatings. Progress in Organic Coatings, **58**, 13–22 (2007).
DOI: 10.1016/j.porgcoat.2006.11.001

[198] Fukushima K., Coulembier O., Lecuyer J. M., Almegren H. A., Alabdulrahman A. M., Alsewailem F. D., McNeil M. A., Dubois P., Waymouth R. M., Horn H. W., Rice J. E., Hedrick J. L.: Organocatalytic depolymerization of poly(ethylene terephthalate). Journal of Polymer Science Part A: Polymer Chemistry, **49**, 1273–1281 (2011).
DOI: 10.1002/pola.24551

[198] Krehula L. K., Hrnjak-Murgić Z., Jelenčić J., Andričić B.: Evaluation of poly(ethylene-terephthalate) products of chemical recycling by differential scanning calorimetry. Journal of Polymers and the Environment, **17**, 20–27 (2009).
DOI: 10.1007/s10924-009-0121-3

[200] Bartolome L., Imran M., Lee K. G., Sangalang A., Ahn J. K., Kim D. H.: Superparamagnetic γ-Fe$_2$O$_3$ nanoparticles as an easily recoverable catalyst for the chemical recycling of PET. Green Chemistry, **16**, 279–286 (2014).
DOI: 10.1039/c3gc41834k

[201] Fukushima K., Coady D. J., Jones G. O., Almegren H. A., Alabdulrahman A. M., Alsewailem F. D., Horn H. W., Rice J. E. Hedrick J. L.: Unexpected efficiency of cyclic amidine catalysts in depolymerizing poly(ethylene terephthalate). Journal of Polymer Science Part A: Polymer Chemistry, **51**, 1606–1611 (2013).
DOI: 10.1002/pola.26530

[202] Katoch S., Sharma V., Kundu P. P.: Synthesis and characterization of saturated polyester and nanocomposites derived from glycolyzed PET waste with varied compositions. Bulletin of Materials Science, **36**, 277–286 (2013).
DOI: 10.1007/s12034-013-0459-y

[203] Duque-Ingunza I., López-Fonseca R., de Rivas B., Gutiérrez-Ortiz J. I.: Synthesis of unsaturated polyester resin from glycolysed postconsumer PET wastes. Journal of Material Cycles and Waste Management, **15,** 256–263 (2013).
DOI: 10.1007/s10163-013-0117-x

[204] Duque-Ingunza I., López-Fonseca R., de Rivas B., Gutiérrez-Ortiz J. I.: Process optimization for catalytic glycolysis of post-consumer PET wastes. Journal of Chemical Technology and Biotechnology, **89**, 97–103 (2014).
DOI: 10.1002/jctb.4101

[205] Chen C-H., Chen C-Y., Lo Y-W., Mao C-F., Liao W-T.: Studies of glycolysis of poly(ethylene terephthalate) recycled from postconsumer soft-drink bottles. II. Factorial experimental design. Journal of Applied Polymer Science, **80**, 956–962 (2001).
DOI: 10.1002/app.1176

[206] López-Fonseca R., Duque-Ingunza I., de Rivas B., Arnaiz S., Gutiérrez-Ortiz J. I.: Chemical recycling of post-consumer PET wastes by glycolysis in the presence of metal salts. Polymer Degradation and Stability, **95**, 1022–1028 (2010).
DOI: 10.1016/j.polymdegradstab.2010.03.007

[207] Viana M. E., Riul A., Carvalho G. M., Rubira A. F., Muniz E. C.: Chemical recycling of PET by catalyzed glycolysis: Kinetics of the heterogeneous reaction. Chemical Engineering Journal, **173**, 210–219 (2011).
DOI: 10.1016/j.cej.2011.07.031

[208] Zahedi A. R., Rafizadeh M., Taromi F. A.: Optimizing synthesis of PET oligomers end capped with phthalic/maleic anhydride *via* recycling of off grade PET using design of experiments. Journal of Thermoplastic Composite Materials, **27**, 1256–1277 (2014).
DOI: 10.1177/0892705712470266

[209] Chen F., Yang F., Wang G., Li W.: Calcined Zn/Al hydrotalcites as solid base catalysts for glycolysis of poly(ethylene terephthalate). Journal of Applied Polymer Science, **131**, 41053/1–41053/10 (2014).
DOI: 10.1002/app.41053

[210] Chaudhary S., Surekha P., Kumar D., Rajagopal C., Roy P. K.: Microwave assisted glycolysis of poly(ethylene terepthalate) for preparation of polyester polyols. Journal of Applied Polymer Science, **129**, 2779–2788 (2013).
DOI: 10.1002/app.38970

[211] Goje A. S., Mishra S.: Chemical kinetics, simulation, and thermodynamics of glycolytic depolymerization of poly(ethylene terephthalate) waste with catalyst optimization for recycling of value added monomeric products. Macromolecular Materials and Engineering, **288**, 326–336 (2003).
DOI: 10.1002/mame.200390034

[212] López-Fonseca R., Duque-Ingunza I., de Rivas B., Flores-Giraldo L., Gutiérrez-Ortiz J. I.: Kinetics of catalytic glycolysis of PET wastes with sodium carbonate. Chemical Engineering Journal, **168**, 312–320 (2011).
DOI: 10.1016/j.cej.2011.01.031

[213] Aguado A., Martínez L., Becerra L., Arieta-araunabeña M., Arnaiz S., Asueta A., Robertson I.: Chemical depolymerisation of PET complex waste: Hydrolysis vs. glycolysis. Journal of Material Cycles and Waste Management, **16**, 201–210 (2014).
DOI: 10.1007/s10163-013-0177-y

[214] Alnaqbi M. A., Mohsin M. A., Busheer R. M., Haik Y.: Microwave assisted glycolysis of poly(ethylene terephthalate) catalyzed by 1-butyl-3-methylimidazolium bromide ionic liquid. Journal of Applied Polymer Science, **132**, 41666/1–41666/7 (2015).
DOI: 10.1002/APP.41666

[215] Saint-Loup R., Robin J-J.: Synthesis of poly[(ethylene terephthalate)-*co*-(ε-caprolactone)]-poly(propylene oxide) block copolyester by direct polyesterification of reactive oligomers. Macromolecular Chemistry and Physics, **206**, 1190–1198 (2005).
DOI: 10.1002/macp.200500079

[216] Saint-Loup R., Robin J-J., Boutevin B., Argalon M., Michel A.: Synthesis of hydroxytelechelic ε-caprolactone/poly(ethylene terephthalate) *co*-oligomers, 1. Macromolecular Chemistry and Physics, **203**, 1249–1256 (2002).
DOI: 10.1002/1521-3935(200206)203:9<1249::AID-MACP1249>3.0.CO;2-J

[217] Saint-Loup R., Jeanmaire T., Robin J-J., Boutevin B.: Synthesis of (polyethylene terephthalate/polyϵ-caprolactone) copolyesters. Polymer, **44**, 3437–3449 (2003).
DOI: 10.1016/S0032-3861(03)00257-X

[218] Saint-Loup R., Robin J-J., Boutevin B.: Synthesis of poly(ethylene terephthalate)-block-poly(tetramethylene oxide) copolymer by direct polyesterification of reactive oligomers. Macromolecular Chemistry and Physics, **204**, 970–982 (2003).
DOI: 10.1002/macp.200390072

[219] Colomines G., Rivas F., Lacoste M-L., Robin J-J.: Study of polyurethane formulations containing diols obtained *via* glycolysis of poly(ethylene terephthalate) (PET) by oligoesters diols through a reactive extrusion process. Macromolecular Materials and Engineering, **290**, 710–720 (2005).
DOI: 10.1002/mame.200400391

[220] Achilias D. S., Redhwi H. H., Siddiqui M. N., Nikolaidis A. K., Bikiaris D. N., Karayannidis G. P.: Glycolytic depolymerization of PET waste in a microwave reactor. Journal of Applied Polymer Science, **118**, 3066–3073 (2010).
DOI: 10.1002/app.32737

[221] Lu M., Kim S.: Unsaturated polyester resins based on recycled PET: Preparation and curing behavior. Journal of Applied Polymer Science, **80**, 1052–1057 (2001).
DOI: 10.1002/app.1189

[222] Mansour S. H., Abd-El-Messieh S. L., Ikaldious N. E.: Utilization of some oligomers based on poly(ethylene terephthalate) wastes as modifiers for polyvinyl chloride. Journal of Applied Polymer Science, **85**, 2501–2509 (2002).
DOI: 10.1002/app.10608

[223] Tawfik M. E., Eskander S. B.: Chemical recycling of poly(ethylene terephthalate) waste using ethanolamine, sorting of the end products. Polymer Degradation and Stability, **95**, 187–194 (2010).
DOI: 10.1016/j.polymdegradstab.2009.11.026

[224] More A. P., Kute R. A., Mhaske S. T.: Chemical conversion of PET waste using ethanolamine to bis(2-hydroxyethyl) terephthalamide (BHETA) through aminolysis and a novel plasticizer for PVC. Iranian Polymer Journal, **23**, 59–67 (2014).
DOI: 10.1007/s13726-013-0200-0

[225] Achilias D. S., Tsintzou G. P., Nikolaidis A. K., Bikiaris D. N., Karayannidis G. P.: Aminolytic depolymerization of poly(ethylene terephthalate) waste in a microwave reactor. Polymer International, **60**, 500–506 (2011).
DOI: 10.1002/pi.2976

[226] Dutt K., Soni R. K.: Synthesis and characterization of bis-amino ethyl terephthalamide from PET waste and its applications as hardener in DGEBA. International Journal of Plastics Technology, **18**, 16–26 (2014).
DOI: 10.1007/s12588-014-9071-2

[227] Jain A., Soni R. K.: Spectroscopic investigation of end products obtained by ammonolysis of poly (ethylene terephthalate) waste in the presence of zinc acetate as a catalyst. Journal of Polymer Research, **14**, 475–481 (2007).
DOI: 10.1007/s10965-007-9131-9

[228] Mittal A., Soni R. K., Dutt K., Singh S.: Scanning electron microscopic study of hazardous waste flakes of polyethylene terephthalate (PET) by aminolysis and ammonolysis. Journal of Hazardous Materials, **178**, 390–396 (2010).
DOI: 10.1016/j.jhazmat.2010.01.092

[229] Mir Mohamad Sadeghi G., Shamsi R., Sayaf M.: From aminolysis product of PET waste to novel biodegradable polyurethanes. Journal of Polymers and the Environment, **19**, 522–534 (2011).
DOI: 10.1007/s10924-011-0283-7

[230] Padhan R. K., Gupta A. A., Badoni R. P. Bhatnagar A. K.: Poly(ethylene terephthalate) waste derived chemicals as an antistripping additive for bitumen – An environment friendly approach for disposal of environmentally hazardous material. Polymer Degradation and Stability, **98**, 2592–2601 (2013).
DOI: 10.1016/j.polymdegradstab.2013.09.019

[231] Parab Y. S., Shukla S. R.: Microwave synthesis and antibacterial activity of 1,4-bis (5-aryl-1,3,4-oxadiazole-2-yl) benzene derivatives from terephthalic dihydrazide obtained through aminolysis of PET bottle waste. Waste and Biomass Valorization, **4**, 23–27 (2013).
DOI: 10.1007/s12649-012-9128-4

[232] Shukla S. R., Harad A. M.: Aminolysis of polyethylene terephthalate waste. Polymer Degradation and Stability, **91**, 1850–1854 (2006).
DOI: 10.1016/j.polymdegradstab.2005.11.005

[233] Soni R. K., Singh S.: Synthesis and characterization of terephthalamides from poly(ethylene terephthalate) waste. Journal of Applied Polymer Science, **96**, 1515–1528 (2005).
DOI: 10.1002/app.21502

[234] Spychaj T., Paszun D.: New trends in chemical recycling of poly(ethylene terephthalate). Macromolecular Symposia, **135**, 137–145 (1998).
DOI: 10.1002/masy.19981350116

[235] Hoang C. N., Dang Y. H.: Aminolysis of poly(ethylene terephthalate) waste with ethylenediamine and characterization of α,ω-diamine products. Polymer Degradation and Stability, **98**, 697–708 (2013).
DOI: 10.1016/j.polymdegradstab.2012.12.026

[236] Geyer B., Röhner S., Lorenz G., Kandelbauer A.: Synthesis of ethylene terephthalate and ethylene naphthalate (PET-PEN) block-*co*-polyesters with defined surface qualities by tailoring segment composition. Journal of Applied Polymer Science, **131**, 40731/1–40731/15 (2014).
DOI: 10.1002/app.40731

[237] Röhner S., Dettinger U., Geyer B., Kandelbauer A., Gadon S., Egelhaaf H., Chassé T., Lorenz G.: Mechanical and optical properties of nanofunctionalized random block-co-polyesters of polyethylene terephthalate (PET) and polyethylene naphthalate (PEN). Journal of Applied Polymer Science, submitted (2016).

Improving the interfacial and mechanical properties of short glass fiber/epoxy composites by coating the glass fibers with cellulose nanocrystals

A. Asadi[1], M. Miller[1], R. J. Moon[2,3], K. Kalaitzidou[1,3]*

[1]G.W. Woodruff School of Mechanical Engineering – Georgia Institute of Technology, GA 30332 Atlanta, United States
[2]The Forest Products Laboratory, U.S. Forest Service, Madison, 53726 Wisconsin, United States
[3]School of Materials Science and Engineering – Georgia Institute of Technology, GA 30332 Atlanta, United States

Abstract. In this study, the interfacial and mechanical properties of cellulose nanocrystals (CNC) coated glass fiber/epoxy composites were investigated as a function of the CNC content on the surface of glass fibers (GF). Chopped GF rovings were coated with CNC by immersing the GF in CNC (0–5 wt%) aqueous suspensions. Single fiber fragmentation (SFF) tests showed that the interfacial shear strength (IFSS) increased by ~69% in composites produced with CNC coated GF as compared to uncoated GF, suggesting an enhancement of stress transfer across the GF/matrix interface. The role of CNC coatings on the tensile, flexural, and thermo-mechanical properties of the CNC-coated GF/epoxy composites was investigated. Incorporation of 0.17 wt% CNC in the composite resulted in increases of ~10% in both elastic modulus and tensile strength, and 40 and 43 % in flexural modulus and strength respectively. In conclusion CNC coatings on GF alter the GF/matrix interface resulting in improvement of the mechanical performance of the corresponding composites.

Keywords: polymer composites, nanomaterials, coatings, mechanical properties

1. Introduction

Short glass fiber (GF) polymer matrix composites (PMC) with 30–50 wt% fiber loading have been widely used in automotive and marine industries as structural components due to their high specific strength and stiffness. Continued development in light-weighted PMC with higher mechanical performance has been fueled by the premise that 10% reduction in the vehicle weight can result in 6–8% increase in fuel efficiency [1]. One approach towards light weighting is the incorporation of nanoparticles either as a reinforcement phase within the matrix polymer, or at the fiber/matrix interface [2–5]. The high surface area per unit volume of nanoparticles enhances the interactions with the other constituents in the composite and subsequently enhances the me-

chanical properties compared to larger dimension particles of the same composition [6]. However, issues such as inhomogeneous dispersion and agglomerate formation should be addressed before using these materials in large scale production of composites.
Alternative nanoparticles that have potential for increasing GF-polymer matrix composites properties are cellulose nanomaterials (CNs). CNs are cellulose-based nanoparticles that are obtained from plants, algae, bacteria and marine animals [7–9]. CN particles are generally grouped based on the cellulose source and the extraction methods, leading to various CN types, including: cellulose nanocrystals (CNC), cellulose nanofibrils (CNF), algae cellulose (AC), bacterial cellulose (BC), etc. One common trait with all CN types is the parallel stacking of cellulose

---

*Corresponding author, e-mail: kyriaki.kalaitzidou@me.gatech.edu

chains along the particle length, and because of this feature the properties of the various CNs are similar to each other, at least within the scatter of experimental testing or atomistic model predictions [9]. With this in mind, as a whole CNs have a unique combination of characteristics [9] that make them attractive for certain composite applications, i.e. low density (1.6 g/cm^3), high surface area and aspect ratio (10–100), tensile strength of 3–7.5 GPa, and elastic modulus of 110–220 GPa, surfaces with accessible hydroxyl side groups (e.g. –OH) that can be readily chemically modified, and low toxicity [10]. In addition, CNs extracted from trees and plants have the potential to be produced at industrial scale quantities, and reasonable price [11]. In the current study, the CN type used was CNC, which are whisker-shaped particles (typically, 3–5 nm in width and 5–500 nm in length), extracted by acid hydrolysis of plants [12], and are considered to have properties within the ranges listed above.

There has been considerable interest in CNs as reinforcement in various polymer systems due to their high specific modulus and strength characteristics, and provided that the CNs are well dispersed within the polymer matrix, increases in mechanical performance of the CN-polymer system and subsequently the corresponding composites can be expected. For most epoxy systems, obtaining well dispersed CNs in epoxies has been exceedingly challenging, especially for high CN volume fraction [13–20]. To address this issues, waterborne epoxies [14, 15, 18], solvent exchange methods [20, 21], CN preforms impregnation [22] and chemical modification of CN surfaces have been used [23], however, the time and cost involved in these processes limit their capability in industrial scale production of GF/epoxy composites.

An alternative approach has been to add CNs to GF/epoxy composites by coating the GF prior to mixing into epoxy, where the CN coating modifies the GF/epoxy interface and subsequently improves the properties. A good review on tailoring interphase through coating the fibers in polymer composites can be found in [24]. Chen *et al.* [25] deposited bacterial cellulose (BC) on the surface of GF during the process of fermentation. The BC coated GF were subsequently compounded into epoxy, where the increase in the interfacial shear strength (IFSS) of BC coated GF/epoxy interface was attributed to the increase in interfacial surface roughness and area, and chemical bonding between the BC coating and the epoxy ma-

trix. However, for large volume uses, growth of the BC film on GF is impractical. Additional work is needed to i) find coating processes that are quick, reliable, and inexpensive and ii) link changes in IFSS to differences in macroscopic mechanical properties of the GF/epoxy composites as a result of the addition of the CN coatings. To the best of the authors' knowledge, no studies exist on simple coating technique of GF with CN and the influence of the CN coating on both the interfacial and mechanical properties.

In this study, the effect of CNC coatings on GF on the GF/epoxy matrix interfacial properties and the subsequent influence on the mechanical properties of short GF/epoxy composites are investigated. GF were coated by immersing them in an aqueous CNC suspension (0–5 wt%), a scalable technique. Interfacial adhesion was characterized by the IFSS using single fiber fragmentation tests (SFF). Changes in the IFSS and stiffness across the GF/matrix interphase as a result of CNC coating on the GF were two potential mechanisms considered for the enhancement in tensile and flexural properties of CNC coated-GF/epoxy composites. The optimum CNC concentration on the GF that resulted in the best mechanical performance was determined.

2. Experimental details
2.1. Materials
Owens Corning (Oak Brook, IL, US) ME1510 multi-end roving GF (TEX 48000, single filament diameter of 10±1 μm) were used as received. The GF rovings were chopped to an average length of 25±0.5 mm. A bicomponent epoxy resin consisting of 635 thin epoxy and 556 slow amine hardener supplied by US Composites (West Palm Beach, FL) was used. CNC in the form of 11.9 wt% never-dried suspension in water [26] were supplied by the USDA Forest Service-Forest Products Laboratory (FPL), Madison, WI, USA. The average length and width of the CNC were 138±22 nm and 6.4±0.6, respectively [18].

2.2. Coating of GF with CNC and fabrication of CNC-coated GF/epoxy composites
CNC coated GF were produced by immersing ~154 g of chopped GF rovings in ~1000 mL of aqueous CNC suspension without agitation for 2 min, after which the GF were taken out and spread on covered trays with ample ventilation to dry 24 h at room temperature. This simple, low cost coating method is conceptually scalable for larger volume applications. The

CNC used were not functionalized or surface treated. For uncoated GF, a similar procedure was followed using distilled water with no CNC to maintain the consistency in fabrication. The CNC suspension was diluted, in order to adjust the CNC coating, using distilled water and then sonicated to achieve a uniform CNC dispersion in water. Sonication was carried out using Misonix S-4000 ultrasonic processor equipped with a 12.5 mm probe diameter at 30% amplitude and 20 W power for 8 min. Aqueous CNC suspensions of 0, 0.5, 1, 1.5, 2, 3 and 5 wt%, were prepared using the above procedure and used to coat the chopped GF rovings. The corresponding naming scheme used to describe the coated fibers is GF, 0.5S-GF, 1S-GF, 1.5S-GF, 2S-GF, 3S-GF, and 5S-GF, respectively. The 'S' in this case represents the concentration of CNC suspension.

For SFF test specimen preparation, individual GF filaments were carefully pulled off from the coated and uncoated GF rovings. Subsequently, a single 120 mm long GF filament was placed in the middle of a dog-bone shaped mold and covered with epoxy resin that was cured at 80 °C for 1 h, followed by post-curing at 100 °C for 4 h. Prior to pour the epoxy in the mold, the single GF filaments were manually pre-strained and the ends of the GF were taped down to ensure that the GF remain in tension during the epoxy curing. The resin was prepared by mixing the epoxy with hardener at 2:1 wt% using a VWR magnetic stirring plate at a 60 rpm, at room temperature for 10 min, and was degassed in a vacuum chamber for 5 min prior to pouring into the mold. SFF test specimens were prepared using the following GF: GF, 0.5S-GF, 1S-GF, 1.5S-GF, 2S-GF, 3S-GF, and 5S-GF. The SFF test dog-bone specimens were made according to the test protocol for SFF test [27], having a gauge length of 25 mm long, 3 mm wide and a depth of 2 mm, with an overall length and width of 80 and 10 mm, respectively.

GF/epoxy composites were produced with a 30 wt% GF content. Chopped GF rovings with or without CNC coatings were added and mixed with the resin using a spatula in a tote and degassed in a vacuum chamber, for 5 min. Then, the mixture was spread in a rectangular mold and cured as described above. Based on the SFF results (see Section 3.2), only 1S-GF, 1.5S-GF and 2S-GF were used to make CNC-GF/epoxy composites. The test coupons were cut from the plate using a waterjet (MAXIEM 1515).

2.3. Characterization techniques
2.3.1. Single-fiber fragmentation tests (SFF)
SFF tests, as described by Hunston *et al*. [27], were used to quantify the effect of CNC coatings on the IFSS. In brief, tensile tests, with applied load along the fiber axis direction, were carried out at a displacement rate of 1 mm/min using an Instron 33R 4466 equipped with a 500 N load cell. The tests continued until the load passed its peak and dropped at 90–95% of maximum load to ensure that no further fiber fragmentation could occur. Since the GF were pre-strained, it was expected that when the epoxy reached at its strain to failure, saturation in the GF fragmentation had occurred. It is noted that if the test continued further than this point, the samples would break into two pieces and the fragmentation lengths could not be recorded. The IFSS was determined by Kelly and Tyson model [28] given in Equation (1):

$$\tau_i = \frac{d_f \sigma_f(l_c)}{2l_c} = \frac{3d_f \sigma_f(l_c)}{8\bar{l}} \tag{1}$$

where τ_i is the IFSS, d_f is the fiber diameter, l_c is the fiber critical fragmentation length, $\bar{l}$ is the average length of fiber fragmentation segments ($l_c = 4\bar{l}/3$) and σ_f is the fiber strength at the critical length. The fiber diameter and fiber fragmentation lengths were measured using polarized microscopy. The GF fiber strength was estimated by tensile testing (ASTM D3822), where a single GF fiber was attached to a paper tab and tested at a displacement rate of 1 mm/min using the Instron. An average GF strength of 2900±350 MPa was measured for a gauge length of 25.4 mm and as expected, the CNC coating process did not affect the single GF ultimate strength. Both the strength value and the IFSS values reported are an average of at least 10 measurements. Weibull distribution was applied for the GF strength data [29] to obtain the Weibull modulus and fiber strength as 4.57 and 2900 MPa respectively. These values were used to extrapolate the GF strength at the critical length required in Equation (1).

2.3.2. Microscopy
A Leica DM2500 polarized light optical microscope was used to characterize CNC coatings on chopped GF rovings, and to measure the fiber fragmentation lengths in SFF tests. A Hitachi SU 8230 field emission scanning electron microscope (FE-SEM) at an acceleration of 5 kV were used to view the CNC coat-

ings on individual GF, and the fracture surfaces of the composites. A plasma sputter (Ted Pella Inc.) was used to apply gold coating on the surface of the samples prior to SEM imaging to minimize charging.

2.3.3. Specific density, thermal stability and CNC content

Water displacement method was used to measure the specific density of the composites according to ASTM D-792. Thermogravimetry analysis (TGA), using TGA SDT Q600 (TA Instruments), was used to assess the thermal stability of CNC and determine the CNC content on the GF. The samples were heated from 50 to 500 °C at 10 °C/min in inert atmosphere. Each data point is an average of at least 3 measurements.

2.3.4. Mechanical and dynamic mechanical testing

The tensile properties of the composites were determined according to ASTM D638 using an Instron 33R 4466 equipped with 10 kN load cell. An extensometer, Instron 2630-35, with a gauge length of 50.8 mm was used. The modulus was calculated between the axial strain values of 0.05 and 0.2%. Each tensile data point is an average of at least five samples. The flexural properties were measured using three-point bending tests with an Instron 33R 4466 equipped with 10 kN load cell according to ASTM D790-02 with a support span of 50 mm and a sample thickness of 5 mm at a displacement rate of 0.85 mm/min. Each flexural data point is an average of at least seven tests. Dynamic mechanical thermal analyses (DMA Q800, TA Instruments) in three-point bending mode was used to measure the storage and loss moduli and the glass transition temperature (T_g) in the 25–160 °C range at a heating rate of 5 °C /min and 1 Hz. A preload of 0.01 N and a maximum strain of 0.05% were applied on the specimens. Each data point is an average of at least five tests.

3. Results and discussion

In order to test the hypothesis that addition of CNC on the GF/epoxy interphase can improve the mechanical properties of the composites, composites with uncoated and CNC coated GF were compared in terms of mechanical properties. First, it was determined whether or not the CNC alter the GF/epoxy interphase (a region around the GF in which the mechanical properties differ from the bulk mechanical

properties of the composite) and the optimum CNC concentration needed to increase the properties of the composites with no weight penalty.

3.1. CNC coatings on GF

GF rovings were coated with CNC according to the process described in Section 2.2. As shown in Figure 1a, 1b, a thin layer of CNC is deposited on the GF surface as a result of physical absorption (e.g. hydrogen bonding of the accessible –OH side groups on the CNC surface as described in Chen *et al.* [25]). Of interest is how the CNC coated the chopped GF rovings, as well as individual GF within the rovings. To observe the surface of individual GF, the GF were pulled out from the chopped GF rovings after the coating process. As shown in Figure 1c–e, the uncoated GF has a smooth surface, while the surface of CNC coated GF is rougher, indicating that CNC have been deposited on the GF surface. Additionally, the coated GF surface roughness appears to increase with the CNC coating deposition concentration, suggesting that more CNC are deposited on the GF surface. Some of the roughness features in the CNC coating on individual GF is likely associated with the CNC coating process using the GF rovings as opposed to individual GF, in which GF-GF meniscus formation within GF rovings during drying would cause deposition variations. In addition, deformation of the CNC coating would occur when separating GF from other GF within the GF roving.

The implications of these observations are that although GF rovings are used in the coating process, the CNC suspension can penetrate the GF rovings and coat individual GF. The differences in the GF surface roughness of individual GF may subsequently alter the stress transfer efficiency at the GF/epoxy interphase in SFF testing that uses individual GF, as seen in Section 3.2, but it is unclear to what extent, roughness will influence the results of the composites testing where much larger-sized chopped GF rovings are used.

3.2. Interfacial properties

Figure 2a shows an optical image of a post-tested SFF 0.5S-GF test coupon with three fracture events along the GF, where the distance between each fracture represents an individual fiber fragment length. The average fiber critical length ($= 4\bar{l}/3$, where is the average of several individual fiber fragment lengths), and the calculated IFSS, as a function of
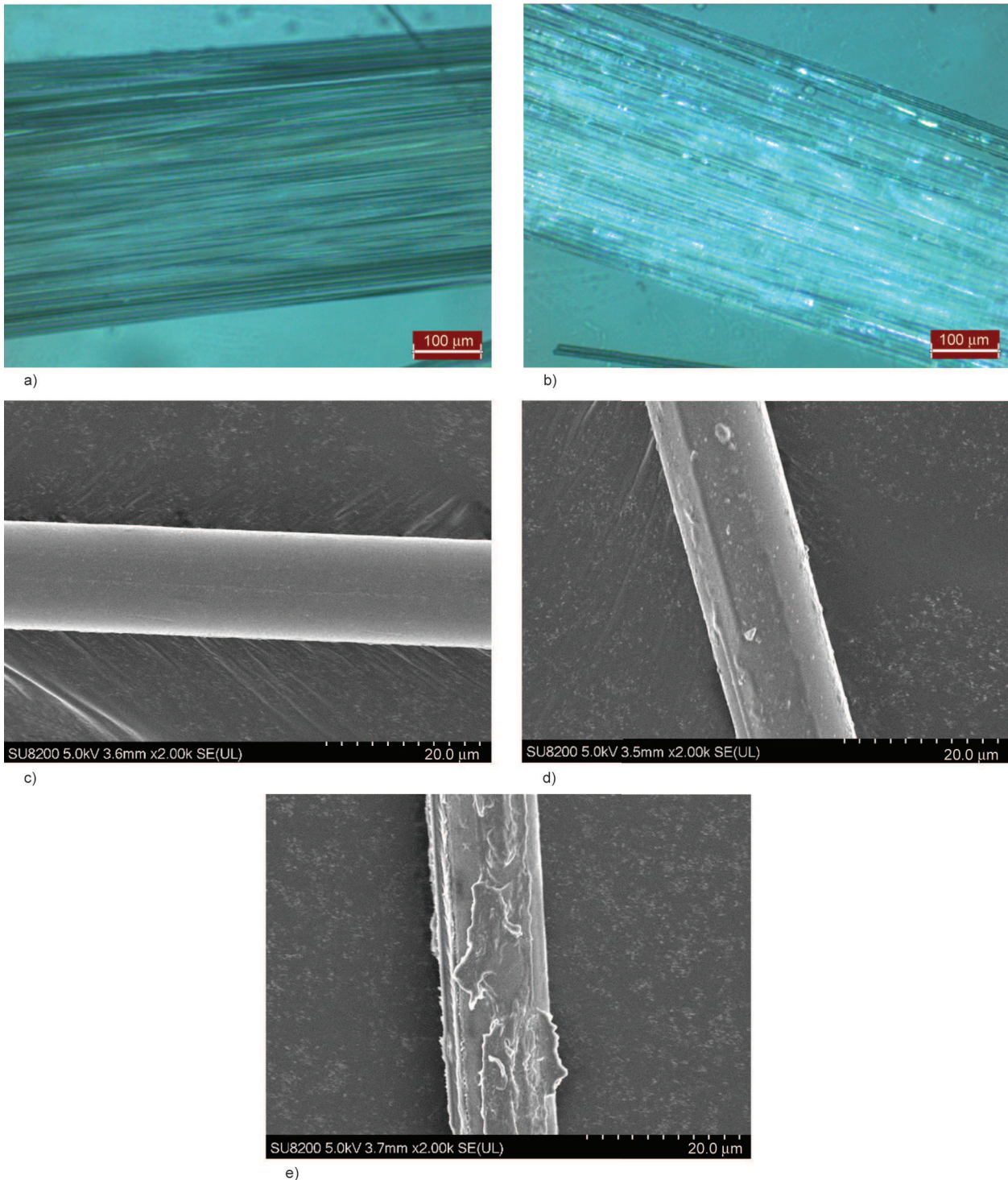
Figure 1. Polarized micrographs (polarized light of 95°) of chopped GF rovings, (a) uncoated, and (b) coated 1.5S-GF; SEM images of single GF coated with CNC (c) 0 wt%, (d) 1 wt % and (e) 5 wt% suspensions

CNC coating concentration on the GF surface are shown in Figure 2b. Changes in both the IFSS and fiber critical length when the GF are coated indicate that the load transfer across the GF/CNC/epoxy interphase has been modified. Possible mechanism are mechanical interlocking between the eGF and epoxy due to the increased GF surface roughness and corresponding increased surface area, as well as differ-ent chemical affinity as a result of the GF having a CNC coating. There appears to be an optimum con-dition i.e. 1S-GF for which the IFSS reaches a max-imum, that corresponds to ~69% increase compared to that of the uncoated GF/epoxy specimen. As the concentration of CNC suspension increases, i.e. for 1.5S-GF, 2S-GF, 3S-GF, and 5S-GF SFF cases, there is a reduction in IFSS. The lower IFSS suggest that

a)

b)
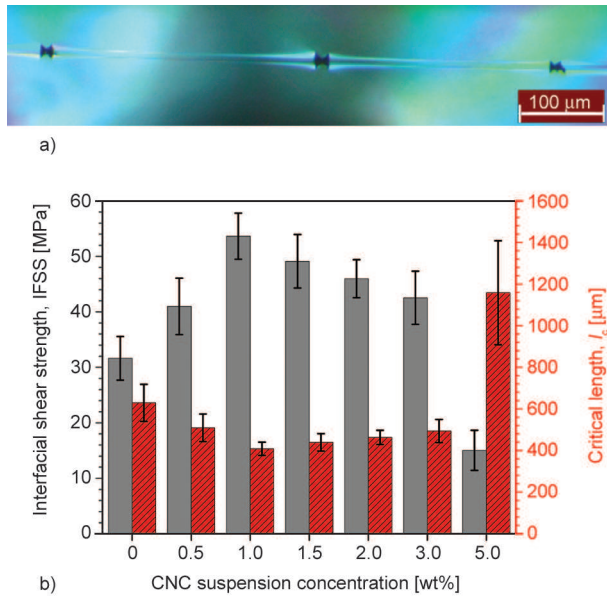
Figure 2. SFF results: (a) Polarized light micrograph of a single GF coated with 0.5CNC-GF (polarized light 80°) embedded in epoxy showing representative critical fragmentation length, (b) Interfacial shear strength (solid gray bars) and critical fragmentation length (striped red bars) for composites as a function of CNC suspension concentration. Error bars are 1 standard deviation.

the CNC coatings have reduced the stress transfer efficiency at the GF/CNC/epoxy interphase. A few mechanisms are plausible, which can be based on the quality of the CNC coating and associated interfacial defects. As shown in Figure 1e, 5S-GF tend to have rougher surfaces and other defects within the CNC coating, e.g. formation of CNC multilayer that can potentially result in slippage of CNC with respect to each other and reduction of the stress transfer efficiency.

There were various fracture modes observed for the specimens with different CNC coating contents, suggesting that there is a change in the interfacial properties at the GF-epoxy interface caused by the CNC coatings. According to Mullin and Mazzio [30], fracture modes in single fiber fragmentation tests can be categorized to three modes based on the fiber/matrix level of adhesion; *mode i:* following the fiber break, a disk shaped matrix crack occurs as a result of normal stresses, shown in Figure 3a, suggesting a strong interface; *mode ii:* following the fiber break, a double cone-shaped matrix crack with 45° angle occurs as a result of shear stresses, shown in Figure 3b, referring to a type of interface in which the matrix shear strength is lower than its tensile strength; and *mode iii:* fiber break is instantly followed by a lim-
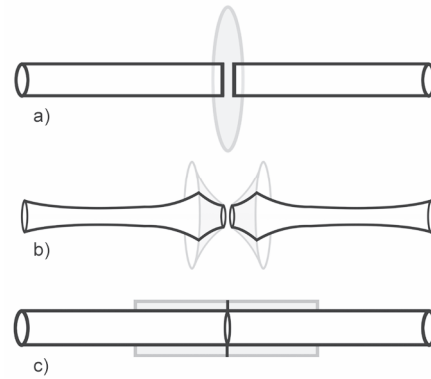

Figure 3. Three modes of fracture in matrix in single fiber fragmentation test; (a) *mode i:* disk-shaped fracture of matrix referring to strong interface, (b) *mode ii:* double-cone matrix fracture suggesting a matrix with a low shear strength, and (c) *mode iii:* debonding of fiber and matrix inferring a weak interface

ited interfacial debonding due to shear stress, shown in Figure 3c, implying a weak interface type. The debonded interface cannot transfer any load from matrix to the fiber and the length of debonding can be used as an indicator of fiber stress and interfacial energy [31]. For epoxies, concurrent disk-shaped and cone-shaped matrix cracks formed at the fiber ends are commonly seen. In the current study, combined fracture *modes i* and *ii* along with few cracks of mode iii were observed for the GF and 0.5S-GF samples, as shown in Figure 4a–c. The fracture mode for 1S-GF, 1.5S-GF, 2-S-GF, and 3S-GF SFF samples were combined modes i and ii, shown in Figure 4d, 4e, suggesting a stronger interfacial bonding compared to uncoated-GF/epoxy samples. The fracture modes for 5S-GF samples were *mode ii* and *mode iii;* however, it was observed that the debonded areas increased compared to that of uncoated GF/epoxy samples implying a weaker interface and a lower IFSS value, as seen in Figure 2.

3.3. Specific density, CNC content and thermal stability

GF/epoxy composites were made using the following chopped GF rovings: GF, 0.5S-GF, 1S-GF, 1.5S-GF and 2S-GF. The density for all these composites was found to be 1.3 ± 0.03 g/cm^3, delineating that the CNC coatings did not significantly increase the composite weight and is consistent with the small CNC wt% deposited on the GF.

The CNC wt% within chopped GF rovings as well as within the composites was correlated with the CNC suspension concentration used in the coating
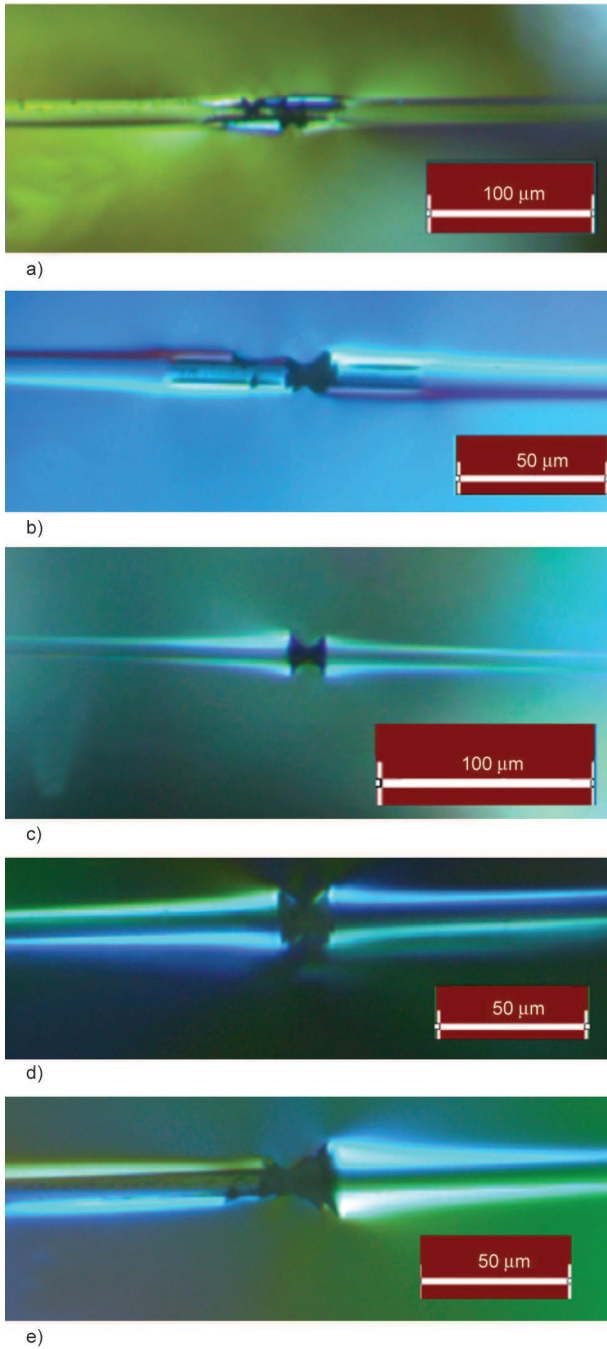
Figure 4. Optical polarized light micrographs of SFF specimens after tensile test showing fracture events at the GF: (a) GF/epoxy (polarized light of 75°), (b) 0.5S-GF (polarized light 120°), (c) 0.5S-GF (polarized light 80°), (d) 1S-GF (polarized light 90) and (e) 2S-GF (polarized light 75°)

process as shown in Figure 5. The uncoated GF used as the baseline for determining the CNC wt% on the coated GF. The CNC content on the GF surface increased from 0.44±0.07 to 3.58±0.02 wt% for 0.5 and 5 CNC wt% suspensions, respectively. It is noted that the CNC wt% on the GF surface is not increasing linearly with the CNC suspension concentration
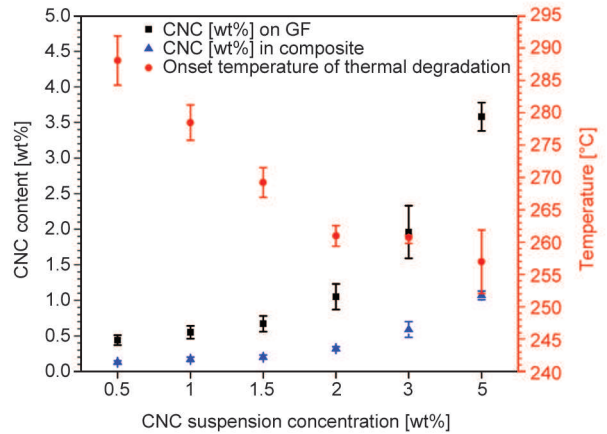
Figure 5. CNC suspension concentration on the GF and composites and onset temperature of thermal degradation for CNC-coated GF as a function of CNC concentration in the aqueous solution. Error bars are 1 standard deviation

used in coating process, e.g. the CNC content on the GF coated with 1 CNC wt% solution is not twice of that of the GF coated with 0.5 CNC wt%.

The thermal stability of the CNC-coated GF is also plotted in Figure 5. The onset temperature of thermal degradation of the neat CNC was 234.23±0.67 °C. All the coated-GF degraded above this temperature (lower bound). The onset temperature of thermal degradation decreased with the increase in the CNC content on the GF which was expected as it should reach the lower bound with the increase in the CNC content.

3.4. Fracture surface morphology

The fracture surface of the composites failed in the tensile testing was studied using a FE-SEM. As shown in Figure 6a, 6b, the main failure mechanism for uncoated GF epoxy composites was interfacial debonding as indicated by the clean pulled-out fibers devoid of the matrix, suggesting weak fiber-matrix adhesion. In contrast, the failure mechanisms for CNC-coated GF epoxy composites were concurrent matrix cracking, fiber breakage and interfacial debonding, shown in Figure 6c, 6d, implying an improvement in the interfacial bonding as a result of CNC coating. Also, matrix residues on the pulled-out fibers (Figure 6d) and a rough fracture surface for both 1S-30GF/epoxy and 2S-30GF/epoxy composites compared to the smooth fracture surface for the uncoated GF/epoxy composites suggest a better adhesion between fiber and matrix.
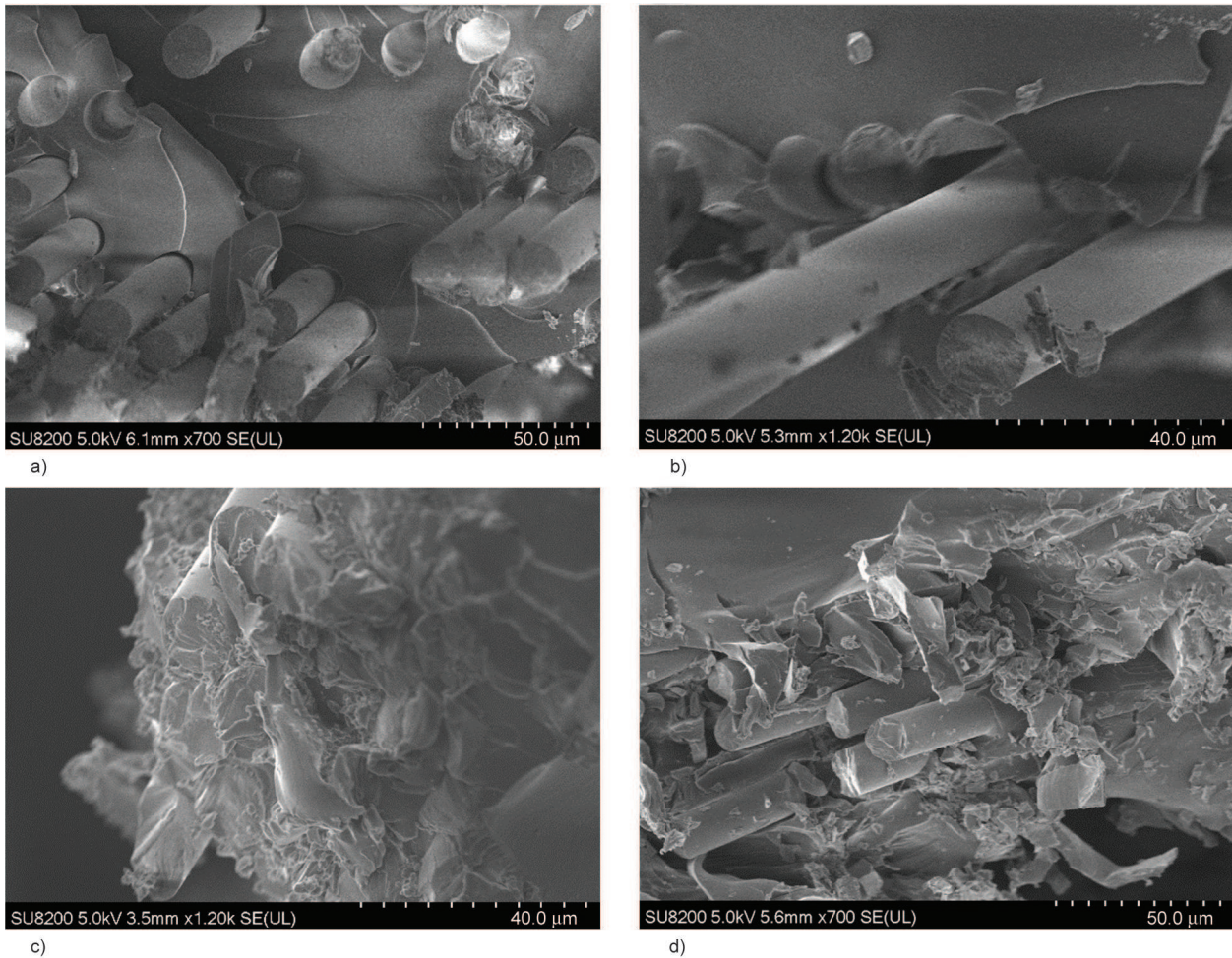
Figure 6. SEM images for fracture surface of different epoxy composites; (a) and (b) uncoated 30GF/epoxy, (c) 1S-30GF/epoxy, (d) 2S-30GF/epoxy

3.5. Tensile and flexural properties

The effect of the CNC content on the tensile and flexural properties of CNC coated GF/epoxy composites are plotted in Figure 7. The incorporation of CNC as a coating to GF enhances the elastic modulus by ~10% for 1S-30GF/epoxy and 1.5S-30GF/epoxy composites with respect to that of uncoated GF/epoxy. This may be a result of the increase in the stiffness of the GF/epoxy interphase due to presence of CNC as according to Hashin [32], for an imperfect interface (i.e. displacement discontinuity across the interface) an interfacial stiffness parameter can be defined where a higher value of this parameter suggests a faster rate of stress transfer across the fiber/matrix interface and thus a higher modulus for the composite [33]. Although this hypothesis could not be validated in this study, Gao and Mäder [34] showed how increases in the apparent modulus at the GF/epoxy interphase resulted in increase in the composite macroscopic modulus, which can be qualita-

tively linked to the current study where enhancement in the apparent modulus of the GF/epoxy interphase resulted in higher macroscopic modulus of the composites. In addition, the tensile strength increased for 1S-30GF/epoxy (~10%) and 1.5S-30GF/ epoxy composites with respect to that of 30GF/ epoxy composites. This increase reflects the higher IFSS (see Figure 2) inferring stronger interfacial interactions and better stress transfer across the fiber/CNC/epoxy interphase as also reported elsewhere [35]. The tensile strength of the 2S-30GF/epoxy composite was ~12% lower despite having higher IFSS compared to that of 30GF/epoxy. This may be due to various mechanisms including void formation within and around the GF rovings as a result of incomplete infiltration of the epoxy within the coated GF rovings and breaking of the CNC coating as it becomes more brittle with increase of its thickness. The strain at break had a trend similar to that of the strength, where the strain at break in 1S-30GF/epoxy and
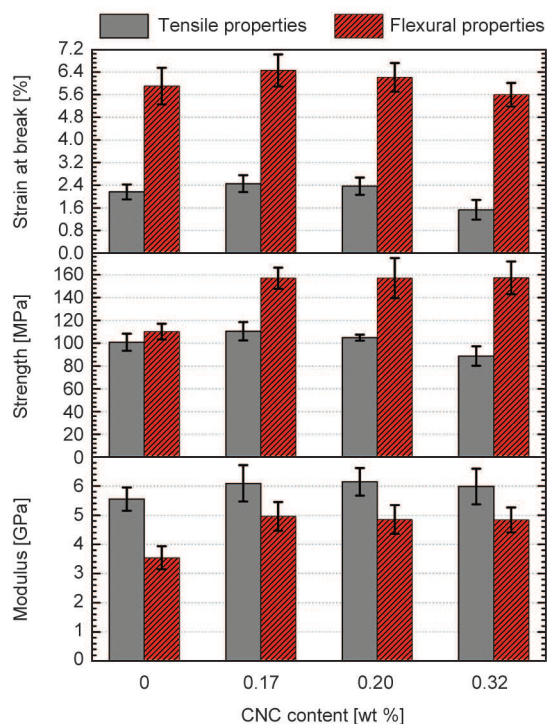
Figure 7. Effect of the CNC content (wt% in composite) in CNC-coated 30GF/epoxy composites on tensile and flexural properties. Error bars are 1 standard deviation

1.5S-30GF/epoxy composites increased by ~14 and ~10% while that of 2S-30GF/epoxy decreased compared to uncoated 30GF/epoxy composites.

For composites made with 1S-GF and 1.5S-GF, the flexural modulus and strength increased by ~40 and ~42%, respectively, with respect to those of uncoated 30GF/epoxy composites indicating better adhesion between the glass fiber and epoxy due to higher IFSS, and stress transfer at a faster rate as discussed above. The strain at break follows similar trend to that of axial strain, where it increased by ~10% for 1S-30GF/epoxy.

It is noted that the enhancement in flexural properties was larger than the enhancement in tensile properties at the same CNC content. The differences in elastic moduli and strengths may result from the difference in tensile and flexural moduli of the epoxy resin. In most epoxy systems, the tensile modulus is higher than the flexural modulus while the tensile strength is lower than the flexural strength (e.g. report by Kinsella *et al.* [36]). In addition, for the strength and the strain at break, a different mechanism may be at play since these properties are typically dominated by defects within the composite. For materials with defect mediated failure, strength and strain at break properties will be dependent on the number of

defects, their size, where they are located with respect to the high stressed portions of the sample and volume subjected to the highest tensile stress. For the samples used in tensile and flexural testing, it is likely that the defect numbers and size distributions are similar in all samples tested; however, in the tensile coupons, all the material in the gauge portion experiences the maximum stress as compared to the to the flexural sample configuration in which only the outer surfaces of specimen are subjected to the maximum stress. With this in mind, for the tensile testing, there is higher probability that a larger number of defects is located in the high tensile stressed portions of the sample and because of this, a lower applied load would be needed to induce fracture. Moreover, the larger enhancement of the flexural properties compared to the enhancement of the tensile properties can be due to the fact that the glass fibers are randomly oriented in plane so that in tensile loading only a portion of their length along the direction of the applied load will bear loading. In case of the three-point bending, the load direction is out of plane and all the fibers (across the whole length) are available to take up load and therefore enhancement in the flexural properties would be higher.

3.6. Dynamic thermo-mechanical properties

The dynamic thermo-mechanical properties of the composites below and above T_g are presented in Table 1. At 25 °C, the incorporation of CNC as a coating to GF rovings was shown to enhance the storage modulus (E') for the 1S-30GF/epoxy and 1.5S-30GF/ epoxy composites, but lower the storage modulus for 2S-30GF/epoxy composites, as compared to that of 30GF/epoxy composites. The increase in the storage modulus at 25 °C can be attributed to the stiffening of the GF/CNC/matrix interphase due to presence of CNC particles, as discussed in Section 3.5. Although the average value of the rubbery moduli (E_r: the storage modulus above T_g) measured at 90 °C for the composites containing CNC-coated GF were lower than that of the composite incorporating uncoated GF, due to the large standard deviation in measured properties, it was concluded that coating of the GF with CNC did not impact the rubbery modulus. Studies have shown that addition of CNC in the epoxy increased the rubbery modulus due to the formation of a network of mechanically percolated CNC [16, 18, 21]. However, it is expected that CNC on the surface of the GF do not form a percolated network

Table 1. Viscoelastic properties of CNC-GF/epoxy composites in three-point bending mode

Composite	E' at 25°C [MPa]	E_r at 90°C [MPa]	T_g [°C]	$\tan\delta$ at T_g
30GF/epoxy	4932±586	250±21	50.3±0.7	0.61±0.06
1S-30GF/epoxy	5213±543	224±31	49.4±0.5	0.61±0.02
1.5S-30GF/epoxy	5614±695	228±22	50.2±0.8	0.65±0.07
2S-30GF/epoxy	4634±257	243±38	49.5±1.1	0.59±0.02

E': storage modulus
E_r: rubbery modulus
T_g: glass transition temperature measured in $\tan\delta$ peak
$\tan\delta$: value of $\tan\delta$ peak
Note: Error bars are 1 standard deviation.

within the polymer matrix. Hence, CNC cannot strongly impact the polymer chain segmental motion and consequently, the rubbery modulus. Presence of CNC has no effect on the $\tan\delta$ and the glass transition temperature (T_g).

4. Conclusions

This study demonstrated that introducing a small amount of CNC in the form of a coating on GF can enhance the IFSS and mechanical properties of short GF/epoxy composites without increasing the weight. The proposed mechanism for altering the composite properties is the improvement of the interfacial adhesion and stress transfer ability and rate across the GF/epoxy interphase due to the CNC coating. Single fiber fragmentation tests showed that coating of GF up to 1.96 wt% (coated in 3 wt% aqueous CNC suspension) was able to increase IFSS; however, the highest increase in IFSS (by 69%) was achieved for CNC coating of 0.55 wt% (coated in CNC 1 wt% aqueous CNC suspension). The CNC-GF/epoxy composites produced using CNC coated chopped GF roving showed increases in tensile and flexural properties, which were attributed to the increase in IFSS associated with the application of the GF coatings. The greatest improvement in properties occurred when CNC coating on GF rovings equal to 0.17 wt% of composite was used. Specifically, the tensile elastic modulus and strength by ~10%, tensile strain at break by ~14%, the flexural modulus and strength by ~40% and flexural strain at break by ~10%. It is noted that the CNC coating did not significantly alter the rubbery modulus, T_g and $\tan\delta$. The results highlight that the use of CNC coatings on GF, is a possible approach for enhancing the mechanical properties of GF/epoxy composites with no weight penalty.

References
[1] U. S. Department of Energy: The quadrennial technology review. p.39 (2011).
[2] Dorigato A., Morandi S., Pegoretti A.: Effect of nanoclay addition on the fiber/matrix adhesion in epoxy/ glass composites. Journal of Composite Materials, **46**, 1439–1451 (2012).
DOI: 10.1177/0021998311420311
[3] Pedrazzoli D., Pegoretti A., Kalaitzidou K.: Synergistic effect of exfoliated graphite nanoplatelets and short glass fiber on the mechanical and interfacial properties of epoxy composites. Composites Science and Technology, **98**, 15–21 (2014).
DOI: 10.1016/j.compscitech.2014.04.019
[4] Pedrazzoli D., Pegoretti A.: Silica nanoparticles as coupling agents for polypropylene/glass composites. Composites Science and Technology, **76**, 77–83 (2013).
DOI: 10.1016/j.compscitech.2012.12.016
[5] Gao S-L., Mäder E., Plonka R.: Nanocomposite coatings for healing surface defects of glass fibers and improving interfacial adhesion. Composites Science and Technology, **68**, 2892–2901 (2008).
DOI: 10.1016/j.compscitech.2007.10.009
[6] Luo J-J., Daniel I. M.: Characterization and modeling of mechanical behavior of polymer/clay nanocomposites. Composites Science and Technology, **63**, 1607–1616 (2003).
DOI: 10.1016/S0266-3538(03)00060-5
[7] Hubbe M. A., Rojas O. J., Lucia L. A., Sain M.: Cellulosic nanocomposites: A review. BioResources, **3**, 929–980 (2008).
[8] Habibi Y., Lucia L. A., Rojas O. J.: Cellulose nanocrystals: Chemistry, self-assembly, and applications. Chemical Reviews, **110**, 3479–3500 (2010).
DOI: 10.1021/cr900339w
[9] Moon R. J., Martini A., Nairn J., Simonsen J., Youngblood J.: Cellulose nanomaterials review: Structure, properties and nanocomposites. Chemical Society Reviews, **40**, 3941–3994 (2011).
DOI: 10.1039/C0CS00108B
[10] Roman M.: Toxicity of cellulose nanocrystals: A review. Industrial Biotechnology, **11**, 25–33 (2015).
DOI: 10.1089/ind.2014.0024
[11] Hansen, F., Brun, V., Keller, E., Wegner, T., Meador, M., Friedersdorf, L.: Cellulose nanomaterials-A Path towards commercialization. USDA Forest Service Workshop report, Washington (2014).
[12] Beck-Candanedo S., Roman M., Gray D. G.: Effect of reaction conditions on the properties and behavior of wood cellulose nanocrystal suspensions. Biomacromolecules, **6**, 1048–1054 (2005).
DOI: 10.1021/bm049300p

[13] Lee K-Y., Aitomäki Y., Berglund L. A., Oksman K., Bismarck A.: On the use of nanocellulose as reinforcement in polymer matrix composites. Composites Science and Technology, **105**, 15–27 (2014).
DOI: 10.1016/j.compscitech.2014.08.032

[14] Xu S., Girouard N., Schueneman G., Shofner M. L., Meredith J. C.: Mechanical and thermal properties of waterborne epoxy composites containing cellulose nanocrystals. Polymer, **54**, 6589-6598 (2013).
DOI: 10.1016/j.polymer.2013.10.011

[15] Ruiz M. M., Cavaillé J. Y., Dufresne A., Graillat C., Gérard J-F.: New waterborne epoxy coatings based on cellulose nanofillers. Macromolecular Symposia, **169**, 211–222 (2001).
DOI: 10.1002/1521-3900(200105)169:1<211::AID-MASY211>3.0.CO;2-H

[16] Tang L., Weder C.: Cellulose whisker/epoxy resin nanocomposites. ACS Applied Materials and Interfaces, **2**, 1073–1080 (2010).
DOI: 10.1021/am900830h

[17] Lu J., Askeland P., Drzal L. T.: Surface modification of microfibrillated cellulose for epoxy composite applications. Polymer, **49**, 1285–1296 (2008).
DOI: 10.1016/j.polymer.2008.01.028

[18] Girouard N., Schueneman G. T., Shofner M. L., Meredith J. C.: Exploiting colloidal interfaces to increase dispersion, performance, and pot-life in cellulose nanocrystal/waterborne epoxy composites. Polymer, **68**, 111–121 (2015).
DOI: 10.1016/j.polymer.2015.05.009

[19] Gabr M. H., Elrahman M. A., Okubo K., Fujii T.: A study on mechanical properties of bacterial cellulose/epoxy reinforced by plain woven carbon fiber modified with liquid rubber. Composites Part A: Applied Science and Manufacturing, **41**, 1263–1271 (2010).
DOI: 10.1016/j.compositesa.2010.05.010

[20] Peng S. X., Moon R. J., Youngblood J. P.: Design and characterization of cellulose nanocrystal-enhanced epoxy hardeners. Green Materials, **2**, 193–205 (2014).
DOI: 10.1680/gmat.14.00015

[21] Ansari F., Galland S., Johansson M., Plummer C. J. G., Berglund L. A.: Cellulose nanofiber network for moisture stable, strong and ductile biocomposites and increased epoxy curing rate. Composites Part A: Applied Science and Manufacturing, **63**, 35–44 (2014).
DOI: 10.1016/j.compositesa.2014.03.017

[22] Barari B., Ellingham T. K., Ghamhia I. I., Pillai K. M., El-Hajjar R., Turng L-S., Sabo R.: Mechanical characterization of scalable cellulose nano-fiber based composites made using liquid composite molding process. Composites Part B: Engineering, **84**, 277–284 (2016).
DOI: 10.1016/j.compositesb.2015.08.040

[23] Miao C., Hamad W. Y.: Cellulose reinforced polymer composites and nanocomposites: A critical review. Cellulose, **20**, 2221–2262 (2013).
DOI: 10.1007/s10570-013-0007-3

[24] Karger-Kocsis J., Mahmood H., Pegoretti A.: Recent advances in fiber/matrix interphase engineering for polymer composites. Progress in Materials Science, **73**, 1–43 (2015).
DOI: 10.1016/j.pmatsci.2015.02.003

[25] Chen Y., Zhou X., Yin X., Lin Q., Zhu M.: A novel route to modify the interface of glass fiber-reinforced epoxy resin composite *via* bacterial cellulose. International Journal of Polymeric Materials and Polymeric Biomaterials, **63**, 221–227 (2013).
DOI: 10.1080/00914037.2013.830250

[26] Postek M. T., Moon R. J., Rudie A. W., Bilodeau M. A.: Production and applications of cellulose. Tappi Press. Peachtree Corners (2013).

[27] Rich M. J., Drzal L. T., Hunston D., Holmes G., McDonough W.: Round robin assessment of the single fiber fragmentation test. in 'Procedings of the American Society for Composites 17th Technical Conference, West Lafayette, USA' p.10 (2002)..

[28] Kelly A., Tyson W.: Tensile properties of fibre-reinforced metals: Copper/tungsten and copper/molybdenum. Journal of the Mechanics and Physics of Solids, **13**, 329–350 (1965).
DOI: 10.1016/0022-5096(65)90035-9

[29] Klein C. A.: Characteristic strength, Weibull modulus, and failure probability of fused silica glass. Optical Engineering, **48**, 113401/1–113401/11 (2009).
DOI: 10.1117/1.3265716

[30] Mullin J. V., Mazzio V. F.: The effects of matrix and interface modification on local fractures of carbon fibers in epoxy. Journal of the Mechanics and Physics of Solids, **20**, 391–394 (1972).
DOI: 10.1016/0022-5096(72)90016-6

[31] Zhou X-F., Nairn J. A., Wagner H. D.: Fiber–matrix adhesion from the single-fiber composite test: Nucleation of interfacial debonding. Composites Part A: Applied Science and Manufacturing, **30**, 1387–1400 (1999).
DOI: 10.1016/S1359-835X(99)00043-3

[32] Hashin Z.: Thermoelastic properties of fiber composites with imperfect interface. Mechanics of Materials, **8**, 333–348 (1990).
DOI: 10.1016/0167-6636(90)90051-G

[33] Nairn J. A.: Generalized shear-lag analysis including imperfect interfaces. Advanced Composites Letters, **13**, 263–274 (2004).

[34] Gao S-L., Mäder E.: Characterisation of interphase nanoscale property variations in glass fibre reinforced polypropylene and epoxy resin composites. Composites Part A: Applied Science and Manufacturing, **33**, 559–576 (2002).
DOI: 10.1016/S1359-835X(01)00134-8

[35] Madhukar M. S., Drzal L. T.: Fiber-matrix adhesion and its effect on composite mechanical properties: II. Longitudinal (0°) and transverse (90°) tensile and flexure behavior of graphite/epoxy composites. Journal of Composite Materials, **25**, 958–991 (1991).
DOI: 10.1177/002199839102500802

[36] Kinsella M., Murray D., Crane D., Mancinelli J., Kranjc M.: Mechanical properties of polymeric composites reinforced with high strength glass fibers. in '33rd International SAMPE Technical Conference, Seattle, USA' Vol. 33, 1644–1657 (2001).

Multifunctional e-spun colloidal nanofiber structures from various dispersed blends of PVA/ODA-MMT with PVP/ODA-MMT, poly(VP-*alt*-MA) and AgNPs incorporated polymer complexes as electro-active platforms

U. Bunyatova[1]*, Z. M. O. Rzayev*[2]**, M. Şimşek*[2]

[1]Department of Biomedical Engineering, Faculty of Engineering, Baskent University, Baglica, 06810 Ankara, Turkey
[2]Institute of Science and Engineering, Division of Nanotechnology and Nanomedicine, Hacettepe University,
 06800 Ankara, Turkey

Abstract. This work presented a new approach to fabricate polymer nanocomposites films with nanofiber structures from solution blends of poly(vinyl alcohol) + octadecyl amine-montmorillonite (ODA-MMT) (matrix) with poly(N-vinylpyrrolidone) + ODA-MMT (partner-1), poly(N-vinylpyrrolidone-*alt*-maleic anhydride) ((poly(VP-*alt*-MA)) + (ODA-MMT) (partner-2) and their silver (Ag)-carrying polymer complexes by electrospinning. Chemical and physical structures, surface morphologies, thermal behaviors, electrical conductivity and thermal resistance parameters of nanofiber structures were investigated. Poly(VP-*alt*-MA) was used both as a crosslinker and a donor of the hydrophilic groups such as –COOH and –NH–C=O amide from pyrrolidone ring. Reactive poly(VP-*alt*-MA), *in situ* generated Ag nanoparticles (AgNPs) and original partner polymer had an significant effect on the morphology and diameter distribution of nanofibers. High and excellent conductive behaviors were observed for the homopolymer and copolymer of VP based fiber structures, respectively. Upon successive chemical cross-linking of the nanofiber structures by reactive partner copolymer, the conductivity of nanofiber films as electro-active platforms dramatically increased to $3.90 \cdot 10^{-2}$ S·cm^{-1} at room temperature. Comparative analysis results also indicated that electrical properties strongly depended on the loaded reactive organoclay and *in situ* generated AgNPs.

Keywords: polymer composites, PVA, PVP, electrospinning, conductivity.

1. Introduction

Recent studies have focused on the fabrication of electrospun (e-spun) nanofibers from solution blends of various polymers and/or polymer nanocomposites as binary multifunctional matrix/partner polymer systems [1–7]. Polymer nanofibers fabricated by electrospinning method have great importance because of their unique properties, i.e. high surface area-to-volume ratio, nanoscale fiber diameter and nanoporous surface morphology [8, 9].

Water-soluble poly(vinyl alcohol) (PVA) has important chemical and physical properties such as film- and fiber forming, emulsifying, surfactant and adhesion. PVA containing intra- and internal hydrogen bonding hydroxyl groups easily forms network and branched structures when it reacts with other functional polymers and compounds. It is also used to fabricate unique nanofiber compositions as a matrix polymer [10, 11]. Some properties of polymers such as thermal, mechanical, and optical properties are

---

significantly improved by adding an organoclay into a polymeric matrix [12, 13].

Due to their unique properties, homo- and co- polymers of N-vinyl-2-pyrrolidone (VP) have attracted considerable academic and industrial interest [14, 15]. Poly(N-vinylpyrrolidone) (PVP) receives special attention among the conjugated polymers due to its good environmental stability, easy processability and moderate electrical conductivity. The reactive pyrrolidone group of PVP easily forms complexes with many inorganic salts, synthetic or natural functional polymers, biomolecules and biomacromolecules. To synthesize alternating copolymers of VP with maleic anhydride (MA), the solution homogeneous or heterogeneous radical copolymerization is usually used by using various solvents such as benzene, toluene [16], and 1.4dioxane [17]. In our previous study [18], poly(N-vinylpyrrolidone-*alt*-maleic anhydride) (poly(VP-*alt*-MA)) was easily dissolved in water. This dissolution process was accompanied by the full hydrolysis of anhydride units and given rise to the formation of strong hydrogen bonding intermolecular fragments.

Conductivity and thermal resistance properties of solid polymer electrolytes can be improved with chemical cross-linking, grafting, graft copolymerization, functionalization of the polymer backbone and side-chains, polymer-polymer interactions and blending with other polymers and doping agents. PVA and PVP-based solid polymer electrolytes are potential materials exhibiting good charge storage capacity and dopant dependent electrical and optical properties. The conductivity of neat PVA nanofibers was reported to be $1.25 \cdot 10^{-15}$ S·cm^{-1} [19] compared with that of PVP ($7.42 \cdot 10^{-8}$ S·cm^{-1}) [20]. Hatta *et al.* [21] observed that solvent casting PVA/PVP thin-film solid electrolytes with a composition of 80% of PVA and 20% of PVP (v/v) exhibited the highest conductivity ($2.2 \cdot 10^{-7}$ S·cm^{-1}). The conductivity of this system enhanced to $1.5 \cdot 10^{-4}$ S·cm^{-1} when KOH (40%) was added. According to Inzelt *et al.* [22] conductivity of functional polymer systems depend on degree of chemical charges (such as dimerization, cross-linking, and ion-pair formation) and structural properties of chosen polymer systems, i.e. chain-segmental motions, changes in surface morphology and slow relaxation. In a study, Rajeswari *et al.* [23] prepared solvent casting polymer blend electrolytes with different concentrations of PVA and PVP. Maximum conductivity was found

$1.58 \cdot 10^{-6}$ S·cm^{-1} at room temperature for 70PVA: 30PVP (v/v) ratio without any doping agents. The authors also found that the conductivity increased to $5.49 \cdot 10^{-5}$ S·cm^{-1} with increasing medium temperature to 100 °C.

Besides their electrical conductivities, ionic conductivity of polymer electrolytes is fundamentally due to the covalent bonding between the polymer backbones with the ionizing groups. The electron donor group in the polymer generates dissolution to the cation constituent in dopant salt and then facilitates ion separation, causing ionic hopping mechanism. Thus, it generates the ionic conductivity. Novel ionic conductive e-spun PVA-chitosan nanofiber membranes were successfully fabricated using ionic liquids by Datta *et al.* [24]. Laforgue *et al.* [25] investigated ionic conductivity of Nafion-PVA and Nafion-poly (ethylene oxide). nanofibers and found that Nafion-PVA mats were found to be more conductive than the Nafion-PEO ones. Ionic conductivities of different polymer systems were also investigated by many researches [26–28].

Recently, many efforts have focused on the design and fabrication of polymer/metal nanoparticle (like silver) complexes due to their remarkable electronic, magnetic, catalytic, thermal and optical properties [29]. Basic principle for the fabrication of silver nanoparticles (AgNPs) involves the reduction of metal salts like silver nitrate (AgNO$_3$) in an appropriate medium using various reducing agents and surfactants to produce colloidal suspensions integrated by nanoparticles [29–32]. Unlike elemental silver, silver salts easily dissolve in water, and they increase the rate of Ag$^+$ ion formation over that from elemental silver. Hong *et al*. [33] prepared PVA nanofibers by electrospinning of PVA/AgNO$_3$ (1%, w/w) aqueous solutions, followed by short heat treatment. Nguyen *et al*. [34] successfully synthesized PVA nanofibers containing AgNPs (2% w/w) through a combination of microwave irradiation and electrospinning. Several studies showed that electrical and ionic conductivity of polymer electrolytes improved in the presence of silver salts [35–38]. PVP has also attracted a great deal of attention as a polymer that can stabilize *in situ* generated Ag nanoparticles [39, 40]. *In situ* formation of Ag-nanoparticles during electrospinning process of polymer-layered silicate nanocomposites and the formation of cross-linking fiber structures as colloidal electrolytes via phase separation processing have been scarcely investi-

gated in the presence of reactive alternating copolymer of VP.

One goal of this work was to develop synthetic pathways for the fabrication of novel polymeric fiber-based electro-active nanostructures with unique self-assembled electron transfer sites via electrospinning nanotechnology. PVA, PVP and poly(VP-*alt*-MA) based multifunctional matrix/partner polymer systems incorporated with an organoclay and AgNPs were fabricated and characterized. Another aim of this work was to evaluate effects of structural factors, origin and fraction of partner polymers, organoclay and *in situ* generated AgNPs on surface morphology and conductivity properties of nanofiber films. This work described physical and covalent functionalisation of octadecyl amine intercalated MMT clay via complexing with functional polymers (PVA, PVP) and AgNPs, and chemical cross-linking and amidization reactions of poly(VP-*alt*-MA) as reactive copolymer with octadecyl amine. All these *in situ* interactions occurred in the silicate layered region. Intercalated octadecyl amine as reactive surfactant and effective compatibilizer and reactive copolymer with alternating structures played important role in the functionalization of nanofiber composites (NFCs) before (dispersing solutions) and during electrospinning process to fabricate NFCs as electro-active nanofiber platforms. The developed approach may open up new possibilities to fabricate novel electrically conductive nanomaterials and devices for various engineering, electronic and nanotechnology applications.

2. Experimental
2.1. Materials
PVA (87–89% hydrolyzed, weight average molecular weight (M_w = 31 000–51 000 g/mol), poly(N-2-vinylpyrrolidone) (Bioshop-PVP504, high purity grade, average M_w = 40 000 Da), ODA-MMT (content of ODA surfactant-intercalant 25–30%, particle size of 8–10 μm, bulk density of 0.41 g/cm^3 and crystallinity of 52.8% (by, X-ray Diffraction), and silver nitrate (AgNO$_3$, 99.995%, m.p. 202 °C with decomposition, (density) d = 4.35 g/cm^3) were purchased from Sigma-Aldrich (Germany). N-vinyl-2-pyrrolidone (VP, Fluka, Germany) was purified by distillation under moderate vacuum. Maleic anhydride (MA, Aldrich, Germany) was purified by recrystallization from anhydrous benzene solution and sublimation in vacuum. Azobisisobutyronitrile
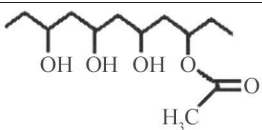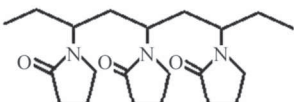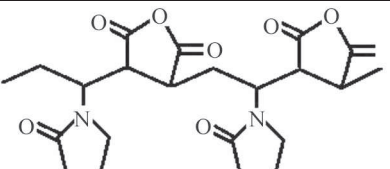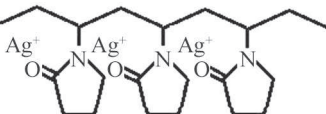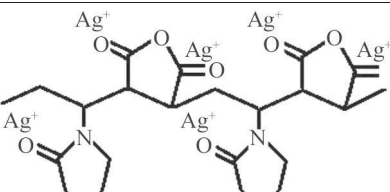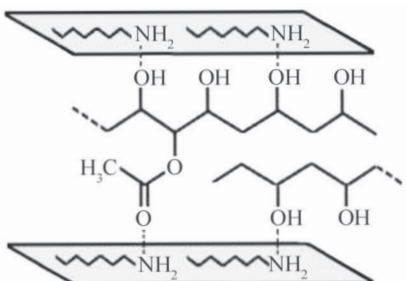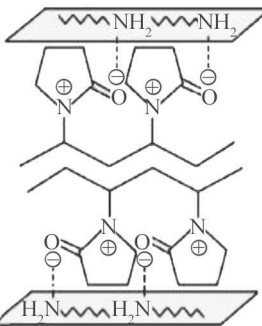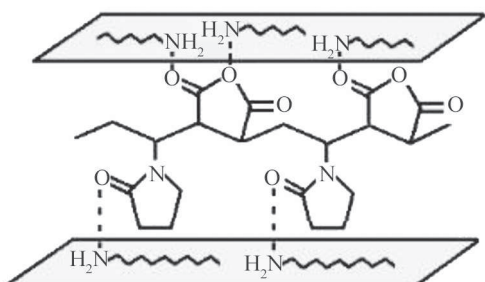
(AIBN, Fluka, Germany) as a radical initiator was recrystallized twice from methanol. All other solvents and reagents were analytical grade and used without purification. Chemical structures, compositions and assignments of the materials used in electrospinning are given in Table 1.

2.2. Synthetic procedures
Alternating partner copolymer of VP with MA (poly(VP-*alt*-MA) was prepared by radical-initiated copolymerization in the presence of AIBN as an initiator. The copolymerization was carried out in 1,4-dioxane solution into glass tube type micro reactor by using molar (1:1) monomer mixture under nitrogen flow at 65 °C. The copolymer was isolated from the resultant mixture, purified by twice precipitation in the presence of 1.4-dioxane solution with diethyl ether, and washed with benzene. After the last extraction by diethyl ether, the copolymer was isolated via centrifugation and dried at 40 °C under moderate vacuum to arrive constant weight. Synthesized poly(VP-*alt*-MA) had the following average characteristics: acid number of 460 mg KOH/g (by alkaline titration); nitrogen content of N = 7.15 mass% (by elemental analysis); molar monomer unit ratio of m_1 (VP)/m_2 (MA) = 1.12 (m_1 and m_2 are relative amounts of VP and MA (in mol) in the copolymer, respectively); intrinsic viscosity of $[\eta]_{in}$ = 0.79 dL/g in deionized water at 25 °C; glass transition temperature of T_g = 159,8 °C (by DSC); and ^{1}H-NMR spectra (in CHCl$_3$-d_1), δ (ppm): 1.30–1.83 CH$_2$ (backbone), 3.56–3.95 CH (CH–N backbone), 1.83–2.33 CH$_2$ and 2.95–3.54 2CH$_2$ (pyrrolidone ring) for VP unit and 4.08–4.45 CH (backbone) for anhydride unit.

PVA + ODA-MMT (3,5 mass%) nanocomposite as a matrix polymer was prepared by dispersed solution intercalating of PVA polymer chains between organoclay galleries in pure water medium under intensive mixing up to the formation of dispersed homogeneous viscous product at 40 °C for 3 h. Water solutions of PVP (homopolymer) + ODA-MMT (5 mass%) and alternating copolymer poly(VP-*alt*-MA) + ODA-MMT (5 mass%) as an intercalated partner nanocomposite were prepared by using a similar procedure. Matrix/partner polymer/AgNO$_3$ complexes were prepared by the addition of powder AgNO$_3$ (1 mass%) to the corresponding polymer solution and each complex was additionally mixed at room temperature for 1 h.

Table 1. Chemical structures, compositions and assignments of the materials used in electrospinning

Materials composition	Chemical structure	Assignments
PVA 60 and 80 mass%		reactive matrix polymer
PVP homopolymer 40 and 20 mass%		non-reactive partner polymer-1
Poly(VP-*alt*-MA) copolymer 40 and 20 mass%		alternating copolymer as a reactive partner polymer-2
Ag-carrying PVP complex in pure water solution 40 and 20 mass%		partner polymer-3
Ag-carrying poly(VP-*alt*-MA) copolymer complex in pure water solution, 40 and 20 mass%		reactive partner polymer-4
ODA-MMT clay 3.5 and 5.0 mas %	$CH_3—(CH_2)_{17}—NH_2$ / MMT	reactive organoclay-nanofiller
Intercalated PVA + ODA-MMT nanocomposite, 60 and 80 mass%		matrix nanocomposite
Intercalated PVP + ODA-MMT (3.5 mass%) nanocomposite 40 and 20 mass%		partner polymer nanocomposite-1
Intercalated Poly(VP-*alt*-MA) + ODA-MMT(5 mass%) nanocomposite 40 and 20 mass%		partner copolymer nanocomposite-2

2.3. Fabrication of nanofiber electrolytes

Solution blends of matrix/partner polymer composites with various volume ratios in the presence and absence of silver precursor were used to fabricate polymer electrolytes with nanofiber structures by electrospinning method. Electrospinning parameters such as polymer concentration, applied voltage, tip-to-collector distance, and flow rate were optimized for each series of nanofiber composites. Randomly oriented nanofibers were obtained by collecting fibers onto an aluminum foil fixed on stationary collector. First series of e-spun nanofibers was fabricated from PVA + ODA-MMT/PVP + ODA-MMT as a matrix/partner polymer composite system and its Ag-carrying composition. For second series of nanofibers, poly(VP-*alt*-MA) copolymer + ODA-MMT as a partner polymer was used. Table 2 presents the composition of matrix/partner polymers, their abbreviations, and optimized electrospinning conditions.

Characterization and methods

The Fourier transfer infrared (FT-IR) spectra were recorded on a FT-IR Nicolet 510 spectrometer in the range of 4000–400 cm^{-1} with a resolution of 4 cm^{-1}.
XRD tests were performed with a PANANALYTI-CAL X-ray diffractometer equipped with a CuK$_\alpha$ tube and Ni filter ($\lambda = 1.5406$ Å). The XRD diffractograms were measured at the angle of reflection in the range 1–70°. XRD data were analyzed using the DIFFRAC-Plus EVA and High Score Plus (particle size) programs, and the patterns were identified using the ICDD PDFMaint computer reference database.
Surface morphology of nanofibers was examined by using a Field Emission Scanning Electron Micro-scope (FESEM, ZEISS SUPRA 40). All specimens were freeze-dried and coated with a thin layer of platinum before testing. Average diameters of fibers were calculated from SEM images of minimum a hundred individual fibers by using ImageJ software (NIH, Bethesda, MD) for each sample. The formation of AgNPs in fibers was visualized by a high contrast transmission electron microscope (CTEM, FEI Tecnai G2 Spirit BioTwin). Energy-dispersive X-ray spectroscopy (EDX) analysis was used to investigate the formation of AgNPs on fiber surfaces.
Thermo gravimetric (TGA) and differential scanning calorimetric (DSC) analyses were performed by using EXTRAR600 TG-DTA6300 and Diamond DSC Perkin Elmer Thermal Analyzers at a linear heating rate of 10 °C/min under nitrogen flow. Samples were measured in a sealed alumina pan with a mass of about 10 mg. The thermal degradation temperature taking into account was the temperature at onset (T_{onset}) and the temperature at maximum weight loss ($T_{d\,(max)}$).
Electrical conductivity and thermal resistance of nanofiber samples as solid/colloidal electrolytes were measured by using a test chamber (JANIS VPF 100 cryostat). Current through thin fiber film was recorded with a Keithley 2400 current-voltage measurement system. Square-shaped samples (0.25 cm^2) with four contact points at the corners were prepared to carry out conductivity measurements which were done according to the van der Pauw method. Experiments were conducted in temperature range of 20–50 °C with 1 °C steps (Keithley 6487 Picoammeter/Voltage source) and pressure range of 50–800 Torr (6.67 to 106.7 kPa). Sample temperature was monitored regularly by using a Pt 100 sensor close to the sample and measured with Lakeshore

Table 2. Compositions of matrix/partner polymer, their abbreviations, and electrospinning conditions

PVA (9%, w/v) + ODA-MMT (3.5%, w/w)/PVP (9%, w/v) + ODA-MMT (5%, w/w) [Matrix/partner]		
Matrix/partner ratio (v/v)	**Abbreviation**	**Electrospinning conditions**
(6/4)	NFC-1	23.5 kV; 0.7 mL/h; 17 cm
(8/2)	NFC-2	23.5 kV; 0.7 mL/h; 15 cm
(8/2)+AgNO$_3$ (1%, w/w)	NFC-2/AgNPs	28 kV; 0.5 mL/h; 17 cm
PVA (9%, w/v) + ODA-MMT (3.5%, w/w)/poly(VP-*alt*-MA) (9%, w/v) + ODA-MMT (5%, w/w) [Matrix/partner]		
Matrix/partner ratio (v/v)	**Abbreviation**	**Electrospinning conditions**
(6/4)	NFC-3	23 kV; 0.7 mL/h; 15 cm
(8/2)	NFC-4	21 kV; 0.7 mL/h; 15 cm
(8/2) + AgNO$_3$ (1%, w/w)	NFC-4/AgNPs	23.5 kV; 0.7 mL/h; 17 cm

model 331-temperature controller with sensitivity of ±0.1 °C. All measurements were performed with a PC through a GPIB converter card.

3. Results and discussion
3.1. Synthetic pathways

The matrix nanocomposite was fabricated by intercalating of PVA between ODA-MMT organoclay tetragonal 1:2 layers through –OH…NH₂– complex formation of hydroxyl groups of PVA with primary amine groups of octadecylamine surfactant-intercalant. First intercalated partner nanocomposite (PVP + ODA-MMT) was prepared through physical interaction (–C=O…NH₂– complex-formation) of carbonyl/amine groups of PVP (pyrrolidone unit) and ODA-MMT (amine), respectively. Second partner copolymer nanocomposite, poly(VP-*alt*-MA) + ODA-MMT, was synthesized under similar intercalating conditions. In order to obtain Ag-carrying matrix/partner nanocomposite complex, certain amount of AgNO₃ was added to solution of matrix/partners nanocomposite and the resultant mixture was additionally mixed for 1 hour. To fabricate e-spun nanofibers, various solution blends of matrix/partner polymer nanocomposites at different ratios (10/0, 8/2 and 6/4 v/v) were used.

Synthetic pathways of nanocomposite nanofibers and chemistry of polymer-polymer covalent crosslinking are schematically represented in Figure 1. Mixing of matrix and partner polymer nanocomposite solutions in water and then the fabrication of nanofibers from different solution blends by electrospinning was accompanied by various interfacial interactions between functional groups of both polymer nanocomposites and organoclay, most likely via hydroxyl-amine, hydroxyl-amide, carbonyl-hydroxyl and carbonyl-amine hydrogen bonding, as well as silver cation-electrondonor functional groups. In the presence of homopolymer in PVP + ODA-MMT nanocomposite as a partner polymer, *in situ* physical interfacial interactions between functional groups of matrix (–OH and –C=O ester) and partner (–NH–C=O amide from pyrrolidone ring) polymers, organic octadecyl amine fractions, and ionized species from MMT clay were predominantly realized.

Number of physical interactions increased in the presence of poly(VP-*alt*-MA) + ODA-MMT as a partner copolymer due to additional presence of reactive anhydride –C=O and carboxyl –COOH groups. Moreover, these reactive groups provided effective grafting (amidization of anhydride unit with octadecyl amine) and covalent cross-linking (esterification
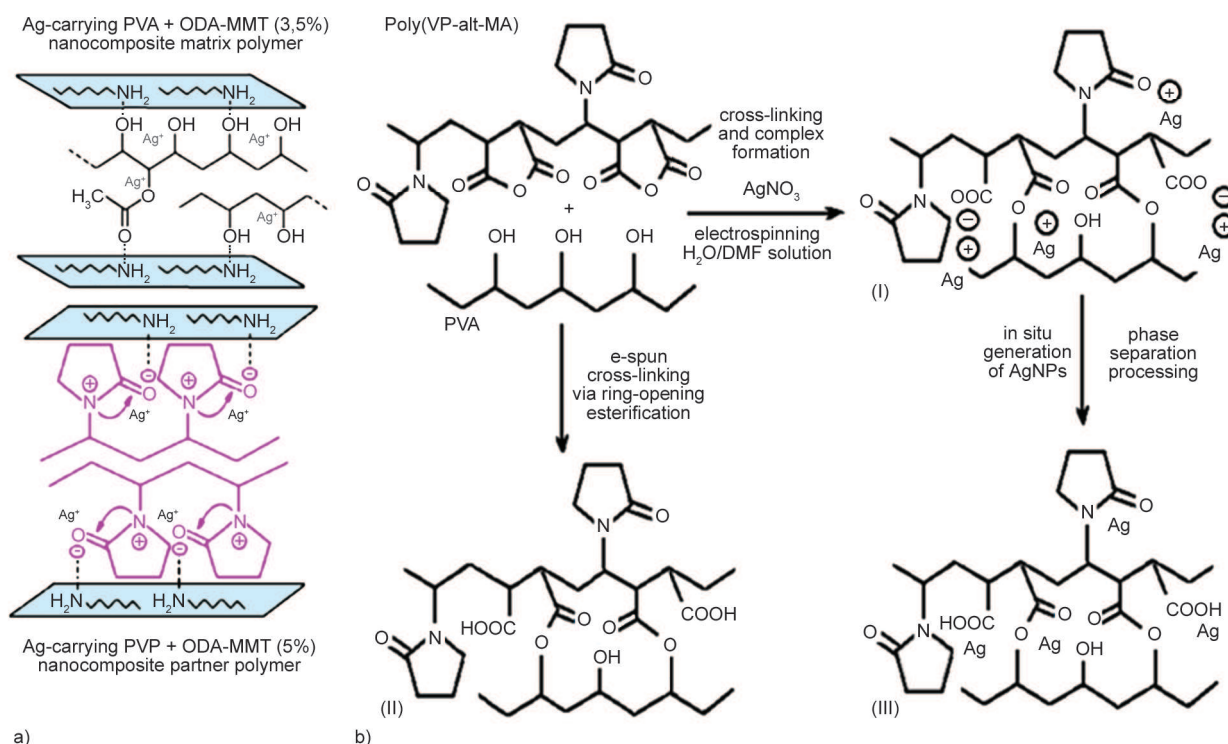

Figure 1. a) The synthetic pathways to fabricate nanocomposites and nanofibers, b) chemistry of covalent cross-linking matrix and partner polymer chains via ring-opening esterification: (I) Ag-carrying polymer complex, (II) cross-linked structure and (III) in situ generated AgNPs onto polymer chains

of anhydride unit with hydroxyl group of matrix polymer) between matrix-partner polymer chains. The observed covalent *in situ* interactions were important structural factors to enhance the stable ion charged sites. Therefore the electrical conductivity of nanofiber structures significantly increased. Polymer-polymer, polymer-organoclay and polymer-silver forces altered the hydrophilic/hydrophobic balance and controlled the phase separation process, resulting in the formation of fiber webs with unique distributed cross-section fibrous morphology. Furthermore, the phase separation process also accelerated significantly with the addition of silver ions through the formation of stable complexes with anion active functional groups as ion transfer sites onto matrix-partner polymer chains. It was demonstrated that the fabricated multifunctional electrolytes incorporated with organoclay and AgNPs exhibited unique dispersed silver nanoparticles onto fiber surface. Silver cations turned into *in situ* generated AgNPs without the use of dominated annealing and UV-irradiation procedures throughout phase separation processing during electrospinning. This observation can be described as a simple and effective method to prepare AgNPs during electrospinning processing.

3.2. Chemical structures of nanofiber composites

Figure 2 shows the IR spectra of the fabricated polymer nanofiber electrolytes. Broad absorption bands around 3314–3293 cm^{-1} in spectra of all fiber compositions were associated with hydrogen-bonded OH and NH_2 stretching from PVA and octadecyl amine chains. Visible shift of this peak to the lower frequency region (NFC-2/AgNPs) can be explained by the increase of hydrogen bonding and complex-formation with AgNPs. Weak C–O–H band appeared around 1320 cm^{-1}. These observations successfully confirmed the formation of cross-linking structure via ring-opening inter-macromolecular esterification of maleic anhydride/carboxyl groups with hydroxyl groups of matrix PVA chains during electrospinning. Pyrrolidone unit (secondary amide) of partner PVP polymer was characterized with the following bands: C=O stretching around 1732 cm^{-1} for amide-I band, NH stretching around 1654 cm^{-1} for amide-II band, and C–N stretching between 1421–1426 cm^{-1} for amide-III band. NH_2 deformation and wagging bands between 848–855 cm^{-1} and
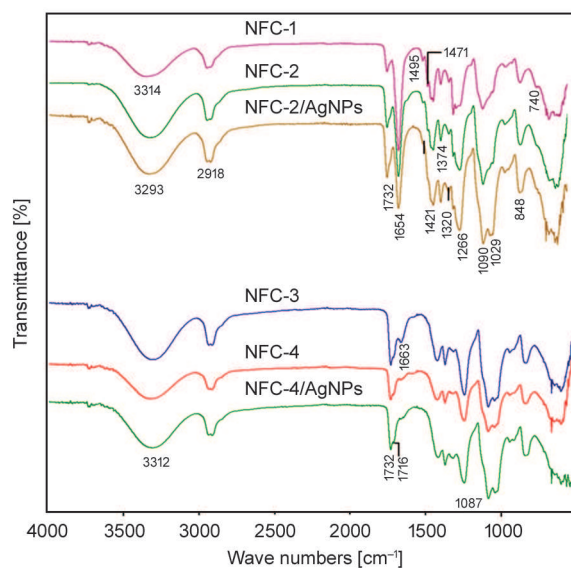

Figure 2. FT-IR spectra of NFC-1, NFC-2, and NFC-2/ AgNPs nanofibers from PVA + ODA-MMT/PVP + ODA-MMT; and NFC-3, NFC-4, and NFC-4/ AgNPs nanofibers from PVA + ODA-MMT/poly (VP-alt-MA) + ODA-MMT

at 1495 cm^{-1} can be attributed to octadecyl amine complex from ODA-MMT clay, and peak around 740 cm^{-1} can be related to $–CH_2–$ rocking band in an octadecyl chain. C–H stretching bands around 2918 cm^{-1} were related to CH, CH_2 and CH_3 groups from octadecyl group and backbone chains, and their bending bands appeared at 1471 and 1374 cm^{-1}. Characteristic broad peaks between 1255–1272 cm^{-1} and around 1090 cm^{-1} were due to C–O and C–O–C absorption bands from carboxyl and ester carboxylate groups, respectively. Silicate band appeared at 1029 cm^{-1} (Si–O–Si). The following absorption bands were observed in FTIR spectra of nanofiber composites containing poly(VP-*alt*-MA)+ODA-MMT: Absence of characteristic absorption bands from anhydride units of copolymer (1776 and 1840 cm^{-1}) [41] in the carbonyl region of the nanofiber's spectra and appearance of C=O and C–O–C bands from ester groups (1732 and 1087 cm^{-1}), and maleate –COOH (1716 and 1663 cm^{-1} for C=O and 3312 cm^{-1} for hydrogen bonded OH in carboxyl group) were observed.

3.3. Physical structures of nanofiber composites

Physical structures of nanofibers were determined by XRD method. Obtained XRD patterns and peak reflection parameters are given in Figure 3. The

well-known Scherrer equation (Equation (1)) was used to calculate particle sizes (τ_{sh}, the mean thickness) in fiber structures [42]:

$$\tau_{sh} = \frac{K_{sh}\lambda}{\beta\cos\theta} \tag{1}$$

where τ is the mean size of the ordered (crystalline) domains, which may be smaller or equal to the grain size; K is a Scherrer constant (K_{sh} of 0.89); λ is the X-ray wavelength ($\lambda = 1.5406$ nm); β is the line broadening at half the maximum intensity (FWHM), after subtracting the instrumental line broadening, in radians. The Bragg equation (Equation (2)) was used to calculate the interlayer spacing (d):

$$n\lambda = 2d\sin\theta \tag{2}$$

where n is the order of reflection and 2θ is the angle of reflection.
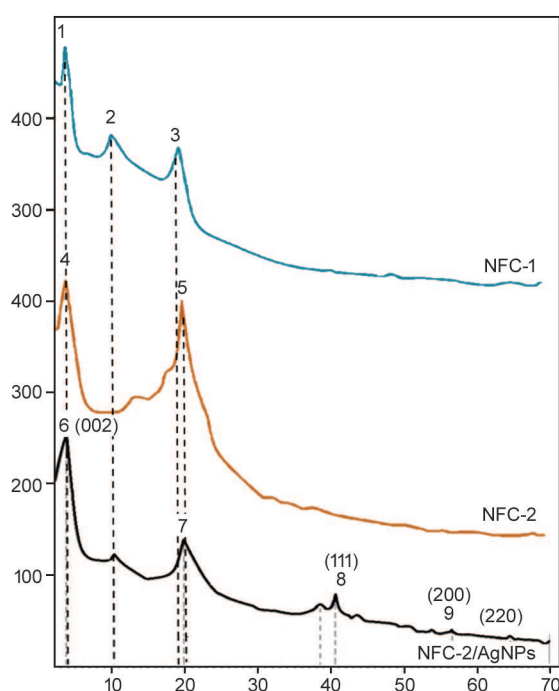
X-ray reflection parameters						
	Peak	2θ	D-spacing [Å]	Intensity (Counts)	FWHM [°2θ]	Particle size [Å]
NFC-1	1	3.81	23.175	100.00	0.444	115.68
	2	10.09	8.765	35.58	0.933	96.60
	3	19.55	4.537	28.74	0.090	14 260
NFC-2	4	3.68	23.963	40.16	0.090	21 720
	5	19.89	4.459	100.00	0.948	73.835
NFC-2/ AgNPs	6	3.68	23.963	51.51	0.090	21 720
	7	19.75	4.491	100.00	1.137	60.96
	8	40.51	2.224	50.81	0.758	98.15
	9	56.57	1.625	14.24	1.137	68.21

Figure 3. XRD patterns and peak reflection parameters of NFC-1, NFC-2, and NFC-2/AgNPs nanofibers

The figure shows polymer composites exhibited semicrystalline structure since they contain crystalline and amorphous structure. Crystalline peaks around 20° 2θ angle belonged to PVA, corresponding to (110) reflection. The intensity of the XRD patterns decreased since the amorphous nature of PVA increased with the addition of PVP. The increase in the amorphous nature of polymer electrolytes causes a reduction in the energy barrier to the segmental motion of the polymer electrolyte resulting in high ionic conductivity [23].

Pristine ODA/MMT clay exhibits a strong peak at $2\theta = 4.45°$ with a distance (d-spacing) of 19.93 Å (002) between two tetragonal layers and several crystallite peaks related to the intermolecular interactions of octadecyl amine and hydroxyl groups from the clay structure via –Si–OH…NH$_2$– hydrogen bonding at edges [43]. The position of reflection peak at 4.45° 2θ shifted to lower region (3.81 and 3.68° 2θ) with an increase in d-spacing from 19.93 Å (002) to 23.17 and 23.96 Å for ODA-MMT (NFC-1 and NFC-2). This observation indicated the formation of nanofibers with low degree of intercalation due to the domination of the colloidal structures in NFCs. The number of crystalline peaks increased with incorporating of AgNPs because of the formation of the characteristic X-ray reflections from crystallinity peaks in XRD patterns. The observed weak peaks at 2θ angles (38.4, 56.5 and 64.6°) can be related to the (111), (200) and (220) planes of *in situ* generated crystalline AgNPs [44]. These results indicated that silver salts successfully turned into *in situ* generated AgNPs during electrospinning process. Relatively low crystallinity was observed in NFCs consisting 60–80 mass% of PVA compared with pristine PVA polymer (around 30–50%) [45]. This fact can be explained by colloidal state of silicate region (broad peak with higher amorphous area) in fiber compositions and tendency of nanofibers to absorption and swelling in applied aqueous medium. The presence of microparticles with size of 2.172 μm confirmed the above mention proposal.

3.4. Morphology of nanofiber electrolytes

The phase separation process during electrospinning and properties of fabricated nanofibers strongly depends on the applied electrospinning parameters, matrix-partner polymer compatibility, chemical and physical structural factors, and various interactions such as hydrogen bonding, complex formation, and

different chemical reactions between functional groups of both polymers. Morphological characteristics and diameters of nanofibers from NFC-1, NFC-2, and NFC-2/AgNPs are given in Figure 4a–c. It can be clearly seen that all fibers exhibit porous surface morphology. Solvent evaporation happens mainly from the surface of polymer jet. In addition,

the diffusion rate of solvent molecules from the core to the surface is usually lower than that of the solvent evaporation. The diffusion of water molecules from the jet to the atmosphere changes the jet composition, as well. Thus, the variation of the jet composition can lead to the formation of heterogeneous regions within the jet. We concluded that PVP molecules limit
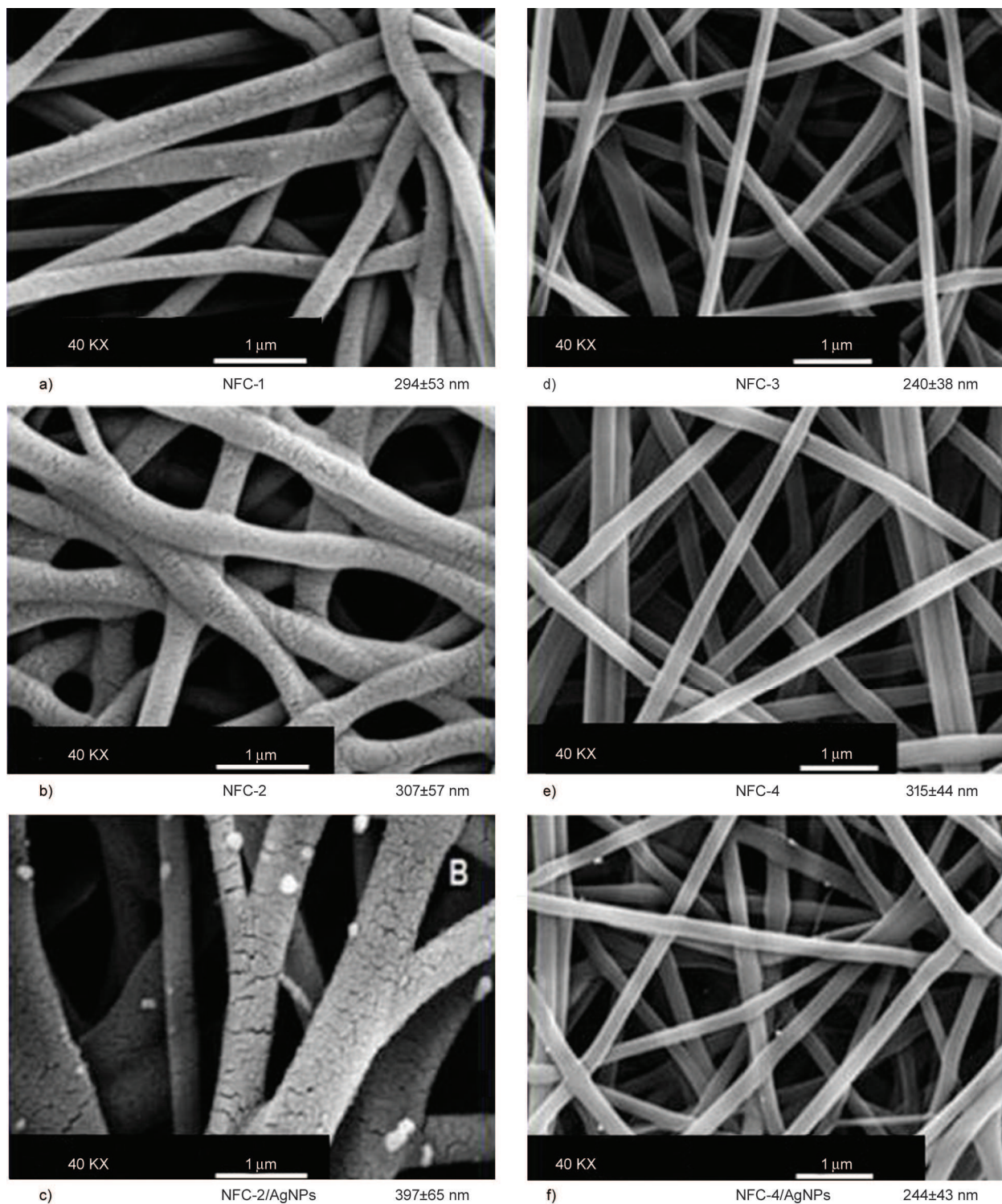
Figure 4. SEM morphology images and diameter distribution of a) NFC-1, b) NFC-2, and c) NFC-2/AgNPs, d) NFC-3, e) NFC-4, and f) NFC-4/AgNPs nanofibers

the ability of the solution to fill the pores during evaporation of the condensed moisture on the fibers and result in a porous fiber. Whereas mean diameters of the fibers were not affected significantly by fiber composition, diameter distribution improved in the presence of *in situ* generated AgNPs (Figure 4c). In this system, silver salts easily transformed to nanoparticle form, which essentially accelerated the phase separation process and improved the distribution and size parameters of nanofibers. Silver salts into polymer solution being ejected not only transformed easily into silver particles during fiber formation, but also were well-dispersed onto the fiber surfaces due to increase of the surface area of the fibers (white points in Figure 4c).

Unlike PVP homopolymer containing nano-porous nanofibers, the nanofibers containing reactive poly (VP-*alt*-MA) copolymer had non-porous and smooth surface morphology due to their covalent bonding network structures which essentially prevented the fast diffusion and elimination of water molecules from inside area of fibers during electrospinning (Figure 4d–f). Fine surface morphology also indicated that matrix and partner polymer show good compatibility. In this composition, the mobility of PVA chains in colloidal/amorphous region was restricted by the presence of the covalent cross-linked fragments in fiber structures. An increase in partner polymer fraction essentially improved fiber diameter distribution and caused the formation of approximately

homogenous fiber size with maximum fraction of 82%. *In situ* generated AgNPs had significant effect on the morphology and diameter distribution parameters of the fibers, as well (Figure 4f). When comparing with the fibers fabricated without silver precursor (Figure 4e), the diameter of NFC-4/AgNPs fibers not only dramatically decreased from 315 to 244 nm, but also their diameter distribution improved (Figure 4f). TEM images reveal that AgNPs around 20–40 nm were also successfully formed into the fiber structure (Figure 5a). EDX analysis confirmed the formation of AgNPs on the surfaces (Figure 5b).

3.5. Thermal behaviors of nanofiber structures consisting poly(VP-*alt*-MA) copolymer

Results of TGA and DTG analyses are given in Figure 6. The TGA-DTG curves of nanofiber film composites showed two steps degradations: $T_{d(max)} = 330.3\,°C$ (first step), $437.1\,°C$ (second step), and total weight loss = 81.31% for NFC-3 (Figure 7a); $T_{d(max)} = 316.5\,°C$ (first step), $433.8\,°C$ (second step), and total weight loss = 88.05% for NFC-4 (Figure 6b). NFC-4/AgNPs nanofiber composite was also exhibited two-stage degradation with different mechanism: $200.7\,°C$ (first step), $324.2\,°C$ (second step), and total weight loss = 73.89% (Figure 6 c). An increase in the fraction of partner copolymer from 20% to 40% increased thermal stability. NFC-4/AgNPs also showed high thermal stability. High ther-
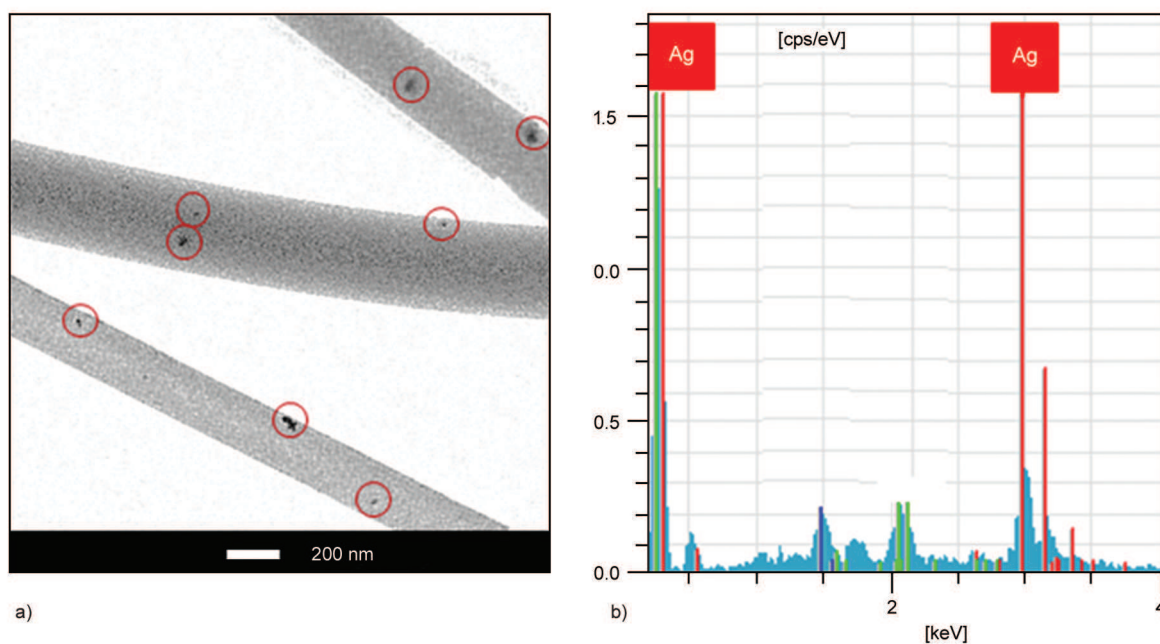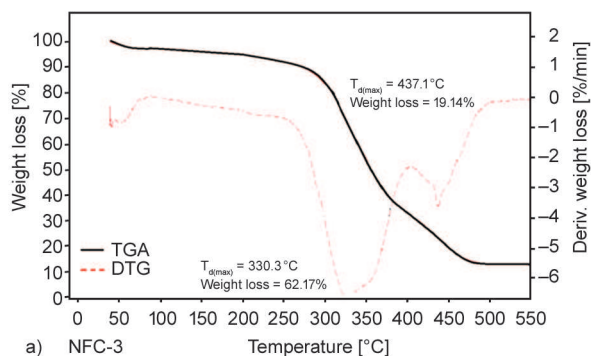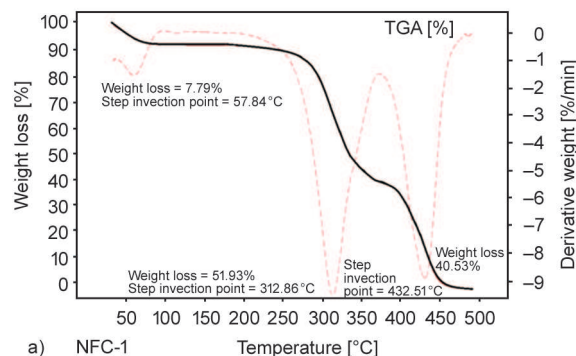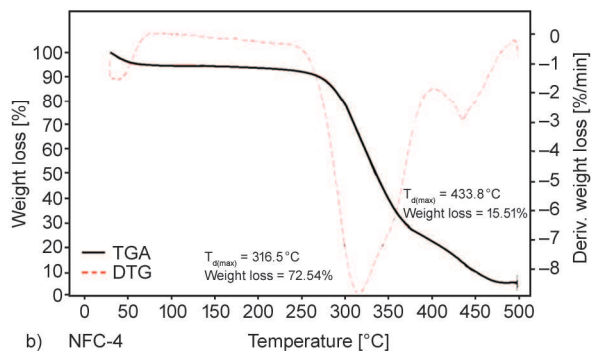

Figure 5. TEM images of (a) NFC-2/AgNPs (Black points in red circles indicate AgNPs with nano-sizes around 20–40 nm) and (b) EDX analysis of AgNPs
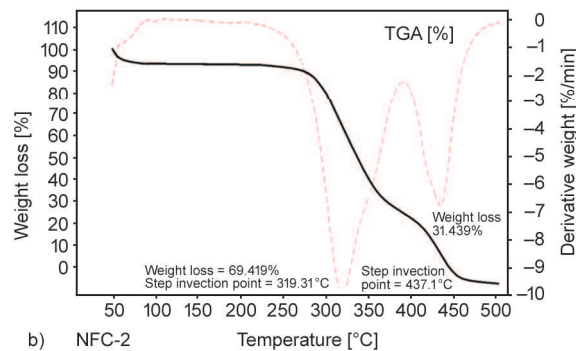
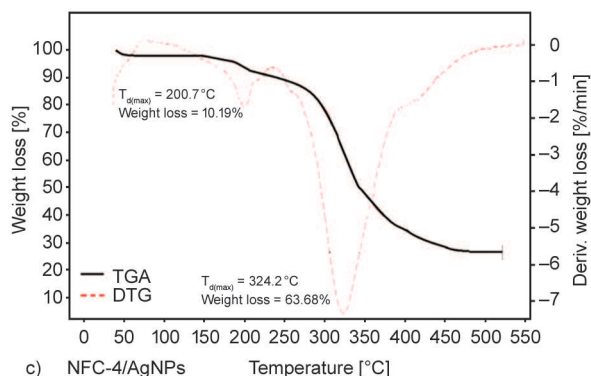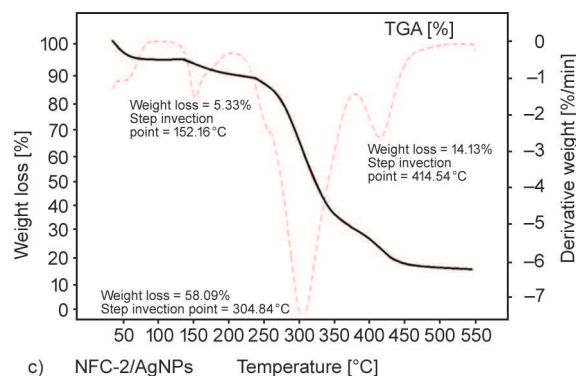**Figure 6.** TGA-DTG thermal degradation curves and thermal stability of a) NFC-3, b) NFC-4, and c) NFC-4/AgNPs (c) nanofibers consisting poly(VP-*alt*-MA) copolymer

Figure 7. TGA-DTG thermal degradation curves and thermal stability of a) NFC-1, b) NFC-2 and c) NFC-2/AgNPs nanofibers consisting PVP homopolymer

mal degradation parameters of poly(VP-*alt*-MA) copolymer based NFCs (cross-linking structures) were also confirmed by DSC analysis (data not shown). DSC results indicated typical curves not including any melting and/or glass-transition peak areas from NFCs for the cross-linked polymer nanofiber structures. The formation of several weak broad exo-peaks in the curves of derivative of heat flow versus temperature can be attributed to various chemical reactions formed in the applied isothermal conditions. Thus, the organoclay and AgNPs incorporated PVA/PVP and poly(VP-*alt*-MA) as matrix/partner polymer nanocomposite complexes were formed in water solution/dispersed medium due to the easy interaction of silver cations with solvent molecules and reg-

ularly repeated free –COOH, –OH and pyrrolidone NH–C=O groups from partner/matrix polymer chains, as well as exchange reaction with clay cations.

These interactions which took place in the nanofiber structures with dominantly colloidal amorphous areas enhanced with multifunctional sites easily realizing the charge transport process onto the nanofiber surface after the elimination of highest fraction of solvent molecules during electrospinnig. Colloidal structure of nanofibers was due to partially swelling and water-absorption behaviors of matrix PVA polymer and organoclay components in the composites. This interpretation is in reasonable agreement with well know Armand's theory which stated that ionic motion in salt-polymer complex was not due to charges hopping from site to site, but

also it was a continuous motion occurring in the amorphous region of the polymeric material [46].

3.6. Thermal behaviors of nanofiber structures consisting PVP (homopolymer)

Thermal analyses results of PVP containing fiber samples are given in Figure 7. The comparative analysis of TGA-DTG curves from Figure 6 and 7 shows that the thermal degradation parameters were relatively higher in NFCs consisting reactive alternating copolymer as a cross-linker, and predominantly chemical interactions occurred in isothermal growing condition (Figure 6). Unlike this observation, thermal degradation of NFCs consisting PVP (homopolymer) proceeded by two step degradation mechanism without any covalent interactions (Figure 7). Moreover, multi-steps degradations were detected for NFC-2/AgNPs. Both silver incorporated samples in structurally different systems showed characteristic middle degradation peak at 152–200 °C relating to decomposition of silver contained complexion linkages.

3.7. Electrical properties of PVA nanofiber composites with PVP homopolymer nanocomposite and AgNPs

PVA is a low conducting polymer. However, PVP and various hydrophilic functional copolymers of VP contain ionizable functional groups and units, and they may exhibit high electrical conductive properties. To improve the conductivity of PVA, many researchers used functional polymers as conducting partner polymers. Water solution blend of PVA/PVP showed physical network structure due to hydrogen bonding between –OH and –C=O groups from PVA and PVP, respectively. The hydrogen bonds are also formed between –OH (PVA) and Si–O (silanol of MMT platelets) in PVAMMT clay aqueous suspension [47, 48]. This unique property improved potential applications of binary polymer systems compared with homopolymers of PVA and PVP [49, 50]. Sengwa and Sankhla [50] synthesized PVA-PVP blend-MMT clay nanocomposite films up to 10 wt% clay loading by aqueous solution intercalation and melt compounding. Their study revealed that the dielectric constant values of these organic-inorganic nano-composite films can be tuned by loading MMT clay in the polymers matrix, which also improved their physical and thermal properties. Here, we presented a self-assembly approach to fabricate

polymer/organoclay nanofiber structures from the binary water solution blends of matrix polymer (PVA), partner polymers (PVP, poly(VP-*alt*-MA), and Ag-carrying matrix/partner nanocomposite complexes) with colloidal dispersed octadecyl amine-MMT clay sheets by green electrospinning nanotechnology. It was proposed that the obtained self-assembled nanostructures could be described as effective electrolyte platforms with higher electrical conductivity, but with lower thermal conductivity due to possible prevention of the transport of thermal energy by interphase nanostructure of clay sheets. To confirm this proposal, effects of composition, origin and fraction of the partner polymers, the organoclay and *in situ* generated AgNPs on the electrical conductivity properties of nanofiber colloidal electrolytes at various temperatures and pressures were investigated. Electrical conductivity of nanofiber composite films was measured by Equation (3) based on direct current conductivity (σ_{dc}) [51]:

$$\sigma_{dc} = \frac{d}{RA} \tag{3}$$

where R is a resistance [Ω], d is a thickness [μm] and A is a surface area (0.25 cm^2) as a standard for each testing sample.

Measurement of these parameters was carried out at the different temperatures (22–50 °C) and pressures (around 50–800 Torr). Obtained results given in Figure 8 indicated that the fibers having different compositions (NFC-2, NFC-2/AgNPs and NFC-1) showed higher electrical conductivity (1.04 10^{-9}, 8·10^{-9} and 1.1·10^{-9} S·cm^{-1}) at room temperature as compared with conductivity of pristine PVA (1.25·10^{-15} S·cm^{-1}) [19] (Figure 8a–c). Incorporation of organoclay to nanofiber structures significantly improved the electron interfacial interactions and enhanced conductivity performance of PVA/PVP based nanofiber composites. In a study, PVA/PVP matrix/partner polymer blend composites with volume ratios of 80:20 and 60:40 fabricated by solution casting method showed relatively higher electrical conductivity (2.2·10^{-7} and 7.3·10^{-8} S·cm^{-1}) at room temperature [21] and at 30 °C (2.29·10^{-7} and 5.24·10^{-7} S·cm^{-1}) [23]. Thus incorporation of organoclay (5 mass%) to nanofiber structures significantly improved the electron interfacial interactions and enhanced the conductivity performance of PVA/PVP based nanofiber composites. Several researchers also investigated the effect of organoclay in various polymer nanocompos-
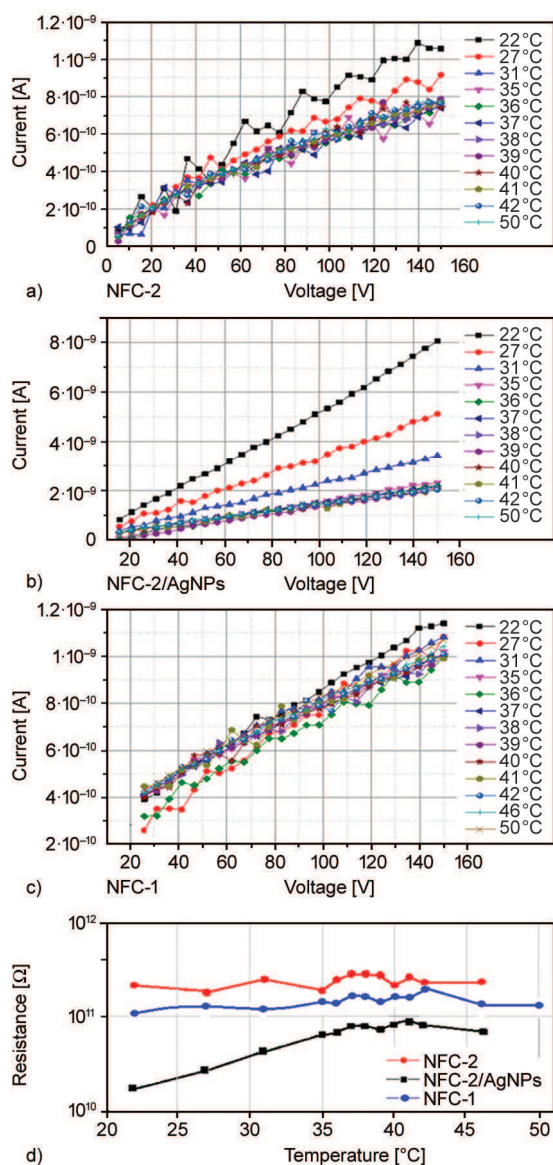
Figure 8. Current (A) versus voltage (V) curves of (a) NFC-2, (b) NFC-2/AgNPs, (c) NFC-1, and (d) their electrical resistance versus temperature curves. Effect of temperature.

ites on electrical conductivity. The hollow spherical morphology of poly(diphenylamine) (PDPA) inside the galleries of montmorillonite organoclay showed different conductive property than PDPA formed by the conventional method due to the confinement effect [52]. Kim *et al*. [53] evaluated effects of organo-MMT clay in the matrix PEO/organoclay nanocomposite electrolytes on the ionic conductivity. They observed that the polymeric electrolyte composites exhibited higher conductivity than pristine Na^+-MMT mineral clay. According to the authors, electrical conductivity of electrolytes depended on the reduced crystallinity and enhanced ion-mobility by the increased interlayer spacing of MMT clay.

Salahuddin *et al*. [54] reported that the electrical conductivity of polyaniline/organoclay nanocomposites increased 30 times more than that of pristine MMT clay.

3.8. Electrical properties of PVA nanofiber composites with VP copolymer nanocomposite and AgNPs

It was suggested that significant covalent bonds could exist between octadecyl amine and partner polymers via amidation of anhydride/carboxyl groups and esterification of anhydride unit with hydroxyl groups in the PVA/PVP (partner-1) and VP copolymer (partner-2) based multifunctional nanofiber composite systems. Comparative analysis results indicated that electrical properties strongly depended on the loaded reactive organoclay and in situ generated AgNPs, which were significantly improved conductivity via accelerating electron transport process. Unlike homopolymer of VP, alternating copolymer of VP containing reactive anhydride units easily interacted with hydroxyl groups of matrix polymer via ring-opening intermolecular esterification-crosslinking. NFC-4 nanofiber composites showed excellent conductivity (Figure 9a) and low thermal resistance (Figure 9b) at temperature ranges from 22 to 50 °C for applied voltages (around 0–2.5 V). This observed phenomenon can be explained by the formation of thermodynamically stable self-assembled negatively charged sites caused by regularly distributed ionized functional groups in alternating partner copolymer. Thus, the ion transport essentially improved in the cross-linked surface structure of the nanofibers. On the other hand, an increase in the fraction of partner copolymer nanocomposite dramatically decreased conductivity (Figure 9c) and increased resistance properties of NFC-3 samples (Figure 9b) because of destroying of the self-assembled and organized ion transfer sites. In conclusion, ratio of applied current [A]/voltage [V] and matrix/partner nanocomposites, as well as origin (reactivity) of partner copolymer significantly influenced conductivity and resistance parameters of NFCs. Salamova *et al*. [55] reported the effect of inorganic salts (co solute) on main parameters of dilute aqueous PVP solutions such as cloud points, phase diagram, low critical solution temperature (LCST) and viscosity. Inclusion of salts into aqueous PVP solution led to the decrease of the LCST and intrinsic viscosity which was caused by the effect of the co solute ions in enhancing
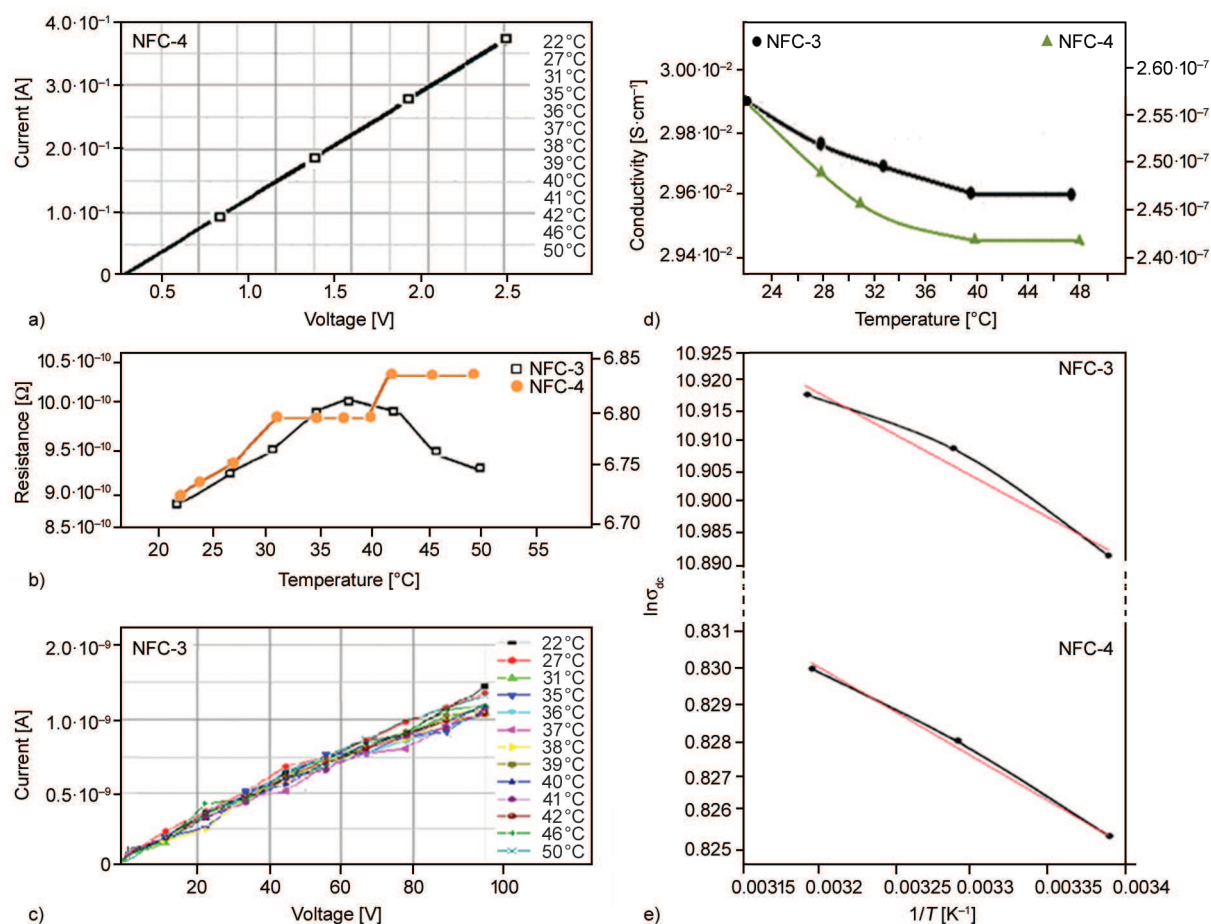
Figure 9. Current versus voltage curves of (a) NFC-4, (c) NFC-3 and (b) their electrical resistance versus temperature; (d) electrical conductivity of NFC-4 and NFC-3 at various temperatures and (e) their activation energy (E_a) calculated from plots of $\ln\sigma_{dc}$ versus reciprocal temperature ($1/T$ [K^{-1}]). Effect of temperature.

the segment-segment interactions. Cho *et al.* [56] prepared fiber-based electrical systems based on poly(vinyl alcohol) (PVA) as a fiber forming carrier polymer, poly(styrenesulfonate) (PSS) as a conducting partner polymer, glutaraldehyde as a crosslinker, and negatively charged poly(maleic anhydride-*alt*-methyl vinyl ether) [poly(MA-*alt*-MVE)] as a doping agent. They found that the cross-linked conducting nanofibers exhibited high conductivity (4–8 S·m^{-1}).

In solid electrolytes, ionic transport is more difficult than electronic charge transport due to the resistance assemblies in the electrode. Resistance, also known as ohmic losses, is due to the losses occurred during ionic and charge transport in amorphous polymer nanofiber electrolyte. It was proposed that the absorption of water molecules in colloidal structure of nanofiber electrolytes with high amorphous area significantly improved ionic charges and their transport, and therefore, increased the conductive sites in polymer nanofiber surface structures. Moreover, these obtained values were very important to evaluate effects of composition, fraction and origin of part-

ner polymer nanocomposites and structural factors from the comparative analysis of two series of different nanofibers structures.

Extremely high electrical conductivity of NFC-4 (Figure 9a) compared with other NFCs can be explained by taking into consideration the following structural factors: (1) cross-linking and complexing factors in this NFC played an important role due to providing high degree of electro-active sites on the nanofiber surface, (2) low conductivity of NFC-4/AgNPs compared with NFC-4 was associated with blocking by silver cations the cross-linking reactions via the formation complexing linkages with hydroxyl groups and salts with carboxyl groups of maleic acid units from partner alternating copolymer, and (3) all other NFCs were prepared from PVA/PVA polymer systems which were not contained chemically reactive units such as maleic acid, and the formation of electro-active sites was limited by only physical interaction between OH groups of PVA with pyrrolidone units, as well as OH groups with octadecyl amine from organoclay. In Figure 9b,

the temperature dependence of electrical resistivity value did not show a linear increase. NFC-4 showed an increase in resistance up to 30 °C and saturated up to 40 °C and then it increased again. Similarly, the electrical resistance of NFC-3 increased up to 37 °C and it dropped beyond that temperature. These observed phenomena as step inflections in curves, can be related to occurrence of lower sub-glass transition processing, coil-glouble conformational changes of polymer chains, elimination of absorbed water molecules and etc., as well as non-controllable *in situ* processes in colloidal amorphous medium.

The plots of electrical conductivity versus temperature (Figure 9d) indicated that the conductivities of NFC-3 and NCF-4 only depended on the applied temperature (22–40 °C). Following increase of temperature did not influence the conductivity values. Activation energy (E_a) can be calculated at above mentioned temperature range by using well-known Arrhenius equation (Equation (4)) [57]. Taking the logarithms of both sides and separating the exponential and pre-exponential terms yields Equation (5). Plots of ln_{dc} versus $1/T$ [K^{-1}] given in Figure 9e clearly indicate that the thermal process follows the Arrhenius equation.

$$\sigma_{dc} = \sigma_0 e^{-\frac{E_a}{RT}} \qquad (4)$$

where E_a is the activation energy, R is the universal gas constant, σ_0 is a temperature-independent constant and T is temperature [K].

$$\ln \sigma_{dc} = \ln \sigma_0 - \frac{E_a}{RT} \qquad (5)$$

The plots showed a linear behavior between $\ln\sigma_{dc}$ and $1/T$ and a good fit to the Arrhenius equation. From the plots of $\ln\sigma_{dc}$ versus $1/T$ the following activation energy values were calculated: 0.226, 0.028 and 0.022 eV for NFC-4; 0.340, 0.076 and 0.017 eV for NFC-3. The mobility of the charge carriers increased with increasing temperature. Activation energy increased with increasing of the partner copolymer ratio. This can be explained by substantially restricting of the mobility of macromolecular chains in matrix/partner systems via polymer-copolymer covalent cross-linking during electrospinning.

Here, it was also investigated the effect of temperature, pressure and conducting time on the electrical and resistance properties of Ag-incorporated nanofiber composites (NFC-4/AgNPs). According to the results given in Figure 10, applied temperature (Figure 10a) and pressure (Figure 10b) significantly improved conductivity parameters of Ag-carrying NFCs. Comparative analysis at 50 and 760 Torr (Figure 10c and d) showed that an increase in pressure had an effect on the conductivity of the nanofiber composites. Similar effect was also observed for conductivity times. This observation indicated that NFCs were thermodynamically stable covalent cross-linked nanostructures. As resistance had a tendency to decrease with increasing temperature (Figure 10e), the dependence on the pressure tended to decrease (Figure 10 f). Several researchers reported the effect of pressure on thermal conductivity of various polymer melts, as well as poly(vinyl alcohol) gels [58, 59]. The thermal conductivity of both amorphous and semi-crystalline polymers was found to increase with increasing applied pressure and generally with increasing temperature. Herein, applied pressure improved the accuracy of *in situ* physical interactions. This process provided an increase in colloidal amorphous area, the mobility and ion-charge ability of functional groups from the nanofibrous structures. It was proposed that the use of pressure improved accuracy of electro-active sites due to increased temperature and across transition temperature, as well as increase of colloidal amorphous area, mobility of functional groups from fibrous structures, which significantly improved the electrical conductivity of polymer nanofiber composites.

4. Conclusions

This work presented a new approach to fabricate novel multifunctional nanofiber electrolytes with linear and cross-linked polymer structures by using PVA + ODA-MMT (matrix), PVP homopolymer + ODA-MMT (partner-1), poly(VP-*alt*-MA) + ODA-MMT (partner-2) and Ag-carrying matrix/polymer system with varying the fraction of partner (co) polymers in nanofiber composites. Morphology and electrical properties strongly depended on the origin and fraction of partner polymer NFCs. Covalent cross-linked nanofiber structures significantly increased the conductivity and thermal behaviors of NFCs. Ag-carrying polymer complexes and *in situ* generated AgNPs onto nanofiber surfaces accelerated phase separation process and considerably enhanced the electrical parameters of NFCs. A covalent bridge of partner alternating copolymer between PVA macromolecules not only reinforced the network
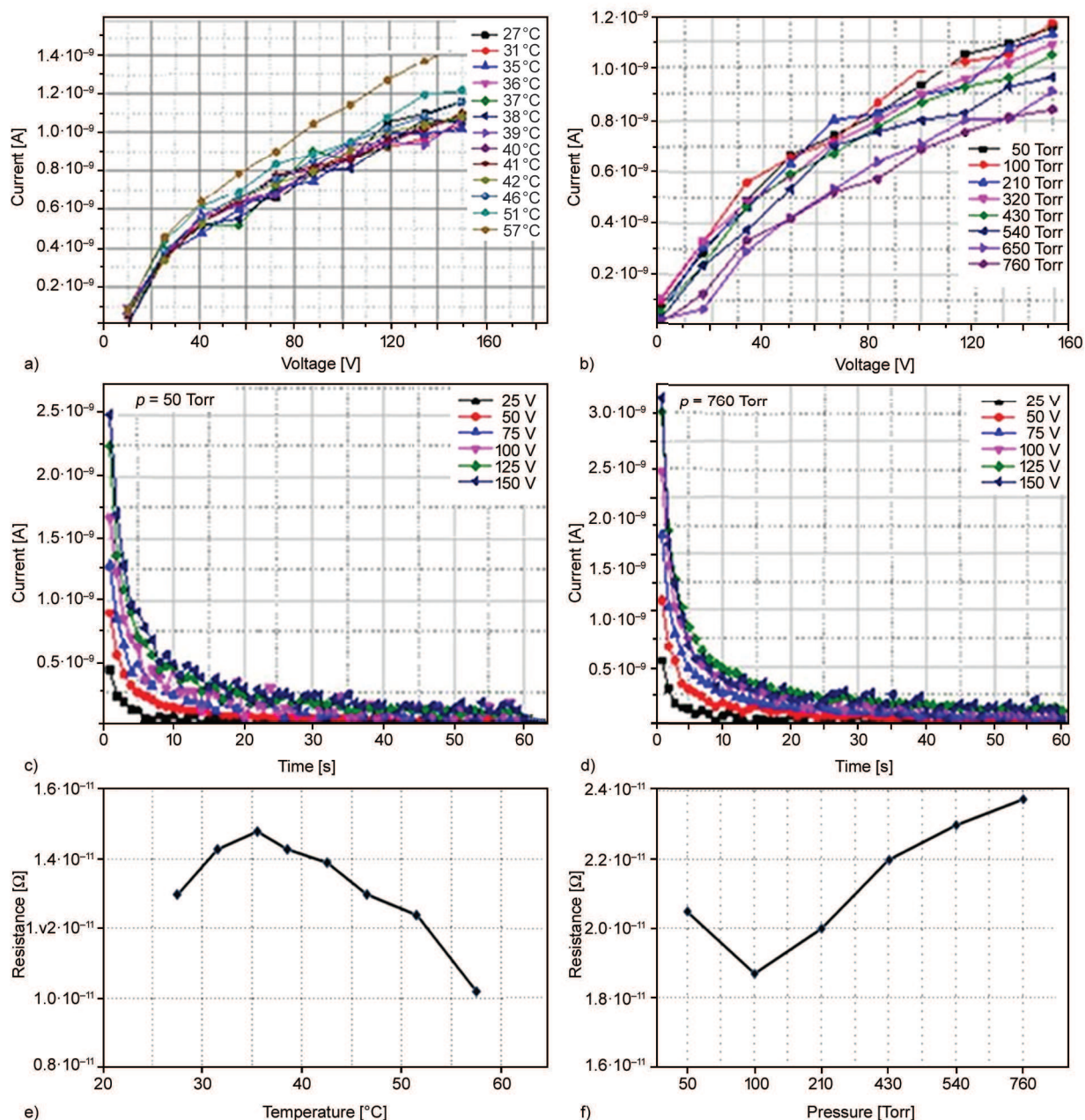
Figure 10. Electrical conductivity and resistance of NFC-4/AgNPs nanofiber composite. Effects of a) temperature, b) pressure, and conduct times at c) 50 Torr and d) 760 Torr on electrical conductivity; effects of e) temperature and f) pressure on resistance

but also provided extra ion charge transport sites due to its regularly repeated functional monomer units onto polymer chains. High and excellent behaviors were observed for the homopolymer and copolymer of VP based fiber structures, respectively. The obtained green nanomaterials with unique properties and higher contact areas can open new avenue for various applications in microelectronics, sensor devices, electrochemical processing, fuel cell, nanolithography and power technologies, as well as in various bioengineering processing as a reactive platform.

References

[1] Agarwal S., Greiner A., Wendorff J. H.: Functional materials by electrospinning of polymers. Progress in Polymer Science, **38**, 963–991 (2013).
DOI: 10.1016/j.progpolymsci.2013.02.001

[2] Cai Y., Zong X., Ban H., Liu Q., Qiao H., Wei Q., Zhao Y., Fong H.: Fabrication, structural morphology and thermal energy storage/retrieval of ultrafine phase change fibres consisting of polyethylene glycol and polyamide 6 by electrospinning. Polymers & Polymer Composites, **21**, 525–532 (2013).

[3] Sahay R., Kumar P. S., Sridhar R., Sundaramurthy J., Venugopal J., Mhaisalkar S. G., Ramakrishna S.: Electrospun composite nanofibers and their multifaceted applications. Journal of Materials Chemistry, **22**, 12953–12971 (2012).
DOI: 10.1039/C2JM30966A

[4] Cui W-W., Tang D-Y., Gong Z-L.: Electrospun poly(vinylidene fluoride)/poly(methyl methacrylate) grafted TiO$_2$ composite nanofibrous membrane as polymer electrolyte for lithium-ion batteries. Journal of Power Sources, **223**, 206–213 (2013).
DOI: 10.1016/j.jpowsour.2012.09.049

[5] Abdelgawad A. M., Hudson S. M., Rojas O. J.: Antimicrobial wound dressing nanofiber mats from multicomponent (chitosan/silver-NPs/polyvinyl alcohol) systems. Carbohydrate Polymers, **100**, 166–178 (2014).
DOI: 10.1016/j.carbpol.2012.12.043

[6] Um-i-Zahra S., Shen X. X., Li H., Zhu L.: Study of sustained release drug-loaded nanofibers of cellulose acetate and ethyl cellulose polymer blends prepared by electrospinning and their *in-vitro* drug release profiles. Journal of Polymer Research, **21**, 602–614 (2014).
DOI: 10.1007/s10965-014-0602-5

[7] Nataraj S. K., Yang K. S., Aminabhavi T. M.: Polyacrylonitrile-based nanofibers – A state-of-the-art review. Progress in Polymer Science, **37**, 487–513 (2012).
DOI: 10.1016/j.progpolymsci.2011.07.001

[8] Pham Q. P., Sharma U., Mikos A. G. M.: Electrospinning of polymeric nanofibers for tissue engineering applications: A review. Tissue Engineering, **12**, 1197–1211 (2006).
DOI: 10.1089/ten.2006.12.1197

[9] Zhang G., Kataphinan W., Teye-Mensah R., Katta P., Khatri L., Evans E. A., Chase G. G., Ramsier R. D., Reneker D. H.: Electrospun nanofibers for potential space-based applications. Materials Science and Engineering: B, **116**, 353–358 (2005).
DOI: 10.1016/j.mseb.2004.05.050

[10] Taepaiboon P., Rundsardthong U., Supaphol P.: Drug-loaded electrospun mats of poly(vinyl alcohol) fibres and their release characteristics of four model drugs. Nanotechnology, **17**, 2317–2329 (2006).
DOI: 10.1088/0957-4484/17/9/041

[11] Jannesari M., Varshosaz J., Morshed M., Zamani M.: Composite poly(vinyl alcohol)/poly(vinyl acetate) electrospun nanofibrous mats as a novel wound dressing matrix for controlled release of drugs. International Journal of Nanomedicine, **6**, 993–1003 (2011).
DOI: 10.2147/IJN.S17595

[12] Strawhecker K. E., Manias E.: Structure and properties of poly(vinyl alcohol)/Na$^+$ montmorillonite nanocomposites. Chemistry of Materials, **12**, 2943–2949 (2000).
DOI: 10.1021/cm000506g

[13] Chang J-H., Jang T-G., Ihn K. J., Lee W-K., Sur G. S.: Poly(vinyl alcohol) nanocomposites with different clays: Pristine clays and organoclays. Journal of Applied Polymer Science, **90**, 3208–3214 (2003).
DOI: 10.1002/app.12996

[14] Khan W. S., Asmatulu R., Eltabey M. M.: Electrical and thermal characterization of electrospun PVP nanocomposite fibers. Journal of Nanomaterials, **2013**, 160931/1–160931/9 (2013).
DOI: 10.1155/2013/160931

[15] Georgiev G., Konstantinov C., Kabaivanov V.: The role of the charge-transfer complex during the copolymerization of N-vinylpyrrolidone and maleic anhydride. Macromolecules, **25**, 6302–6308 (1992).
DOI: 10.1021/ma00049a029

[16] Bacu E., Chitanu G. C., Couture A., Grandclaudon P., Singurel G., Carpov A.: Potential drug delivery systems from maleic anhydride copolymers and phenothiazine derivatives. European Polymer Journal, **38**, 1509–1513 (2002).
DOI: 10.1016/S0014-3057(02)00040-X

[17] Veron L., Revol M., Mandrand B., Delair T.: Synthesis and characterization of poly(N-vinyl pyrrolidone-*alt*-maleic anhydride): Conjugation with bovine serum albumin. Journal of Applied Polymer Science, **81**, 3327–3337 (2001).
DOI: 10.1002/app.1789

[18] Temiz A., Toğay S. O., Şener A., Güven G., Rzaev Z. M. O., Piskin E.: Antimicrobial poly(N-vinyl-2-pyrrolidone-*alt*-maleic anhydride)/poly(ethylene imine) macrocomplexes. Journal of Applied Polymer Science **102**, 5841–5847 (2006).
DOI: 10.1002/app.24903

[19] Ahmad Zamri M. F. M., Sharif Zein S. H., Abdullah A. Z., Basir N. I.: Improved electrical conductivity of polyvinyl alcohol/multiwalled carbon nanotube nanofibre composite films with MnO$_2$ as filler synthesised using the electrospinning process. International Journal of Engineering and Technology, **11**, 20–26 (2011).

[20] Ravi M., Kumar K. K., Rao V. V. R. N.: Investigation on electrical and dielectric properties of PVP: KCLO (4) polymer electrolyte films. Indian Journal of Pure and Applied Physics, **51**, 362–366 (2013).

[21] Hatta F. F., Yahya M. Z. A., Ali A. M. M., Subban R. H. Y., Harun M. K., Mohamad A. A.: Electrical conductivity studies on PVA/PVP-KOH alkaline solid polymer blend electrolyte. Ionics, **11**, 418–422 (2005).
DOI: 10.1007/BF02430259

[22] Inzelt G., Pineri M., Schultze J. W., Vorotyntsev M. A.: Electron and proton conducting polymers: Recent developments and prospects. Electrochimica Acta, **45**, 2403–2421 (2000).
DOI: 10.1016/S0013-4686(00)00329-7

[23] Rajeswari N., Selvasekarapandian S., Karthikeyan S., Prabu M., Hirankumar G., Nithya H., Sanjeeviraja C.: Conductivity and dielectric properties of polyvinyl alcohol–polyvinylpyrrolidone poly blend film using non-aqueous medium. Journal of Non-Crystalline Solids, **357**, 3751–3756 (2011).
DOI: 10.1016/j.jnoncrysol.2011.07.037

[24] Datta R. S., Said S. M., Shahrir S. R., Abdullah N., Sabri M. F. M., Balamurugan S., Miyazaki Y., Hayashi K., Hashim N. A., Habiba U., Afifi A. M.: Ionic liquid entrapment by an electrospun polymer nanofiber matrix as a high conductivity polymer electrolyte. RSC Advances, **5**, 48217–48223 (2015).
DOI: 10.1039/C5RA03935E

[25] Laforgue A., Robitaille L., Mokrini A., Ajji A.: Fabrication and characterization of ionic conducting nanofibers. Macromolecular Materials and Engineering, **292**, 1229–1236 (2007).
DOI: 10.1002/mame.200700200

[26] Lu X., Zhou J., Zhao Y., Qiu Y., Li J.: Room temperature ionic liquid based polystyrene nanofibers with superhydrophobicity and conductivity produced by electrospinning. Chemistry of Materials, **20**, 3420–3424 (2008).
DOI: 10.1021/cm800045h

[27] Pisesweerayos P., Dangtip S., Supaphol P., Srikhirin T.: Conductive nanocomposite aligned fibers of PVA-AgNPs-PEDOT/PSS. Advanced Materials Research, **1033–1034**, 1009–1019 (2014).
DOI: 10.4028/www.scientific.net/AMR.1033-1034.1009

[28] Manoratne C. H., Rajapakse R. M. G., Dissanayake M. A. K. L.: Ionic conductivity of poly(ethylene oxide) (PEO)-montmorillonite (MMT) nanocomposites prepared by intercalation from aqueous medium. International Journal of Electrochemical Science, **1**, 32–46 (2006).

[29] Ravindran A., Chandran P., Khan S. S.: Biofunctionalized silver nanoparticles: Advances and prospects. Colloids and Surfaces B: Biointerfaces, **105**, 342–352 (2013).
DOI: 10.1016/j.colsurfb.2012.07.036

[30] Ilker M. F., Nüsslein K., Tew G. N., Coughlin E. B.: Tuning the hemolytic and antibacterial activities of amphiphilic polynorbornene derivatives. Journal of the American Chemical Society, **126**, 15870–15875 (2004).
DOI: 10.1021/ja045664d

[31] Sambhy V., MacBride M. M., Peterson B. R., Sen A.: Silver bromide nanoparticle/polymer composites: Dual action tunable antimicrobial materials. Journal of the American Chemical Society, **128**, 9798–9808 (2006).
DOI: 10.1021/ja061442z

[32] Galya T., Sedlařík V., Kuřitka I., Novotný R., Sedlaříková J., Sáha P.: Antibacterial poly(vinyl alcohol) film containing silver nanoparticles: Preparation and characterization. Journal of Applied Polymer Science, **110**, 3178–3185 (2008).
DOI: 10.1002/app.28908

[33] Hong K. H., Park J. L., Sul I. H., Youk J. H., Kang T. J.: Preparation of antimicrobial poly(vinyl alcohol) nanofibers containing silver nanoparticles. Journal of Polymer Science Part B: Polymer Physics, **44**, 2468–2474 (2006).
DOI: 10.1002/polb.20913

[34] Nguyen T-H., Lee K-H., Lee B-T.: Fabrication of Ag nanoparticles dispersed in PVA nanowire mats by microwave irradiation and electro-spinning. Materials Science and Engineering: C, **30**, 944–950 (2010).
DOI: 10.1016/j.msec.2010.04.012

[35] Pollo L. D., Duarte L. T., Anacleto M., Habert A. C., Borges C. P.: Polymeric membranes containing silver salts for propylene/propane separation. Brazilian Journal of Chemical Engineering, **29**, 307–314 (2012).
DOI: 10.1590/S0104-66322012000200011

[36] Shukur M. F., Ithnin R., Sonsudin F., Yahya R., Ahmad Z., Kadir M. F. Z.: Conduction mechanism and dielectric properties of solid biopolymer electrolyte incorporated with silver nitrate. Advanced Materials Research, **701**, 115–119 (2013).
DOI: 10.4028/www.scientific.net/AMR.701.115

[37] Suthanthiraraj S. A., Kumar R., Paul B. J.: Impact of ZrO_2 nanoparticles on ionic transport and electrochemical properties of nanocomposite gel polymer electrolyte: PPG (4000)–$AgCF_3SO_3$:ZrO_2. International Journal of Nanoscience, **10**, 241–246 (2011).
DOI: 10.1142/S0219581X11007855

[38] Rzayev Z. M. O., Şimşek M., Bunyatova U., Salamov B.: Novel colloidal nanofiber semiconductor electrolytes from solution blends of PVA/ODA–MMT, poly(itaconic anhydride-*alt*-2-vinyl-1,3-dioxalan) and its Ag-carrying polymer complex by reactive electrospinning. Colloids and Surfaces A: Physicochemical and Engineering Aspects, **492**, 26–37 (2016).
DOI: 10.1016/j.colsurfa.2015.12.011

[39] Dhakal T. R., Mishra S. R., Glenn Z., Rai B. K.: Synergistic effect of PVP and PEG on the behavior of silver nanoparticle-polymer composites. Journal of Nanoscience and Nanotechnology, **12**, 6389–6396 (2012).
DOI: 10.1166/jnn.2012.6561

[40] Jin W-J., Lee H. K., Jeong E. H., Park W. H., Youk J. H.: Preparation of polymer nanofibers containing silver nanoparticles by using poly(N-vinylpyrrolidone). Macromolecular Rapid Communications, **26**, 1903–1907 (2005).
DOI: 10.1002/marc.200500569

[41] Lambert J. B., Shurvell H. F., Verbit L., Cooks R. G., Stout G. H.: Organic structural analysis. Collier Macmillan, London (1976).

[42] Jenkins R., Snyder R. L.: Introduction to X-ray powder diffractometry. Wiley, New York (1996).

[43] Rzayev Z. M. O., Şenol B., Denkbaş E. B.: Functional copolymer/organo-montmorillonite nanoarchitectures. IX. Synthesis and nanostructure–morphology–thermal behaviour relationships of poly[(maleic anhydride)-*alt*-(acrylic acid)]/organo- montmorillonite nanocomposites. Polymer International, **60**, 1446–1454 (2011). DOI: 10.1002/pi.3099

[44] Li G., He D., Qian B., Guan B., Gao S., Cui Y., Yokoyama K., Wang L.: Fungus-mediated green synthesis of silver nanoparticles using *Aspergillus terreus*. International Journal of Molecular Sciences, **13**, 466–476 (2012). DOI: 10.3390/ijms13010466

[45] Peppas N. A., Tennenhouse D.: Semicrystalline poly (vinyl alcohol) films and their blends with poly(acrylic acid) and poly(ethylene glycol) for drug delivery applications. Journal of Drug Delivery Science and Technology, **14**, 291–297 (2004). DOI: 10.1016/S1773-2247(04)50050-3

[46] Berthier C., Gorecki W., Minier M., Armand M. B., Chabagno J. M., Rigaud P.: Microscopic investigation of ionic conductivity in alkali metal salts-poly(ethylene oxide) adducts. Solid State Ionics, **11**, 91–95 (1983). DOI: 10.1016/0167-2738(83)90068-1

[47] İşci S., Günister E., Ece O. T., Güngör N.: The modification of rheologic properties of clays with PVA effect. Materials Letters, **58**, 1975–1978 (2004). DOI: 10.1016/j.matlet.2004.01.001

[48] Jung H. M., Lee E. M., Ji B. C., Deng Y., Yun J. D., Yeun J. H.: Poly(vinyl acetate)/poly(vinyl alcohol)/ montmorillonite nanocomposite microspheres prepared by suspension polymerization and saponification. Colloid and Polymer Science, **285**, 705–710 (2007). DOI: 10.1007/s00396-006-1623-3

[49] Sengwa R. J., Sankhla S., Choudhary S.: Dielectric characterization of solution intercalation and melt intercalation poly(vinyl alcohol)-poly(vinylpyrrolidone) blend-montmorillonite clay nanocomposite films. Indian Journal of Pure and Applied Physics, **48**, 196–204 (2010).

[50] Sengwa R. J., Sankhla S.: Dielectric dispersion study of coexisting phases of aqueous polymeric solution: Poly(vinyl alcohol) + poly(vinyl pyrrolidone) two-phase systems. Polymer, **48**, 2737–2744 (2007). DOI: 10.1016/j.polymer.2007.03.030

[51] Kamoun E. A., Youssef M. E., Abu-Saied M. A., Fahmy A., Khalil H. F., Abdelhai F.: Ion conducting nanocomposite membranes based on PVA-HA-HAP for fuel cell application: II. Effect of modifier agent of PVA on membrane properties. Interantional Juornal of Electrochemical Science, **10**, 6627–6644 (2015).

[52] Gopalan A. I., Lee K-P., Hong M-H., Santhosh P., Manesh K. M., Kim S-H.: Nanostructuring of poly(diphenylamine) inside the galleries of montmorillonite organo clay through self-assembly approach. Journal of Nanoscience and Nanotechnology, **6**, 1594–1601 (2006). DOI: 10.1166/jnn.2006.240

[53] Kim S., Hwang E-J., Jung Y., Han M., Park S-J.: Ionic conductivity of polymeric nanocomposite electrolytes based on poly(ethylene oxide) and organo-clay materials. Colloids and Surfaces A: Physicochemical and Engineering Aspects, **313–314**, 216–219 (2008). DOI: 10.1016/j.colsurfa.2007.04.097

[54] Salahuddin N., Ayad M. M., Ali M.: Synthesis and characterization of polyaniline–organoclay nanocomposites. Journal of Applied Polymer Science, **107**, 1981–1989 (2008). DOI: 10.1002/app.27180

[55] Salamova U., Rzaev Z. M. O., Altindal Ş., Masimov A. A.: Effect of inorganic salts on the main parameters of the dilute aqueous poly(vinylpyrrolidone) solutions. Polymer, **37**, 2415–2421 (1996). DOI: 10.1016/0032-3861(96)85353-5

[56] Cho D., Hoepker N., Frey M. W.: Fabrication and characterization of conducting polyvinyl alcohol nanofibers. Materials Letters, **68**, 293–295 (2012). DOI: 10.1016/j.matlet.2011.10.109

[57] Schwaab M., Pinto J. C.: Optimum reference temperature for reparameterization of the Arrhenius equation. Part 1: Problems involving one kinetic constant. Chemical Engineering Science, **62**, 2750–2764 (2007). DOI: 10.1016/j.ces.2007.02.020

[58] Andersson O., Johari G. P.: Effect of pressure on thermal conductivity and pressure collapse of ice in a polymer-hydrogel and kinetic unfreezing at 1 GPa. Journal of Chemical Physics, **134**, 124903/1–124903/10 (2011). DOI: 10.1063/1.3568817

[59] Dawson A., Rides M., Nottay J.: The effect of pressure on the thermal conductivity of polymer melts. Polymer Testing, **25**, 268–275 (2006). DOI: 10.1016/j.polymertesting.2005.10.001

Study on an amine-containing benzoxazine: Homo- and copolymerization with epoxy resin

L. Zhang[1]*, M. Wang*[2]*, J. Wu*[1,2*]

[1]Department of Mechanical and Aerospace Engineering, The Hong Kong University of Science and Technology, Clear Water Bay, Kowloon, Hong Kong
[2]Center for Engineering Materials and Reliability, Fok Ying Tung Research Institute, The Hong Kong University of Science and Technology, Nansha, Guangzhou, China

Abstract. An amine-containing benzoxazine (P-deta) based homopolymer and its epoxy (Ep) copolymers are investigated in this study. The structure of benzoxazine, prepared from phenol, diethylenetriamine and formalin, is confirmed by Fourier transform infrared spectroscopy (FT-IR) and nuclear magnetic resonance spectroscopy (NMR). The viscosity of P-deta is much lower than that of commercialized benzoxazine monomers. The curing profiles of P-deta with various Ep ratios are studied by deconvolution and the related mechanism is clarified. Epoxy will not increase the curing temperature of P-deta, instead, it helps P-deta overcome the conversion limitation and promotes the curing rate. The thermal and viscoelastic properties were determined and compared. The copolymer of P-deta/Ep = 50/50 (wt/wt) shows the highest glass transition temperature, higher than both individual homopolymers and other copolymers. Increasing benzoxazine fraction enhances modulus at room temperature but deteriorates the crosslink density. It can also enhances the char yield, but deteriorates the thermal stability of the copolymers.

Keywords: thermosetting resins, benzoxazine, epoxy resin, copolymerization

1. Introduction

Polybenzoxazines constitute a new generation of thermosets, which combine the thermal properties of phenolic resins with the mechanical properties and the molecular design flexibility of epoxy resin [1]. Moreover, they possess other features, such as low flammability, low water absorption, high chemical resistance and minimal shrinkage upon curing [2]. Therefore, they are considered as promising materials in IC packaging, aerospace engineering and HT-PCB industry and become one of the rare new polymers commercialized in the nearest 30 years [3].

However, several disadvantages appear in practical use. For instance, the solid phase of most benzoxazine (Bz) monomers and the high liquefying temperature hinder their handling [2, 4]. Adding reactive diluents is one method to decrease the operation temperature, however, simultaneously sacrifice some properties, such as flexural strength and glass transition temperature (T_g) [5]. Another method is to develop more monomers with low liquefying temperature, but only very few related researches have been reported so far [4, 6].

Another drawback is the low crosslink density in consequence of hydrogen bonding constraint [7]. This can be addressed by copolymerization with epoxy resin (Ep), but will lead to higher curing temperature, known as Ep dilution effect [8]. Because epoxy group is inert to oxazine ring, introducing Ep dilutes the concentration of Bz, thus leads to higher Bz ring-opening temperature. Besides, copolymerization with Ep happens only when phenol generates after ring-

---

opening of Bz. Similar phenomena were also found in a main-chain type Bz/Ep binary copolymer [9]. In addition, Bz fraction should be larger than 50 mol% in order to achieve copolymers with good quality. Generally, two methods can overcome the challenges. One is introducing a reactive promoter. Based on the cationic ring-opening mechanism [10], various promoters have been reported till now, among which, phenols, thiols, amines and imidazoles have attracted intensive attention since they are applied in epoxy curing as well. In 2000, phenolic resin was first selected due to its wide application in electronic packaging [11, 12]. The material properties were significantly enhanced although the dilution effect still can be observed. Besides, Chow *et al*. [13] had used a phenol monomer, 4,4′-thiodiphenol to study the curing behavior of a Bz/Ep/phenol ternary system. In 2005, Rao and Pathak [14] managed to use a phenalkamine to prevent the dilution effect through prior reaction between phenalkamine and Ep at room temperature before mixing with Bz. More recently, Grishchuk *et al*. [15] selected aliphatic, cycloaliphatic and aromatic amines to fabricate the Bz/Ep copolymers. They found that amines, which are both reactive to Bz and Ep, can efficiently promote the copolymerization. In addition, they also found that the promotion effect was influenced by both amine type and amount. The related mechanism was later clarified by Sun *et al*. [16], who purposed that the promotion effect is based on the basicity of amines. Moreover, Ambrožič *et al*. [17] used o-dianisidine to prepare novel Ep-Bz emulsions for water-based coatings to ensure a highly cross-linked structure. Meanwhile, Zhao *et al*. [18] and Wang *et al*. [19] studied a Bz/Ep/imidazole ternary system, through which the curing steps were optimized to motivate reaction-induced phase separation so that toughness can be enhanced. Ručigaj *et al*. [20] had implemented a comprehensive study on the curing Bz with many accelerators with different functional groups. Based on the conversion prediction, 4,4′-thiodiphenol is considered as the most effective accelerator among them. However, the solid forms of Bz and many additives generally require pretreatment before polymerization. Another method is to incorporate reactive groups, such as amine, onto the Bz structures. But, only few studies have been reported until now due to relatively tedious preparation procedure [21, 22].

In this research, we attempted to apply a low viscous amine-containing Bz to facilitate processing, promote polymerization as well as achieve homo- and copolymers with good performance. Meanwhile, we also tried to find its differences from a Bz/Ep/amine ternary system. The present study deals with the synthesis of the Bz, preparation of its homopolymer and copolymers, investigation of the curing behavior as well as evaluation of the thermal and mechanical properties.

2. Experimental
2.1. Materials
All reagents for synthesis are commercially available and used as received. Phenol (99%), bisphenol A (99%), aniline (99%) and deuterated chloroform (with 0.03 vol% of tetramethylsilane as reference) were purchased from Aladdin Reagent (Shanghai) Co. Ltd., Shanghai, China. Formaldehyde solution (40 wt%), paraformaldehyde (96%), soldium sulfate anhydrous (99%), diethylenetriamine (DETA) (99%) and potassium bromide (99.5%) were acquired from Sigma-Aldrich, St. Louis, U.S. Sodium carbonate anhydrous (99.9%) and dichloromethane (99.8%) were obtained from VWR, Radnor, U.S. A bifunctional diglycidyl ether bisphenol A (DGEBA) based epoxy resin (E51, epoxy equivalent weight: 185–208 g/ep.) was supported by Wuxi resin company, Wuxi, China.

2.2. Sample preparation methods
2.2.1. Synthesis of N,N-bis[2-(3,4-dihydro-2H-1,3-benzoxazin-3-yl)ethyl] amine (P-deta)
The synthesis method is a modification of preparing a main-chain type benzoxazine polymer reported elsewhere [23, 24]. Specifically, phenol (18.8 g, 0.2 mol) was dissolved in dichloromethane (50 mL) in a 250 mL flask before adding DETA (10.3 g, 0.1 mol). The mixture was then kept below 10 °C in an ice bath and stirred when formaldehyde solution was added dropwise. The molar ratio is maintained at phenol:DETA:formaldehyde = 2:1:4. The mixture reacted overnight and the solution gradually changed from colorless to yellow. Later on, the mixture was washed by 1 N sodium carbonate solution and deionized water, respectively. After being dried by sodium sulfate anhydrous, the obtained liquid was dried under vacuum at room temperature to evaporate solvent before obtaining a homogeneous yellow viscous liquid (Yield = 85%).

2.2.2. Synthesis of benzoxazine precursor (BA-a)

For comparison, N-phenyl bisphenol A based benzoxazine precursor (BA-a) was prepared according to the solventless method patented by Ishida [25]. (Yield > 90%)

2.2.3. Preparation of P-deta homopolymer and P-deta/Ep copolymers

P-deta was mixed with Ep under room temperature at ratios of P-deta:Ep = 100/0, 75/25, 50/50 and 25/75 (wt/wt) before intensively stirring for 5 min. After degassing at 50 °C for 10 min, all of them were stepwise cured at 125 °C/1 h, 150 °C/1 h and 180 °C/4 h.

2.3. Characterization methods

The Fourier transform infrared spectroscopy (FT-IR) spectra of P-deta were recorded by a Bruker TENSOR27 FT-IR spectrometer (Bruker Corporation, Karlsruhe, Germany) with 16 scans at a 4 cm^{-1} resolution. It was also applied to monitor the curing process underwent isothermal treatment (100, 125, 150, 175, 200 °C). Potassium bromide (KBr) pellet technique was used.

The structures of the compounds were verified by nuclear magnetic resonance spectroscopy (NMR) using a Varian Mercury VX 300 NMR, Varian Inc., Palo Alto, U.S. The characterization was conducted at room temperature using deuterated chloroform (CDCl$_3$) as solvent and tetramethylsilane (TMS) as internal standard.

The viscosity of the precursors was recorded by a rheometer, (AR2000ex, TA Instrument, New Castle, U.S.) under steady shear mode. The rotation frequency was set at 1 s^{-1} with a temperature range from room temperature to above gel point and a heating rate of 2 °C/min. The polymerization processes of all samples were monitored by a differential scanning calorimeter (DSC), (Q200, TA Instrument, New Castle, U.S.). All samples with 3–5 mg were sealed in aluminum pans before measurement. The thermograms were obtained at a heating rate of 10 °C/min from room temperature to 300 °C under nitrogen atmosphere.

The viscoelastic properties of all samples were investigated by a dynamic mechanical analyzer (DMA), (Q800, TA Instrument, New Castle, U.S). The specimen dimension was 10×70×2 mm. The measurement was performed in a three-point bending mode with 50 mm span length at a frequency of 1 Hz with a strain value of 0.1% and a heating rate of 2 °C/min. The glass transition temperature (T_g) was determined by the peak temperature of loss factor (tan δ).

The thermal stability and char yield are characterized through a thermogravimetric analyzer (TGA), (Q50, TA Instrument, New Castle, U.S.). The test was performed under nitrogen atmosphere at a heating rate of 10 °C/min.

3. Results and discussion

3.1. Characterization of P-deta

The structure of P-deta was first studied by FT-IR, as shown in Figure 1. The reaction scheme is plotted in Figure 1 as well. The formation of oxazine ring was evidenced by the peak at 930 cm^{-1} (1,2-substituted benzene with oxazine ring attaching), the sy4mmetric and asymmetric stretching of C–O–C at 1034 and 1226 cm^{-1}, and the peak at 1150 cm^{-1} which indicates the formation of C–N–C bond. The peak at 1489 and 756 cm^{-1} prove the presence of an ortho-substituted benzene ring. Since hydroxyl group is removed by base washing, the shoulder peak near 3300 cm^{-1} is assigned to the heavily overlapped hydrogen bonded amino group. These results confirm the formation of the P-deta.

NMR was further applied to characterize the structures, the results of which are shown in Figure 2. Specifically, the characteristic proton resonances at 4.0 and 4.9 ppm are corresponding to the Ar–CH$_2$–N and N–CH$_2$–O structures of oxazine ring, respectively. The resonances at 6.8–7.2 ppm are assigned to the protons on aromatic rings. The peaks in the range of 3.7–3.9 ppm were assigned to Ar–CH$_2$–N and N–CH$_2$–N structures, which has been reported in other literatures as well [16, 23, 24]. A resonance chemical shift at 3.5 ppm confirms the formation of N–H. The aliphatic groups of amines are confirmed by the resonances at 2.7–2.9 ppm, respectively. The
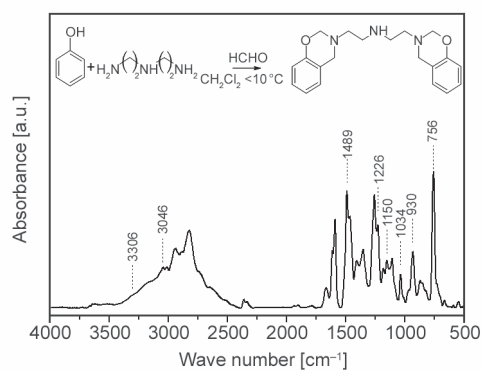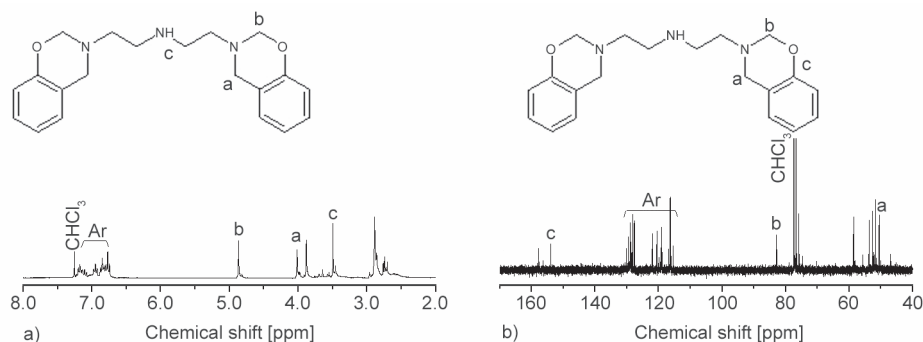

Figure 1. FT-IR spectrum of P-deta

Figure 2. (a) ^{1}H-NMR and (b) ^{13}C-NMR results of P-deta

product was also characterized by ^{13}C-NMR (Figure 2b). The characteristic oxazine rings appear at 83 and 50 ppm. The peaks at 115–130 and 154 ppm indicate the phenyl carbons. The chemical shift at 158 ppm is assigned to the ring-opened Bz structures. The chemical shift at 76 ppm confirms the existence of triazine structure. The peaks between 50–60 ppm indicate various Ar–CH$_2$–N and N–CH$_2$–N structures, which is consistent with the ^{1}H-NMR results.

Before polymerization, the viscosity of P-deta and P-deta/Ep mixture was investigated (Figure 3). A typical benzoxazine monomer, BA-a, was used for reference. Comparing with BA-a, the viscosity of P-deta is very low (<1 Pa·s) under room temperature. This makes it suitable for some specific processing methods, like resin transfer molding (RTM). The storage condition can significantly change the viscosity of P-deta. It can be seen that the viscosity of P-deta increased to above 2000 Pa·s after being kept under room temperature for more than 1.5 month, which is due to the ring-opening of benzoxazine caused by amines. Therefore, low temperature storage is required for the resin. Here, the gel point is defined as the temperature when viscosity suddenly increases to above 100 Pa·s, and the processing window is de-

fined as the temperature range, within which the viscosity of the sample is lower than 100 Pa·s. The gel point of P-deta/Ep (50/50, wt/wt) mixture is at 150 °C, while it is more than 200 °C where BA-a reaches its gel point. The gel point of pure P-deta cannot be determined due to the extremely low viscosity when heated P-deta up to 100 °C. The processing window of P-deta/Ep (50/50, wt/wt) mixture is larger than 125 °C (R.T. to 150 °C).

3.2. Polymerization of P-deta and P-deta/Ep mixtures

DSC and FT-IR were applied to investigate the polymerization of P-deta and P-deta/Ep mixtures of various ratios. Comparing with the reported mono-curing peak of BA-a [15], multi-curing peaks can be found in P-deta, which can be assigned to several different reactions. In fact, it becomes more complicated when Ep is introduced. In order to clarify the possible reaction of each peak, the curing profiles of P-deta and P-deta/Ep mixtures have been deconvoluted. The DSC profiles and peaks achieved by deconvolution are summarized in Figure 4. Specifically, three peaks appear during P-deta homopolymerization which, from low to high temperature, are related to amine catalyzed Bz ring-opening, Bz thermal-in-
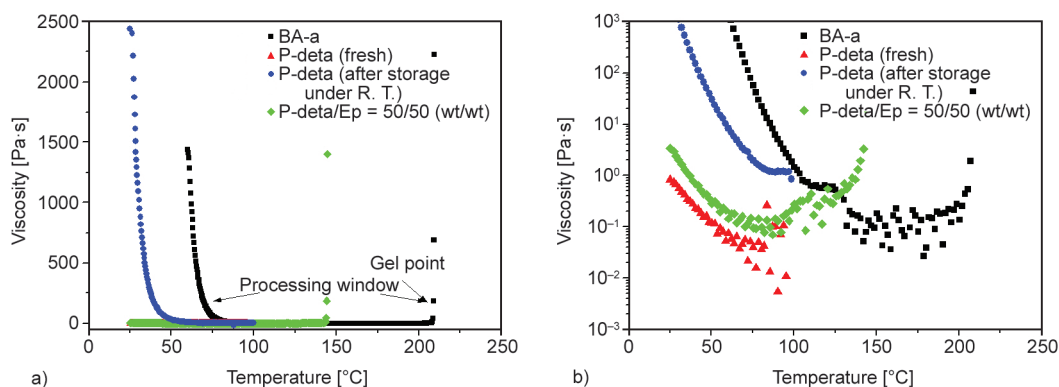

Figure 3. (a) Prcessing window and (b) viscosity of P-deta, P-deta/Ep (50/50, wt/wt) and BA-a
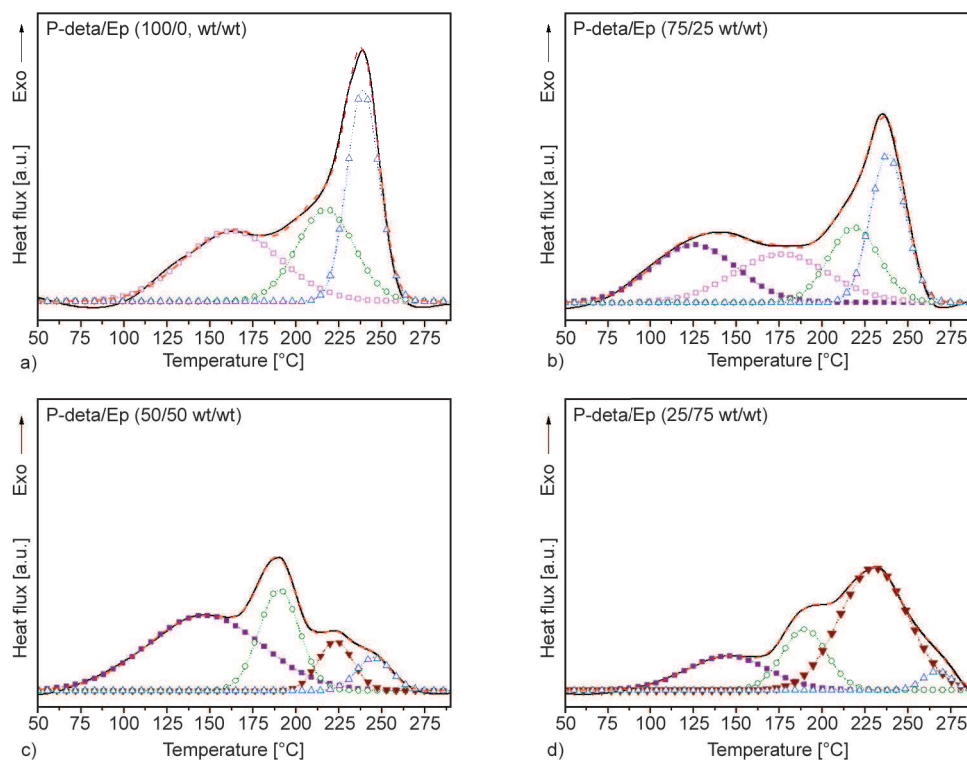
Figure 4. DSC profiles (solid line) and deconvolution peaks (dash line) of P-deta with different amount of Ep. (P-deta/Ep = (a) 100/0, (b) 75/25, (c) 50/50 and (d) 25/75, wt/wt). Peak assignment: (□) amine-catalyzed Bz ring-opening; (■) amine-Ep ring-opening; (○) Bz ring-opening; (△) intermediate conversion; (▼) hydroxyl-Ep ring-opening.

duced polymerization and conversion of amine-Bz intermediate to final structure [16], respectively. It is worth to note that, intermediate conversion can happen at the temperature either higher [16] or lower [15] than the origin, it is higher than Bz polymerization in this case. When mixed with Ep at P-deta/Ep = 75/25 (wt/wt), one additional peak can be found at low temperature range. It can be assigned to the reaction between amine and Ep, which takes place at relatively low temperature. This reaction can also be proved by the shift of onset temperature from 90 °C to 60–70 °C as long as Ep was added. Further increasing Ep amount to 50 wt.% (Figure 4c) leads to an increase in intensity at 190 °C but a decrease around 240 °C. Although the peak at 190 °C is close to the second peak position in Figure 4b, it is impossible due to large consumption of amine during amine-Ep reaction. In fact, it is probably caused by Bz ring-opening, which is promoted by the hydroxyl group due to the same reaction [26]. The rest small amount of excess Ep can react with phenol (generated after Bz ring-opening) or hydroxyl group, which results in the third peak in Figure 4c. The intensity is obviously enhanced in Figure 4d due to the increase of Ep to 75 wt%. In addition, the last tiny peaks in both Figure 4c and Figure 4d may be as-

signed to the conversion of intermediate. Since the reactions between amine-Bz and amine-Ep are partially overlapped, it is possible that a small portion of amine reacts with Bz when simultaneously most of it reacts with Ep. It is worth to mention that, by prior reaction between Ep and amine (in Bz), the dilution effect caused by Ep can be eliminated, based on our study.

The possible reactions take place during the polymerization were further investigated through FT-IR, as shown in Figure 5. The samples are partially cured under different isothermal conditions. Concerning P-deta (Figure 5a and 5b), the peak at 930 cm^{-1}, which represents the out-of-plane bending of benzene ring with oxazine ring being attached, dramatically decreases after heating at 125 °C for 1 hour and almost disappeared after heating at 150 °C. The decrease of overlapped peaks near 3300 cm^{-1} proved the amine-promoted ring-opening process. The intensity increase around 3450 cm^{-1} is attributed to the hydroxyl group, which formed after Bz ring-opening. Moreover, the intensity decrease at 1489 cm^{-1}, which represents the consumption of Bz. However, no observable intensity change can be found in BA-a even heated at 175 °C for 1 hour (Figure 5c, 942 cm^{-1}). It is until 200 °C that most of the BA-a precursors un-
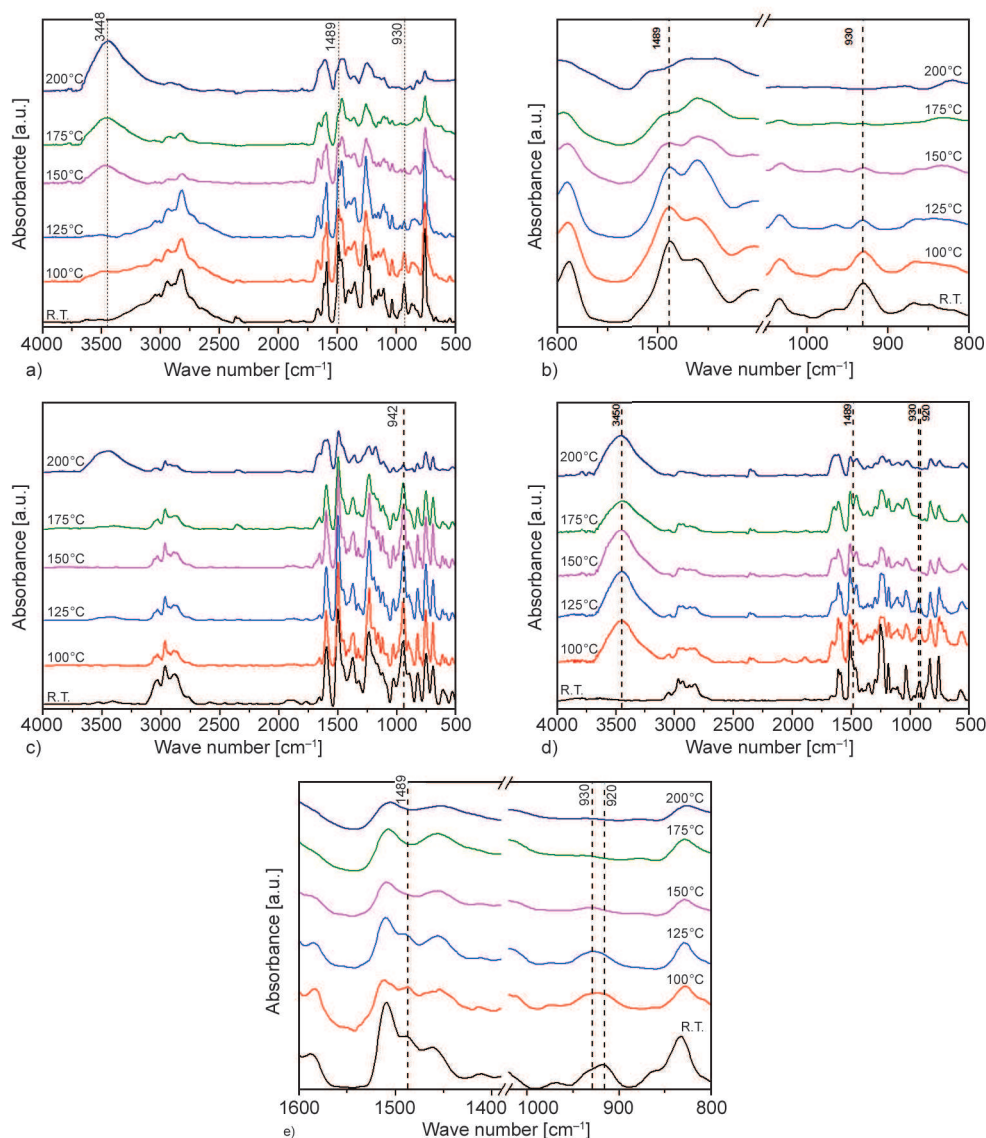
Figure 5. FT-IR spectra of (a) and (b) P-deta, (c) BA-a and (d) and (e) P-deta/Ep = 50/50 (wt/wt) after isothermally cured at 100, 125, 150, 175 and 200 °C for 1 hour, respectively

dergo ring-opening polymerization. The curing process changes when Ep was introduced. The FT-IR results of P-deta/Ep = 50/50 (wt/wt) are summarized in Figure 5d. Comparing with P-deta precursor, a conspicuous peak at 3450 cm^{-1} can be found even heated at 100 °C for 1 hour, which is attributed to the hydroxyl groups generated after the reaction between amine and Ep. This is also proved by the decrease at 920 cm^{-1} in Figure 5e, which represents the epoxy ring. Besides, the peaks at 1489 cm^{-1} (1,2-substituted benzene ring) and 930 cm^{-1} (out-of-plane benzene ring with oxazine attaching) disappear at 150 °C, which confirmed the ring-opening of oxazine as well. These results are consistent with the DSC peaks observed in Figure 4.

The partially cured polymers under isothermal conditions are examined by DSC as well (Figure 6). The degree of conversion (α) in Figure 6d is calculated through Equation (1), based on the DSC thermograms:

$$\alpha\,[\%] = \left(1 - \frac{\Delta H_p}{\Delta H_0}\right) \cdot 100 \qquad (1)$$

where ΔH_p is the curing enthalpy change of the partially cured samples and ΔH_0 is the curing enthalpy change of the original samples. Initially, the conversion rate of P-deta is much faster than BA-a, due to the amine-promoted ring-opening reaction. However, the degree of conversion reached a limit and no further progress was observed. Comparing with Fig-
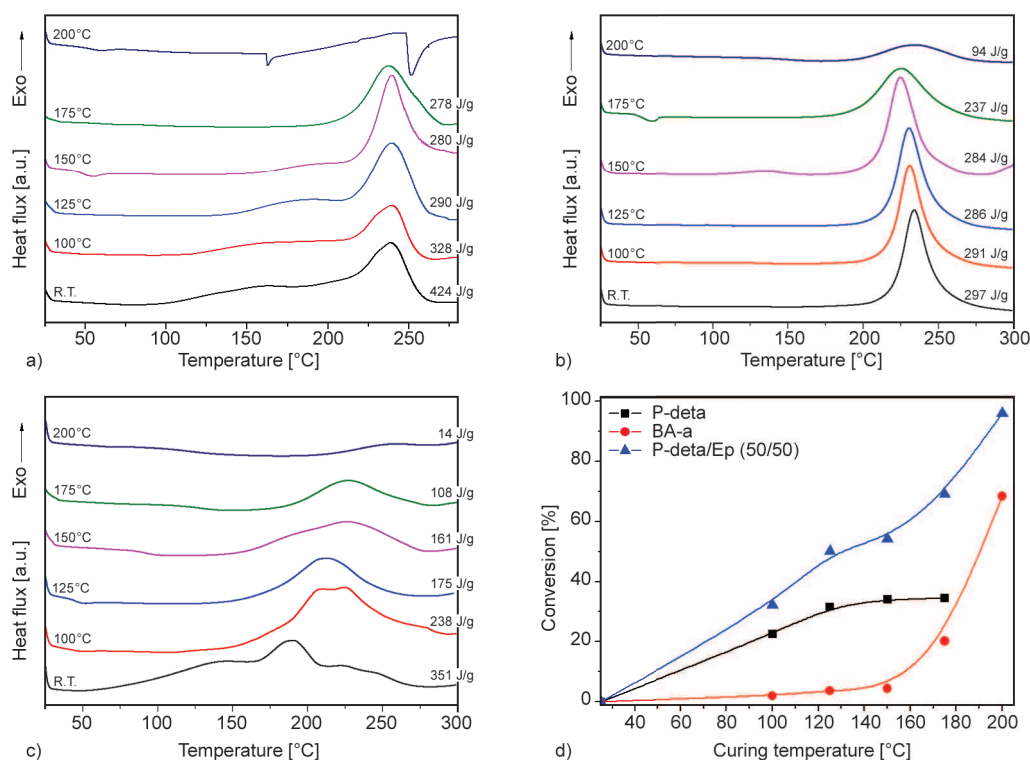
Figure 6. DSC thermograms of (a) P-deta, (b) BA-a, (c) P-deta/Ep = 50/50 (wt/wt) and (d) conversion based on enthalpy change after isothermal curing at 100, 125, 150, 175 and 200 °C for 1 hour, respectively

ure 4, the residue peak in Figure 6a at above 150 °C is assigned to intermediate conversion. It cannot be the Bz ring-opening, otherwise, the conversion (Figure 6d) will be more like a autocatalytic process, similar to BA-a, rather than reached a limit. Copolymerization of Ep and P-deta changes the reactions, thus conversion will not be confined by the equilibrium, as shown in Figure 6c and 6d. A mixture of P-deta/Ep = 50/50 (wt/wt) can almost be thoroughly cured after heating at 200 °C for 1 hour. Besides, the conversion rate of P-deta/Ep mixture is higher than P-deta and BA-a. This is attributed to the hydroxyl group generated from the reaction between epoxide and amine, which can promote the ring-opening polymerization of Bz [26].

3.3. Thermal and viscoelastic properties of P-deta and its epoxy alloy

The storage moduli and loss factors of all samples are measured through DMA, and the results are shown in Figure 7. The important data is summarized in Table 1. It is worth to note that, a P-deta/Ep = 25/75 (wt/wt) copolymer, beyond the mixing limit (Bz > 50%) of general Bz/Ep binary system [8], had been successfully prepared with good mechanical properties. This is due to the reaction between amine in P-deta and Ep. Besides, amine can increase the
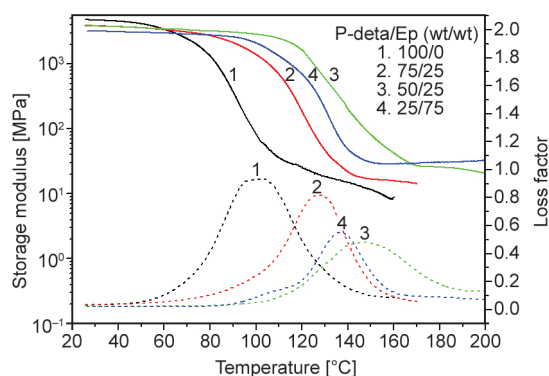

Figure 7. Storage moduli (E') and mechanical loss factors (tan δ) as a function of temperature for P-deta/Ep mixtures at various ratios

hydrogen bond density, thus enhances the storage modulus at room temperature of P-deta homopolymer (4.8 GPa). The modulus of copolymers decreases with the increase of Ep fraction. This is due to the concentration of hydrogen bond density of Bz decreases when Ep is incorporated. Moreover, since glass state stiffness is related to the resistance of molecular segments motion, the DGEBA structure appears less able to store elastic energy, which leads to a lower modulus than Bz [9]. The peak temperature of loss factor is applied to determine the T_g of the samples. Unlike modulus, the T_g of P-deta homopolymer is relatively low (100 °C). The highest T_g at 147 °C

is obtained in a P-deta/Ep (50/50, wt/wt) copolymer, which is 47 °C higher than P-deta homopolymer and 17 °C higher than the reported Ep (cured by DETA) [15]. It is interesting to find that the result is quite different from the Bz/Ep/amine ternary copolymers, the T_g of which is between the Bz and Ep homopolymers or worse [15, 27]. In fact, it is more close to Bz/Ep binary copolymers, which has a T_g higher than both homopolymers at certain mixing ratios [10]. Specifically, at low Ep fraction, the polymer network is enhanced by Ep-amine and Ep-hydroxyl reactions. When Ep amount is in excess, it acts as a plasticizer to deteriorate the mechanical properties. The mono-peak of tan δ showed that no apparent phase separation can be found, which is consistent with other Bz/Ep binary systems [8]. The height and width of tan δ are summarized in Table 1. The 50/50 copolymer shows the lowest tanδ height, which indicates strongest segmental restriction. The FWHM (full width at half mount) of tan δ implies the variety of structure species. Although no certain trend of FWHM can be observed among all samples, the FWHM of 50/50 sample shows the largest FWHM value (43 °C), which indicates the most various structures in the polymer. Based on the statistical theory on rubbery elasticity [28], the crosslink density can be estimated through Equation (2) by obtaining the elastic modulus in rubbery state:

$$\nu = \frac{E'_R}{3\varphi RT} \qquad (2)$$

where ν is the crosslink density, R is the gas constant and φ equals to 1 for ideal rubber. In this experiment, the elastic modulus E'_R is selected at the absolute temperature T equals to $T_g + 30$ °C. It is worth to note that, this equation is only valid in light crosslink polymers since high crosslink density results in a failure of Gaussian chain assumption [29, 30]. Therefore, an empirical Nielsen equation (Equation (3)),
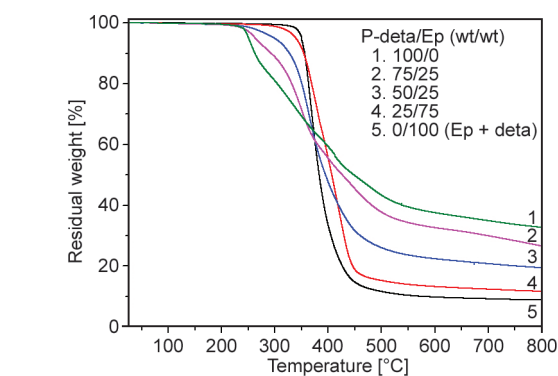

Figure 8. TGA thermograms of P-deta and P-deta/Ep polymers

which shows better results among high crosslink structures, is also selected here [31]:

$$\lg\left(\frac{E'_R}{3}\right) = 7 + 293\nu \qquad (3)$$

The calculated results based on both methods are concluded in Table 1. Specifically, the crosslink density of P-deta is very low, which is 1790 and 2660 mol/m³ based on different calculation methods. Increasing Ep fraction was found to enhance the crosslink density of the copolymers, which is consistent with the trend of Bz/Ep binary copolymers [8] but different from some Bz/Ep/amine ternary copolymers [14, 27]. The thermal stability of all samples was studied by TGA (Figure 8) and the results have been summarized in Table 1. The decomposition temperature of P-deta homopolymer is similar to MCBP BA-tepa [24] and P-ad6 [32]. The similar aliphatic diamine structure is probably the dominant cause of the initial decomposition. Incorporation of Ep enhances the thermal stability of the copolymers. This can be explained by the increase in crosslink density when increasing the Ep fraction. Meanwhile, the residual weight after heating at 800 °C becomes lower when less Bz is introduced into the copolymers. The decrease in char yield percentage is quite consistent

Table 1. Viscoelastic and thermal properties of P-deta and P-deta/Ep polymers

Sample (P-deta/Ep, wt/wt)	T_g [°C][a]	E' [MPa]		Crosslink density [·10³ mol/m³]		Loss factor		$T_{5\%}$ [°C][b]	Char yield [%][c]
		RT	$T_g + 30$ °C	Rubber elasticity	Nielsen's equation	FWHM [°C]	Height		
100/0	100	4785	18	1.79	2.66	37	0.93	251	33
75/25	128	3876	16	1.49	2.48	30	0.82	263	27
50/50	147	3928	26	2.32	3.20	43	0.43	299	20
25/75	137	3220	29	2.64	3.36	26	0.55	339	12
0/100[d]	130[e]	2690[e]	33[e]	3.06[e]	3.55	–	–	350	9

[a]peak temperature of tan δ; [b]temperature at which 5% weight loss is monitored; [c]weight residue at 800 °C; [d]Ep was cured by DETA; [e]data obtained from reference [15].

with the decrease in benzoxazine fraction. Apparently, rather than crosslink density, Bz fraction is more dominant to determine the char yield of the copolymers.

In summary, comparing with a Bz monomer (P-ad6 in [32]) and a main-chain type Bz polymer (BA-tepa in [24]) of similar molecular structures, P-deta homopolymer exhibits higher modulus under room temperature than both while thermal stability and char yield in-between. P-deta/Ep copolymers inherits the high modulus from P-deta homopolymer. Meanwhile, they also show comparable properties with other Bz/Ep binary copolymers [8] and Bz/Ep/amine tertiary copolymers [14, 15] in T_g, crosslink density and char yield. The thermal stability is worse when P-deta fraction in the copolymers is high.

4. Conclusions

This study focuses on an amine-containing Bz prepared from phenol, diethylenetriamine and formaldehyde, its homopolymerization and copolymerization with Ep. The viscosity of P-deta is lower than 1 Pa·s, which is much lower than BA-a and suitable for low temperature RTM. Polymerization of P-deta undergoes amine-promoted ring-opening, Bz ring-opening and intermediate conversion. However, the conversion is confined to lower than 40%, based on enthalpy calculation. Mixing Ep-with P-deta changes reaction pathways. The copolymerization can be sufficiently proceeded with a faster conversion than P-deta and BA-a. The limit of Bz fraction (>50%) and the dilution effect of EP in general Bz/Ep binary system are eliminated in this study. The viscoelastic properties of the homo- and copolymers are also studied. At a 50/50 (wt/wt) ratio, the copolymer exhibits higher T_g than both P-deta homopolymer and Ep cured by DETA. This is quite different from those ternary systems, in which amines were introduced as additives. Accompanied with increasing Ep fraction, the crosslink density is enhanced, while the moduli at room temperature is decreased. Concerning the thermal properties, incorporating more Ep improves the thermal stability of the copolymer, although the char yield becomes less. In conclusion, P-deta homopolymer and P-deta/Ep copolymers show comparable properties with many other reported Bz polymer and copolymer systems, while the liquid phase and low viscosity make it more attractive than those solid Bz in application.

References

[1] Ning X., Ishida H.: Phenolic materials via ring-opening polymerization of benzoxazines: Effect of molecular structure on mechanical and dynamic mechanical properties. Journal of Polymer Science Part B: Polymer Physics, 32, 1121-1129 (1994).
DOI: 10.1002/polb.1994.090320515

[2] Ishida H., Agag T.: Handbook of benzoxazine resins. Elsevier, Amsterdam (2011).

[3] Zhang L., Zhu Y., Li D., Wang M., Chen H., Wu J.: Preparation and characterization of fully renewable polybenzoxazines from monomers containing multi-oxazine rings. RSC Advances, 5, 96879–96887 (2015).
DOI: 10.1039/c5ra17164d

[4] Xu G-M., Shi T., Liu J., Wang Q.: Preparation of a liquid benzoxazine based on cardanol and the thermal stability of its graphene oxide composites. Journal of Applied Polymers Science, 131, 40353/1–40353/8 (2014).
DOI: 10.1002/app.40353

[5] Jubslip C., Takeichi T., Rimdusit S.: Effect of novel benzoxazine reactive diluent on processability and thermomechanical characteristics of bi-functional polybenzoxazine. Journal of Applied Polymer Science, 104, 2928–2938 (2007).
DOI: 10.1002/app.25929

[6] Shi J., Zheng X., Xie L., Cao F., Wu Y., Liu W.: Film-forming characteristics and thermal stability of low viscosity benzoxazines derived from melamine. European Polymer Journal, 49, 4054–4061 (2013).
DOI: 10.1016/j.eurpolymj.2013.09.011

[7] Ishida H., Allen D. J.: Physical and mechanical characterization of near-zero shrinkage polybenzoxazines. Journal of Polymer Science Part B: Polymer Physics, 34, 1019–1030 (1996).
DOI: 10.1002/(SICI)1099-0488(19960430)34:6<1019:: AID-POLB1>3.0.CO;2-T

[8] Ishida H., Allen D. J.: Mechanical characterization of copolymers based on benzoxazine and epoxy. Polymer, 37, 4487–4495 (1996).
DOI: 10.1016/0032-3861(96)00303-5

[9] Uchida S., Kawauchi T., Furukawa N., Takeichi T.: Polymer alloys of high-molecular-weight benzoxazine and epoxy resin. High Performance Polymers, 26, 846–855 (2014).
DOI: 10.1177/0954008314532480

[10] Wang Y-X., Ishida H.: Cationic ring-opening polymerization of benzoxazines. Polymer, 40, 4563–4570 (1999).
DOI: 10.1016/S0032-3861(99)00074-9

[11] Rimdusit S., Ishida H.: Synergism and multiple mechanical relaxations observed in ternary systems based on benzoxazine, epoxy, and phenolic resins. Journal of Polymer Science Part B: Polymer Physics, **38**, 1687–1698 (2000).
DOI: 10.1002/1099-0488(20000701)38:13<1687::AID-POLB20>3.0.CO;2-T

[12] Rimdusit S., Ishida H.: Development of new class of electronic packaging materials based on ternary systems of benzoxazine, epoxy, and phenolic resins. Polymer, **41**, 7941–7949 (2000).
DOI: 10.1016/S0032-3861(00)00164-6

[13] Chow W. S., Grishchuk S., Burkhart T., Karger-Kocsis J.: Gelling and curing behaviors of benzoxazine/epoxy formulations containing 4,4′-thiodiphenol accelerator. Thermochimica Acta, **543**, 172–177 (2012).
DOI: 10.1016/j.tca.2012.05.015

[14] Rao B. S., Pathak S. K.: Thermal and viscoelastic properties of sequentially polymerized networks composed of benzoxazine, epoxy, and phenalkamine curing agents. Journal of Applied Polymer Science, **100**, 3956–3965 (2006).
DOI: 10.1002/app.23008

[15] Grishchuk S., Mbhele Z., Schmitt S., Karger-Kocsis J.: Structure, thermal and fracture mechanical properties of benzoxazine-modified amine-cured DGEBA epoxy resins. Express Polymer Letters, **5**, 273–282 (2011).
DOI: 10.3144/expresspolymlett.2011.27

[16] Sun J., Wei W., Xu Y., Qu J., Liu X., Endo T.: A curing system of benzoxazine with amine: Reactivity, reaction mechanism and material properties. RSC Advances, **5**, 19048–19057 (2015).
DOI: 10.1039/c4ra16582a

[17] Ambrožič R., Šebenik U., Krajnc M.: Novel epoxy-benzoxazine water-based emulsions with reactive benzoxazine surfactants for coatings. Express Polymer Letters, **8**, 574–587 (2014).
DOI: 10.3144/expresspolymlett.2014.61

[18] Zhao P., Zhou Q., Deng Y. Y., Zhu R. Q., Gu Y.: Reaction induced phase separation in thermosetting/thermosetting blends: Effects of imidazole content on the phase separation of benzoxazine/epoxy blends. RSC Advances, **4**, 61634–61642 (2014).
DOI: 10.1039/c4ra10484f

[19] Wang H., Zhao P., Ling H., Ran Q., Gu Y.: The effect of curing cycles on curing reactions and properties of a ternary system based on benzoxazine, epoxy resin, and imidazole. Journal of Applied Polymer Science, **127**, 2169–2175 (2013).
DOI: 10.1002/APP.37778

[20] Ručigaj A., Alič B., Krajnc M., Šebenik U.: Curing of bisphenol A-aniline based benzoxazine using phenolic, amino and mercapto accelerators. Express Polymer Letters, **9**, 647–657 (2015).
DOI: 10.3144/expresspolymlett.2015.60

[21] Agag T., Arza C. R., Maurer F. H. J., Ishida H.: Primary amine-functional benzoxazine monomers and their use for amide-containing monomeric benzoxazines. Macromolecules, **43**, 2748–2758 (2010).
DOI: 10.1021/ma902556k

[22] Kawaguchi A. W., Sudo A., Endo T.: Thiol-functionalized 1,3-benzoxazine: Preparation and its use as a precursor for highly polymerizable benzoxazine monomers bearing sulfide moiety. Journal of Polymer Science Part A: Polymer Chemistry, **52**, 1448–1457 (2014).
DOI: 10.1002/pola.27131

[23] Chaisuwan T., Komalwanich T., Luangsukrerk S., Wongkasemjit S.: Removal of heavy metals from model wastewater by using polybenzoxazine aerogel. Desalination, **256**, 108–114 (2010).
DOI: 10.1016/j.desal.2010.02.005

[24] Alhwaige A. A., Agag T., Ishida H., Qutubuddin S.: Biobased chitosan/polybenzoxazine cross-linked films: Preparation in aqueous media and synergistic improvements in thermal and mechanical properties. Biomacromolecules, **14**, 1806–1815 (2013).
DOI: 10.1021/bm4002014

[25] Ishida H.: Process for preparation of benzoxazine compounds in solventless systems. U.S. Patent 5543516, USA (1996).

[26] Baqar M., Agag T., Huang R., Maia J., Qutubuddin S., Ishida H.: Mechanistic pathways for the polymerization of methylol-functional benzoxazine monomers. Macromolecules, **45**, 8119–8125 (2012).
DOI: 10.1021/ma301963d

[27] Grishchuk S., Schmitt S., Vorster O. C., Karger-Kocsis J.: Structure and properties of amine-hardened epoxy/benzoxazine hybrids: Effect of epoxy resin functionality. Journal of Applied Polymer Science, **124**, 2824–2837 (2012).
DOI: 10.1002/app.35302

[28] Tobolsky A. V.: Properties and structure of polymers. Wiley, New York, (1962).

[29] Katz D., Tobolsky A. V.: Rubber elasticity in highly crosslinked polyesters. Journal of Polymer Science Part A: Polymer Chemistry, **2**, 1587–1594 (1964).
DOI: 10.1002/pol.1964.100020405

[30] Katz D., Tobolsky A. V.: Rubber elasticity in highly crosslinked polyethyl acrylate. Journal of Polymer Science Part A: Polymer Chemistry, **2**, 1595–1605 (1964).
DOI: 10.1002/pol.1964.100020406

[31] Nielsen L. E.: Mechanical properties of polymers and composites, Vol. I. Marcel Dekker, New York (1983).

[32] Allen D. J., Ishida H.: Effect of phenol substitution on the network structure and properties of linear aliphatic diamine-based benzoxazines. Polymer, **50**, 613–626 (2009).
DOI: 10.1016/j.polymer.2008.11.007